

# UC San Diego

## UC San Diego Electronic Theses and Dissertations

### Title

Non-Equilibrium Simulations of Defects, Damage, and Phase Transformations in Extreme Regimes

### Permalink

<https://escholarship.org/uc/item/79j2w03v>

### Author

Hahn, Eric Nicholas

### Publication Date

2016

Peer reviewed|Thesis/dissertation

UNIVERSITY OF CALIFORNIA, SAN DIEGO

Non-Equilibrium Simulations of Defects, Damage, and Phase Transformations  
in Extreme Regimes

A dissertation submitted in partial satisfaction of the  
requirements for the degree of Doctor of Philosophy

in

Materials Science and Engineering

by

Eric Nicholas Hahn

Committee in charge:

Marc A. Meyers, Chair  
Gaurav Arya  
Farhat Beg  
Brian Maple  
Vitali Nesterenko  
Bruce A. Remington

2016

Copyright

Eric Nicholas Hahn, 2016

All rights reserved.

The Dissertation of Eric Nicholas Hahn is approved, and is acceptable in quality and form for publication on microfilm and electronically:

---

---

---

---

---

---

---

Chair

University of California, San Diego

2016

# Dedication

To my mother and father,  
Ann Elizabeth Hahn and Steven Richard Hahn.

Eric Nicholas Hahn

## Epigraph

*We may regard the present state of the universe as the effect of its past and the cause of its future. An intellect which at a certain moment would **know all forces that set nature in motion, and all positions of all items of which nature is composed**, if this intellect were also vast enough to **submit these data to analysis**, it would embrace in a single formula the movements of the greatest bodies of the universe and those of the tiniest atom; for such an intellect **nothing would be uncertain** and the future just like the past would be present before its eyes.*

— Pierre Simon Laplace, *A Philosophical Essay on Probabilities*

# Table of Contents

Signature Page .....	iii
Dedication .....	iv
Epigraph.....	v
Table of Contents .....	vi
List of Figures .....	x
List of Tables .....	xviii
Acknowledgements.....	xix
Vita.....	xxiv
ABSTRACT OF THE DISSERTATION .....	xxv
1. Introduction .....	1
1.1. Research Objectives .....	2
1.2. Motivation .....	3
2. Background.....	7
2.1. Compression.....	8
2.1.1. Laser Compression.....	10
2.2. Isentropic Release .....	14
2.2.1. Ultimate Tensile/Cohesive Strength .....	23
2.3. Crystalline Structure and Defects Therein .....	30

2.3.1.	Dislocations.....	30
2.3.2.	Grain Boundaries .....	31
3.	Molecular Dynamics.....	38
3.1.	Computational capability: present and predictions .....	38
3.2.	Simulation Process .....	44
3.2.1.	Initialization .....	45
3.2.2.	Equilibration and Ensembles .....	46
3.2.3.	Run Integration .....	47
3.3.	Simulation Codes .....	48
3.3.1.	LAMMPS.....	48
3.3.2.	SPASM .....	48
3.4.	Simulation Set-up.....	49
3.4.1.	Single Crystalline Structures.....	50
3.4.2.	Polycrystalline Structures .....	50
3.4.3.	Non-Equilibrium Molecular Dynamics .....	52
3.5.	Pre, Peri, and Post-Processing.....	57
3.5.1.	Strain-Rate .....	59
3.5.2.	Stress State .....	59
3.5.3.	Temperature .....	60



3.5.4.	Centro-Symmetry Parameter .....	61
3.5.5.	Common Neighbor Analysis (CNA) .....	63
3.5.6.	Coordination; Pair Correlation Function .....	64
3.5.7.	Dislocation Extraction Algorithm; Crystal Analysis Tool.....	65
3.6.	Interatomic Potentials.....	67
3.6.1.	Tantalum .....	69
3.6.2.	Silicon .....	73
4.	Results and Discussion .....	84
4.1.	Tantalum.....	84
4.1.1.	Bicrystals.....	84
4.1.2.	Tensile “Spall” Failure.....	93
4.1.2.1.	Specific Spall Methods.....	95
4.1.2.2.	Spall Strength as a Function of Strain Rate.....	98
4.1.2.3.	Spalling of Single Crystalline Tantalum .....	103
4.1.2.4.	Spall of Nano and Crystalline Tantalum .....	113
4.1.2.5.	The Role of Temperature during and after Spall Failure .....	119
4.1.2.6.	Theoretical Predictions of Tensile Strength .....	123
4.1.3.	Phase Transformation .....	125
4.2.	Silicon.....	130

4.2.1.	Hugoniot Elastic-Plastic Limit.....	134
4.2.2.	Dislocation Density and Mobility.....	140
4.2.3.	Shear Induced Amorphization/Melting.....	149
5.	Conclusions .....	159
	References.....	163
	Appendix A – LAMMPS Input Files.....	196
	A-1, Bicrystal Grain Boundaries .....	197
	A-2, Piston-Driven Shock.....	202
	A-3, Flyer-Target Shock.....	205
	A-4, Quasi Isentropic Loading .....	207
	Appendix B – Orientation Algorithm .....	209
	Appendix C – Bicrystal Data .....	210
	Appendix D – HYADES.....	213
	Appendix E – Two Phase Method .....	215
	Appendix F – Quasi-Isentropic Loading.....	217

# List of Figures

Figure 1-1. Iterative cycle between experiments, simulation, and constitutive modeling.. 2

Figure 1-2. Impact of a 20 nm cluster into a single crystal block. Left, penetration damage and splashing can be seen. Right, only defective atoms are shown indicating liquid atoms in red and dislocation substructures in blues and yellows. From Anders et al. [6]. ..... 4

Figure 1-3. The origin of the Earth and its Moon by accretion. From Canup [7]..... 5

Figure 1-4. Rayleigh-Taylor hydrodynamic instabilities observed in pusher-fuel interface from Sakagami and Nishihara [8] and core collapse supernova from Hachisu et al. [9]. .. 5

Figure 1-5. Ultrahigh strength of 50 nm nanocrystal under shock loading. From Bringa et al. [10]. ..... 6

Figure 2-1. Time-dependent material response across varying length scales. Compression shown in red and tension shown in blue. Adapted from Asay [11]. ..... 7

Figure 2-2. Shock wave traveling from left to right. The crystal is undeformed ahead of the shock front. The shock front is a one-dimensional strain state that transitions into a hydrostatic (often termed three-dimensional) stress state under varying forms of plastic relaxation..... 9

Figure 2-3. Interaction of ultrashort laser pulses with materials. From Rethfeld et al. [27]. ..... 11

Figure 2-4. Position-Time (x-t) diagram shaded by evolving temperature for a 1 ps laser pulse at with an absorbed fluence of  $\sim 400 \text{ mJ/cm}^2$  into a bulk Ni target. The laser arrives from the left and impacts the surface at the 0 nm position at time 0 ps..... 13

Figure 2-5. Experimental setup schematic. Target discs of varying thickness are covered by an ablator/heat shield and subject to laser ablation in order to drive a planar shock wave through the system. (a-d) Recovery experiments used a carbon aerogel foam to catch debris, decelerate and catch the tantalum for characterization. .... 15

Figure 2-6. Position-Time (x-t) diagram shaded by evolving density. The imparted wave steepens into a shock wave at the shock breakout point. From there, an elastic-plastic shock wave propagates into target until each wave (traveling at different speeds) reflects from the rear surface..... 16

Figure 2-7. Experimental setup schematic. (a) Blue wavelength laser impinging on the front surface of a target package consisting of an ablator and target material. A second laser is directed at the rear surface and is reflected back through an optical setup..... 17

Figure 2-8. Schematic (From [36]) and simulation of spall process and related variables. ....	18
Figure 2-9. Simulated VISAR trace and corresponding visualization of the material at representative points. Color is qualitatively given according to stress state, blue for compression, red for tension. ....	21
Figure 2-10. Example Morse [79] interatomic potential compared to a universal EOS for metals by Rose [80,81]. The U-V response is given by the dashed red line for Rose and the dotted black line for Morse. The P-V relation is given by the solid red line for Rose and dot dashed black line for Morse. ....	25
Figure 2-11. (a) Ultimate tensile strength plotted according to the element's bulk modulus using the predictions of Grady [46] and Rose [80,81]. (b) Linear fit of the relationship between the predictions giving a slope of 1.4. ....	28
Figure 2-12. Periodic table showing trends in ultimate tensile strength. Predictions calculated using Rose et al. [80] EOS model. ....	28
Figure 2-13. Segmented 3D volume derived from $\mu$ -CT imaging of the polycrystalline tantalum system subjected to spall conditions where the transparent purple is the tantalum and the solid blue material is the contained void. ....	29
Figure 2-14. The increase in the volume fraction of grain boundaries and triple junctions as a function of grain size in the nanocrystalline (<100 nm) and ultrafine grain (100 nm–1 $\mu$ m) regimes. ....	32
Figure 2-15. Low energy configurations of $\Sigma$ 3 boundary. (Left) Expected twin boundary. (Right) Unexpected $\Sigma$ 3 boundary without mirror symmetry. ....	34
Figure 3-1. Time scale and number of atoms are the primary computational cost components. Plotted against one another they represent the currently achievable simulation space extending towards petaflop and exaflop computational resources. ....	40
Figure 3-2. Future projection of computational power of the Moore's Law type to achievable grain sizes for atomistic simulation by an empirical potential. ....	44
Figure 3-3. Left, 2D Voronoi tessellation of increasing complexity and number of "centers". Right, SPaSM 300x300x300 unit cell construction of bcc tantalum with 36 randomly oriented grains with orientations represented as RGB combinations and rendered by MD_Render code. ....	51
Figure 3-4. Methods used to create high strain-rate compression and release: (a) flyer-target geometry; (b), piston directed compression and release that varies a function of time; and (c) quasi-isentropic compression followed by quasi-isentropic tension. ....	53

Figure 3-5. Isotemporal lines given every ps from 0 to 15 ps. The piston is accelerated over 5 ps and then held steady for 20 ps. The result is a compressive wave that transitions completely to a shock wave by the 15 ps mark. ....	55
Figure 3-6. Visualization of a dislocation traversing a nanocrystalline grain by six different analysis coloring schemes. From Swygenhoven [183]. ....	58
Figure 3-7. Schematic of a post-processing pipeline implemented in OVITO. Image from [185]. ....	58
Figure 3-8. Centro-Symmetry Parameter (CSP) distinguish between plastically deformed regions of dislocations and stacking faults (asymmetry) from purely elastically deformed regions (which would have symmetry). From [189]. ....	62
Figure 3-9. 12 nearest neighbor atoms surrounding a FCC center atom, where the 3 dashed atoms belong in plane A (red), the 7 atoms belong in plane B (green) and the last 3 dotted atoms belong in plane C (blue). ....	62
Figure 3-10. CNA Analysis is derived based on the number of common neighbors (k) shared by an atom pair (i-j) [189]. ....	64
Figure 3-11. Pair correlation function of bcc Tantalum. ....	65
Figure 3-12. Comparison of (a) a conventional atomistic visualization using CNA filtering in tantalum and (b) a geometric line visualization of the dislocations provided by DXA. From [196]. ....	66
Figure 3-13. Orientation imaging map using Euler angles as proposed by Rudd [198]...	67
Figure 3-14. Increasing single CPU cost of running many-body potentials in seconds per atom per time step as a function of year. The black line is indicative of computational cost doubling similar to Moore's law. From Plimpton et al. [204]. ....	69
Figure 3-15. Left, pressure dependent $C_{ij}$ of Ta1 and Ta2. Right, Volume change as a function of hydrostatic pressure. EAM potentials as developed by Ravelo et al. [95]. ....	71
Figure 3-16. Cohesive energy as a function of hydrostatic pressure. ....	71
Figure 3-17. Left, pressure dependence of the elastic modulus of silicon. Right, pressure dependence of the ratio of maximum shear over pressure. ....	78
Figure 3-18. General stacking fault energies for the MOD potential plotted by displacement in terms of $1/2[110]$ Burgers vector. Melting curve for silicon under dynamic compression illustrating kinetic effects. ....	79
Figure 3-19. $C_{ij}$ of eight interatomic potentials as compared to DFT results by Karki et al. [258]. Melting was previously evaluated for many potentials by Mazhukin et al. [260] and	

compared with experimental points, a linear Clausis-Clapeyron relationship and a thermodynamic liquidus curve from Deb et al. [261].	81
Figure 3-20. (a) Hugoniot of several potentials compared to experimental measurements [177,256,257,264–267]. (b) Pressure-volume diagram for the same potentials and experiments. Inset shows data in the sensitive area near the elastic-plastic transition as measured by laser shock.	82
Figure 4-1. Excess grain boundary energy as a function of misorientation for the four tilt axes $\langle 100 \rangle$ , $\langle 110 \rangle$ , $\langle 111 \rangle$ , and $\langle 112 \rangle$ . GBEs for Ta are shown as black asterisks and a complete description of all boundaries calculated in the present work can be found in the supplemental material.	87
Figure 4-2. Grain boundary energy as a function of misorientation for four tilt axes. GBEs for Ta are shown as black asterisks. Also provided is predicted/extrapolated values from Wolf [126,283] using the energy values in Zhang et al. [287]. The gray region represents the predicted range of values for grain boundary energies for Tantalum.	88
Figure 4-3. Configurations of $\Sigma 3\langle 011 \rangle$ boundary colored by eV/atom shown for two projections. In each projection the GB normal is horizontal. (Left) EAM symmetric twin boundary. (Middle) EAM quasi-symmetric boundary with broken mirror symmetry in both (110) and (111) projections. (Right) SNAP quasi-symmetric boundary.	90
Figure 4-4. $\Sigma 5$ boundary visualization with color according to atomic potential energy in eV/atom. (Top) Boundary structural unit $B$ identified in the typical fashion [295]. (Bottom) Projection illustrating broken mirror symmetry shift.	91
Figure 4-5. Assorted high coincident site density boundary structures for each of the four tilt axis with equivalent coloring scheme as Fig. 3. From left to right the boundaries are: $\Sigma 13(051)\langle 001 \rangle$ , $\Sigma 11(332)\langle 011 \rangle$ , $\Sigma 27(552)\langle 011 \rangle$ , $\Sigma 7(231)\langle 111 \rangle$ , $\Sigma 7'(231)\langle 111 \rangle$ , $\Sigma 13(341)\langle 111 \rangle$ , $\Sigma 11(131)\langle 112 \rangle$ .	92
Figure 4-6. Illustration of free surface position and its temporal derivative to give free surface velocity.	95
Figure 4-7. Simulated VISAR showing (a) shock pulse attenuation with increasing sample length and (b) effect of cross section on pullback signal.	96
Figure 4-8. Cross section determined spall pullback response. The difference in signal is representative of defects and voids interacting with themselves across periodic boundaries. Inset corresponds to the small run where voids interact with themselves across periodic boundaries.	96
Figure 4-9. Controlled deramp/deceleration of piston velocity controls the release rate as measured by the free surface velocity as a function of time.	97

Figure 4-10. Strain rate as function of deceleration time and required sample length. Green indicates simulations that are easily achievable given current computational resources while red represents those that are currently impossible. The yellow and possibly orange lines may be achievable with dedicated allocations. .... 97

Figure 4-11. Spall damage as a function of sample length, each with an equivalent particle velocity drive. .... 98

Figure 4-12. Compilation of reported spall strength as a function of strain rate. Different colors refer to different grain sizes: single crystal (black), polycrystal (blue), nanocrystal (red), ultra-fined grained (purple) and unknown (brown). .... 99

Figure 4-13. Power-law fits for single (black, left), polycrystal (blue, center), and nanocrystal (red, right) tantalum spall strength vs strain rate data. Solid data markers are experiments and open markers are simulations. Points with crosses through them were not included in fits..... 100

Figure 4-14. Measured spall strength vs strain rate (from Tables 4-2 and 4-3). Dislocations are shown as dark lines, twin boundaries as transparent turquoise surfaces, and voids as transparent red surfaces. Regions of dislocation, twin, and de-cohesion dominated spall processes are separated by vertical dashed lines..... 102

Figure 4-15. Snapshots of the spallation process for flyer plate and piston methods shocked along [001] single crystal Ta. Snapshots are given at the time of maximum tensile stress ( $t_{max}$ ); and 2, 4, and 6 ps before and 2 and 4 ps after this time.. .... 104

Figure 4-16. Site of first void nucleation during a  $U_p = 0.75$  km/s shock of 5-10-20 shock wave form (5 ps ramp, 10 ps hold, and 20 ps deramp). Twins are identified by green twin boundary atoms in the host 001 matrix..... 105

Figure 4-17. Three-dimensional views of void nucleation sites. Left, voids nucleate at the “tip” and “kinks” of twin-twin intersections. Void surfaces at  $t=48$  ps..... 106

Figure 4-18. (a) Snapshot of twin structures at 26, 29, and 32 ps during QI expansion of a Ta [001] single crystal at a strain rate of  $10^{10}$  s<sup>-1</sup>. Defective atoms are colored off white and void surfaces are colored light blue. All other atoms are colored according to their local longitudinal stress. .... 107

Figure 4-19. Evolution of voids from the early stages of nucleation, growth, and rapid coalescence. This piston-driven simulation contains a broad tensile pulse that passes through the system traveling to the left as the bulk motion continues to carry the system to the right. .... 108

Figure 4-20. Evolution of porosity and dislocation density during the critical void nucleation and growth event for a strain rate of  $10^7$  s<sup>-1</sup>. Insets show snapshots in time. The

critical void nucleation site is along a dislocation running perpendicular to the loading direction. .... 110

Figure 4-21. (a) Snapshot of dislocation structures at 25.4 ns during QI expansion at a strain rate of  $10^7 \text{ s}^{-1}$ ; larger version of inset within Fig. 8. (b) Orthogonal projection highlighting shear loops (SL) and prismatic loops (PL) and traveling along the  $\langle 111 \rangle$  direction. This nucleation event has been described previously by Remington et al. [270]. ..... 111

Figure 4-22. Snapshots of quasi-isentropic simulations of nanocrystalline tantalum ( $d=21 \text{ nm}$ ) at different strain rates, each shown at the time of maximum tension. Strain rates are (a)  $10^8 \text{ s}^{-1}$ , (b)  $10^9 \text{ s}^{-1}$ , and (c)  $10^{10} \text{ s}^{-1}$ . The strains at which each frame is displayed are provided in Table 4-3. .... 114

Figure 4-23. Comparison between single and nanocrystalline spall simulations using the piston methodology. Voids nucleate along the grain boundaries in the nanocrystal, typically at grain boundaries that are perpendicular to the loading direction. .... 116

Figure 4-24. Spall process occurring in a 20 nm nanocrystal. Spall voids open at grain boundaries. .... 117

Figure 4-25. x-t diagram colored by atom count per voxel. Left, single crystal. Right,  $\Sigma 5$  bicrystal. Orange represents equilibrium, yellow compression, purple tension, and black complete spall. .... 117

Figure 4-26 Overlay of void structure for single (teal) and  $\Sigma 5$  bicrystal (brown). Notice the extended spall volume for the single crystal. .... 118

Figure 4-27 x-t diagram colored by longitudinal stress. Left, single crystal. Right,  $\Sigma 5$  bicrystal. Contours represent decreasing density as seen in the previous figure. .... 118

Figure 4-28. Spall strength as a function of temperature at a strain rate of  $10^9 \text{ s}^{-1}$ . The melting temperature as a function of pressure was determined from 2 phase simulations (full details can be found in the supplemental material). .... 120

Figure 4-29. Spall temperature evolution of piston-driven simulation from 60 to 100 ps. After initial void nucleation and growth, coalescence is largely affected by regions of high temperature, some of which approach and exceed the melting temperature of tantalum.  $T_m$  is defined as the equilibrium melting temperature of 3033 K. .... 122

Figure 4-30. Simulated cold curves for tantalum. Two tantalum EAM potentials (Ta1 and Ta2 from Ravelo et al. [95]) are compared against an equation of state (EOS) from Rose et al.[80], a Morse potential, and density functional theory (DFT) calculations of Ravelo et al.[95]. .... 124

Figure 4-31. Simulated cold curves for varying tantalum potentials: EAM (Ta1 and Ta2), Ravelo et al. [340]; Extended Finnis-Sinclair (EFS), Dai et al.[341]; Angular-dependent interatomic potential (ADP), Pan et al.[342]; Morse parameters[338,339]. .... 125



Figure 4-32. Molecular dynamics simulation of shocked $\langle 110 \rangle$ tantalum crystal at a particle velocity of 1.1 km/s (shock pressure $\sim 120$ GPa). (a) Hexagonal phase as filtered by adaptive common neighbor analysis [32] and colored by neighbor count. ....	127
Figure 4-33. Internal energy (U) vs normalized volume curve for Ta1.....	128
Figure 4-34. Enthalpy as a function of tensile pressure for Ta1.....	129
Figure 4-35. Limited stability of fcc phase during isentropic expansion following shock compression. Renders of the defective atoms (white) and fcc/hcp atoms (green/red) are shown compared to bcc atoms (blue). Selected diffraction patterns are generated along the [010] direction for the respective features. ....	130
Figure 4-36. Snapshots from a shock simulation showing $\{111\}$ and $\{110\}$ stacking faults. (a) depth perspective showing interaction between the mutual stacking fault planes. (b) thin section illustrating the resultant angles of the $\{111\}$ and $\{110\}$ stacking fault planes with the $\langle 110 \rangle$ direction. (c) simulated diffraction patterns of the faulted areas. ....	135
Figure 4-37 Observation of $\{111\}$ and $\{110\}$ stacking faults in Uniaxial impact loading of $\langle 001 \rangle$ single crystalline silicon. Color indicated by coordination number. Snapshots taken at 0.85 km/s, 12 GPa. ....	137
Figure 4-38. Shock pressure and resolved shear stress vs particle velocity. Crosses represent data points from a system undergoing shock compression. The dashed blue line is a curve fit to the derived relationship between shear and pressure corresponding to the predicted shear stress based on the pressure. ....	137
Figure 4-39 (a) Homogenous nucleation of stacking faults on $\{111\}$ slip planes occurring at $\sigma_z = 32.5$ GPa and $\tau = 6.4$ GPa as a shock wave travels from left to right. Atomic color is indicative of the absolute value of the local shear stress. (b) Significant relaxation (blue color) is seen in the 4 ps time step. ....	141
Figure 4-40. Identification of partial dislocation near shock front by potential energy criterion. The partial dislocation tip is identified by the furthest blue atom corresponding to a shift in the lattice across the stacking fault. ....	142
Figure 4-41. Analytical dislocation density prediction where each curve represents a unique strain rate. The dislocation density is highly dependent on the HEL and curves are truncated below this limit corresponding to an elastic response; the material would have a dislocation density unchanged from its intrinsic value. ....	146
Figure 4-42. Dual projection view showing $\{111\}$ slip plane several activated burgers slip directions giving rise to a stacking fault of representative shape. Arrows indicate the fastest moving partials, the distance between which the length and corresponding velocity are measured for.....	147

Figure 4-43. Time sequence from 2.2 to 2.9 ps showing partial dislocation velocity burst at 2.2 ps and velocity burst of secondary partial between 2.7 and 2.9 ps. .... 148

Figure 4-44. Molecular dynamics time evolution showing formation of amorphous nucleus following inter snapshot at 15 ps of a [001] silicon crystal shocked to 14.5 GPa ..... 151

Figure 4-45. Tridimensional view of the stacking faults (SF) as the precursors of the amorphization: multiple stacking faults and their intersections can be observed ahead of the disordered region. A disordered region was left behind. .... 152

Figure 4-46. Piston/particle velocity of 1.5 km/s. Near-[110] projection view. (a) Coordination indicating the relatively higher average coordination ~5 (light blue) of the stacking fault layer and the even higher average coordination of the molten layer ~4 to 10 (green-yellow to dark red). .... 153

Figure 4-47. MD simulation (a) shows several {111} stacking fault as the precursor of the amorphization; and TEM observation (b) also shows stacking faults bounding the amorphous materials. .... 154

Figure 4-48. Simulated recovery of shock loaded Si at 1.1 km/s. Left, during compressive loading. Right, after recovery as detailed above. Color according to local coordination. Unloading reduces unstable stacking faults and decreases the average coordination from 6.7 to 5.1 within the amorphous region. .... 155

Figure 4-49. Slice along the [111] direction of a MD simulation of [100] shocked silicon using the MOD potential. Bulk amorphization/melting near the shocked surface, directional amorphization/melting, partial dislocation activity, and formation of bct5 bands can be identified. .... 156

## List of Tables

Table 3-1. Parameters for Grain Size “Moore’s Law” Computation.....	43
Table 3-2. Parameters that are applied in equations of EA, EA2, and MOD potentials...	77
Table 4-1. Surface Energy (mJ/m <sup>2</sup> ) for bcc Ta, Fe, and Mo. Data from Zhang et al. [287]. .....	89
Table 4-2. Simulations of single crystalline tantalum. Measurements at the peak tensile stress in the shock direction ( $\sigma_{zz}$ ) and the corresponding hydrostatic pressure (P), deviatoric shear stress( $\tau$ ), temperature (T), and strain ( $\epsilon$ ).....	101
Table 4-3. Simulations of nanocrystalline tantalum, d = 21 nm. Measurements at the peak tensile stress in the shock direction ( $\sigma_{zz}$ ) and the corresponding hydrostatic pressure (P), deviatoric shear stress( $\tau$ ), temperature (T), and strain ( $\epsilon$ ).....	101
Table 4-4. Phase changes under tension for Ta1 potential. ....	128
Table 4-5. Phase changes under tension for Ta2 potential .....	128
Table 4-6. Ambient and High Pressure (P < 25 GPa) Polymorphs of Silicon. Data from multiple sources [239,369,374,375].....	133

## Acknowledgements

Financial support from DOE Office of Science, Office of Advanced Scientific Computing (ASCR) via the Exascale Co-design Center for Materials in Extreme Environments (Karen Pao, program manager); UC Research Laboratories Grant (09-LR-06-118456-MEYM); and by the U.S. Department of Energy (DOE) NNSA/SSAP (DE-NA0002080). Los Alamos National Laboratory, an affirmative action/equal opportunity employer, is operated by Los Alamos National Security, LLC, for the National Nuclear Security Administration of the U.S. Department of Energy under contract DE-AC52-06NA25396.

I would like to thank Prof. Meyers for all the dynamic insight and opportunities that opened through his guidance; Drs. Ramon Ravelo, Jim Hammerberg, and Tim Germann for help with my understanding of shock-loading simulations and the use of SPaSM; Prof. Eduardo Bringa for his help and guidance regarding molecular dynamics simulations of silicon; and Dr. Saryu Fensin for support of bi-crystalline and sweeping wave simulations. Many useful discussions with Bruce Remington, Robert Rudd, Chris Wehrenberg, Diego Tramontina, Carlos Ruestes, Vincent Sherman, Tane Remington, Shiteng Zhao, Zach Sternberger are gratefully acknowledged. Finally, a warm thanks to the members of my committee for their constructive criticisms and suggestions.

Chapter 2, in part, is a reprint of material that has been published: E.N. Hahn, M.A. Meyers, Grain-size dependent mechanical behavior of nanocrystalline metals. 646 (2015) 101–134. doi:10.1016/j.msea.2015.07.075. The thesis author was the first author of this article.

Chapter 2, in part, is a reprint of material that has been published: E.N. Hahn, S.J. Fensin, T.C. Germann, M.A. Meyers, Symmetric tilt boundaries in body-centered cubic tantalum, *Scripta Materialia*. 116 (2016) 108–111. doi:10.1016/j.scriptamat.2016.01.038. The thesis author was the first and corresponding author of this article.

Chapter 2, in part, is currently being prepared for submission for publication: E.N. Hahn, M.A. Meyers, *Laser-Driven Shocks and Dynamic Failure*. The thesis author was the first author of this article.

Chapter 2, in part, is currently being prepared for submission for publication: T.P. Remington, J.C.E. Mertens, E.N. Hahn, S. Sabbaghianrad, T.G. Langdon, C.E. Wehrenberg, B.R. Maddox, D.C. Swift, B.A. Remington, N. Chawla, M.A. Meyers, Spall Strength Dependence on Strain Rate and Grain Size in Tantalum. The thesis author was the third author of this article.

Chapter 3, in part, is a reprint of material that has been published: E.N. Hahn, M.A. Meyers, Grain-size dependent mechanical behavior of nanocrystalline metals. 646 (2015) 101–134. doi:10.1016/j.msea.2015.07.075. The thesis author was the first author of this article.

Chapter 3, in part, is a reprint of material that has been published: E.N. Hahn, S.J. Fensin, T.C. Germann, M.A. Meyers, Symmetric tilt boundaries in body-centered cubic tantalum, *Scripta Materialia*. 116 (2016) 108–111. doi:10.1016/j.scriptamat.2016.01.038. The thesis author was the first and corresponding author of this article.

Chapter 3, in part, is a reprint of material that has been published: S. Zhao, B. Kad, E.N. Hahn, B.A. Remington, C.E. Wehrenberg, C.M. Huntington, H.-S. Park, E.M. Bringa, K.L. More, M.A. Meyers, Pressure and shear-induced amorphization of silicon, *Extreme*

Mechanics Letters. 5 (2015) 74–80. doi:10.1016/j.eml.2015.10.001. The thesis author was the third author of this article.

Chapter 3, in part, has been submitted for publication of the material as it may appear in: E.N. Hahn, T.C. Germann, R.J. Ravelo, J. Hammerberg, M.A. Meyers, On the Ultimate Tensile Strength of Tantalum, *Acta Materialia*. (2016). The thesis author was the first and corresponding author of this article.

Chapter 3, in part, is currently being prepared for submission for publication: E.N. Hahn N., Y. Wang, R. Flanagan, S. Zhao, M.A. Meyers, Computational Evaluation of Silicon under Shock Compression, (2016). The thesis author was the first and corresponding author of this article.

Chapter 4, in part, has been accepted for publication of the material as it may appear in: E.N. Hahn, T.C. Germann, R.J. Ravelo, J.E. Hammerberg, M.A. Meyers, Non-Equilibrium Molecular Dynamics Simulations of Spall in Single Crystal Tantalum, *AIP Conference Proceedings*. In press (2016). The thesis author was the first and corresponding author of this article.

Chapter 4, in part, has been submitted for publication of the material as it may appear in: E.N. Hahn, T.C. Germann, R.J. Ravelo, J. Hammerberg, M.A. Meyers, On the Ultimate Tensile Strength of Tantalum, *Acta Materialia*. (2016). The thesis author was the first and corresponding author of this article.

Chapter 4, in part, is currently being prepared for submission for publication: E.N. Hahn, M.A. Meyers, Laser-Driven Shocks and Dynamic Failure. The thesis author was the first author of this article.

Chapter 4, in part, is currently being prepared for submission for publication: T.P. Remington, J.C.E. Mertens, E.N. Hahn, S. Sabbaghianrad, T.G. Langdon, C.E. Wehrenberg, B.R. Maddox, D.C. Swift, B.A. Remington, N. Chawla, M.A. Meyers, Spall Strength Dependence on Strain Rate and Grain Size in Tantalum. The thesis author was the third author of this article.

Chapter 4, in part, is a reprint of material that has been published: C.-H. Lu, E.N. Hahn, B.A. Remington, B.R. Maddox, E.M. Bringa, M.A. Meyers, Phase Transformation in Tantalum under Extreme Laser Deformation, *Scientific Reports*. 5 (2015) 15064. doi:10.1038/srep15064. The thesis author was the second author of this article.

Chapter 4, in part, is a reprint of material that has been published: E.N. Hahn, S. Zhao, E.M. Bringa, M.A. Meyers, Supersonic Dislocation Bursts in Silicon, *Scientific Reports*. 6 (2016) 26977. doi:10.1038/srep26977. The thesis author was the first author of this article.

Chapter 4, in part, is a reprint of material that has been published: S. Zhao, B. Kad, E.N. Hahn, B.A. Remington, C.E. Wehrenberg, C.M. Huntington, H.-S. Park, E.M. Bringa, K.L. More, M.A. Meyers, Pressure and shear-induced amorphization of silicon, *Extreme Mechanics Letters*. 5 (2015) 74–80. doi:10.1016/j.eml.2015.10.001. The thesis author was the third author of this article.

Chapter 4, in part, is a reprint of material that has been published: S. Zhao, E.N. Hahn, B. Kad, B.A. Remington, E.M. Bringa, M.A. Meyers, Shock compression of [001] single crystal silicon, *Eur. Phys. J. Spec. Top.* (2016) 1–7. doi:10.1140/epjst/e2016-02634-7. The thesis author was the second author of this article.

Chapter 4, in part, is a reprint of material that has been published: S. Zhao, E.N. Hahn, B. Kad, B.A. Remington, C.E. Wehrenberg, E.M. Bringa, M.A. Meyers, Amorphization and nanocrystallization of silicon under shock compression, *Acta Materialia*. 103 (2016) 519–533. doi:10.1016/j.actamat.2015.09.022. The thesis author was the second author of this article.

Chapter 4, in part, is currently being prepared for submission for publication: E.N. Hahn N., Y. Wang, R. Flanagan, S. Zhao, M.A. Meyers, Computational Evaluation of Silicon under Shock Compression, (2016). The thesis author was the first and corresponding author of this article.

Chapter 5, in part, is currently being prepared for submission for publication: E.N. Hahn N., Y. Wang, R. Flanagan, S. Zhao, M.A. Meyers, Computational Evaluation of Silicon under Shock Compression, (2016). The thesis author was the first and corresponding author of this article.

Chapter 5, in part, is a reprint of material that has been published: E.N. Hahn, S.J. Fensin, T.C. Germann, M.A. Meyers, Symmetric tilt boundaries in body-centered cubic tantalum, *Scripta Materialia*. 116 (2016) 108–111. doi:10.1016/j.scriptamat.2016.01.038. The thesis author was the first and corresponding author of this article.

Chapter 5, in part, has been submitted for publication of the material as it may appear in: E.N. Hahn, T.C. Germann, R.J. Ravelo, J. Hammerberg, M.A. Meyers, On the Ultimate Tensile Strength of Tantalum, *Acta Materialia*. (2016). The thesis author was the first and corresponding author of this article.



## Vita

- 2012 B.Sc. Materials Engineering – California Polytechnic State University, San Luis Obispo
- 2013 M.Sc. Materials Science and Engineering – University of California, San Diego
- 2016 Ph.D. Materials Science and Engineering – University of California, San Diego

## Publications

E.N. Hahn, S. Zhao, E.M. Bringa, M.A. Meyers, Supersonic Dislocation Bursts in Silicon, *Scientific Reports*. 6 (2016) 26977. doi:10.1038/srep26977.

S. Zhao, B. Kad, E.N. Hahn, B.A. Remington, C.E. Wehrenberg, C.M. Huntington, H.-S. Park, E.M. Bringa, K.L. More, M.A. Meyers, Pressure and shear-induced amorphization of silicon, *Extreme Mechanics Letters*. 5 (2015) 74–80. doi:10.1016/j.eml.2015.10.001.

S. Zhao, E.N. Hahn, B. Kad, B.A. Remington, E.M. Bringa, M.A. Meyers, Shock compression of [001] single crystal silicon, *Eur. Phys. J. Spec. Top.* (2016) 1–7. doi:10.1140/epjst/e2016-02634-7.

E.N. Hahn, S.J. Fensin, T.C. Germann, M.A. Meyers, Symmetric tilt boundaries in body-centered cubic tantalum, *Scripta Materialia*. 116 (2016) 108–111. doi:10.1016/j.scriptamat.2016.01.038.

S. Zhao, E.N. Hahn, B. Kad, B.A. Remington, C.E. Wehrenberg, E.M. Bringa, M.A. Meyers, Amorphization and nanocrystallization of silicon under shock compression, *Acta Materialia*. 103 (2016) 519–533. doi:10.1016/j.actamat.2015.09.022.

C.-H. Lu, E.N. Hahn, B.A. Remington, B.R. Maddox, E.M. Bringa, M.A. Meyers, Phase Transformation in Tantalum under Extreme Laser Deformation, *Scientific Reports*. 5 (2015) 15064. doi:10.1038/srep15064.

E.N. Hahn, M.A. Meyers, Grain-size dependent mechanical behavior of nanocrystalline metals, *Materials Science and Engineering: A*. 646 (2015) 101–134. doi:10.1016/j.msea.2015.07.075.

B. Wang, J. Sun, E.N. Hahn, X. Wang, Shear Localization and its Related Microstructure Mechanism in a Fine-Grain-Sized Near-Beta Ti Alloy, *J. of Materi Eng and Perform*. 24 (2015) 477–483. doi:10.1007/s11665-014-1285-0.

ABSTRACT OF THE DISSERTATION

Non-Equilibrium Simulations of Defects, Damage, and Phase Transformations  
in Extreme Regimes

by

Eric Nicholas Hahn

Doctor of Philosophy in Materials Science and Engineering

University of California, San Diego, 2016

Professor Marc Meyers, Chair

The combination of high-energy pulsed-laser experiments and molecular dynamics simulations yields an improved understanding of the deformation and failure mechanisms under extreme loading conditions. Coordination of these techniques improves as the

characteristic spatial and temporal scales of state-of-the-art laser experiments overlap increasingly with massive atomistic simulations. SPaSM and LAMMPS molecular dynamics codes were employed to simulate atomic systems containing up to one billion atoms. The extreme stress states generated by laser-driven shocks persist for incredibly short durations (picoseconds to nanoseconds). Over severely reduced time scales, extreme stresses activate novel phase transformations and defect mechanisms. An overarching theme of the present thesis is the role of limited time and superimposed stresses and strains via laser-generated shocks on the resulting deformation mechanisms occurring during the passage of the pulse. At the reduced time scales (picoseconds to nanoseconds), novel phase transformations and defect mechanisms are activated.

This dissertation focuses on two representative materials: tantalum, a body-centered cubic metal; and silicon, a diamond-cubic (covalently bonded) semiconductor. Significant structural changes were obtained experimentally and by molecular dynamics. In tantalum, the competition between dislocations and twinning is shown to be determined, *inter alia*, by the strain rate. Additionally, an unexpected phase transition to hexagonal at large compressive strains and to face-centered cubic at large tensile strains is revealed. The strain-rate dependence of spalling is modeled and successfully compared with experimental results; the effect of grain boundaries is established. An estimate of the ultimate tensile strength of tantalum, obtained by extrapolation of the strain-rate dependent spall strength to the Debye frequency of atoms as well as by an evaluation of the equation of state, is shown to be 33 GPa. In silicon, we identified supersonic dislocations bursts, which have durations of fractions of picoseconds; bulk and shear-induced amorphization; and intermediate phase changes to higher-coordinated structures.

# 1. Introduction

The formation and motion of defects within a regular crystal lattice is fundamental to our understanding of intrinsic material strength and ultimate failure. Failure can arrive through diverse means, ranging from gradual accumulation to a sudden avalanche of damage and phase change. Covalent and metallic (delocalized covalent) materials often deform through the nucleation and flow of dislocations, or crystal line defects. They move in response to shear stresses and their motion is governed by the local density of dislocations, available slip systems, and strain rate. The formation of mechanical twins may occur in order to relieve shear stresses at large strain rates or in the absence of mobile dislocations. Local instabilities can lead materials to deform via shear localization resulting in the formation of amorphous bands. Likewise, alternate shear instabilities may prompt phase transformations. Phase transitions may also be thermodynamically motivated due to high pressures, shear stresses, and temperatures involved. Phase transformation kinetics may exclude certain transitions from occurring based upon the experimental time scale. During extreme tensile loading a material may deform by the physical decohesion of atoms leading to void nucleation, growth, and coalescence – a process known as spallation. At the far extremes of pressure, temperature, and strain rate these processes are often interpolated from experimental pre- and post-mortem recovered specimens. Additionally, *in situ* diagnostics such as x-ray diffractometry and laser interferometry help us to determine the deformation physics [1–4].

Computer simulation enables *in silico* evaluations of extreme environments with spatial resolution on the scale of individual atoms and temporal resolution faster than the

vibrational period of atoms. The result is a virtual atomic laboratory, tracing every particle and every interaction in time on a computer. The precise simulation of material defects informs our interpretation of experimental results, provides a unique means to evaluate strength models, and holds the potential to directly visualize defect mechanisms governing the strength of materials. Simulations should not exist in isolation and conclusions must be tempered by experimental results. Furthermore, experiments and simulations alike should aim to expose and isolate fundamental physics such that it can be condensed into representative constitutive models. This iterative cycle, shown below in Figure 1-1, is central to effectively leveraging the strengths and weaknesses of simulations, experiments, and modeling.

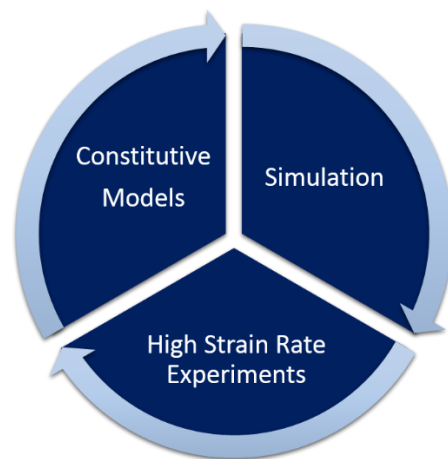


Figure 1-1. Iterative cycle between experiments, simulation, and constitutive modeling.

### 1.1. Research Objectives

The objective of the present investigation was to advance our understanding of the extreme response of model diamond-cubic (dc) and body-centered cubic (bcc) crystal structures. The overall investigation had two components: an experimental one using laser-launched short-duration shock pulses, and a computational one, using non-equilibrium

molecular dynamics. Its goal was to address the questions below for elemental tantalum and silicon:

- What is the balance and relationship between dislocation slip and twinning deformation processes under shock compression?
  - What roles do shock amplitude, grain size, and texture play?
  - What roles do shear instability and phase change play in silicon?
- What role do phase transformations play?
  - Can kinetic effects be quantified?
- What transpires to these defects upon unloading?
  - Are slip, twinning, or phase transitions preferentially retained?
- What role, if any, do these defects and grain boundaries play in spall failure process when the sample goes into dynamic tension?
  - What do grain boundary structures in bcc tantalum look like?
  - Why are specific nucleation sites preferred?
  - What makes other boundaries/defects strong or weak?
- How are dynamic experimental results correlated to local phenomena and measures obtained through molecular dynamics?
  - What is the relationship between spall strength and strain rate?
- What are the mechanisms of void nucleation and growth in dynamic tensile failure?

Many of these questions will be answered, others merely brushed upon – requiring substantial research effort in the future.

## 1.2. Motivation

A deeper understanding of high strain-rate phenomena is critical in many fields of physics and materials science ranging from astro/geophysics, to defense applications, to inertial confinement fusion [1,5]. Tantalum serves as an important element to study bcc deformation phenomena and silicon is ubiquitous throughout modern technology. Furthermore, both elements are important electrical components used within laser chamber optics and diagnostics. Such tools are essential to scientific discovery and innovation in the regime of high energy density physics. Diffuse laser reflections are not uncommon and can damage laser diagnostics and shielding. Replacing diagnostics and shielding is costly

both in terms of reducing laser shot frequency and increasing operation costs that ultimately determine the economics of energy production.

In the field of astrophysics, many high-strain-rate phenomena are informed by simulations and laser experiments. Simulations of hypervelocity impact of nano-projectiles up to 55 nm in diameter were able to show remarkable size effects and a transition between plasticity, melting, and evaporation as shown in Figure 1-2 [6].

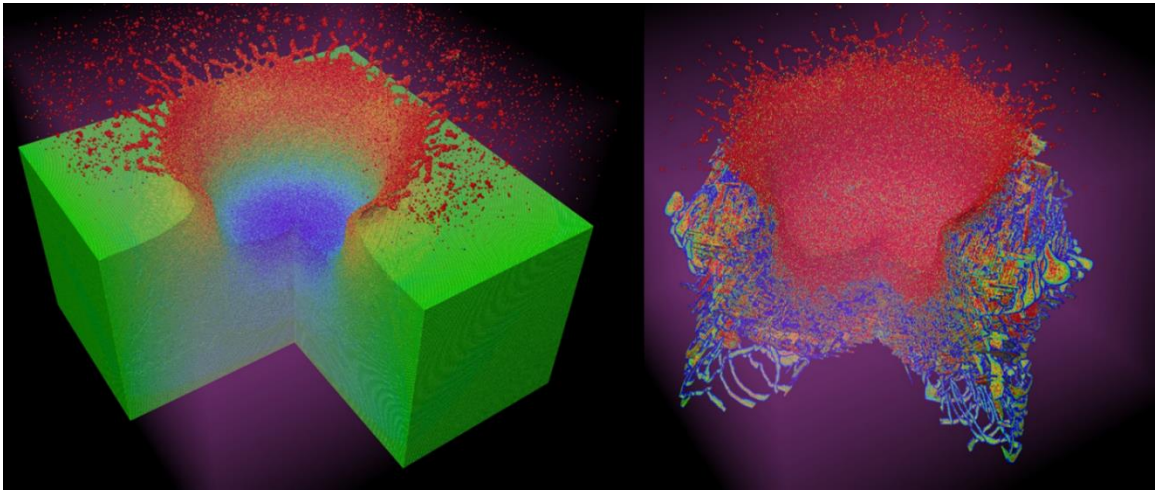


Figure 1-2. Impact of a 20 nm cluster into a single crystal block. Left, penetration damage and splashing can be seen. Right, only defective atoms are shown indicating liquid atoms in red and dislocation substructures in blues and yellows. From Anders et al. [6].

The collision of planetary bodies has also been simulated, testing theoretical explanations for the formation of the moon [7]. Figure 1-3 shows a simulation providing support for the formation of the moon by accretion. An experiment of this scale is entirely infeasible and, thus, simulations provide a necessary and critical tool that allows for scientific inquiry into such phenomena.

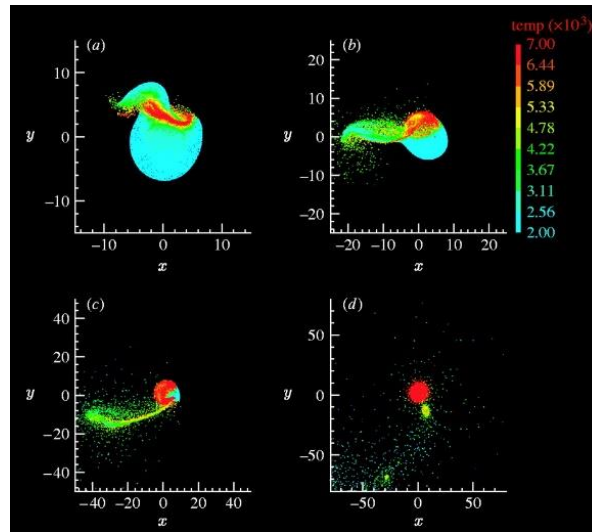


Figure 1-3. The origin of the Earth and its Moon by accretion. From Canup [7].

Several hydrodynamic instabilities are shown in Figure 1-4. It is remarkable that Rayleigh-Taylor hydrodynamic instabilities observed in the pusher-fuel interface (Sakagami and Nishihara [8]) and core collapse supernova (Hachisu et al. [9]) show striking similarity over vastly different length scales. This illustrates that appropriately scaled simulations have the potential to extrapolate far beyond their size and again shows that material strength plays a role across vast length scales.

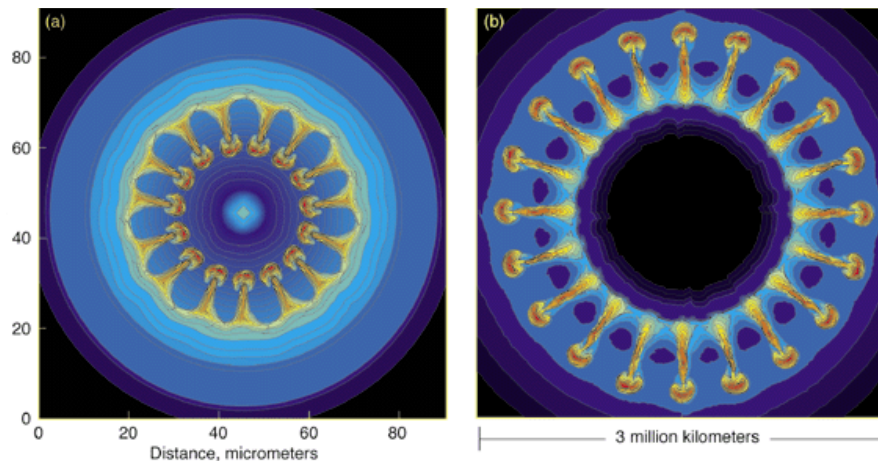


Figure 1-4. Rayleigh-Taylor hydrodynamic instabilities observed in pusher-fuel interface from Sakagami and Nishihara [8] and core collapse supernova from Hachisu et al. [9].



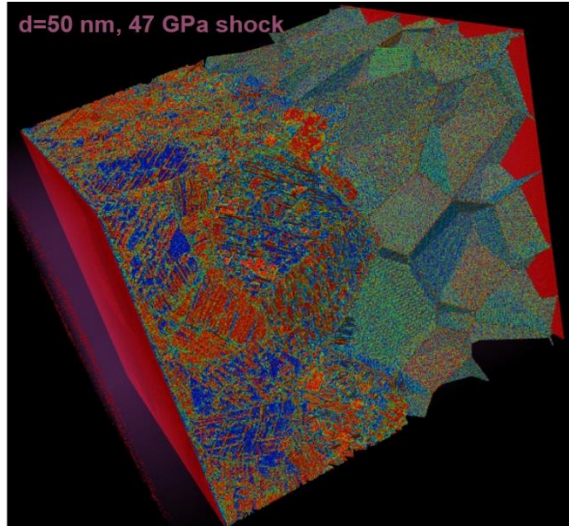


Figure 1-5. Ultrahigh strength of 50 nm nanocrystal under shock loading. From Bringa et al. [10].

Simulations also allow for studies for material systems, such as nanocrystals, that are experimentally difficult to manufacture. A simulation of such a nanocrystal is shown in Figure 1-5; it is able to illustrate ultra-high strength under shock loading. Fundamentally, a key piece to furthering our understanding of materials physics is the ability to precisely observe how materials accommodate plastic flow; flow may occur by dislocation nucleation and motion, twinning, phase transformation, or atomic decohesion and will be strongly correlated to stress, strain rate, temperature, and the intrinsic bonding strength of these materials.

## 2. Background

In order to comprehend dynamic phenomena, it is essential to understand wave propagation. Figure 2-1 displays a relevant description of general events that occur in shock compression and tensile release. It is appropriate to begin with compression and here high strain-rate experimental methods such as laser-driven shock waves are detailed.

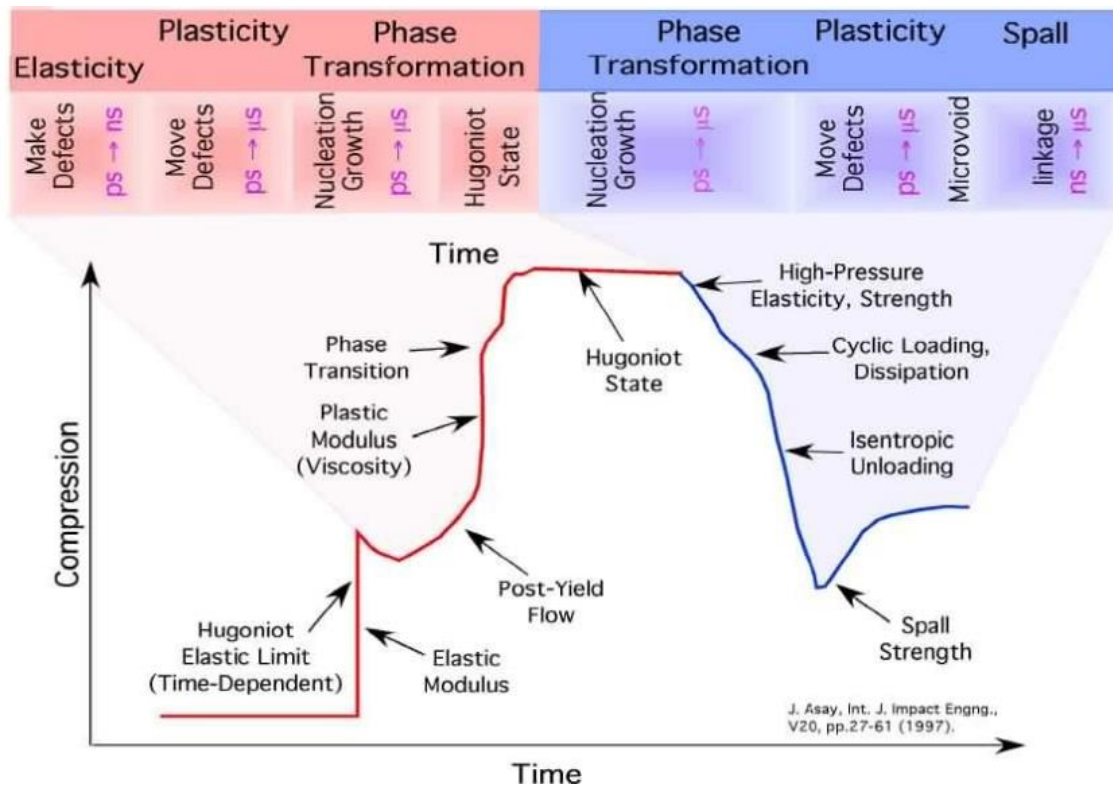


Figure 2-1. Time-dependent material response across varying length scales. Compression shown in red and tension shown in blue. Adapted from Asay [11].

Subsequently, an examination is conducted of release phenomena occurring by reflected tensile waves that follow compressive waves impacting a free surface or interface. Third, primary defects, dislocations and grain boundaries, associated with dynamic deformation in both compression and release are examined. Throughout each section of

this chapter, the role of defects as well as phase transitions under dynamic conditions are highlighted. Each section attempts to levy computational and physical experiments to reinforce mutual context and conclusions. Phenomena specific to tantalum and silicon are emphasized throughout. The sentiment that as “*defects are always present in real metals, more effort should be put into studying effects of defects*” is continually reiterated [12].

## 2.1. Compression

It is appropriate to begin a discussion of dynamic phenomena with shock compression as, at the very least, it serves as a precursor to several modes of damage mentioned from here on out. When the dominant effect is shock-wave pressure, such as observed in one-dimensional stress or strain states (experiments such as split Hopkinson pressure bar or laser driven systems respectively) the deviatoric stresses will induce different microstructural responses than those induced by hydrostatic pressure alone [13–16]. The one-dimensional strain state is illustrated in Figure 2-2. Above a certain threshold, termed the Hugoniot elastic limit (Figure 2-1), plasticity/phase change relaxes the deviatoric stress and more hydrostatic stress state is produced.

The Rankine[17]-Hugoniot[18] equations (recently reviewed with historical insight by Salas [19]) satisfy conservation of mass, momentum, and energy and define relationships between velocity, density, pressure and energy:

$$\rho_0 U_s = \rho_1 (U_s - U_p) \quad (1)$$

$$P_1 - P_0 = \rho_1 U_p (U_s - U_p) = \rho_0 U_s U_p \quad (2)$$

$$P_1 U_p = \rho_0 U_s \left( \frac{1}{2} U_p^2 + e_1 - e_0 \right) \quad (3)$$

How they relate to the shocked state can be seen later in Figure 3-4. It is experimentally observed that for many materials there is a linear relationship between shock ( $U_s$ ) and particle velocity ( $U_p$ ):

$$U_s = c_0 + sU_p \quad (4)$$

Not all materials exhibit this linear response and additional terms may be necessary to accurately describe the shock behavior [20].

Constitutive models typically utilize an equation of state (EOS) based on Equations 1 to 4 and various models for plasticity; a recent review of such models was conducted by Remington et al. [21] and some parameters for tantalum are given in Appendix D. Both the dynamic loading and the temperature increase significantly affect the mechanical and failure response of the material. The energy is transmitted so quickly that deformation develops at extreme strain rates as stress waves travel through the continuum body.

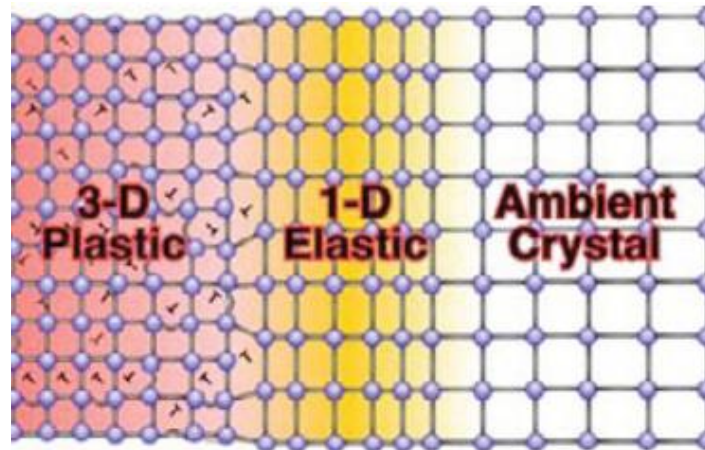


Figure 2-2. Shock wave traveling from left to right. The crystal is undeformed ahead of the shock front. The shock front is a one-dimensional strain state that transitions into a hydrostatic (often termed three-dimensional) stress state under varying forms of plastic relaxation.

### 2.1.1. Laser Compression

Of the current methods to generate large strain rates and high pressures, laser compression is predominant. However, there are a variety of methods used to probe and study materials at elevated pressures and strain rates and a brief review is justified. The most widely known technique to produce strain rates in the dynamic regime ( $d\varepsilon/dt > 5 \times 10^3 \text{ s}^{-1}$ ) are flyer-plate experiments [13]. The basis of the flyer-plate method is the acceleration of a projectile (typically with large lateral dimensions in comparison to its thickness) towards a sample target. The acceleration can be accomplished by gas/powder guns, electromagnetic capacitor discharge, or direct energy deposition (commonly using explosives). Typical durations of shock pulses are 1-3  $\mu\text{s}$  for explosively-driven flyer plates and 0.1-1  $\mu\text{s}$  for gas guns with impact velocities that can range from 200 m/s to 10 km/s for multi-stage gas guns. Upon collision of the flyer plate with the target, two shock waves are created, one in each, flyer and target, traveling in opposite directions. The governing principle driving the shocks is Newton's third law: when a body exerts a force on another body, the secondary body exerts a reaction force on the first body that is equal in magnitude and opposite in direction. Intimately tied to Newton's third law is the conservation of momentum – it will be subsequently clear how this applies to shocks created by laser ablation. Owing to the fact that the two masses (the flyer and the target) are in contact, the time over which the forces are applied will be equivalent. Newton's second law can be formulated and manipulated as follows:

$$F = m\ddot{x} = m \dot{x}/dt, \quad (5)$$

$$Fdt = m\dot{x} \quad (6)$$

The form of Equation 6 indicates that the impulse is equivalent to the change in momentum. It should be clear that altering the mass (by either changing the material and/or the flyer thickness) and/or changing the flyer velocity will impart shocks of different magnitude into the target system.

High-power pulsed-lasers have been increasingly used to generate shock waves in materials [1,5,22]. Following the first operational laser in 1960, several research initiatives have paved the way for current laser shock studies. Askaryon and Morez [23], White [24], Andelholm [25], Inal and Murr [26], and others made seminal contributions to the field, demonstrating how lasers can be used to generate pressure pulses. The duration of the shock pulse generated by lasers is significantly lower than for flyer-plate experiments. The timescales range from femtoseconds (fs) to 10s of nanoseconds (ns). Lasers can be used to generate shocks in several manners.

Figure 2-3 shows laser-matter interaction as a function of laser pulse length for metals and semiconductors.

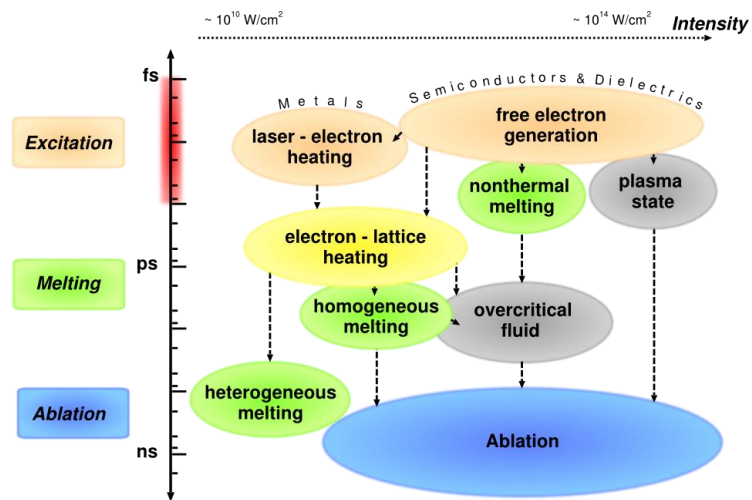


Figure 2-3. Interaction of ultrashort laser pulses with materials. From Rethfeld et al. [27].

A large component of effective laser-matter coupling is the wavelength of light being used in addition to the absorptivity/reflectivity of the incipient surface. Plastic ablators such as polystyrene are typically used to easily generate rapidly expanding “CH” plasmas. In other cases such as laser shielding, unintentional targets, or applications at high temperatures where many plastics melt, metals or insulators (including foams) might be used.

The simplest method of producing a shock wave with a laser is direct bombardment; when a laser impinges upon the surface material, it interacts with the electrons, exciting them to elevated energy levels if the energy of the laser is sufficiently large. As this process continues the temperature rapidly rises. Given a suitable laser intensity (energy passing through a given area per time) it is possible to create rapidly expanding matter/plasma that emanates from the laser spot. A result of the matter/plasma traveling away from the surface of the target is the acceleration of the target itself – a result of an applied reaction force. This is governed by the rocket effect:

$$\dot{x} = v \ln \frac{m_0}{m_1}, \quad (7)$$

The ensuing shock will be determined by the amount of lost mass,  $m$ , and the velocity,  $v$ , at which the plasma exhausts. It is typical that the mass is small and the velocity is quite large. A representation of this process is given as Figure 2-4.

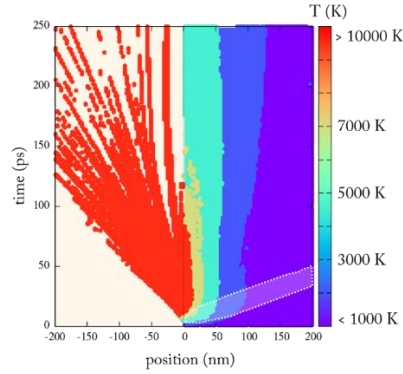


Figure 2-4. Position-Time ( $x$ - $t$ ) diagram shaded by evolving temperature for a 1 ps laser pulse at with an absorbed fluence of  $\sim 400 \text{ mJ/cm}^2$  into a bulk Ni target. The laser arrives from the left and impacts the surface at the 0 nm position at time 0 ps. Blank areas indicate densities below 10% of the initial solid density and the resultant shock wave of 10 GPa is marked by a dotted white line inside the solid sample. Figure adapted from [28].

This conceptual description is a simplification of the laser-plasma-matter interaction and the reader is directed to alternative sources for more in-depth information [29,30]. Often a low  $Z$  (atomic number) material is used simultaneously as an ablator and a heat shield. The resultant plasma is more uniform and the final result is a planar shock wave with an effective shock pressure pulse that is typically pseudo-Gaussian in shape. It is also possible to drive a shock into a system by using lasers to generate x-rays that subsequently launch a wave into the sample [29,31], or to use a laser to accelerate a flyer plate [32,33].

An effective empirical relationship between laser parameters and shock pressure is Lindl's equation [29]:

$$P = C_A \left( \frac{I_{12}}{\lambda_{\mu\text{m}}} \right)^{2/3}, \quad (8)$$

where  $P$  is resultant peak shock pressure (GPa),  $I_{12}$  is the laser intensity in (given in  $\text{TW/cm}^2$ ), and  $\lambda$  is the wavelength in micrometers. This equation can be derived by assuming that a given fraction of laser intensity is absorbed and that the resulting pressure



is approximately equal to the density times the square of the velocity. A typical adsorption coefficient,  $C_A$ , is 40 and the scaling law holds well for low  $Z$  ablation materials. Holding the wavelength constant, a more empirical value of the scaling exponent is 0.71, taken from diamond ablaters at OMEGA (Laser Facility at the University of Rochester's Laboratory for Laser Energetics), which uses 532 nm lasers [34]. The laser intensity can be simply determined by dimensional analysis to be:  $I=E/(At)$ .  $E$  is the laser energy,  $t$  is the pulse duration, and  $A$  is the spot size of the laser. The laser intensity can be imagined as an energy flux per unit time. Taking an example laser pulse that might be generated at OMEGA - a 532 nm laser pulse of 50 J with a pulse duration of 3 ns applied with a square phase plate of  $1 \text{ mm}^2$  - the resulting initial peak pressure will be 100 GPa.

## **2.2. Isentropic Release**

An understanding of release phenomena is vital to many technologically-critical applications including the design of debris shields used within the National Ignition Facility (NIF) and numerous programs relating to nuclear materials operated by the Department of Energy (DOE), National Nuclear Stockpile Stewardship (NNSA), and Stockpile Stewardship Academic Programs (SSAP). The study of spall fracture is inherently multidisciplinary, involving continuum mechanics, thermodynamics, fracture mechanics, and metallurgy. Again, built into the fundamentals of spallation is an understanding of how mechanical/stress waves propagate within solid matter.

Spall occurs when a material is put into a state of dynamic tension of a critical magnitude for a critical duration. This is often the result of intersecting decompression waves that originate when the original compression pulse is reflected from a (stress-free)

surface or interface. Spall strength is here defined as the maximum tensile strength reached during the dynamic spall process. Historically the term has also been applied to the stress at which voids nucleate. For modest strain rates these two values are often interchangeable.

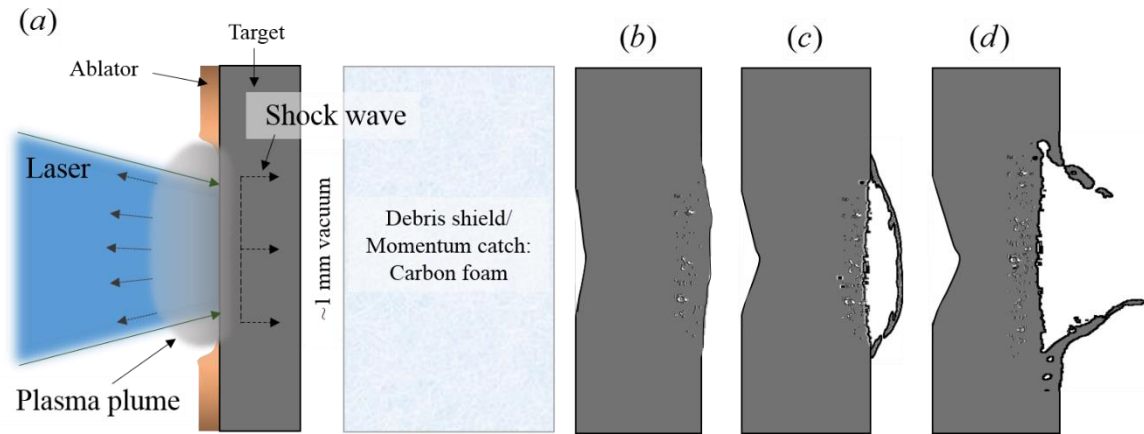


Figure 2-5. Experimental setup schematic. Target discs of varying thickness are covered by an ablator/heat shield and subject to laser ablation in order to drive a planar shock wave through the system. (a-d) Recovery experiments used a carbon aerogel foam to catch debris, decelerate and catch the tantalum for characterization. Depending on the laser energy, three states are expected (b) initial stages of incipient spall to identify void nucleation; (c) intermediate incipient spall where a clear spall bubble can be evaluated for void nucleation and growth; (d) complete spall failure resulting in ejecta.

As the shock wave progresses from the surface of the sample into the bulk, the pressure will decay rapidly due to varying dispersion effects. This effect is magnified for short duration pulses where the shock wave is “unsupported”. Dispersion also occurs laterally and plays a large role in determining the lateral spall volume. Figure 2-5 shows a schematic of an experimental setup to drive and capture a spalled target. The spall bubble (Figure 2c) is a direct consequence of the imposed shape of the laser spot, laser intensity, and dispersion that takes place as the shock wave travels. Figure 2-5b and Figure 2-5c are examples of incipient spall failure, or spall that is incomplete. Figure 2d gives an example of complete spall failure where pieces of the rear surface are ejected. If the sample is sufficiently thin the initial laser crater will merge with the spalled volume. Figure 2-6

shows a simulated position-time ( $x-t$ ) diagram of a pulsed laser and the subsequent wave interactions. In this scenario the reflected wave is strong enough to pull the material apart resulting in a large jump in porosity and thus, damage.

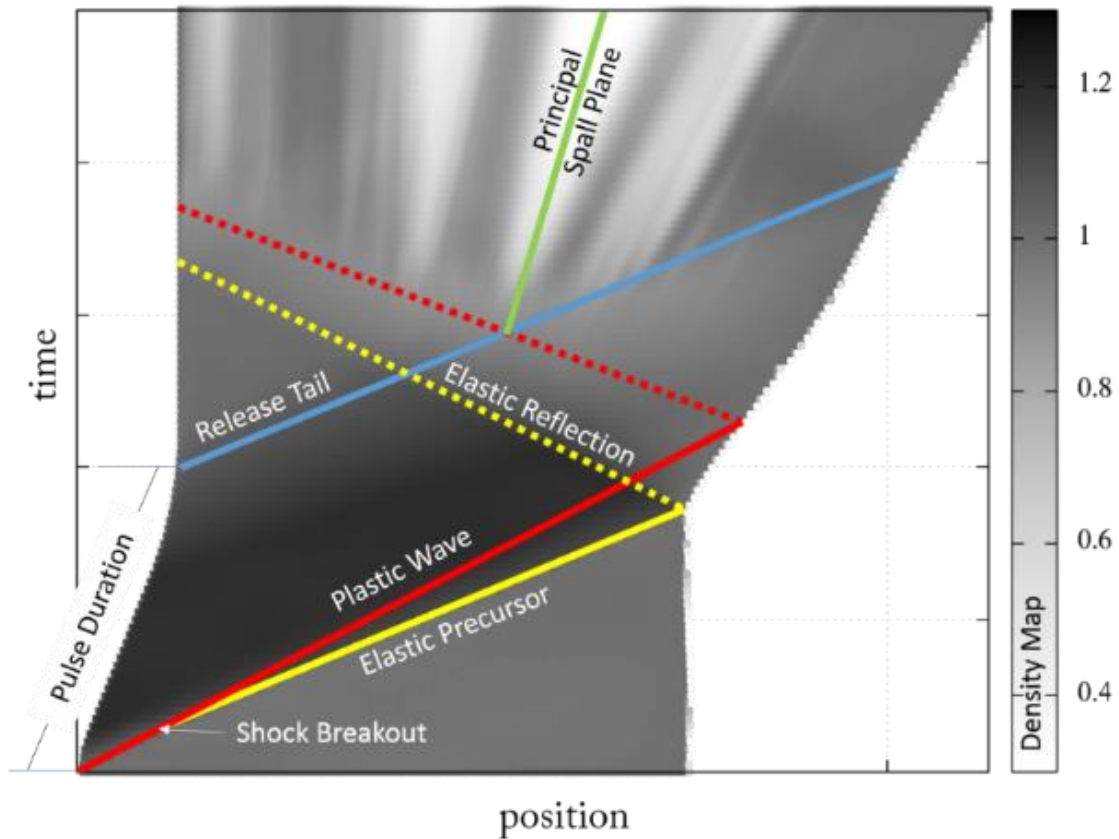


Figure 2-6. Position-Time ( $x-t$ ) diagram shaded by evolving density. The imparted wave steepens into a shock wave at the shock breakout point. From there, an elastic-plastic shock wave propagates into target until each wave (traveling at different speeds) reflects from the rear surface. The pulse duration controls the point at which the release tail “travels” into the system to interact with the plastic reflection. This point is the focus of the maximum tensile stress.

An alternate experimental setup is perhaps more common, utilizing an interferometer system to record the rear surface velocity (Figure 2-7).

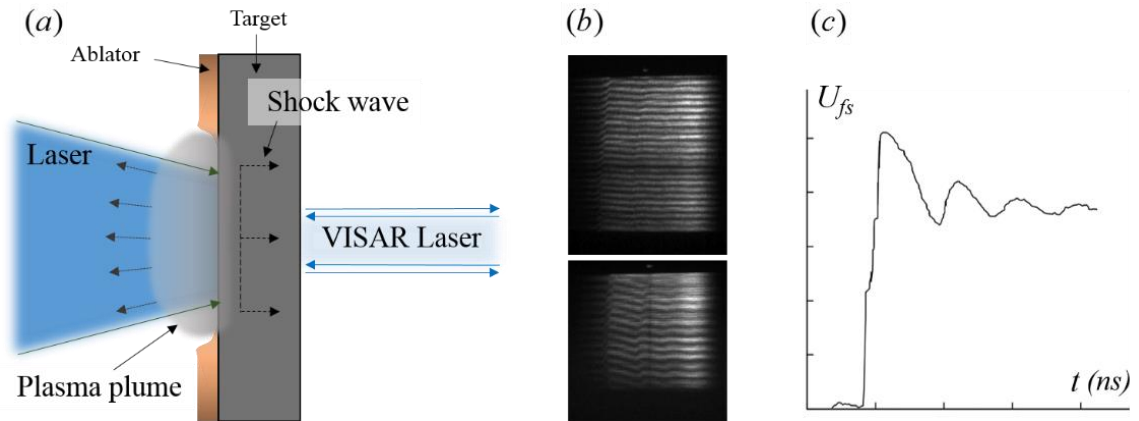


Figure 2-7. Experimental setup schematic. (a) Blue wavelength laser impinging on the front surface of a target package consisting of an ablator and target material. A second laser is directed at the rear surface and is reflected back through an optical setup. Using etalons (typically optical quartz) the phase of the laser is shifted and a Doppler type effect can be observed. This is captured by a streak camera and the result is shown in (b). (c) Fourier analysis can transform this data into a free surface velocity as a function of time.

A common technique is termed VISAR (Velocity Interferometer System for Any Reflector) and uses a laser and a system of optics with various etalons to shift the arrival time of the laser reflecting off the rear surface [35]. The result is a Doppler effect that produces fringes in a streak camera (Figure 4b). Fourier analysis can be completed to reproduce the rear surface velocity as a function of time. The profile of this curve provides important information about the failure process, but this information needs to be extracted using knowledge of how waves propagate within the material.

This process and representative variables are illustrated schematically and by a simulation in Figure 2-8.

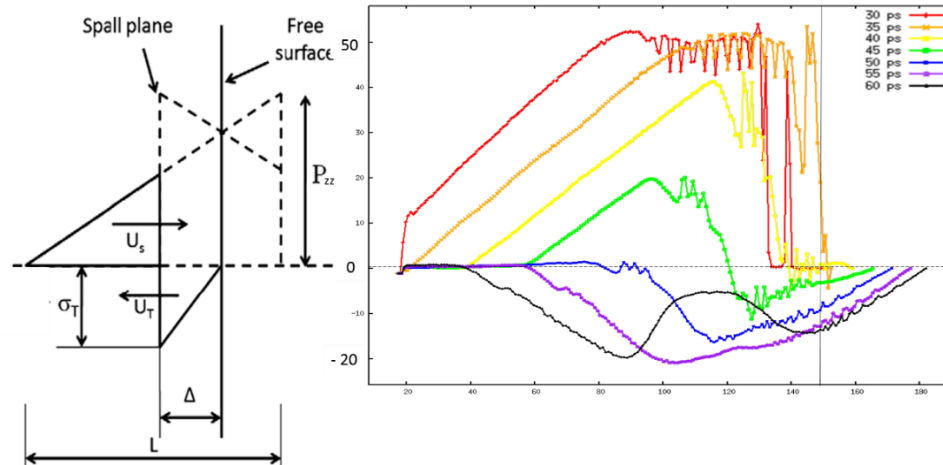


Figure 2-8. Schematic (From [36]) and simulation of spall process and related variables.

The first observation of spall in literature traces back to Hopkinson [37] with deeper investigations beginning in the early 60's by Kolsky [38], Smith [39], and Rinehart and Pearson [40]. From these early studies the primary observation is that spallation is an evolutionary damage process where spall fracture, referring to complete spall often resulting in fragmentation, develops from a collection of nucleating and growing microfractures. Breed et al. [41] first proposed spall criteria including stress rate in addition the previously proposed critical tensile stress characteristic. Tuler and Butcher [42] supplemented the existing spall theory by introducing a cumulative damage criterion where spall develops according to an integral of the stress history in a material. Tobolsky and Eyring [43] and Zhurkov et al. [44] each described spall damage according to a rate-controlled process obeying Arrhenius [45] rate equations for bond breaking/healing. Taken together, early studies show that spall is a process of dynamic damage where voids/cracks are nucleated at local microstructure/atomic protuberances and evolve with stress, strain, and temperature-dependent rates. As damage can ultimately lead to spall fracture it is no surprise that energy principles associated with the Griffith criterion for crack stability were

applied by Grady and Kipp to account for fragmentation under extreme stresses and strain rates [46–48].

Many generations of studies have followed using explosives, gas guns, flyer plates, and lasers [46,49–58] to induce tensile failure at strain rates ranging from  $10^4$  to  $5 \times 10^9 \text{ s}^{-1}$ . Tensile failure in this regime is commonly known as “spall” - a process of physical damage evolution that is initiated by a rarefaction wave, or set of waves, whose amplitude exceeds the local tensile strength of the material [52]. There is a strong experimental and theoretical foundation that shows an increase in spall strength with increasing strain rate [46,50,56,58]. There is also significant evidence that polycrystallinity decreases the spall strength as compared to single crystals [53,59,60]. Christy et al. [61] performed experiments on polycrystalline copper and observed clear differences that were rationalized later by Meyers [62] and Meyers and Zurek [63].

The tensile strength of metals is determined by the nucleation, growth, and coalescence of voids and/or cracks. At low strain rates, the applied traction generates an internal stress state that is relaxed by the introduction of these defects. As the strain rate is increased, stress-wave propagation becomes gradually more important and the stress state becomes increasingly non-uniform. Concomitantly, the competition between void nucleation, void growth, and wave propagation effects increases the complexity of the process.

The high strain-rate regime is attained in uniaxial strain, a characteristic feature of shock wave propagation, and in a geometry for which the lateral dimensions of the specimen are larger than the pulse length. Upon exceeding the local tensile strength of a material, ductile voids or brittle cracks nucleate and subsequently grow to relax the stress

by dislocation emission, twinning, or displace phase transformations [64]. In addition to the microstructure, the duration and speed of the release dictates void concentration, sizes, and distributions thereof. Voids often grow via dynamic dislocation generation [50] and coalesce into interconnected void volumes that may cause the material to undergo complete failure. If full separation of the material is incomplete, the response is deemed incipient spall. The process of void nucleation, growth, and coalescence is of critical interest in many fields due to the prevalence of spall damage in engineering applications such as ballistic penetration as well as dynamic fragmentation during hypervelocity impact events that occur in near orbit and outer space.

A classic method to measure spall strength relates the free surface velocity to the stress inside the material as communicated by stress waves. The free surface velocity measurement supplies us with important information: foremost, pressure is null at the boundary and the particle velocity is double (superposition of two waves of equivalent particle velocity) [13,50] providing adequate boundary conditions to obtain a unique solution for several waves interacting at the rear surface. The clear disadvantage is that this measurement is inherently indirect. Spall occurs within the sample and it is only through “communication” that the rear surface represents the bulk response. Furthermore, the rear surface velocity is essentially a continuum level measurement that relates multiple failure events into a “single” spall signal as shown in Figure 2-9.

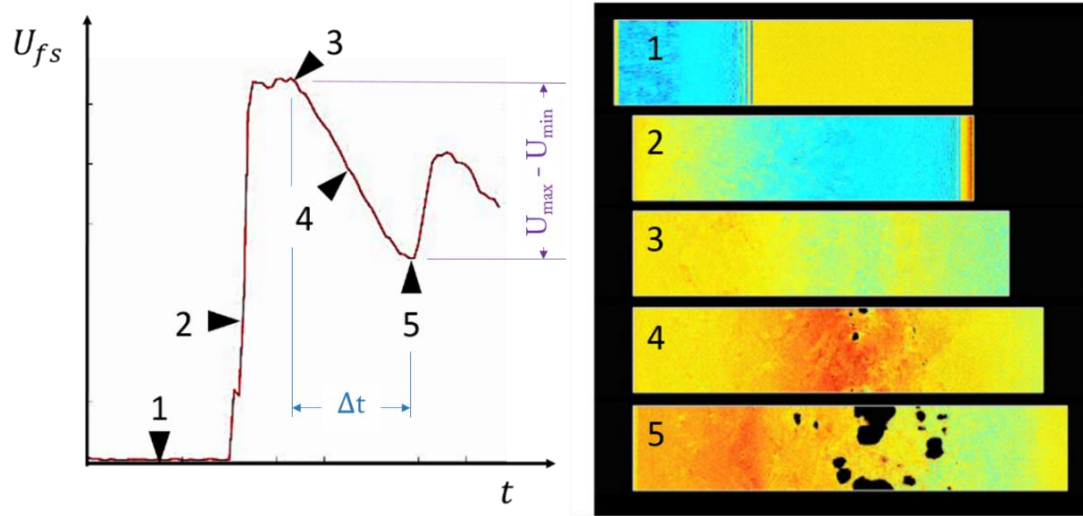


Figure 2-9. Simulated VISAR trace and corresponding visualization of the material at representative points. Color is qualitatively given according to stress state, blue for compression, red for tension.

A typical approximation made in spall calculations is the general solution of wave equations assuming two waves ( $f_1$  and  $f_2$ ) traveling in opposite directions and interacting at Lagrangian position  $h$  and time  $t$ :

$$P(h,t) = f_1\left(\frac{h}{c_0} + t\right) + f_2\left(\frac{h}{c_0} - t\right). \quad (9)$$

This result follows from a reformulation of conservation of momentum (Equation 2) in a Lagrangian coordinate system:

$$\frac{\partial u}{\partial t} + \frac{1}{\rho_0} \frac{\partial p}{\partial h} = 0 \quad (10)$$

Solving for the Lagrangian coordinate gives:

$$h = \int_0^x \frac{\rho}{\rho_0} dx \quad (11)$$

If we take a solution at the rear surface boundary condition ( $h=0$ ,  $P=0$ ,  $u_{fs}=2u_p$ ) and assume that the relationship between the time and place at which spall occurs is:



$$t_{spall} = \frac{1}{2} \cdot (t_{u_{max}} + t_{u_{min}}), \quad (12)$$

$$h_{spall} = \frac{1}{2} \cdot c_0 \cdot (t_{u_{max}} - t_{u_{min}}), \quad (13)$$

we obtain a first order solution of the spall stress and strain rate:

$$\sigma_{spall} = \frac{1}{2} \rho_0 c_0 (u_{max} - u_{min}) \quad (14)$$

$$\dot{\epsilon} = \frac{(u_{max} - u_{min})}{(t_{u_{max}} - t_{u_{min}})} \cdot \frac{1}{2c_0} \quad (15)$$

where  $\rho_0$  is the initial density of the material,  $c_0$  is the sound velocity,  $u_{max}$  is the peak velocity of the free rear surface (shock breakout), and  $u_{min}$  is the first minimum free surface velocity following  $u_{max}$  and is referred to as spall pull-back [65,66]. Several corrections have been developed that account for the elastic-plastic response of the material with significant effort led by Kanel and Fortov [51,67]. The most popular and applicable of these corrections adjusts for the difference in the plastic ( $C_b$ ) and elastic ( $C_l$ ) sound speeds plus a term that accounts for the stress gradient of the refracted wave which is determined by the pulse shape:

$$\sigma_{spall} = \frac{1}{2} \rho_0 c_0 (u_{max} - u_{min}) \left( \frac{1}{1 + \frac{c_l}{c_b}} \right) + \Delta\sigma \quad (16)$$

Critical points on the  $u_{fs}$ - $t$  diagram are identified in Figure 2-9. Points 1-5 correspond to characteristic times leading up to, during, and after spall failure. Point 1 indicates the stationary free surface while the compressive wave traverses the sample. Point 2 indicates the rapid shock rise shortly after the arrival of the shock wave, and right below

this point is the typical kink indicative of the Hugoniot elastic limit. Point 3 corresponds to the maximum rear surface velocity,  $u_{\max}$ , and marks the start of relaxation [68] – the rarefaction wave begins returning into the sample at the beginning of the preceding plateau and for short pulse durations the width of the plateau approaches zero. Point 4 is the material undergoing tensile failure at the spall plane. Point 5 is the arrival of the plastic release wave at the rear surface and marks the minimum rear surface velocity,  $u_{\min}$  [69]. Point 4 is approximately half way between points 3 and 5; for a perfect acoustic system where the sound speed does not depend on density, the point is exactly half. With these methods it is possible to infer the tensile strength and the corresponding tensile strain rate.

In addition to free-surface velocimetry [55,70] indirect measures such as Laue diffraction [71,72] can be used to infer the internal stress states of the material during dynamic failure. Although highly useful, these experimental measurement techniques rely on accurate Hugoniot and EOS data [35,57,70,73] as well as several bulk acoustic assumptions and simplifications that break down for realistic microstructures, high strain rates, or large amounts of plasticity and/or damage evolution [74]. Several studies utilize post-mortem microscopy to identify damage, but it is often difficult to trace damage back to a specific source [59] and the spall strength and damage field are not unique to one another [75]. Other techniques are being developed, such as the use of high speed imaging [76], that may address some of the issues enumerated here. Critically, spall models strongly rely on empirical data [74,77,78] for which many important quantities are often lacking.

### **2.2.1. Ultimate Tensile/Cohesive Strength**

The ultimate strength of materials represents the stress at which the interatomic forces can no longer sustain the cohesion of the structure. In quasi-static uniaxial

stress/tension the value is never reached or even approached as a variety of mechanisms conspire to lower the maximum sustained tensile stress. However, as the strain rate is increased, this value rises and in the shock-wave regime the stress state (uniaxial strain) and the kinetics of void/crack nucleation, growth, and coalescence are such that the ultimate stress can be reached. The theoretical strength in tension is an important parameter because spall strengths below a critical strain rate should be a fraction of this value. The ultimate tensile strength of the material is limited by the bonds/interaction between atoms. From a physics perspective, the interaction between atoms is universally described by the equation of state. From an interatomic potential perspective, this is defined through the internal energy as a function of the volume an atom occupies. The Morse potential provides a means to evaluate the strength via the following reasoning. A generalized volume-dependent Morse potential has the following form:

$$U = U_c \left\{ e^{\left[ \frac{-2(V-V_0)}{a} \right]} - 2e^{\left[ \frac{-(V-V_0)}{a} \right]} \right\} \quad (17)$$

$U$  is the internal energy,  $U_c$  is the equilibrium cohesive energy,  $V$  is the specific volume ( $V=1/\rho$ ),  $V_0$  is the specific volume at zero pressure, and  $a$  is a parameter constrained by the bulk modulus. The attractive (tension) and repulsive (compression) nature of the  $U$ - $V$  curve can be shown in Figure 2-10. Figure 2-10 displays how  $U$ - $V$  relates to the resultant  $P$ - $V$  curve.

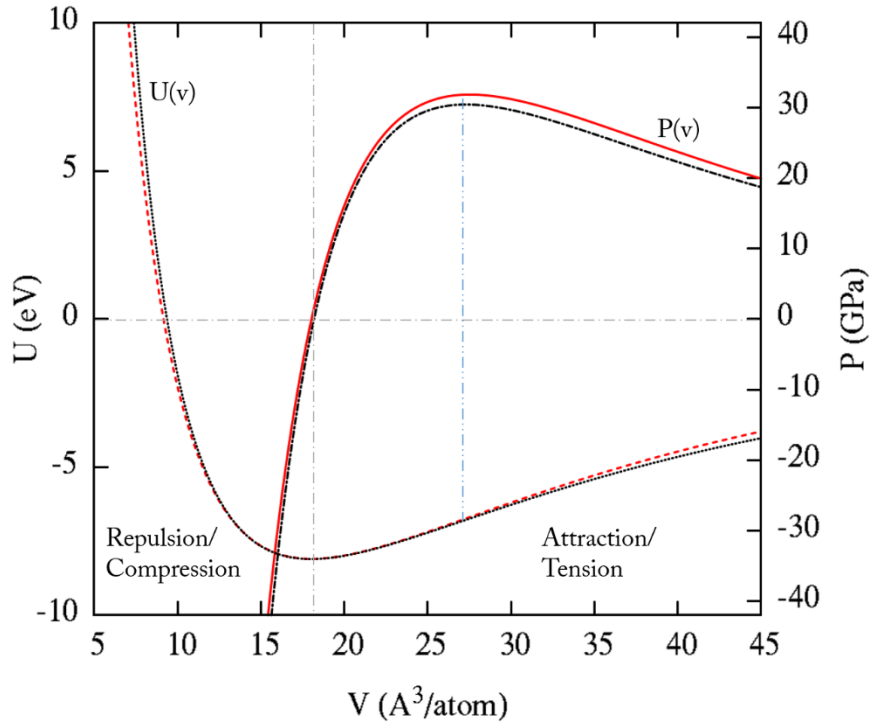


Figure 2-10. Example Morse [79] interatomic potential compared to a universal EOS for metals by Rose [80,81]. The U-V response is given by the dashed red line for Rose and the dotted black line for Morse. The P-V relation is given by the solid red line for Rose and dot dashed black line for Morse. A positive pressure denotes a tensile pressure. A vertical gray line intersects the U-v curve at the minimum internal energy (corresponding to the equilibrium cohesive energy) which defines the volume at which the pressure of the system is zero. Notice that the maximum of the P-v curve occurs at an inflection point in the U-V curve. Subtle differences in the interatomic potential tail play a significant role in the determination of the maximum tensile state.

The pressure is defined as:

$$P = -\frac{dU}{dV} \quad (18)$$

The bulk modulus of the potential is obtained from its formal definition:

$$B_0 = V \left. \frac{d^2U}{dV^2} \right|_{V=V_0} \quad (19)$$

$$B_0 = \frac{2V}{a^2} U_c \left\{ 2e^{\left[\frac{-2(V-V_0)}{a}\right]} - e^{\left[\frac{-(V-V_0)}{a}\right]} \right\} \Bigg|_{V=V_0} \quad (20)$$

$$B_0 = \frac{2V_0}{a^2} U_c \quad (21)$$

Thus, the parameter  $a$  is defined as:

$$a = \sqrt{2V_0 U_c / B_0} \quad (22)$$

The cold pressure is related to the internal energy directly by:

$$P = \frac{dU}{dV} = \frac{d}{dV} \left( U_c \left\{ e^{\left[\frac{-2(V-V_0)}{a}\right]} - 2e^{\left[\frac{-(V-V_0)}{a}\right]} \right\} \right) \quad (23)$$

$$P = \frac{2}{a} U_c e^{\left[\frac{-(V-V_0)}{a}\right]} \left\{ e^{\left[\frac{-(V-V_0)}{a}\right]} - 1 \right\} \quad (24)$$

The theoretical cohesive stress/strength, as developed by Grady [46], is derived from the minimum (or maximum if the negative pressure is given) of the  $P$ - $V$  curve such that

$$P_{th} = P \Big|_{\frac{dP}{dV}=0},$$

$$0 = \frac{dP}{dV} = \frac{d}{dV} \left( \frac{2}{a} U_c e^{\left[\frac{-(V-V_0)}{a}\right]} \left\{ e^{\left[\frac{-(V-V_0)}{a}\right]} - 1 \right\} \right) \quad (25)$$

$$0 = \frac{4}{a^2} U_c e^{\left[\frac{-2(V-V_0)}{a}\right]} - \frac{2}{a^2} U_c e^{\left[\frac{-(V-V_0)}{a}\right]} \quad (26)$$

$$V - V_0 = a \ln(2) \quad (27)$$

Equation 26 represents the volume condition that satisfies the minimum of the pressure-volume relationship and can be plugged into Equation 23 or 24 yielding:

$$P_{th} = \sqrt{\frac{B_0 U_{coh}}{8V_0}} \quad (28)$$

It should be noted that changing the initial form of the Morse potential, such as by switching the “2” factor in Equation 17, will lead to estimates that differ in the coefficient in the denominator of Equation 28. This is emphasized by Grady [46] by demonstrating that an analogous relationship equating the elastic energy storage to a volumetric cohesive energy gives a similar result, differing by a constant. Thus, a general form of the predicted strength can be written as:

$$P_{th} = s \sqrt{\frac{B_0 U_{coh}}{V_0}} \quad (29)$$

Where  $1/s$  represents a constant that is usually between 1.5 and 3. It is worth noting is that this definition of ultimate strength is inherently hydrostatic. It should be expected that stress anisotropy will be significant, especially under laser compression and release.

The theoretical tensile strength can also be evaluated by utilizing a known equation of state. A prime example of an applicable EOS is the universal EOS for metals developed by Rose et al. [80] for metals and expanded upon for solids in general [81]. The predictions by Rose provide an improved description of atomic anisotropy. Figure 2-11a gives a plot of the predictions from Grady-Morse and from Rose as a function of bulk modulus. Figure 12b plots the predictions of the two interatomic potentials with respect to one another. A linear trend can be identified with a slope of 1.4.

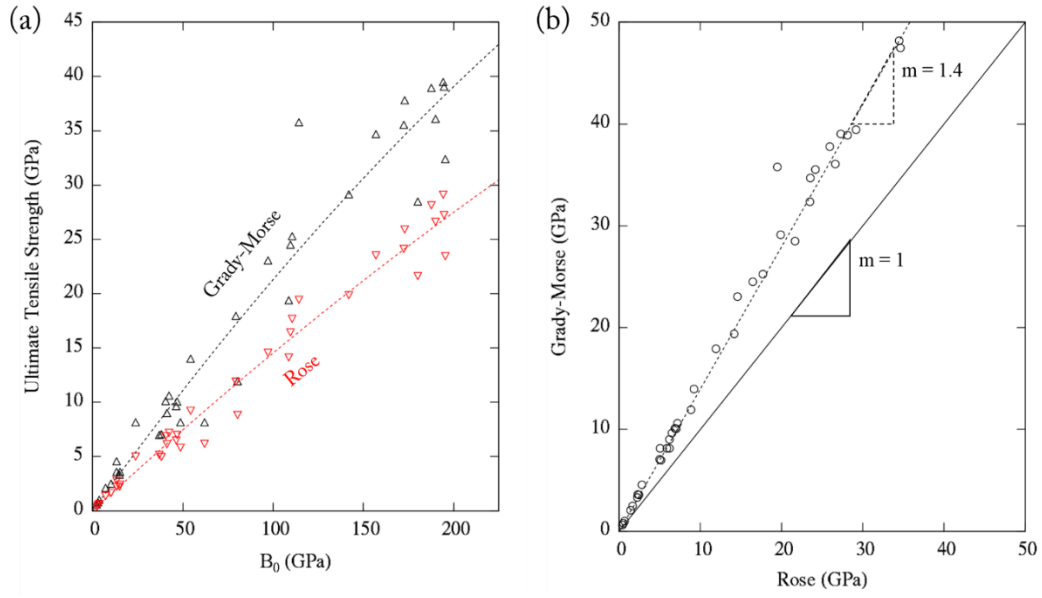


Figure 2-11. (a) Ultimate tensile strength plotted according to the element’s bulk modulus using the predictions of Grady [46] and Rose [80,81]. (b) Linear fit of the relationship between the predictions giving a slope of 1.4.

Taking this correction into account, the 1/s value in Equation 29 is ~2. A map of the periodic table of elements and their predicted ultimate tensile strengths are given in Figure 2-12, colored by the magnitude thereof.

1																	2																		
	H																	He																	
3	Li	4	Be													5	B	6	C	7	N	8	O	9	F	10	Ne								
	2.79		19.45														13	14	15	16	17	18													
11	Na	12	Mg														Al	Si	P	S	Cl	Ar													
	1.39		5.17														11.91																		
19	K	20	Ca	21	Sc	22	Ti	23	V	24	Cr	25	Mn	26	Fe	27	Co	28	Ni	29	Cu	30	Zn	31	Ga	32	Ge	33	As	34	Se	35	Br	36	Kr
	0.66		2.43				16.46		23.55		26.61				24.14		27.27		28.14		19.88		8.84												
37	Rb	38	Sr	39	Y	40	Zr	41	Nb	42	Mo	43	Tc	44	Ru	45	Rh	46	Pd	47	Ag	48	Cd	49	In	50	Sn	51	Sb	52	Te	53	I	54	Xe
	0.52		7.19				14.60		25.95		34.49				40.98		23.46		14.13		6.21		6.50												
55	Cs	56	Ba	*	72	Hf	73	Ta	74	W	75	Re	76	Os	77	Ir	78	Pt	79	Au	80	Hg	81	Tl	82	Pb	83	Bi	84	Po	85	At	86	Rn	
	6.50		1.65				17.70		29.13		40.85		48.30		44.45		34.61		21.64				4.97		5.86										
87	Fr	88	Ra	**	104	Rf	105	Db	106	Sg	107	Bh	108	Hs	109	Mt	110	Ds	111	Rg	112	Cn	113	Uut	114	Fll	115	Uup	116	Lv	117	Uus	118	Uuo	
	5.86																																		
*	57	La	58	Ce	59	Pr	60	Nd	61	Pm	62	Sm	63	Eu	64	Gd	65	Tb	66	Dy	67	Ho	68	Er	69	Tm	70	Yb	71	Lu					
				5.02									2.24		6.09				6.17				7.02			2.26									
**	89	Ac	90	Th	91	Pa	92	U	93	Np	94	Pu	95	Am	96	Cm	97	Bk	98	Cf	99	Es	100	Fm	101	Md	102	No	103	Lr					
				9.23																															

Figure 2-12. Periodic table showing trends in ultimate tensile strength. Predictions calculated using Rose et al. [80] EOS model.

Lastly, the experimental spall plane may be non-uniform due to the shape of the laser pulse. This can be seen in Figure 2-13 where a spall bubble has formed. This has interesting ramifications when comparing results to simulations that often assume periodic conditions lateral to the shock.

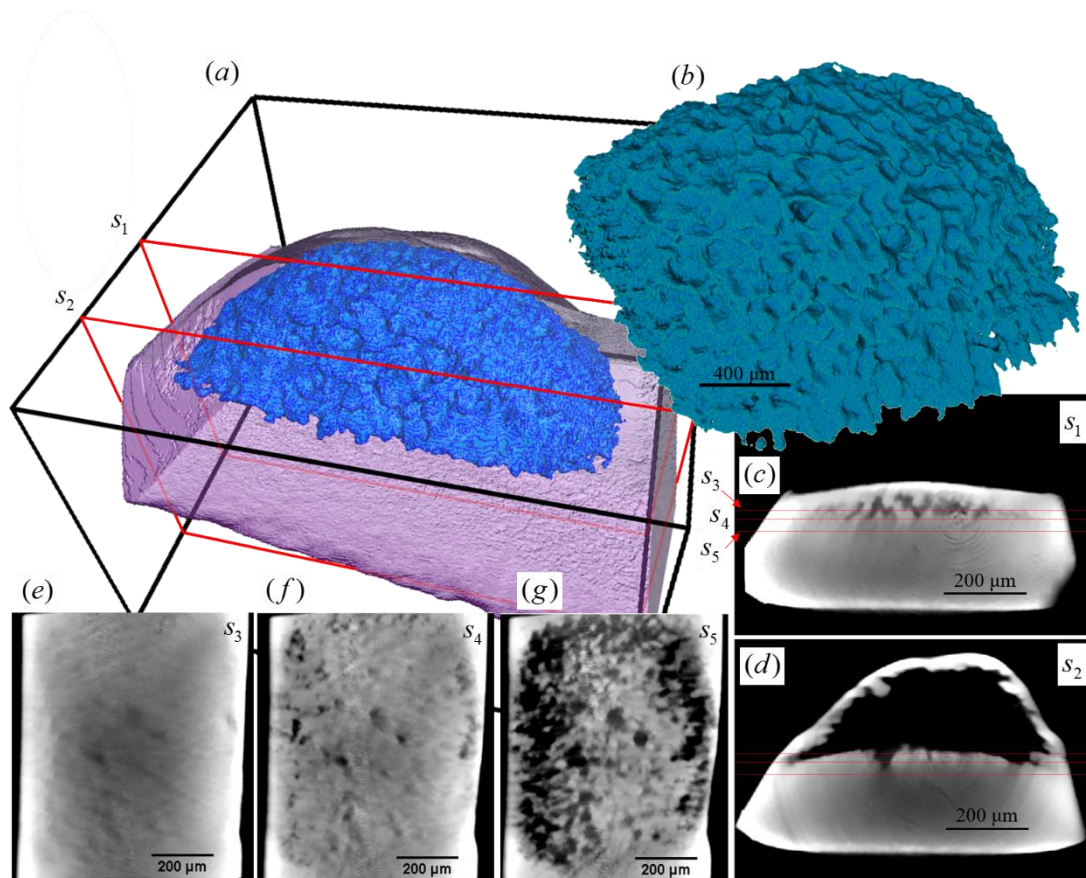


Figure 2-13. Segmented 3D volume derived from  $\mu$ -CT imaging of the polycrystalline tantalum system subjected to spall conditions where the transparent purple is the tantalum and the solid blue material is the contained void. The surface of the spall bubble is shown in (b). (c,d) Cross sections identified in (a) showing (c) a view through the lateral edge of the spall bubble and (d) the center of the spall bubble. In (c,d) there is clear evidence of failure at grain boundaries by the presence of intact grains at the top and bottom of the bubble. Three “depth” progression views (e-g) correspond to the red lines of (c,d), laying parallel to the spall plane. Starting (e) near the edge of the spall bubble just within the tantalum, and going (f) 30  $\mu\text{m}$  toward the bubble from part ‘e’, and (g) 50  $\mu\text{m}$  toward the bubble from part ‘e’. Submitted work: Remington et al. [82].



### 2.3. Crystalline Structure and Defects Therein

A crystal or a crystalline solid takes its name from Greek origins fusing the terms for ice, rock, and cold, but, alas, our modern definition is a solid with three-dimensional periodicity of atoms, molecules, and/or ions. The majority of inorganic solids that we encounter on a daily basis are not single crystals, but polycrystals consisting of multiple crystal grains that vary in size, shape, and orientation. Between each grain and its neighbors exists an interface called a grain boundary. This boundary is an example of a planar defect. The density of grain boundaries is proportional to the average surface area of each grain divided by twice the total volume of the grain as each boundary is common to two adjacent grains. Although characterized as a plane, a grain boundary typically has a thickness that relates to the specific crystal structure, atomic size, and various measures of misorientation to adjacent crystals. Due to these boundaries, the mechanical properties of polycrystalline metals are drastically different from monocrystalline metals; likewise, nanocrystalline metals behave distinctly from their large-grained counterparts.

#### 2.3.1. Dislocations

Dislocations were first theorized (simultaneously) in 1934 by Orowan [83], Taylor [84] and Polanyi [85]. Volterra [86] (distortion) provided the necessary analytical framework that was readily used by Taylor [84] to account for shear strengths far below their predicted values of  $\frac{\sigma}{2\pi}$ . Dislocations are essentially lattice interruptions that allow for atomic motion over smaller barriers than climbing lattice site to lattice site. Much work followed this discovery and important contributions by Burgers [87,88], Cottrell [89], Nabarro [90], and Eshelby [91] proposed other imperfections and defect interactions that

have paved the way for understanding the mechanical properties of crystalline solids. A look at dislocation slip, densities, and mobility during shock is succinctly given by Meyers et al. [92]. Many books exist on the topic of dislocations including the work of Hull and Bacon [93] and Bulatov and Cai [94] focused on the simulation of dislocations.

The possibility of experimentally observing dislocations in compression of single crystalline tantalum occurs at pressures near 25 GPa. Homogeneous dislocation nucleation for  $\langle 100 \rangle$  crystals for two prominent potentials are: Ravelo EAM,  $P_{zz} = 56$  GPa [95]; MGPT:  $P_{zz} = 65.9$  GPa. Without appropriate sources for heterogeneous nucleation, neither of the leading potentials predict dislocations at 25 GPa. Instead, twins as well as dislocations are often observed at higher pressures.

### **2.3.2. Grain Boundaries**

Crystalline solids commonly consist of many grains separated by planar interfacial defects, grain boundaries. Nanostructured materials provide us with a means to study the intrinsic nature of solid interfaces with the potential to extend structure-property relationships down to the atomic regime. Grain-boundary atoms divide adjacent crystals of differing orientation. It is clear from both simulation and characterization that crystallinity extends right up to the interface and that an interface may grow or shrink during plastic deformation.

Within the last two decades it has been shown that transitions to smaller grain sizes, and thus greater grain boundary density, introduce unique mechanical deformation mechanisms. Enlargement of interfacial volume fraction and the associated reduction of bulk volume fraction are responsible for causing several atomic-scale interactions, such as dislocation accumulation, to fail to manifest below a critical grain size. The volume fraction

of interfaces increases to the first order as  $3\delta/d$ , where  $\delta$  represents the interface thickness shared by two grains and  $d$  represents the average grain diameter. A similar relationship also exists for the volume fraction of triple junctions. Using space filling tetrakaidehedra, Tschopp et al. [96] produced volume fractions shown in Figure 2-14, agreeing well with previous illustrations [97].

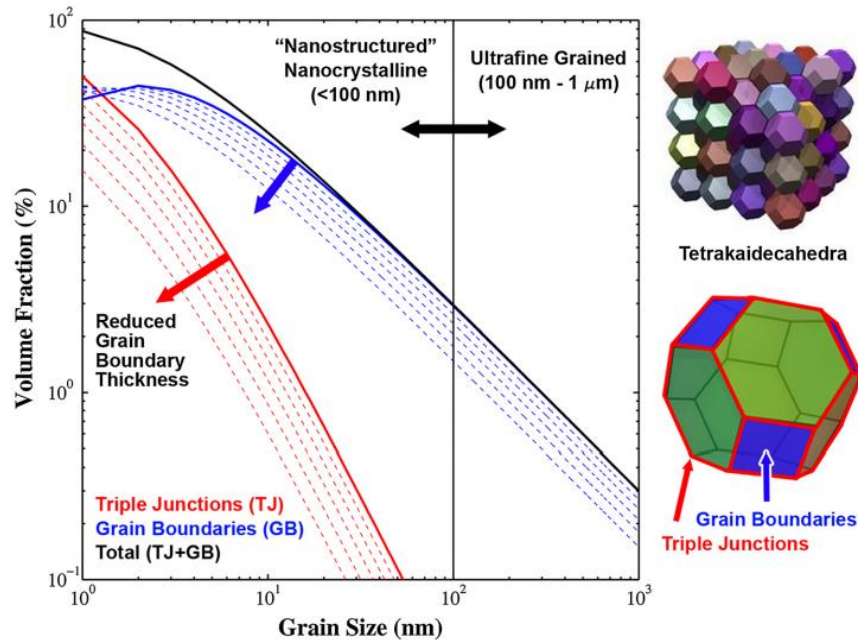


Figure 2-14. The increase in the volume fraction of grain boundaries and triple junctions as a function of grain size in the nanocrystalline (<100 nm) and ultrafine grain (100 nm–1 μm) regimes. These plots are based on space-filling tetrakaidehedra grains with a grain boundary thickness of 1 nm (thick line), where the dotted lines show the evolution for grain boundary thicknesses of 0.9 nm to 0.5 nm in increments of 0.1 nm. From Tschopp et al. [96].

Typical interface thicknesses on the order of 2-3 atomic distances dictate that the volume fraction of grain boundary atoms is as large as 50% for 4 nm grains, 25% for 12 nm grains, 10% for 24 nm grains, and 1% for 200 nm grains. Without dominating grain interior deformation, the strength of nanocrystalline metals is affected by the growing volume fraction of grain boundaries, providing a greater number of available shear/sliding points [98] and increasing the effective porosity of the sample [99].

Early work by Ashby [100] approaches the problem of polycrystalline aggregates by differentiating between grain boundary interiors and boundaries, representing polycrystals as heterogeneous materials. It is also known that grain boundaries come in a wide variety [101–107] and that many interfaces are stronger than others [59,108–112]. The interaction of grain boundaries with dislocations, the traditional carrier of plasticity, is of critical importance to the strength of metals [113–116].

Grain boundaries play a critical role in the determination of mechanical, chemical, and thermal properties of polycrystalline materials. Specifically, the internal GB structure and energy can strongly determine grain boundary stability and influence the deformation response by affecting dislocation nucleation, dislocation motion, grain boundary sliding, diffusion, and radiation damage processes [59,108,117–121]. The distribution and character of grain boundaries is especially important in controlling the strength of metals [122], especially tantalum [123–125]. The nature of grain boundaries is complex because their energy is dependent on their character, which depends on five degrees of freedom. To these, one could add translation, which also changes the nature of the boundaries and has been shown to be particularly important for bcc metals [126]. A number of analytical approaches have been developed to treat GB structures: coincidence site lattice (CSL), displacement shift complete (DSC), and other topological treatments, e.g. [107]. To investigate the dependence of deformation mechanisms on GB structural details, we first must understand the structural and energetic landscape of GBs as in recent surveys of face-centered cubic (fcc) [127] and some body-centered cubic (bcc) [128] materials.

The boundary between two crystals, now referred to as a single system called a bicrystal, can be represented by 5 independent degrees of freedom (based on 6 rotations

with 2 dependent rotations). These five degrees of freedom can be described as rotations of either the crystalline grain to a reference grain (3 degrees of freedom) or the boundary plane dividing the two crystals (two degrees of freedom). It has been shown that there is at least one set of rotations that describes a given interface, but there is no requirement for uniqueness, particularly if a given rotation relates to the inherent crystal symmetry ( $\overline{m3m}$  for cubic systems, of which body centered cubic and diamond cubic will be the two systems of primary evaluation). Additional dependent translations parallel and perpendicular to the grain boundary normal allow for equilibration of the grain boundary and are important in effective grain boundary energy minimization. It is worth mentioning that, during equilibration, global minimum energy positions exist alongside local troughs in the energy surface; an example of locally stable structures can be seen in Figure 2-15.

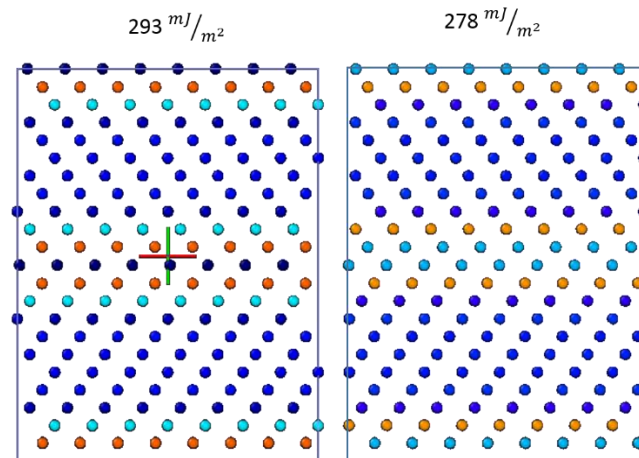


Figure 2-15. Low energy configurations of  $\Sigma 3$  boundary. (Left) Expected twin boundary. (Right) Unexpected  $\Sigma 3$  boundary without mirror symmetry.

### 2.3.2.1. Nanocrystals

The dependence of the strength of metals on the grain size has fascinated researchers since the first half of the twentieth century when Hall [129] and Petch [130]

obtained the inverse dependence of strength on grain size. This subject has been treated in thousands of publications and has recently been superbly reviewed by Armstrong and Li [99,131]. The classic  $d^{-1/2}$  relationship is an approximation which breaks down for small grains. Measurements on iron [132,133] and an analytical model by Meyers and Ashworth [134] proposed a gradual decrease in the Hall-Petch slope at very small grain sizes. Gleiter's classic work on nanocrystalline metals [135,136] tipped the scale towards the exploration of ultrafine and nanocrystalline grain sizes, and this decrease in this Hall-Petch slope was unveiled for a number of materials.

The breakthrough work by Chokshi et al. [137], reporting a negative Hall-Petch slope in the nanocrystalline region was followed by intense activity [e.g. Meyers et al. [97,122]]. There is still considerable debate as to the soundness of the experimental results by Chokshi et al. [137] and the pervading effect of varying the residual porosity [133,138,139], but the work stimulated global interest.

The number of computational works now grows daily and the amount of work is monumental. A decade ago, two review papers on nanocrystalline metals emphasized the unknowns, complexity, and appeal of nanocrystalline metals. The review by Wolf et al. [140] tackled the fundamental question of the extent to which atomic simulations capture reality and, similarly, the review by Meyers et al. [97] evaluated the ability of numerous models to accurately predict deformation behavior at the nanoscale. The complementary conclusions of each indicate that molecular dynamics (MD) simulations' capacity to directly visualize defects with atomic resolution provide utility unmatched by experimental characterization, but that they must be tempered with experimental results. As computation power climbs and cost plummets, it is to be expected that fundamental insights into the

structure and properties of crystalline defects, as well as physical mechanisms ranging from atomic diffusion to interface migration to grain rotation will be made through atomic-scale simulation and modeling. Simulations deriving from atomic and ab initio models extend their reach by providing invaluable input criteria for multi-scale models, continuum models, and materials design [141–147] especially in an iterative feedback loop [148].

The “negative” deviation in yield strength behavior results from the scale-determined interruption of dislocation pile-up associated with the traditional explanation for the Hall-Petch effect; as grain size is reduced, the number of dislocations associated with a given grain boundary is reduced and the summative contribution to the stress field is diminished. Yet, although the stress field associated with a single grain is diminished, the influence of stress fields emanating across neighboring grains provide sufficient motivation for relaxation of grain boundaries and triple junctions by grain-boundary sliding [149].

Fundamentally, a key piece to further our understanding of nanostructured phenomenon is the ability to precisely observe how emission, transmission, absorption, rearrangement, accommodation, and storage of dislocation defects at grain boundaries of different dense crystal systems (here bcc, and dc). Also of critical interest is how varying degrees of misorientation as well as the grain size itself changes dislocation interactions.

Chapter 2, in part, is a reprint of material that has been published: E.N. Hahn, M.A. Meyers, Grain-size dependent mechanical behavior of nanocrystalline metals. 646 (2015) 101–134. doi:10.1016/j.msea.2015.07.075. The thesis author was the first author of this article.

Chapter 2, in part, is a reprint of material that has been published: E.N. Hahn, S.J. Fensin, T.C. Germann, M.A. Meyers, Symmetric tilt boundaries in body-centered cubic tantalum, *Scripta Materialia*. 116 (2016) 108–111. doi:10.1016/j.scriptamat.2016.01.038. The thesis author was the first and corresponding author of this article.

Chapter 2, in part, is currently being prepared for submission for publication: E.N. Hahn, M.A. Meyers, *Laser-Driven Shocks and Dynamic Failure*. The thesis author was the first author of this article.

Chapter 2, in part, is currently being prepared for submission for publication: T.P. Remington, J.C.E. Mertens, E.N. Hahn, S. Sabbaghianrad, T.G. Langdon, C.E. Wehrenberg, B.R. Maddox, D.C. Swift, B.A. Remington, N. Chawla, M.A. Meyers, Spall Strength Dependence on Strain Rate and Grain Size in Tantalum. The thesis author was the third author of this article.



### **3. Molecular Dynamics**

Molecular dynamics (MD) simulations provide the complete information of each atom for each time step evolution. Thus, these simulations allow for the direct observation of the atomic mechanisms necessary to fully describe mechanical phenomena, albeit often at great computation cost. Simulations are particularly useful for the visualization of experiments where normally only the initial and final characterization can be observed. MD is also uniquely suited for conducting “computer experiments” because there are often no intrinsic assumptions made about the material and processes beyond characterizing accurate interatomic interactions. In the following sections, the details of current computational capability and simulation schemes are enumerated. This section gives information

#### **3.1. Computational capability: present and predictions**

A recent review by Farkas [150] emphasizes that, in spite of a large gap in achievable time scales, atomistic modeling continues to serve as a unique tool for direct visualization of defects that influence microstructural evolution. This has been more so the case as both computational power and our ability to characterize complex simulations continue to advance at an impressive rate. Spanning 2005-2015, the power of our personal computers has reached what was capable by supercomputers 15 years earlier. An example of recent efforts aimed towards bridging the gap between simulation and experimentation is [151] where simulations are extended to sample lengths reaching several micrometers long in the shock direction, yet limited to tens of nanometers cross-sections repeated

through periodic boundary conditions. Atomic modeling techniques such as molecular dynamics provide the ability to develop “atomic resolution movies” of dynamic material behavior through subsequent integration of Newton’s equations of motion [152]. The ability of high performance computing has been demonstrated with trillion-atom molecular dynamics simulations using a pairwise Lennard-Jones form in 2008 [153] and billion atom simulations of many-body potentials in 2012 [154]. Approximately  $10^9$  atoms form, in tridimensional space, a simulation box with lateral dimensions of  $10^3$  atoms, approximately 200 nm. MD time steps must be small enough to capture the frequency of thermal vibrations in order to accurately evolve each time step; thus, each step must be less than the Debye period ( $10^{-13}$  s, derived from the maximum vibrational frequency called the Debye frequency,  $\sim 10^{13}$  1/s). For this reason a typical time step is one femtosecond (fs) or  $10^{-15}$  s and typical simulations are limited to picosecond and nanosecond timescales. Access to supercomputers with the ability to run hundreds of processors in parallel presents the opportunity to run many permutations of simulated experiments in realistic time frames. The number of atoms and accessible time scale are plotted in Figure 3-1.

Taking a few standardized variables, such as a femtosecond time step and nanosecond total simulation time, grain sizes as large as  $\sim 50$  nm can be simulated, limited largely by the number of grains in each dimension required to ensure a good measure of polycrystallinity. The current and projected capability of personal and high performance computers are shown in Figure 3-2 using projections derived from the Top500 list for high performance computing (HPC) and NVidia graphics cards for desktop computers. The equations relating the computable grain size to year (relative to 1992) are:

$$d_{HPC} = 1.32e^{(0.214(y-1993))} \quad (30)$$

$$d_{desk} = 0.55e^{(0.132(y-1993))} \quad (31)$$

This places the micron (or microsecond) regime between 2025 and 2050 respectively.

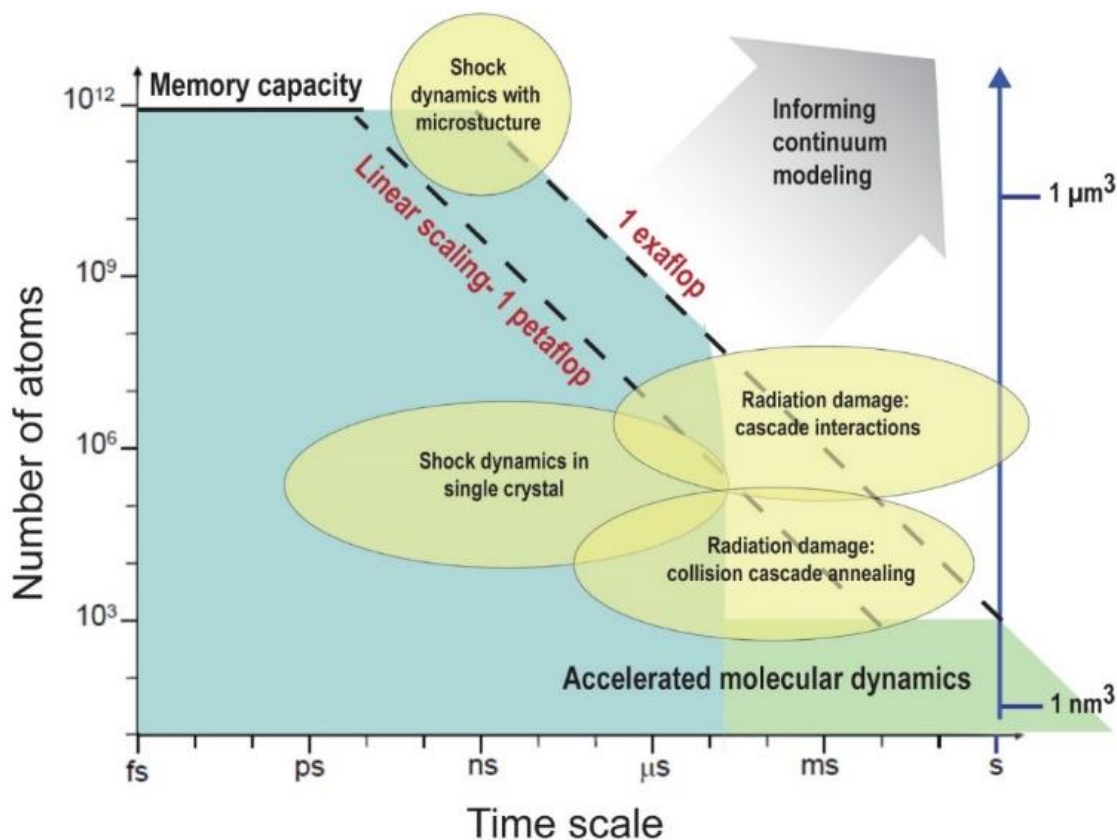


Figure 3-1. Time scale and number of atoms are the primary computational cost components. Plotted against one another they represent the currently achievable simulation space extending towards petaflop and exaflop computational resources. Simulations in the bottom left are computationally cheap while towards the top right requires multi-scale models that pass on information from molecular dynamics simulations.

To put the processing requirements of molecular dynamics in perspective, an introductory aim of my thesis proposal was the determination of computationally feasible grain sizes as a function of the calendar year in a rigorous manner. A good starting point for this calculation was an evaluation of the total floating point operations (FLOP) needed to complete the simulation divided by the achievable floating point operations per second

(FLOPPS). This provides the total number of seconds necessary to run the simulation to completion. For ease of interpretation, seconds are adjusted to years by  $3.15569 \cdot 10^7$  seconds/year. In order to classify a simulation as achievable during a specific calendar year, the total computation time is set equal to 1 year. We neglect the possibility of running a simulation over a multi-year timespan as we are mainly interested in a representation of what is feasible for a specialized researcher who obtains a one-time, limited-duration allocation. Thus we begin with:

$$y = \frac{FLOP}{FLOPPS} \frac{1}{3.15569 \cdot 10^7} \rightarrow FLOP = FLOPPS \cdot 3.15569 \cdot 10^7 \quad (32)$$

To obtain an estimate of FLOP we take the number of FLOP per pair per integration for a Lennard-Jones (LJ) potential multiplied by the number of atoms,  $N$ , by the number of interacting neighbors  $N_c$ , for a given number of iterations to advance the system in time. A typical number of FLOP per pair taking a double precision integration is 16 for LJ [155]. Later we may take a larger multiple of this number to account for different potential schemes and refer to this as a potential multiplier (PM). The number of iterations,  $I$ , is equivalent to the desired simulation time,  $t_s$ , divided by the timestep  $\Delta t$ . Together we have the following baseline definition for FLOP:

$$FLOP = 16 \cdot N \cdot N_c \cdot \frac{t_s}{\Delta t} \quad (33)$$

To evaluate the number of atoms in a given simulation we introduce a relationship between the grain size and an idealized lattice of grains inside a cubic sample. Thus sample size,  $S$ , is equivalent to  $x$  grains in each dimension:  $S = (xD)^3$ . For non-cubic systems,  $S = uvwD^3$  and  $x$  is a general quantity factor by,  $x = (uvw)^{1/3}$ . We then relate sample

size to total number of atoms by an atomic density:  $N = S \cdot \rho_a$ , where  $\rho_a = \frac{\rho \cdot N_A}{AW}$  and  $\rho$  is the mass density,  $N_A$  is Avogadro's number, and  $AW$  is the atomic weight. The number of atoms within a given cutoff radius,  $r_c$ , can be estimated by taking a spherical cutoff volume,  $V_c = \frac{4}{3} \pi r_c^3$ , and is used to approximate the number of interacting neighbors,  $N_c = (V_c/V_0) \cdot n_{a_0}$ , where  $V_0 = a_0^3$  and  $n_{a_0}$  is the number of atoms per unit cell. Not simplifying for Newton's third law, the number of pairs is equal to the number total atoms times the number of interacting neighbors,  $pairs = N \cdot N_c$ . Not accounting for communication time between processors nor resorting neighbor lists we can write a simple relationship between the total number of required integrations in terms of pairs (number of integrations at a given timestep) and the total number of timesteps given by  $t_T = \frac{t_s}{\Delta t}$ , where  $t_s$  is the total simulation time and  $\Delta t$  is each timestep.

Taking the TOP500 as the standard for processing power following the LINPACK benchmark and a history detailing the top supercomputer twice annually since 1993, the following effective Moore's Law fit is taken in GigaFLOPPS as a function of calendar year:

$$GFLOPPS = 2^{4.932138 + 0.9233(n-1993)} \quad (34)$$

Note that this places the exascale ( $10^{18}$ ) computing threshold at 2020! A last modification to the number of FLOPPS available are modifiers that account for factors such as allocation percentage (AP) and parallel scaling performance (PSP). Below are steps taken to solve for maximum grain size as a function of year.

$$FLOP = FLOPPS \cdot 3.15569 \cdot 10^7 \quad (35)$$

$$FLOP = 16 \cdot N \cdot N_c \cdot \frac{t_s}{\Delta t} \cdot PM \quad (36)$$

$$FLOPPS = 10^9 \cdot 2^{4.932138+0.9233(n-1993)} \cdot AP \cdot PSP \quad (37)$$

$$16 \cdot (xD)^3 \cdot \frac{\rho_m \cdot N_A}{AW} \cdot \frac{4\pi r_c^3}{3a_0^3} \cdot \frac{t_s}{\Delta t} \cdot PM = 10^9 \cdot 2^{4.932138+0.9233(n-1993)} \cdot AP \cdot PSP \cdot 3.15569 \cdot 10^{38} \quad (38)$$

$$(xD)^3 = 1.427 \cdot 10^{15} \cdot \frac{AW a_0^3 2^{4.932138+0.9233(n-1993)\Delta t}}{\rho_m N_A \pi r_c^3 t_s} \cdot AP \cdot PSP \cdot PM^{-1} \quad (39)$$

$$D = \frac{1}{x} \sqrt[3]{1.427 \cdot 10^{15} \cdot \frac{AW a_0^3 2^{4.932138+0.9233(n-1993)} \Delta t}{\rho_m N_A \pi r_c^3 t_s} \cdot AP \cdot PSP \cdot PM^{-1}} \quad (40)$$

$$D = \frac{9.103 \cdot 10^{-4} a_0}{x r_c} \cdot \sqrt[3]{\frac{AW \cdot \Delta t}{\rho_m \cdot t_s} (AP \cdot PSP \cdot PM^{-1})} \cdot 2^{1.644+0.308(n-1993)} \quad (41)$$

Table 3-1 shows the parameters used to estimate the grain size as a function of time for a typical simulation metal, Au. Light blue rows represent material specific parameters, while light yellow rows represent model/simulation specific parameters.

Table 3-1. Parameters for Grain Size “Moore’s Law” Computation.

$a_0$	4.090 Å
$AW$	107.8682 AU
$\rho_m$	10.501 g/mol
$x$	5
$r_c$	7.2 Å
$\Delta t$	1 fs
$t_s$	1 ns
$AP$	$10^{-2}$
$PSP$	0.8
$PM$	2.3

A fit of Moore’s law for desktop computers was also determined by assuming GPU computing using nVidia’s gforce line of video cards:

$$GFLOPPS = 1.7154^{0.3952(n-1993)} \quad (42)$$

The relationship for HPC and desktop computers are plotted in Figure 3-2.

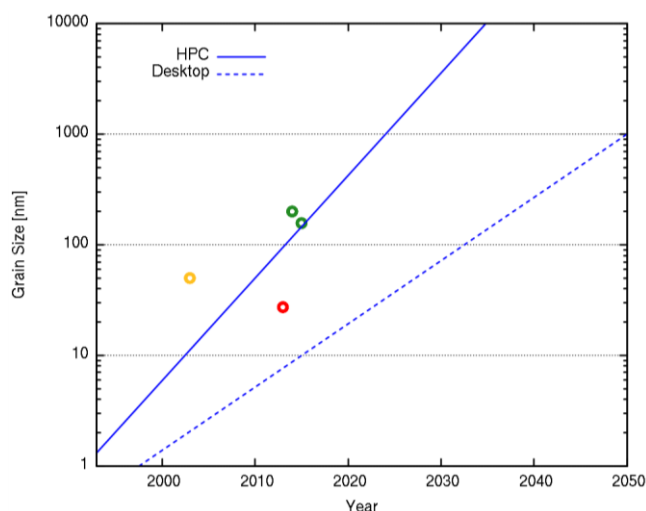


Figure 3-2. Future projection of computational power of the Moore's Law type to achievable grain sizes for atomistic simulation by an empirical potential. Green circles are representative of runs completed at US national labs [155,156], the yellow circle by one of the first systematic studies of 5-50 nm grains [157], and the red circle is a systematic study of grain sizes smaller than 27.3 nm [158].

It can be seen that in 2022 the grain size of 1  $\mu\text{m}$  will be reachable, bringing MD very close to realistic grain sizes of polycrystals, and enabling the identification of defect evolution in them.

### 3.2. Simulation Process

All realizations of molecular dynamics simulations follow a set of procedures that take place in the following stages: (1) construction/initialization of the simulation domain; (2) setting ensembles, fixes, and equilibration schemes; (3) the run itself consisting of subsequent integration of Newton's laws of motion; and (4) post-processing of data output during the run.

### 3.2.1. Initialization

The process of building a simulation domain imparts size, boundaries, and overall microstructure – this is often referred to as simulated fabrication. Atoms and/or molecules are, at least, given initial conditions and their interactions are defined by an interatomic potential which will be discussed later in further detail. Periodic boundary conditions may be applied such that a material infinitely repeats itself in a specified direction. This is useful as it allows for semi-bulk material simulations instead of being limited to nanostructured configurations. Other boundary conditions include fixed boundaries that act as spectral reflectors or shrink-wrap boundaries that adjust to the motion of atoms that would cross the boundary by expanding (or contracting if compression occurs). From here, knowledge of the crystal structure allows for the propagation of a unit cell periodically in space. A single crystalline structure can be simply fabricated in this way by changing the initial orientation and thus the uniaxial loading direction can be changed.

Polycrystalline materials require more complex treatment, building many geometric grains and assigning orientations. Later sections will cover the techniques used to adjust crystal orientation and build polycrystalline samples. As discussed in Section 3.1, the overall domain size is limited by the processing power that determines the number of atoms and effectively the number of integrated time steps when running for a set amount of time. A typical number of atoms for a molecular dynamics simulation lies between  $10^4$  and  $10^8$  and in general represents domain cells of order 10 to 200 nm and possibly up to 1  $\mu\text{m}$  in the loading direction if the cross-section is modest. A typical number of time steps is between  $10^4$  and  $10^9$  corresponding to simulations that model many ps and few ns events (Figure 3-1). It is important to take the spatially and temporally achievable scales when



looking towards what molecular dynamics simulations can tell us about physical phenomena.

### **3.2.2. Equilibration and Ensembles**

Beyond the size and scope of the simulation, it is important that the simulated fabrication be representative of reality. This is typically accomplished by equilibration procedures that minimize the potential energy of a system (including representative structures/defects) before the simulation proceeds. Equilibration is crucial especially when the initial fabrication involves the presence of inhomogeneities such as intrinsic defects. The relaxation of a polycrystalline sample is an example where equilibrium conditions are vital to simulating realistic processes. The initial fabrication of polycrystalline samples often produces non-equilibrium planar grain boundaries that kink and adjust themselves during annealing.

Often this stage of the simulation includes defining ensembles that serve as additional boundary conditions. A typical microcanonical ensemble (NVE) defines the  $N$ , the number of atoms,  $V$ , the volume, and  $E$ , the energy of the system, to remain constant. Within a given ensemble additional relaxations or restrictions can occur that drive the system; for instance a uniaxial tension test could define a rescaling in the loading direction with each time step thereby adjusting the  $V$  constraint to vary linearly with time if a constant engineering strain is imposed. It should be noted that the shrink-wrap variable also allows for the volume to change within an NVE ensemble as this boundary condition is very common in shock simulations. This sort of simulation is termed non-equilibrium molecular dynamics (NEMD).

### 3.2.3. Run Integration

The run takes place under sequential numerical integration of Newton's equations according to previously defined boundary conditions. These conditions can be adjusted in real time according to the type of materials science simulation occurring. Typical conditions include homogenous tension/compression, shock loading, nano-indentation, diffusion driven by specified gradients, etc. A typical approach will integrate the system through a discrete time step,  $\delta t$ , by a method of finite differences. The codes detailed in Section 3.3 utilize a velocity Verlet algorithm written in terms of changing momentum:

$$\mathbf{p}(t + \frac{1}{2} \delta t) = \mathbf{p}(t - \frac{1}{2} \delta t) + \mathbf{F}(t) \delta t \quad (43)$$

$$\mathbf{r}(t + \delta t) = \mathbf{r}(t) + \frac{1}{m} \mathbf{p}(t + \frac{1}{2} \delta t) \delta t \quad (44)$$

Here the momentum  $\mathbf{p}$ , and positions,  $\mathbf{r}$ , are written as functions of half steps forward and backward. A practical implementation follows:

$$\mathbf{p}(t + \frac{1}{2} \delta t) = \mathbf{p}(t) + \frac{1}{2} \mathbf{F}(t) \delta t \quad (45)$$

$$\mathbf{r}(t + \delta t) = \mathbf{r}(t) + \frac{1}{m} \mathbf{p}(t + \frac{1}{2} \delta t) \delta t \quad (46)$$

$$\mathbf{p}(t + \delta t) = \mathbf{p}(t + \frac{1}{2} \delta t) + \frac{1}{2} \mathbf{F}(t + \delta t) \delta t \quad (47)$$

As written above, the forces are computed between the second and third step according to the positions found in the first step. The force added to the momentum in the final step is equivalent to the force utilized in the increment of the momentum in the first time step in the following time step. Performing these three calculations in parallel gives the first equation of the classical leapfrog algorithm. The velocity-Verlet algorithm provides both the position and momentum of each atom at every time step [159,160].

### **3.3. Simulation Codes**

There are a number of molecular dynamics codes, each with their own advantages; below are two primary codes utilized for the work completed for my dissertation. Both molecular dynamics simulation codes utilize spatial decomposition techniques in parallel environments. Non-trivially, the implementation of broadly applicable community codes for materials modeling and simulation has been a boon to the success of atomistic computational modeling as highlighted by a recent opinion article on community codes by Plimpton and Gale [161] based on the well-received LAMMPS code developed in 1995 by Plimpton [162].

#### **3.3.1. LAMMPS**

Large-scale Atomic/Molecular Parallel Simulator (LAMMPS) is a molecular dynamics code developed by Steve Plimpton in the early 90's at Sandia National Laboratories [162] and continues to be an effective open-source platform for enabling molecular dynamics simulations [161]. Spatial decomposition plus shrink-wrap boundary conditions allow for efficient use of parallel computation where no computational power is dedicated to free volume.

#### **3.3.2. SPASM**

The Scalable Parallel Short-range Molecular Dynamics (SPaSM) code was first developed in 1992 at Los Alamos National Laboratory (LANL) with the specific purpose of performing short-range molecular dynamics simulations in massively parallel high-performance computing environments at an effective cost [163–168]. The SPaSM code was built to alleviate “data-glut” resulting from the inherent decoupling of simulation and analysis resulting in costly data communication between separate tools and machines. A

common result of this decoupling is the frustrating outcome of running a large simulation to discover after the fact that the simulation itself was flawed. Another flaw of decoupling is incomplete data sets and the requirement of duplicated calculations.

Recent advances of the SPaSM code have allowed supercomputers to simulate upwards of a trillion atoms using Lennard-Jones (LJ) interatomic potentials. SPaSM typically implements three types of boundaries to simulate shock behavior: lateral periodic boundaries, a spectral momentum mirror, and an event horizon. The spectral momentum mirror is used to introduce a shock wave; a particle traveling across this boundary has its momentum vector elastically reflected. This is accomplished entirely through manipulating the incoming and outgoing velocity vector. Taking  $z$  as the traditional shock direction, the  $z$ -velocity sign is flipped, i.e.  $v_z' = -v_z$ , while the transverse velocity components are taken equivalently  $v_x' = v_x$  and  $v_y' = v_y$ . The result is no loss in momentum. A sample initially traveling in the negative  $z$  direction will impact and a shock wave will be produced traveling in the positive  $z$  direction.

### **3.4. Simulation Set-up**

There are multiple reasons why a sample must be thermalized before a simulation begins. The lattice parameter used to create the periodic lattice is dependent on temperature through the volume dependent thermal expansion coefficient. If the run initializes before an equilibrium lattice spacing is obtained the result can manifest itself as a small wave itself. For instance, most crystals are initialized at zero K temperature and would then prefer to expand to an equilibrium volume if the simulation is to be run at room temperature.

### 3.4.1. Single Crystalline Structures

Single crystalline structures are generated by replicating the unit cell in each of the three dimensions of space. In a typical shock simulation the lateral directions will be enforced by periodic boundaries and the longitudinal direction will be free, fixed, or shrink-wrapped (scaling with the dimension without affecting velocities, and thus forces, in any way). An example of how crystals are oriented can be seen in Section 3.4.2.1 and Appendix A. Simply stated, the desired shock direction defines a set of orthogonal vectors. Each vector is normalized such that propagating the lattice produces a length of one “unit cell” in any given direction.

### 3.4.2. Polycrystalline Structures

Various simulated fabrication methods for producing grain boundary networks will manifest similar results to varying experimental manufacturing techniques: different mechanical properties. Wolf et al. [140] provides a description of various *in silico* polycrystalline fabrication techniques such as the vertex growth method and Voronoi tessellation. The diversity, or lack there-of, of grain boundary configurations can alter the resulting mechanical properties [169] and the development of realistic grain boundary networks for implementation in molecular dynamics simulations has been a long-standing goal in the field. Xu et al. [170] and Li [171] investigated the appropriateness of a Voronoi tessellation [172] to represent physical materials such as polycrystalline aggregates. Theirs is the principal work that investigates the statistical representation of grain size and structure distributions that does not draw as much attention as deformation mechanisms. Voronoi tessellation works by dividing a volume into a polygons such that each polygon represents a volume closest in distance to a grain center. An example of Voronoi

tessellation is shown for two and three dimensions in Figure 3-3. By definition all polygons are convex, satisfying a relationship that is also true for physical polycrystals.

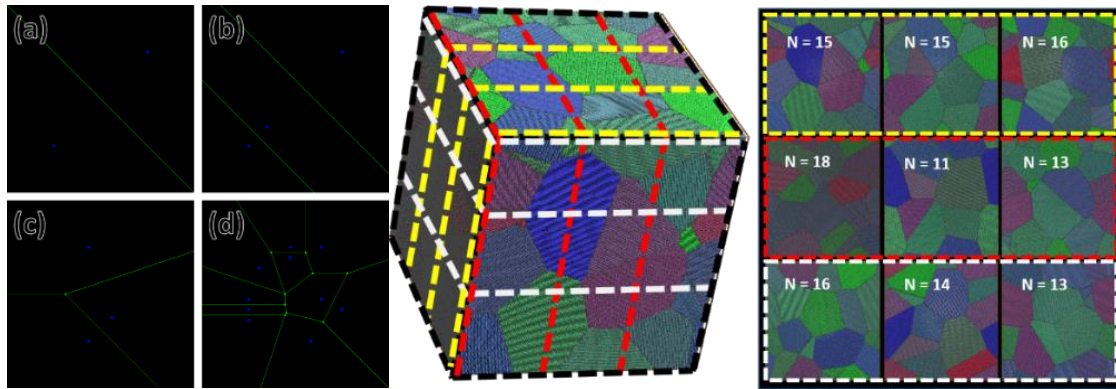


Figure 3-3. Left, 2D Voronoi tessellation of increasing complexity and number of “centers”. Right, SPaSM 300x300x300 unit cell construction of bcc tantalum with 36 randomly oriented grains with orientations represented as RGB combinations and rendered by MD\_Render code. Grain size for cubic ( $K = 1.5$ ), tetrakaidecahedral ( $K = 1.76$ ), and spherical ( $K = 2.25$ ) geometric grain shapes give planar intercept determined grain sizes from 39.31 nm to 58.97 nm for this construction whereas linear intercept determined grain sizes range from 34.71 nm to 52.07 nm [173]. ASTM grain size is determined to be 51 nm.

Using methods developed for microscopy, informed choices of grain size are based on the number and location of grain centers. Texture can be simulated by constraining the random matrices that determine each crystal’s orientation and by using weighted Voronoi methods that create polygons of different shape distributions. It is worth noting that a typical grain size distribution is log-normal for randomly generated grain structures.

#### 3.4.2.1. Bicrystal Construction

Building a specific bicrystal requires careful alignment of the two neighboring crystals. Special grain boundaries such as coincident site lattice (CSL) are described by the inverse density of shared lattice points across the boundary. For example, a  $\Sigma 3$  boundary would share 33% or 1/3 of its lattice points with its neighboring grain. The  $\Sigma 3$  grain boundary is a coherent twin boundary in BCC metals and the energy of the boundary plays

a significant role in the plastic deformation of BCC metals by determining the propensity for twinning deformation.

Given a tilt axis and its angle, along with the plane of intersection, we can back out the mutual orientations of both grains, now referred to as grain 1 and grain 2, though there is no requirement for which is which due to symmetry. For instance, from the following information,  $\Sigma 5(310)[001]$ – $36.87^\circ$  misorientation angle, we can take the plane (with plane normal in the y-direction) crossed with the tilt axis to get out grain 1 x-axis:  $(310)_x[001] = [1\bar{3}0]$ . For grain 1 we now have an orthogonal basis

$x[1\bar{3}0], y[310], z[001]$  or  $\begin{bmatrix} 1 & \bar{3} & 0 \\ 3 & 1 & 0 \\ 0 & 0 & 1 \end{bmatrix}$ . For grain 2 we will take an equivalent tilt axis z,

reverse the sign of the y component of the x axis, and reverse signs of the x and z

components of the y-axis producing our second orthogonal basis set,  $\begin{bmatrix} 1 & 3 & 0 \\ \bar{3} & 1 & 0 \\ 0 & 0 & 1 \end{bmatrix}$ .

The LAMMPS script used to build and relax the bicrystal structures can be found in Appendix A and is constructed based on a script written by Tschopp [174,175].

### 3.4.3. Non-Equilibrium Molecular Dynamics

Multiple non-equilibrium molecular dynamics (NEMD) simulation methods are employed to evaluate the strain-rate space of  $10^7 \text{ s}^{-1} - 10^{13} \text{ s}^{-1}$ . Three main NEMD methodologies are employed, illustrated graphically in Figure 3-4. They are discussed in Section 3.4.3.1 to 3.4.3.3.

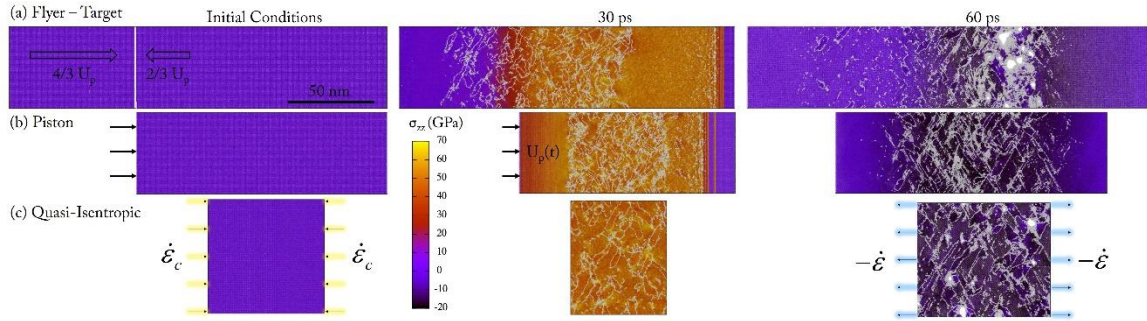


Figure 3-4. Methods used to create high strain-rate compression and release: (a) flyer-target geometry; (b), piston directed compression and release that varies a function of time; and (c) quasi-isentropic compression followed by quasi-isentropic tension. Methods (a) and (b) create shock waves in the system whereas (c) mimics the strain-rate history of a Lagrangian volume in the region of potential spall.

#### 3.4.3.1. Flyer Plate and Target

The collision between a flyer plate and a target (Figure 3-4(a)) provides supported square wave stress profiles, where tensile failure is well defined at a spall plane based on geometric relationships and acoustic approximations for wave speeds [176]. Both the flyer and the target are assigned velocities in the shock direction such that the spall plane remains close to constant position with nearly zero center of mass velocity [176]. The flyer plate itself is often not analyzed and results in wasted computational resources. Lower strain rates can only be achieved by extending the lengths of the flyer plate and target, allowing the two resulting rarefaction fans more time to spread before they collide and pull the target into tension. The computational cost thus grows quadratically with (inverse) strain rate, as a 10x slower strain rate requires 10x more atoms for a 10x longer simulated time, a 100x more expensive computation.



### 3.4.3.2. Controlled loading via a smoothly accelerated and decelerated piston

More general loading conditions, such as those arising from high explosive (HE), lasers, or magnetic drives, can be modeled by an arbitrary time-dependent piston velocity (Figure 3-4(b)). The controlled acceleration and deceleration profiles can reproduce the stress profile reminiscent of those achieved during laser shock or high explosive (HE) experiments, with uniaxial strain followed by a dispersive tail [177,178]. The strength, duration, and shape of the imposed piston velocity (which translates directly to the particle velocity,  $U_p$ ) will dictate the prescribed shock volume and strain rate [20]. For the present simulations, the piston is linearly ramped to  $U_p=750$  m/s over 5 picoseconds (ps). A resultant shock wave is formed, which can be seen visually in Figure 3-4.

The transition from the ramped compression wave to a shock wave occurs in 15 ps under the prescribed conditions. The figure below demonstrates that the transition which occurs well before the wave reaches 75 nm, which would be half of the total length (150 nm). The z component of the velocity tensor is shown, which corresponds to the particle velocity. The shock wave can also be seen visually in the middle frame of Figure 3-5 of the main manuscript, the front is localized in space and the color is uniform behind and in front of the shock wave.

The piston velocity is maintained at this magnitude to 20 ps and then undergoes a linear deceleration to stationary over 20 ps – this implementation creates an unsupported shock wave. In order to control the strain rate it is necessary to extend the system size and simulation time to decrease the strain rate towards those achieved in experiments.

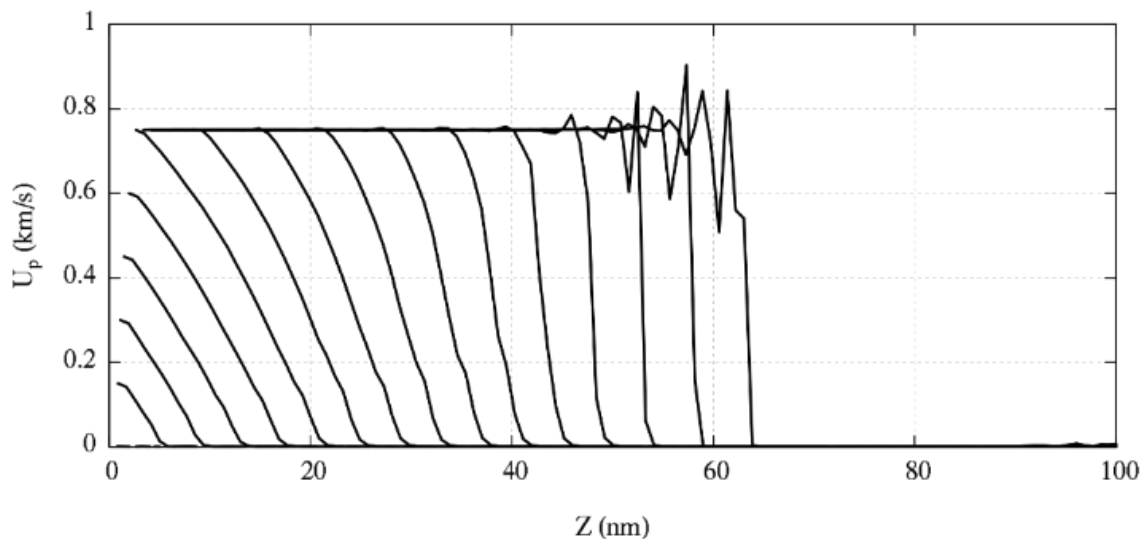


Figure 3-5. Isotemporal lines given every ps from 0 to 15 ps. The piston is accelerated over 5 ps and then held steady for 20 ps. The result is a compressive wave that transitions completely to a shock wave by the 15 ps mark.

This requires a precise description of non-linear dissipation mechanisms that contribute to the decay of the shock as it travels and large dimensions in the shock direction to achieve steady state and slower strain rates, with the same quadratic computational cost as the flyer plate and target approach, but with approximately two thirds of the total atoms. While both the flyer-target and controlled piston non-equilibrium molecular dynamics (NEMD) simulations are more expensive, they provide the correct density of defects which develop within nanoseconds in relevant laser shock experiments.

### 3.4.3.3. Quasi-isentropic compression and expansion

The quasi-isentropic (QI) technique shown in Figure 3-4(c) allows for compression and expansion of the material at a constant and well-defined strain rate across the entire sample while maintaining a near-constant temperature [179]; the temperature solely evolves due to plastic work. The QI method is implemented in LAMMPS using a microcanonical (NVE) ensemble modified to employ a well-defined affine scale each time

step. The magnitude of the scale allows for precise control of the strain rate during the simulation. With this method, failure can occur at any point in the simulated volume, where the strength is weakest. This method also allows for a reduction in simulated volume that extends the possible strain rates that can be achieved for a comparable computational cost.

For the present QI simulations, we employ a fully periodic cubic system with side lengths of 66 nm consisting of 16 million atoms. The primary limitation of the system size is the communication between growing voids [20,180]. The system undergoes compression to 0.17 strain at a strain rate of  $10^9 \text{ s}^{-1}$  remapping the atomic positions in the loading direction every time step (1 fs) after which the stress state is held constant for 100 ps. The “hold” allows for defect relaxations - analogous to relaxations that occur behind the shock front. The strain rate of  $10^9 \text{ s}^{-1}$  was chosen to lie between the Swegle-Grady [181] strain-rate approximation (with the response of tantalum measured by [182]) for the NEMD piston shock,  $\dot{\epsilon} = 27.34 \cdot 10^{36} (\sigma_{zz}^4) = 2.5 \cdot 10^8 \text{ s}^{-1}$ , and an acoustic approximation using a longitudinal sound speed of 5400 m/s,  $\dot{\epsilon} = U_p / (t \cdot C_L) = 2.8 \cdot 10^{10} \text{ s}^{-1}$ . It is important to note that adjusting the compressive strain rate will result in different defect structures, which in turn will influence the tensile response. A promising avenue for a future study would be to detail this dependence. The strain of 0.17 strain was chosen to match the peak shock pressure in the NEMD simulations. The peak longitudinal stress for [001] crystals is 55.5 GPa and the nanocrystalline system sees 54.5 GPa. The initial QI compression is followed by QI tension (at varying strain rates) until failure – this sequence is meant to be comparable to shock compression or a fast ramp to a specified shock pressure followed by different release tails. Because the required simulation volume is independent of strain rate

(with the only requirement being that it is large enough to contain a representative defect and void microstructure), the computational cost is only linear in tensile strain rate, allowing much lower strain rates to be accessed.

### **3.5. Pre, Peri, and Post-Processing**

Pre-processing refers to preparatory simulations and manipulation such as sample construction. Peri-processing refers to processing that is completed concurrently with the simulation while post-processing refers to processing that takes place after the simulation is complete. During the run a specified set of “dump” commands dictates what outputs are written and how often. The basic set of outputs includes the run log which includes global parameters and can include energies, length scales, temperatures, pressures, velocities, etc. Additionally, a dump file at a given time step includes particle id, positions, and velocities - all three of which are required for initializing a restart from a given dump file. Additional atomic calculations of interest defined for each particle such as volumetric stress tensor components, kinetic energy, and potential energy, which are common among many others.

Molecular dynamics simulation schemes are widely used to study crystalline materials at the atomic scale. As continuously enumerated, defects play a unique role in materials phenomena and therefore, their proper identification is a fundamental molecular dynamics tool for developing an in-depth understanding of material behavior. The recovery of crystal defects from the complete simulation domain often involves time consuming post-processing steps that may surpass the time employed during the simulation itself. Post-processing is often unavoidable for proper interpretation of simulation results and the

importance of appropriate selection can be shown by the different methods of evaluating the same time step as seen in Figure 3-6.

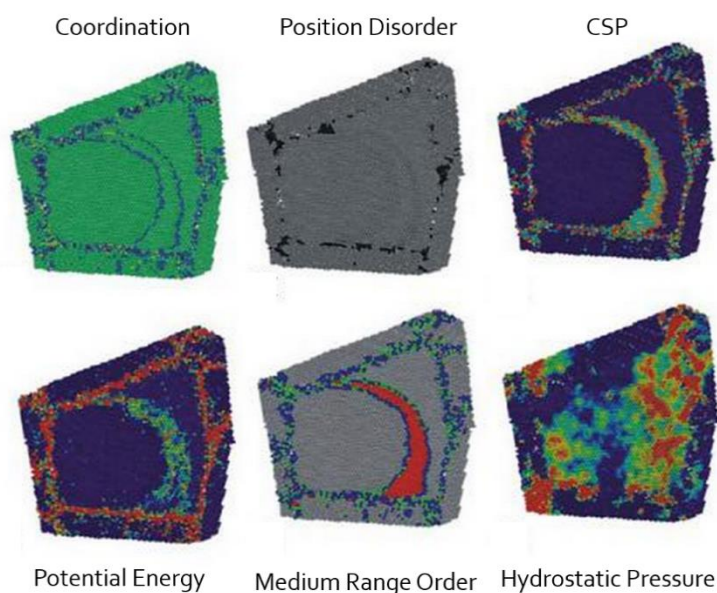


Figure 3-6. Visualization of a dislocation traversing a nanocrystalline grain by six different analysis coloring schemes. From Swygenhoven [183].

Improved computational analysis methods provide greater insight into atomic level processes and inform coupling of atomistic to mesoscale simulations [12,184]. Several post-processing tools such as OVITO utilize processing pipelines allowing for creative data visualization (Figure 3-7).

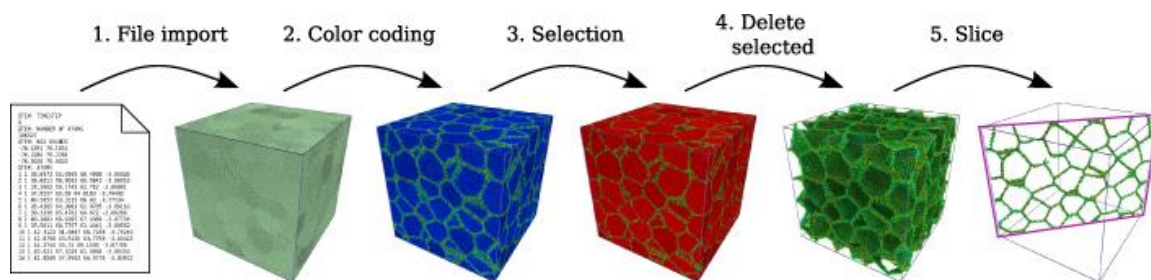


Figure 3-7. Schematic of a post-processing pipeline implemented in OVITO. Image from [185].

The following sections present a succinct overview of the defect identification methods based on structural analyses that are currently used in the present MD studies;

their appearance is based loosely on its computational cost, building from least to most expensive. Calculations of strain, strain-rate, and stress will also be introduced here.

### 3.5.1. Strain-Rate

Taking the instantaneous true strain rate at Eulerian coordinate  $z$  during loading can be directly found from the density and its time derivative. The equation is:

$$\dot{\epsilon} \equiv -\frac{1}{\rho} \frac{\partial \rho}{\partial t} \Big|_z. \quad (48)$$

Furthermore, the strain rate can also be evaluated at a single time step by staking the spatial derivatives of each the velocity  $u$  and density  $\rho$  of the Eulerian mass conservation equation:

$$\dot{\epsilon} = \left( \frac{\partial u}{\partial z} + \frac{u}{\rho} \frac{\partial \rho}{\partial z} \right) \Big|_t. \quad (49)$$

For most metals and liquids the spatial derivative of density is insignificant and thus the second term is often ignored. It should be noted that the at larger and larger strain rates this term may contribute approximately 5 or 10% to the total strain rate.

### 3.5.2. Stress State

The basic stress state is taken as the virial stress, a measure of the mechanical stress determined on an atomic scale volume. This is a direct manifestation of the interatomic potential where the force between interacting atoms is determined by the spatial derivative of the potential energy, i.e.  $F = dU/dx$ . From here, the simple application of stress as a force applied over an area,  $\sigma = F/A$  or  $\sigma = F/(dy*dz)$ , yields  $\sigma = dU/dV$ . Viewed as such, the definition of volume becomes the sticking point when defining stress state. Typical continuum mechanics breaks down when attempting to isolate the stress acting on a single

atomic volume. The absolute smallest applicable volume is often the unit cell or atomic Wigner-Sietz polygon where the relationship between number of atoms and volume at a given pressure and temperature is known. We take a virial stress definition [186]:

$$\sigma_{\alpha\beta} = -\frac{1}{\Omega_a} \left[ mv_{\alpha}v_{\beta} + \frac{1}{2} \sum_{n=1}^N r_{1\alpha}F_{1\beta} + r_{2\alpha}F_{2\beta} \right]. \quad (50)$$

$\Omega_a$  is the atomic volume;  $m$  is the mass;  $v$  is the velocity;  $\alpha$  and  $\beta$  mark the Cartesian components;  $N$  is the number of paired neighbors looped over by the variable  $n$ ;  $F_1$  and  $F_2$  are the forces on a pair of atoms; and  $r_1$  and  $r_2$  are the positions of the atoms in the pairwise interaction. The kinetic energy term accounts for binned center-of-mass translational motion. For stress calculations we bin along the shock direction taking a virial stress definition [186] and reintroduce the kinetic energy term through a temperature calculation that accounts for binned center of mass motion.

In all of the present simulations, we measure the stress in the shock direction,  $\sigma_{zz}$ , the strain ( $\epsilon$ ), temperature ( $T$ ), hydrostatic pressure ( $P$ ), and deviatoric shear stress ( $\tau$ ). The hydrostatic pressure is calculated as

$$P = (\sigma_{xx} + \sigma_{yy} + \sigma_{zz}) / 3. \quad (51)$$

Lateral stresses ( $\sigma_{xx}$  and  $\sigma_{yy}$ ), roughly equivalent to one another, are used in the calculation of deviatoric shear stress [187]:

$$\tau = \frac{1}{2} \left( \sigma_{zz} - \frac{1}{2} (\sigma_{xx} + \sigma_{yy}) \right). \quad (52)$$

### 3.5.3. Temperature

Temperature is calculated as:

$$T = \frac{1}{n} \sum_{n=1}^n \frac{m}{3k_b N_A} (v_{n,x}^2 + v_{n,y}^2 + v_{n,z}^2). \quad (53)$$

The mass of tantalum  $m = 180.95$  u,  $k_b$  is Boltzmann's constant,  $N_A$  is Avogadro's number, and the components of the velocity vector are  $v_x$ ,  $v_y$ , and  $v_z$ . During spall failure we limitedly employ a two-dimensional definition of temperature ( $T \propto (v_x^2 + v_y^2)/2k$ ) in order to negate the need to subtract the center of mass translational velocity from the longitudinal velocity component,  $v_z$ . This is critical when evaluating the temperature evolving around a three dimensional defect, such as a void, where an average center-of-mass translational velocity for a group of atoms may not be representative of the translational velocity at a particular point in space.

#### 3.5.4. Centro-Symmetry Parameter

The centro-symmetry deviation parameter, commonly named the centrosymmetry parameter (CSP), is a robust method that relies on a characteristic that is common to simple cubic (sc), fcc and bcc structures: every atom is a center of inversion symmetry, which means that taking an atom as a center, its neighboring atoms are (centro)symmetric relative to it. This property can be used to distinguish these atoms from other structures when the local bond symmetry is not verified or it deviates from an established value.

This metric for structural identification was developed by Kelchner et al in equation form and practical applications can be found in several references [94,188].

$$CSP = \sum_{i=1}^{N/2} |\vec{R}_i + \vec{R}_{i+N/2}|^2 \quad (54)$$

Here the  $N$  nearest neighbors, specified as an input parameter, of each atom are identified such that  $\vec{R}_i$  and  $\vec{R}_{i+N/2}$  are the vectors from the central atom to a given pair of



opposing neighbor atoms. Opposite pairs of atoms for FCC, BCC, and HCP are indicated in Figure 3-8 by atoms of the same color. For an atom sitting on an expected lattice point the CSP determined by this sum will be 0. Thermal vibrations will not cause much fluctuation from 0, but defects that break symmetry will produce a larger (positive) CSP value.

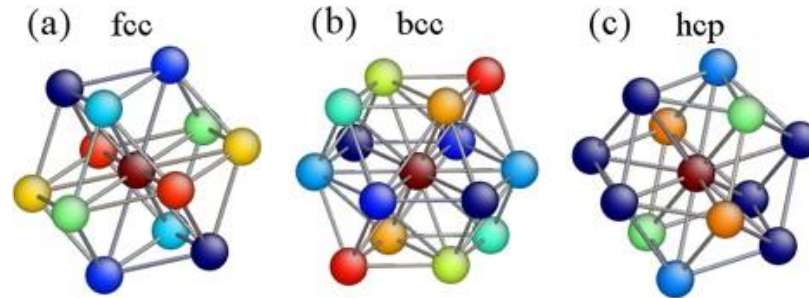


Figure 3-8. Centro-Symmetry Parameter (CSP) distinguish between plastically deformed regions of dislocations and stacking faults (asymmetry) from purely elastically deformed regions (which would have symmetry). From [189].

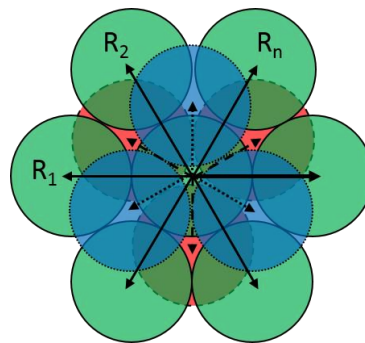


Figure 3-9. 12 nearest neighbor atoms surrounding a FCC center atom, where the 3 dashed atoms belong in plane A (red), the 7 atoms belong in plane B (green) and the last 3 dotted atoms belong in plane C (blue).

Figure 3-9 shows a schematic representation of ABC packing where a central atom in fcc is surrounded by 12 close neighbors, diametrically opposed in pairs. Note that bcc structures have 8 neighbors (though the second shell is often considered, totaling 14) and sc have 4. As seen in its definition, the CSP parameter is just a scalar quantity and therefore, its applicability to oriented defective structures is limited. The parameter is not suitable for

treatment of hcp, diamond cubic (dc) and some other structures that do not have the symmetrical characteristic described before. The identification of defects with this method is significantly affected by elevated temperatures, as shown by Stukowski [190].

### 3.5.5. Common Neighbor Analysis (CNA)

Albeit at a higher computational cost compared to CSP, structure analysis algorithms that employ high-dimensional signatures to characterize atom arrangements are usually more effective to discern between structures, especially in systems where phase changes may be present. The Common Neighbor Analysis (CNA) is one of this methods. Proposed by Honeycutt and Andersen [191] and later further developed by Faken and Jonsson [192] and Tsuzuki, Brancio, and Rino [189], the CNA computes a characteristic signature from the topology of bonds that connect an atom to its surrounding neighbors.

The neighborhood of an atom is defined by a cutoff distance so that all the atoms within that distance are said to be neighbors. Each neighbor is taken into account in the calculation of three characteristic numbers that are computed, yielding a triplet that when compared with a set of reference signatures allow the establishment a structural type to the atom whose triplet is evaluated.

Unlike CSP, CNA can be used on non-centro-symmetric structures such as HCP crystals. The latter are centrosymmetric only if the  $c/a$  ratio is ideal, 1.633 (the metal that comes closest to ideal hcp is magnesium). To see how one of the triplets are computed, a representative Common Neighborhood Parameter (CNP) can be defined as:

$$Q_i = \frac{1}{n_i} \sum_{j=1}^{n_i} \left| \sum_{k=1}^{n_{ij}} (R_{ik} + R_{jk}) \right|^2 \quad (55)$$

The index  $j$  evaluates the  $n_i$  nearest neighbors of atom  $i$ , and the index  $k$  evaluates  $n_{ij}$  common nearest neighbors of atom  $i$  and atom  $j$ . This is visually represented in Figure 3-10 where  $k$  atoms are common neighbors to atom  $i$  and atom  $j$ .

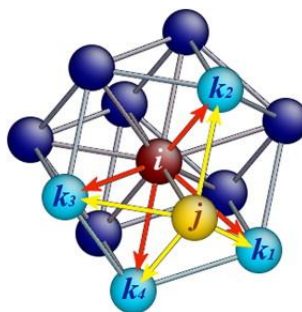


Figure 3-10. CNA Analysis is derived based on the number of common neighbors ( $k$ ) shared by an atom pair ( $i$ - $j$ ) [189].

The Adaptive Common Neighbor Analysis (a-CNA), recently proposed by Stukowski [190] takes CNA as a basis, and is particularly suitable for multi-phase systems, adapting the cutoff distance of the standard CNA to each individual atom depending on a reference structure for comparison purposes. The reader is referred to the cited article for a thorough explanation and example of the methodology. This method was also extended to the silicon system where second common neighbors are necessary as the diamond cubic system does not share common neighbors. It is important to note that the identification of structures depends on a robust and accurate library of CNP values for known structures.

### 3.5.6. Coordination; Pair Correlation Function

Coordination is defined through a static measure of the number of neighbors in a given spherical shell surrounding a given atom. The probability of an atom lying at a given radius away is defined as the pair correlation function, or radial distribution function, or  $g(r)$  and is represented in Figure 3-11 for bcc tantalum. The  $g(r)$  function for short, provides a means of characterizing the local and long range order of both crystalline and disordered

materials [193,194]. For a crystalline solid there are strong peaks that can be related to a structure factor through a Fourier transform of the  $g(r)$  function. This provides analogous results to diffraction patterns where characteristic lattice spacing constructively and destructively interferes. A coordination number can be evaluated through the first shell atoms represented by the atoms that contribute from 0 to the first trough.

For simulations with free surfaces or voids, the coordination will decrease near free volumes. This can be used to roughly gauge void surfaces. Coordination is an important distinguishing feature for silicon as well.

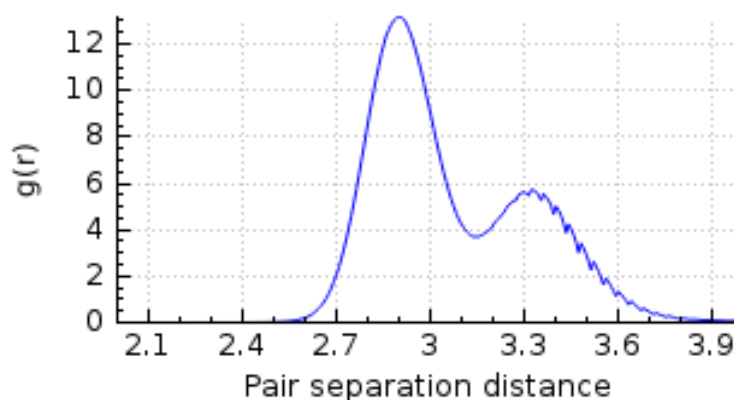


Figure 3-11. Pair correlation function of bcc Tantalum.

It assists in distinguishing phase changes and between disordered regions where there can exist liquid and amorphous structures of varying density and thus varying coordination. The pair-correlation function can also help diagnose important characteristics of disordered regions such as preferred coordination and atomic arrangements.

### 3.5.7. Dislocation Extraction Algorithm; Crystal Analysis Tool

Detection of defects from crystalline structures is valuable, but the current state-of-the-art is the differentiation of one defect from another. Two new tools by have been developed by Stukowski [185,190,195] termed dislocation extraction algorithm (DXA)

and Crystal Analysis Tool (CAT). The ‘sharpness’ of dislocations is seen in Figure 3-12 in contrast with CNA filtering. This enables a better determination of dislocation densities, since no dislocations are missed by superposition as shown by Ruestes et al. [196]. The voids from which these dislocations emanate are visible in DXA but cannot be easily distinguished by CNA.

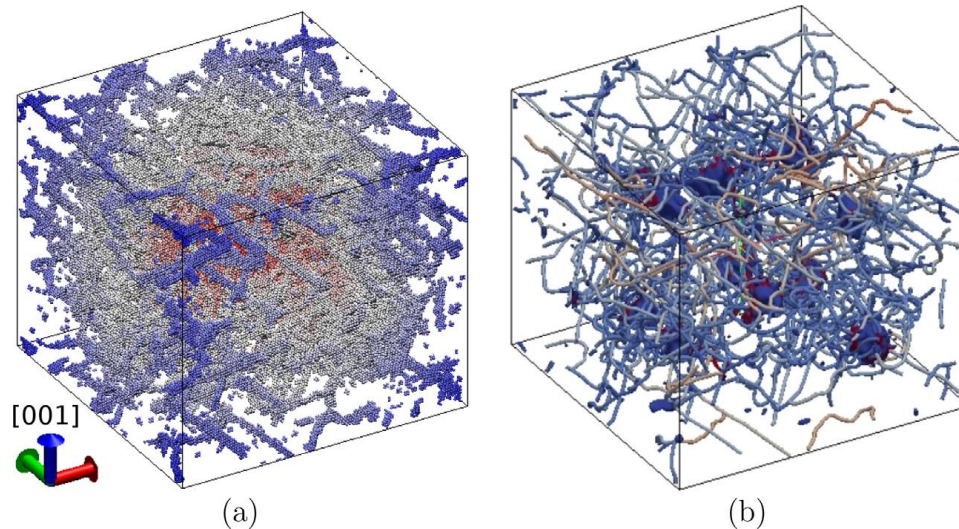


Figure 3-12. Comparison of (a) a conventional atomistic visualization using CNA filtering in tantalum and (b) a geometric line visualization of the dislocations provided by DXA. From [196].

### 3.5.8. Orientation Imaging Map (OIM)

Typical materials exhibit some degree of texture (non-random grain orientation distribution) imparted by processing or past deformation. Twinning is one such deformation mechanism that can impart texture by preferentially adjusting the orientation in soft grains. The first implementation of an orientation imaging map to atomistic simulations was accomplished by Rudd [197] and can be seen in Figure 3-13.

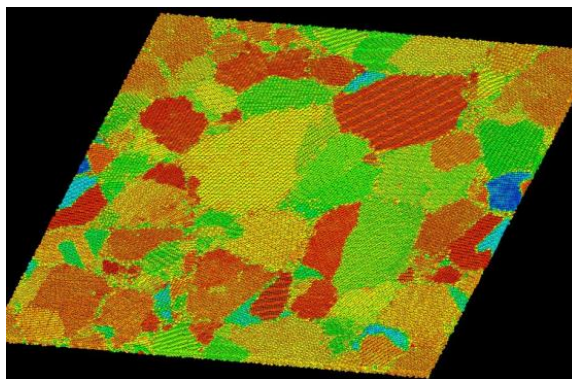


Figure 3-13. Orientation imaging map using Euler angles as proposed by Rudd [198].

Ravelo et al. [95] also demonstrated an OIM mapping function in the application of the SPaSM code. The foundation of the method lies in a centro-symmetry-like formulation where nearest neighbors are located for each atom and an extended sample algorithm is provided in Appendix C.

Wang et al. [199] also developed a methodology akin to electron backscattered diffraction in order to evaluate crystallographic orientation of neighboring grains. It is clear that grain orientation plays a major role in the mechanical response of individual grains and their collective behavior. Several other researchers have developed similar techniques.

### **3.6. Interatomic Potentials**

The importance of an accurate and transferable interatomic potential cannot be stressed enough. It is for this reason that a significant portion of my work is dedicated to evaluating potential accuracy, applicability, and transferability. The accuracy of an interatomic potential, often shorthand as potential, describes its ability to simulate correct behavior or properties in a well-defined, thus applicable, environment. A transferable potential describes its ability to predict real phenomena and properties without being explicitly fit to them. As the majority of potentials are likely fit to data beside the

regime typical to shock physics, it is critical to evaluate the transferability of the potential to high strains, pressures, and temperatures.

A significant advancement in the field of computing metals was the development of the embedded atom model (EAM) by Daw & Baskes [200]. Further reading on the direct contributions of the embedded-atom method to material science and engineering can be found in a recent review article [201] and a historical comparison of its projected influence back in 1996 [202]. Our approach to understanding and simulating materials at the atomic scale has historically been semi-empirical. Parameters are drawn from experimental results and from quantum mechanics modeling (referred to as *ab initio* methods or with varying functionals representing spatially-dependent electron density termed density functional theory (DFT)). Interatomic potentials are then fit to parameters that commonly include elastic constants, cohesive energy, defect energies, and other measures of interest. Semi-empirical potentials principally allow for simulations that would be otherwise prohibitively costly in terms of computation time.

Interatomic potential development, specifically many-body potentials as applied to metals, stems from our basic understanding of how electrons operate in solids [203]. One ramification of spherically projected potential forms such as EAM is the difficulty of fitting to non-fcc metals [201]. For example, bcc is difficult to accurately fit to due to large contributions of d-shell electrons, and hcp is challenging due to a high degree of mechanical and structural anisotropy.

Computational complexity continues to grow, evaluating a greater quantity of interactions and offering the possibility of increased realism. A valuable way to look at complexity was visualized by Plimpton and Thompson [204] and reproduced here in Figure

3-14. This illustration is similar to the familiar Moore's law as expressed previously in the grain size "growth" of simulations.

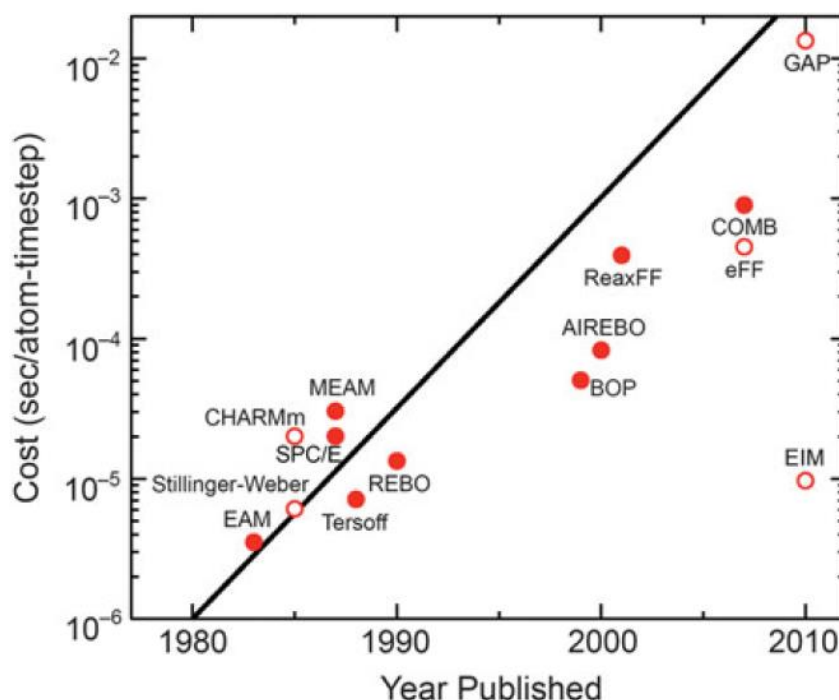


Figure 3-14. Increasing single CPU cost of running many-body potentials in seconds per atom per time step as a function of year. The black line is indicative of computational cost doubling similar to Moore's law. From Plimpton et al. [204].

Implementation of increasingly accurate and costly interatomic potentials represents a desire to increase the reality, complexity, and accuracy of simulated systems. This goal is in conflict with the desire to extend molecular dynamics to increasing length and time scales. For a digital compendium of applicable potentials readers are directed to the Interatomic Potentials Repository Project [205] and the work of Sheng [206].

### 3.6.1. Tantalum

Among candidate models for MD simulations of bcc metals, Fe and Ta are the most prevalent. Fe is generally chosen in order to further develop our understanding of one of the most ubiquitous elements used in materials science as well as to explore pressure and



temperature-dependent solid-solid phase transitions. Tantalum is selected for the stability of its bcc phase with regards to both melting and phase change [207]. Specifically, Ta has a simple phase diagram that is not expected to exhibit solid-solid phase changes with pressure or temperature and has a high melting temperature that is useful in extreme molecular dynamics simulations. Ta is an excellent choice to gain a deeper understanding of the bcc crystal phase which, in general, displays increased temperature and strain-rate dependence in comparison with fcc metals.

### 3.6.1.1. Embedded Atom Method

The foundation of this method is to include delocalized interactions in addition to nearest neighbor contributions. The EAM potential takes the following form:

$$E_{Tot} = \sum_i F_i(\rho_i(R_i)) + \frac{1}{2} \sum_{i,j} \varphi(R_{ij}) \quad (56)$$

The first term evaluates the contribution of electron density,  $\rho_i$ , at each site,  $R_i$ , through a functional,  $F$ . The second term considers a short-range pair potential,  $\varphi$ , for each atom pair,  $R_{ij}$ , where the “ $\frac{1}{2}$ ” avoids double counting. The embedding term essentially takes into account the entire environment of the atom. The relevant properties of two EAM potentials developed by Ravelo et al. [95] specifically suited for shock studies are shown below. The two potentials are denoted Ta1 and Ta2. The elastic moduli under tension and compression are shown in Figure 3-15. Cohesive energy as function of pressure is shown in Figure 3-16.

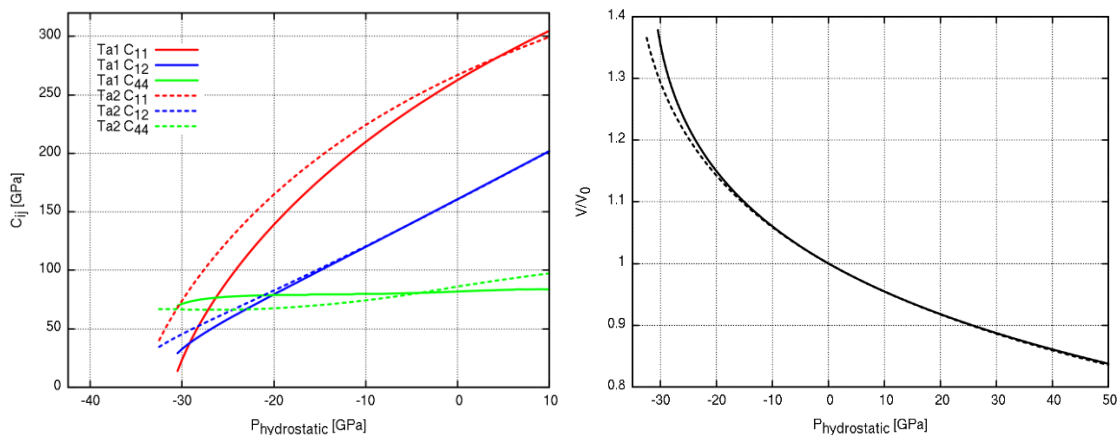


Figure 3-15. Left, pressure dependent  $C_{ij}$  of Ta1 and Ta2. Right, Volume change as a function of hydrostatic pressure. EAM potentials as developed by Ravelo et al. [95].

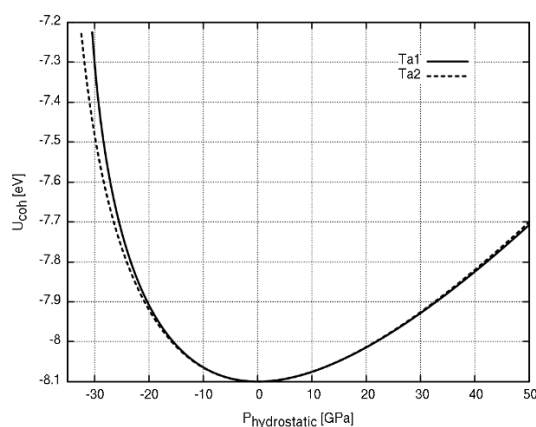


Figure 3-16. Cohesive energy as a function of hydrostatic pressure.

### 3.6.1.2. Model Generalized Pseudopotential Theory

Model Generalized Pseudopotential Theory (MGPT) lies between density functional theory and semi-empirical potentials, such as EAM or LJ, in terms of both accuracy and computational cost. The potential form was derived by Moriarty [208–211] and has been shown to be particularly useful for transition metal elements such as tantalum and uranium [212].

$$U = NE_{vol} + \sum_{i>j} \varphi(r_{ij}) + \sum_{i<j<k<m} tr(\mathbf{H}_{ij}\mathbf{H}_{jk}\mathbf{H}_{km}\mathbf{H}_{mi}) + \sum_{i>j>k} \left( \begin{array}{l} tr(\mathbf{H}_{ij}\mathbf{H}_{jk}\mathbf{H}_{ki}) \\ + \mathbf{H}_{ij}\mathbf{H}_{jk}\mathbf{H}_{kj}\mathbf{H}_{ji} \end{array} \right) \quad (57)$$

$H_{ij}$  is a bond matrix,  $E_{vol}$  is a volume dependent constant, and  $\varphi$  is a pair-wise-energy function. As indicated by the indices  $i$  through  $m$ , the potential is evaluated for each close pair of atoms, akin to an EAM potential, and an additional energy term is calculated for each n-tuple, i.e. each pair triplet, and quadruplet, through the traces of products of bond matrices. This functional form is implemented into the LAMMPS code as of 2016 with strong scaling [213]. The strength of this functional form lies in its ability to evaluate non-spherical behavior through 3- and 4-body terms that are better able to capture the energies of non-spherical d and f shell electrons as compared to the spherical projection of the EAM embedding function.

### 3.6.1.3. Spectral Neighbor Analysis Potential

The spectral neighbor analysis potential (SNAP) developed by Thompson et al. [28] uses bispectrum components to represent the local neighborhood of each atom. It is similar in framework to that of Gaussian Approximation Potentials (GAP) developed by Bartok et al. [214,215]. SNAP, unlike GAP, assumes a linear relationship between atom energy and bispectrum components.

$$U_{SNAP}^i(B_1^i, \dots, B_K^i) = \beta_0^{\alpha_i} + \sum_{k=1}^K \beta_k^{\alpha_i} B_k^i \quad (58)$$

The energy,  $U$ , of atom  $i$  is expressed as a weighted sum of  $K$  bispectral components,  $B_k^i$ , using linear interpolation coefficients,  $\beta_k^{\alpha_i}$ , which depend on the snap “element”,  $\alpha_i$ .

### 3.6.2. Silicon

The mechanical properties of silicon continue to be extensively studied under numerous conditions, including deformation at extreme stresses and ultra-fast strain rates. Regarding atomistic simulations, silicon is one of the most studied elemental materials alongside iron, due its technological relevance. Therefore, there are a large number of empirical potentials fit to address different scenarios, including thermal properties and melting [216,217], dislocation properties [218,219], phase transformations [220], defects and disordered phases [221–223], etc. A comparison of some potentials can be found [216,224]. However, none of these potentials have been developed specifically for the conditions achieved during shock loading and care must be taken to evaluate their transferability. Oleynik et al. [225] carried out large-scale shock simulations and showed that shocks could heal defects in bulk single crystal silicon. In another study [226] they showed that the Stillinger-Weber (SW) potential provided stress-strain curves for the diamond-cubic structure that compared well with ab-initio results when the strain is below 15-20% corresponding to shear stresses below 7.5 GPa and a subsequent investigation [227] reproduced two-wave shocks consisting of a plastic wave preceded by an elastic precursor using the environmentally dependent interatomic potential (EDIP). Work by Mogni et al. [228] used a Tersoff-family potential and shocked Si along its  $\langle 001 \rangle$  axis; analysis identified a phase transition from dc to a new phase (Imma) and they note consistency with shear stress relief provided by direct shock-induced phase transition without intermediate plastic deformation. Recent simulations of plasticity in Si nanospheres by Hale et al. [229] employ the SW potential and show a  $\{110\}$  slip response in addition to the expected  $\{111\}$  shuffle/glide-set planes. MOD, a more recent Tersoff-

family bond order potential by Kumagai [217], was developed to reproduce both elastic constants and melting point. MOD has been shown to describe reasonably well crystalline as well as disordered phases such as liquid and solid amorphous structure, the kinetics of the crystalline to liquid transition [230], and the decrease of melting temperature with pressure between -1 and 3 GPa [231].

Of foremost importance is the phase diagram of silicon at the high pressures and temperatures as anticipated under shock compression. This need is emphasized by the variety of phase changes and number of possible potentials to select from. The SW potential was recently surveyed and the stability of a simple cubic allotrope, sc16, was shown at pressures (at 300 K) between 9.54 and 13.67 GPa where coexistence with  $\beta$ -tin is predicted [232]. Si-III, or bc8 was shown to be energetically unfavorable compared to sc16 for all temperatures and pressures. The negative Clausius-Clapeyron melting temperature with increasing pressure is again demonstrated and a triple point (quadruple point including hexagonal diamond (hd) structure of thermodynamically equivalence to dc) between dc, liquid, and sc16 at 1302 K and 7.28 GPa. The hexagonal diamond phase should not be overlooked as bc8 Si transforms to hexagonal diamond (also termed as the lonsdaleite structure) upon annealing [233]. In reality, hd is likely a manifestation of annealing twins or evidence of severe plastic deformation in the form of stacking faults and twinning as shown by experimental evidence from recovered meteorite impact or deformation within Earth's mantle at elevated temperatures (600-1000 K) [234][235]. The transformation is described as relating to deformation twinning and often as a martensitic transformation at twin-twin intersections. One way to think of hexagonal diamond is the separation of a twinning super lattice with separation of just two bilayers [236]. The

transition of diamond cubic to hexagonal diamond is analogous to intrinsic stacking faults in face-centered cubic metals manifesting as hexagonal close packed structures.

Other phase transitions in silicon under high pressure and temperature indentation have also been reported [237] and a recent review of diamond machining of silicon offers considerable insight into potential phase transformation and directional anisotropy of deformation in silicon [238]. Earlier, Boyer et al. demonstrated the metastability of a body centered tetragonal five (bct5) structure using the SW potential by the application of specific shear strains and emphasized likelihood of observing this phase lies in avoiding fracture, possibly through shock experiments [239]. Noted is the possibility of simultaneous application of hydrostatic pressure and deviatoric stresses to achieve the bct5 structure. In general, shear stress is known to increase polymorphic transitions and reaction speeds [14–16], and has been shown to decrease the dc to  $\beta$ -tin transition from 11.4 to 3.9 GPa and transition pressure can be evaluated as a function of orthogonal shear components [240–242]. Recent in situ Raman imaging of deformation under indentation report an observation of a new phase tentatively identified as bct5 [40][41], strengthening previous simulation results identifying a bct5 deformation pathway using a Tersoff potential [245–248].

In order to accurately perform computational experiments of shock-loaded silicon it was necessary to evaluate the ability of multiple potentials to represent properties critical to shock phenomenon in silicon. These properties and their importance are as follows:

- Hugoniot relationships – namely relationships between particle velocity, volume, pressure, and shock velocity required to evaluate physical properties during shock compression.
- General stacking fault energies – critical to preferential defect formation and defect stability.

- Pressure-dependent elastic constants – including bulk moduli and shear/pressure ratios derived therefrom.
- Pressure-dependent melting temperature – necessary for materials such as silicon with a negative Clapeyron slope.
- Shock-induced temperature rise – important for ductile to brittle transition of covalently bonded materials in addition to influencing the thermal barrier to dislocation motion/nucleation.

### 3.6.2.1. Stillinger-Weber

The Stillinger-Weber (SW) potential form is one of the most widely used forms for covalent materials, especially silicon, as it was developed for, and ice. The energy is computed by a linear combination of two and three body terms as follows:

$$E = \sum_i \sum_{j>i} \varphi_2(r_{ij}) + \sum_i \sum_{j \neq i} \sum_{k>j} \varphi_3(r_{ij}, r_{ik}, \theta_{ijk}) \quad (59)$$

$$\varphi_2(r_{ij}) = A_{ij} \epsilon_{ij} \left[ B_{ij} \left( \frac{\sigma_{ij}}{r_{ij}} \right)^{p_{ij}} - \left( \frac{\sigma_{ij}}{r_{ij}} \right)^{q_{ij}} \right] \exp \left( \frac{\sigma_{ij}}{r_{ij} - a_{ij} \sigma_{ij}} \right) \quad (60)$$

### 3.6.2.2. Tersoff

The Tersoff bond order potential computes 2-body and 3-body terms in addition to environment and angular functions. The reader is directed to the papers of Tersoff [220,249,250] and Erhart and Albe [251] for the potential form, fitting functions, and modifications.

$$E = \frac{1}{2} \sum_i \sum_{j \neq i} V_{ij} \quad (61)$$

$$V_{ij} = f_C(r_{ij}) [f_R(r_{ij}) + b_{ij} f_A(r_{ij})] \quad (62)$$

$$f_C(r) = \begin{cases} 1 & : r < R - D \\ \frac{1}{2} - \frac{1}{2} \sin \left( \frac{\pi r - R}{D} \right) & : R - D < r < R + D \\ 0 & : r > R + D \end{cases} \quad (63)$$

$$f_R(r) = A \exp(-\lambda_1 r) \quad (64)$$

$$f_A(r) = -B \exp(-\lambda_2 r) \quad (65)$$

$$b_{ij} = (1 + \beta^n \zeta_{ij}^n)^{-\frac{1}{2n}} \quad (66)$$

$$\zeta_{ij} = \sum_{k \neq ij} f_C(r_{ik}) g(\theta_{ijk}) \exp[\lambda_3^m (r_{ij} - r_{ik})^m] \quad (67)$$

$$g(\theta) = \gamma_{ijk} \left( 1 + \frac{c^2}{d^2} - \frac{c^2}{[d^2 + (\cos \theta - \cos \theta_0)^2]} \right) \quad (68)$$

Table 3-2. Parameters that are applied in equations of EA, EA2, and MOD potentials.

	<b>EA</b>	<b>EA2</b>	<b>MOD</b>
A [eV]	2145.7128	1899.386	3281.5905
B [eV]	219.521624	361.557	121.00047
$\lambda_1$ [1/Å]	2.83318929	2.615479	3.2300135
$\lambda_2$ [1/Å]	1.53810493	1.66591	1.345797
$\lambda_3$ [1/Å]	0	0	-
$\eta$	-	-	1
$\eta \times \delta$	-	-	0.53298909
$\alpha$	-	-	2.3890327
$\beta$	1	1	1
$\bar{\beta}$	-	-	1
$\gamma$	0.114354	0.09253	-
c1	-	-	0.20173476
c2	-	-	730418.72
c3	-	-	1000000.0
c4	-	-	1
c5	-	-	26
c	2.00494	1.13681	-
d	0.81472	0.63397	-
h	-	-	-.365
m	1	1	-
n	1	1	.93810551
R [Å]	2.82	2.9	3
D [Å]	0.14	0.15	0.3
$\cos(\theta_0)$	-0.259	-0.335	-



The modified Tersoff potential employs modifications to Equation 67 and 68 as follows. Full details can be found in Kumagai et al. [217].

$$\zeta_{ij} = \sum_{k \neq i,j} f_c(r_{ik}) g(\theta_{ijk}) \exp[\alpha(r_{ij} - r_{ik})^\beta] \quad (69)$$

$$g(\theta) = c_1 + g_o(\theta) g_a(\theta) \quad (70)$$

$$g_o(\theta) = \frac{c_2(h - \cos\theta)^2}{c_3 + (h - \cos\theta)^2} \quad (71)$$

$$g_a(\theta) = 1 + c_4 \exp[-c_5(h - \cos\theta)^2] \quad (72)$$

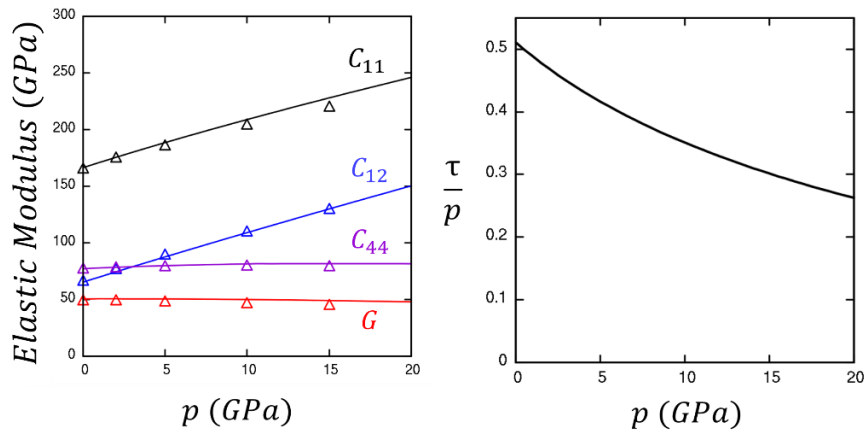


Figure 3-17. Left, pressure dependence of the elastic modulus of silicon. Right, pressure dependence of the ratio of maximum shear over pressure.

Figure 3-18 shows the GSFE and the melting temperature as a function of pressure calculated by three methods. Molecular dynamics simulations using the MOD potential were conducted by taking a single phase system, initially diamond cubic in structure, consisting of 27,000 atoms (15x15x15 diamond unit cells, with 8 atoms each) thermalized to a given temperature. The sample was then uniaxially compressed, while maintaining a constant temperature by a NVT ensemble.

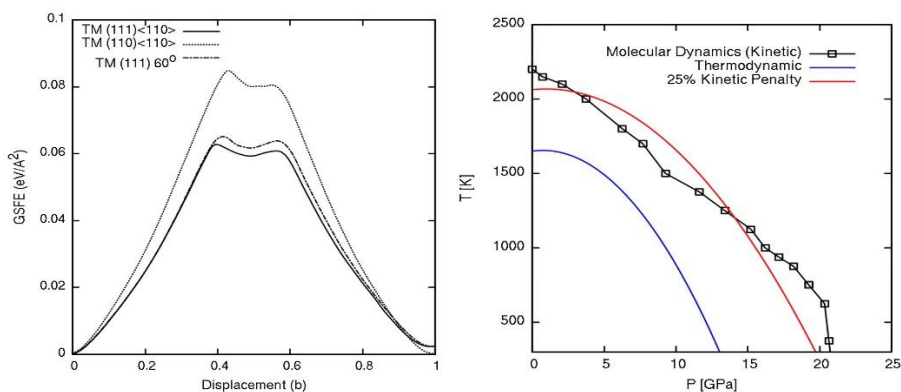


Figure 3-18. General stacking fault energies for the MOD potential plotted by displacement in terms of  $1/2[110]$  Burgers vector. Melting curve for silicon under dynamic compression illustrating kinetic effects.

Melting is identified when a liquid cluster with more than 10 atoms is identified. Liquid phase was determined based on coordination, with a radial cut-off of 0.295 nm, corresponding to the maximum expected bond length. Liquid silicon atoms have coordination 6 (experimental value of 6.4), compared to 4-coordinated solid-phase atoms. We note that there is a bias in the results since uniaxial compression might lead to a non-spherical coordination shell, but this produces marginal error due to the large separation between first and second neighbor shells of diamond-cubic structure. Complications may arise if the beta-tin or other structural change is present due to the second neighbor shell decreasing to near 0.32 nm for several high pressure allotropes.

### 3.6.2.3. Environmentally Dependent Interatomic Potential

The environmentally-dependent interatomic potential (EDIP) computes 2- and 3-body interactions. Note that SW is limited to 2-body interactions. The 3-body interaction is indicative of a consideration for the atomic “environment” of the atom, hence the name “environmentally-dependent”. The potential was developed by Bazant et al. [221] and Justo et al. [222].

$$E = \sum_{j \neq i} \phi_2(R_{ij}, Z_i) + \sum_{j \neq i} \sum_{k \neq i, k > j} \phi_3(R_{ij}, R_{ik}, Z_i) \quad (73)$$

$$\phi_2(r, Z) = A \left[ \left( \frac{B}{r} \right)^\rho - e^{-\beta Z^2} \right] \exp\left(\frac{\sigma}{r-a}\right) \quad (74)$$

$$\phi_3(R_{ij}, R_{ik}, Z_{ijk}) = \exp\left(\frac{\gamma}{R_{ij}-a}\right) \exp\left(\frac{\gamma}{R_{ik}-a}\right) h(\cos\theta_{ijk}, Z_i) \quad (75)$$

$$Z_i = \frac{1}{2} \sum_{m \neq i} f(R_{im}) \quad f(r) = \begin{cases} 1 & : r < c \\ \exp\left(\frac{\alpha}{1-x^{-3}}\right) & : c < r < a \\ 0 & : r > a \end{cases} \quad (76)$$

$$h(L, Z) = \lambda \left[ \left( 1 - e^{-Q(Z)(l+\tau(Z))^2} \right) + \eta Q(Z)(l+\tau(Z))^2 \right] \quad (77)$$

$$Q(Z) = Q_0 e^{-\mu Z} \quad \tau(Z) = u_1 + u_2(u_3 e^{-u_4 Z} - e^{-2u_4 Z}) \quad (78)$$

The reader is directed to the original papers for a full definition of the variables.

#### 3.6.2.4. Evaluation of Potentials

There is a large spread in experimental results [250,252–257], and MD simulations agree reasonably with many these experiments in the range of interest. In order to evaluate which silicon potentials were suited to shock conditions, a preliminary evaluation of the elastic constants of dc Si as a function of pressure was conducted; under the effect of shock compression, physical properties vary along with the increment of pressure. Results are compared with ab-initio calculations completed by Karki et al. [258]. A reactive force field (reaxFF [259]) is also included for comparison. As seen in Figure 3-19, as compression increases,  $C_{11}$  increases for all potentials except the curves simulated with SW and ReaxFF [259]. MOD provides the best fit to the ab-initio results, followed by EA2. Notably, both SW and EA significantly underestimate  $C_{44}$ .

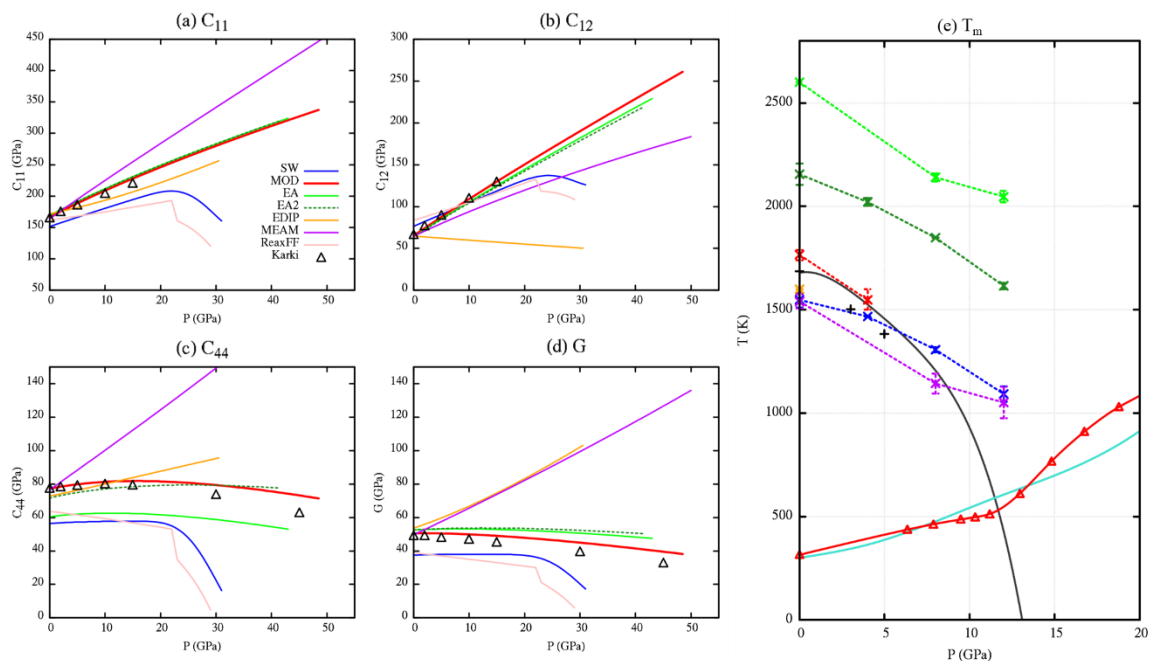


Figure 3-19.  $C_{ij}$  of eight interatomic potentials as compared to DFT results by Karki et al. [258]. Melting was previously evaluated for many potentials by Mazhukin et al. [260] and compared with experimental points, a linear Clausius-Clapeyron relationship and a thermodynamic liquidus curve from Deb et al. [261]. Pressure dependent melting temperature from potentials as evaluated by Mazhukin et al. [260] and theoretically by Deb et al. [261].

Results for the melting temperature as a function of pressure are drawn from Mazhukin et al. [262] and limited experimental data. These data are compared with a linear Clausius-Clapeyron equation and an analytical calculation by Deb et al. [261]. Several additional points are calculated here using a 2-phase method (see Appendix E). MOD, SW, EDIP, and MEAM most accurately capture the trend of the melting curve. Overestimates of the decrease in  $T_m$  with increasing  $P$  may lead to an underestimation of  $T_m$  with increasing pressure which may influence its tendency to favor disordered states at elevated temperature and pressure. EA and EA2 substantially overestimate the melting curve, suggesting that amorphization as well as melting may be suppressed.

Additionally, several locus states on the shock Hugoniot were mapped using the multi-scale shock technique (MSST) [263]. The relationship between the shock and

particle velocities are fundamental to the nature of the shock wave. Figure 3-20a presents the plot of the shock velocity,  $U_s$ , versus the particle velocity,  $U_p$ , for EA, EA2, EDIP, MEAM, MOD, and SW potentials in comparison to available literature data. Figure 2b shows the relationship between shock pressure and volume. The inset of Figure 3-20b shows data in the elastic regime and early plastic regime. The high strain-rates used in the MD simulation extend the expected elastic limit to higher values than the experiments. MOD and EA2 agree well with the elastic shock response as expected from the  $C_{ij}$  response reported in Figure 3-19.

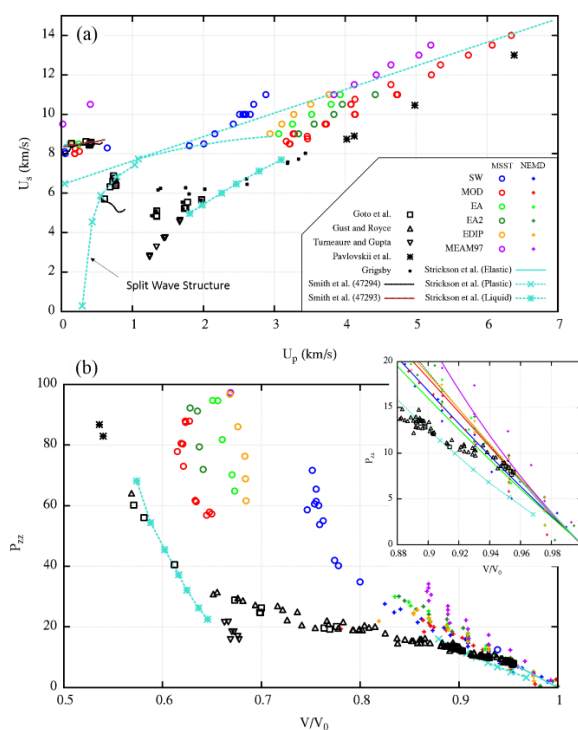


Figure 3-20. (a) Hugoniot of several potentials compared to experimental measurements [177,256,257,264–267]. (b) Pressure-volume diagram for the same potentials and experiments. Inset shows data in the sensitive area near the elastic-plastic transition as measured by laser shock.

Chapter 3, in part, is a reprint of material that has been published: E.N. Hahn, M.A.

Meyers, Grain-size dependent mechanical behavior of nanocrystalline metals. 646 (2015)

101–134. doi:10.1016/j.msea.2015.07.075. The thesis author was the first author of this article.

Chapter 3, in part, is a reprint of material that has been published: E.N. Hahn, S.J. Fensin, T.C. Germann, M.A. Meyers, Symmetric tilt boundaries in body-centered cubic tantalum, *Scripta Materialia*. 116 (2016) 108–111. doi:10.1016/j.scriptamat.2016.01.038. The thesis author was the first and corresponding author of this article.

Chapter 3, in part, is a reprint of material that has been published: S. Zhao, B. Kad, E.N. Hahn, B.A. Remington, C.E. Wehrenberg, C.M. Huntington, H.-S. Park, E.M. Bringa, K.L. More, M.A. Meyers, Pressure and shear-induced amorphization of silicon, *Extreme Mechanics Letters*. 5 (2015) 74–80. doi:10.1016/j.eml.2015.10.001. The thesis author was the third author of this article.

Chapter 3, in part, has been submitted for publication of the material as it may appear in: E.N. Hahn, T.C. Germann, R.J. Ravelo, J. Hammerberg, M.A. Meyers, On the Ultimate Tensile Strength of Tantalum, *Acta Materialia*. (2016). The thesis author was the first and corresponding author of this article.

Chapter 3, in part, is currently being prepared for submission for publication: E.N. Hahn N., Y. Wang, R. Flanagan, S. Zhao, M.A. Meyers, Computational Evaluation of Silicon under Shock Compression, (2016). The thesis author was the first and corresponding author of this article.

## 4. Results and Discussion

### 4.1. Tantalum

Tantalum was used as a model bcc metal; the goals are to characterize the deformation structures in both shock compression and release for mono and nanocrystalline specimens and to compare calculated results with experiments using high amplitude pulsed lasers; this effort complements the experimental work by Lu et al. [178,268,269] and Remington [270]. In order to understand the role of grain boundaries on defect generation and damage in extreme deformation, the energies of grain boundaries are calculated as a function of grain misorientation in Section 4.1.1. Section 4.1.2 focuses on failure by spalling in mono and nanocrystals and establishes the effect of strain rate, comparing it with experimental results. Extrapolation to the inverse of the Debye frequency leads to an ultimate tensile strength, for the first time. This is done in Sections 4.1.2.1-6. The possibility of a phase transformation revealed by Lu et al. [178], is confirmed through MD calculations in Section 4.1.3.

#### 4.1.1. Bicrystals

There has been a significant amount of work on bcc iron bicrystals, but more limited work on molybdenum and tantalum. For Iron,  $\Sigma 5$  boundaries have been evaluated, [271–274],  $\Sigma 3$  [101,275], and other boundaries in response to deformation [102,276,277]. Molybdenum is limited to study of the  $\Sigma 5$  boundary [278,279]. Recent work by Wang et al. [280] investigated the properties of tantalum nanopillar bicrystals with twist boundaries. Twist boundaries do not require mirror symmetry across the boundary and, thus, periodic

boundary conditions are not possible in transverse directions either. This requires either vast sample sizes to negate surface effects, or the study of nanopillar structures.

There have been numerous studies using both simulations and experiments to understand the GB structure and energies of fcc materials [127,281,282]. These studies have included both symmetric and asymmetric tilt boundaries on (111), (100), (110) and (113) planes [127,174]. In contrast, only a handful of studies exist on bcc transition metals including the work of Wolf on Fe/Mo [126,283], Yeşiltepe and Arias on Mo [284], Ratanaphan et al. on Fe/Mo [128], and Shibuta et al. on Fe [275]. However, there are only a few experimental and/or simulation reference points for atomistic GB structures in tantalum; the principal reference is the structure of the  $\Sigma 5$  (310)/[001] symmetric tilt boundary investigated experimentally and theoretically by Campbell et al. [285,286]. Hence, there is clearly a deficiency in available data for GBs in Ta within the current literature.

Owing to the lack of grain-boundary energies available for bcc tantalum, preliminary work of this thesis was to design and implement a code to scan energies as a function of tilt boundary and misorientation. These results are visualized in Figure 4-1 and detailed descriptions of their basis, orientations, coincident site lattice value, and exact energies can be found in Appendix C. Figure 4-1 shows the calculated GBEs as a function of misorientation angle alongside previous results for other bcc elements. GB structures presented in subsequent figures are indicated by dashed lines. Based on calculations of surface energies for bcc transition metals, the energy of tantalum interfaces are bracketed between iron and molybdenum [287]. We note that it is to be expected that GBEs calculated



in this work will be slightly lower than those calculated by tight binding or ab-initio methods [282,288].

Minima in energy are observed at specific misorientations for each of the tilt axes similar to fcc materials. However, in our case, the most prominent minimum in energy is associated with the  $\Sigma 3 \langle 110 \rangle$  boundary shown in bold in Figure 4-1b. The  $\Sigma 3$  boundary is a coherent twin boundary in bcc metals and can play a critical role in plasticity by determining the propensity to nucleate deformation twins. Pressure and shear can alter barriers to deformation such as stacking fault energies and the Peierls-Nabarro stress; relative energy barriers determine whether full or partial dislocations are produced to relieve strain and ultimately influence the kinetics of deformation.

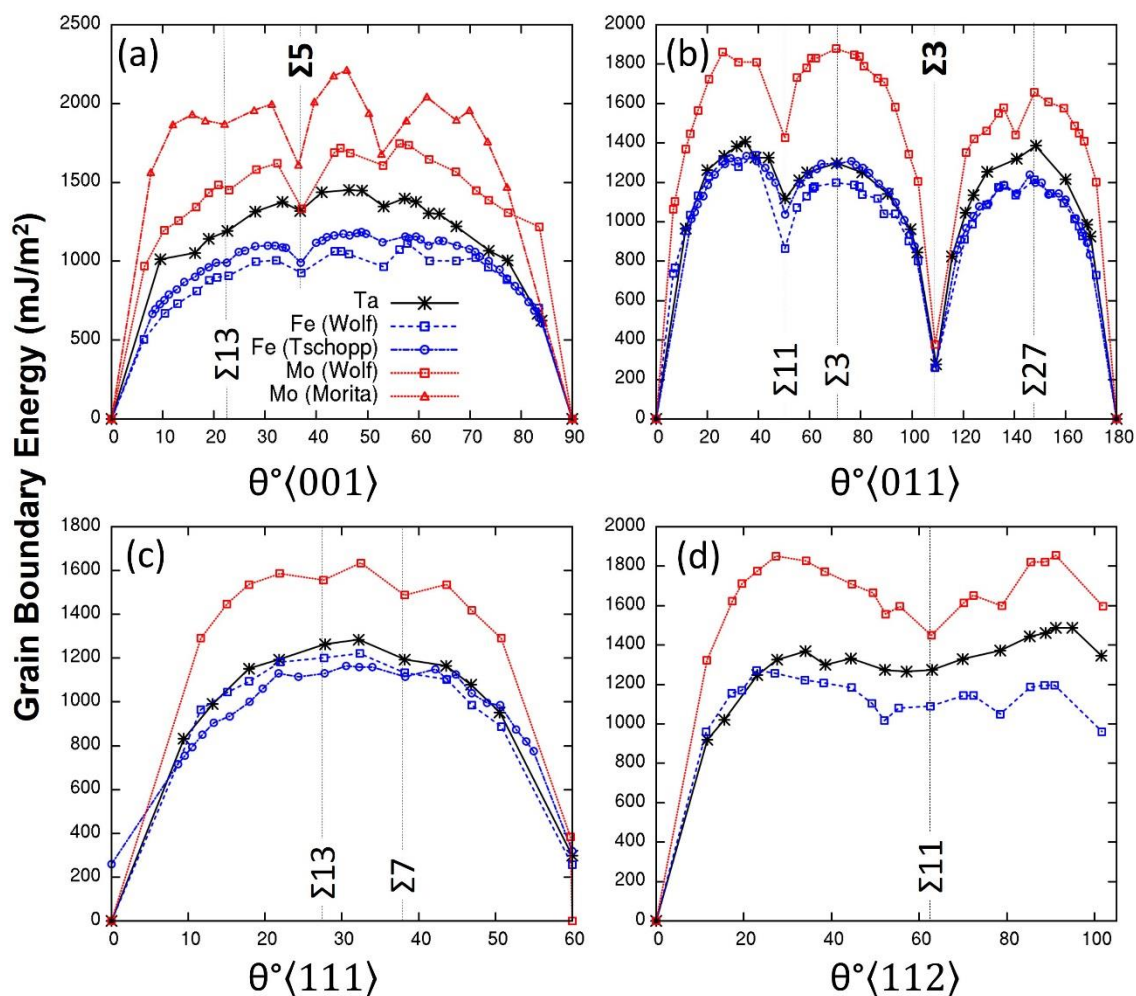


Figure 4-1. Excess grain boundary energy as a function of misorientation for the four tilt axes  $\langle 100 \rangle$ ,  $\langle 110 \rangle$ ,  $\langle 111 \rangle$ , and  $\langle 112 \rangle$ . GBEs for Ta are shown as black asterisks and a complete description of all boundaries calculated in the present work can be found in the supplemental material. Also provided is relevant data for bcc Fe (blue) and bcc Mo (red) from empirical potentials by Wolf [126,283], Morita and Nakashima [289], and Tschopp et al. [120] showing similar trends.

Figure 4-2 shows an extrapolation of the Fe and Mo grain boundary energies from Wolf [126,283] to Ta using the ratio of energies given above. It is clear that this method is insufficient to rigorously evaluate the grain boundary energies of tantalum, especially for the  $\langle 011 \rangle$ ,  $\langle 111 \rangle$  and  $\langle 112 \rangle$  orientations. One might imagine improving the predictive nature of our estimate by accounting for the differences in  $\langle 100 \rangle$ ,  $\langle 110 \rangle$ ,  $\langle 111 \rangle$ , and  $\langle 112 \rangle$  surface energies provided by Zhang et al. [287]. However, Table indicates that the

energy ratios are all larger than 1.18 for Fe and 0.93 for Mo; by observing that the  $\langle 011 \rangle$ ,  $\langle 111 \rangle$  and  $\langle 112 \rangle$  grain boundary energy predictions are overestimates, the corrected ratios would not improve the extrapolation, only worsen it. This stresses the need to evaluate the energies of tantalum grain boundaries themselves, as accomplished in the current work.

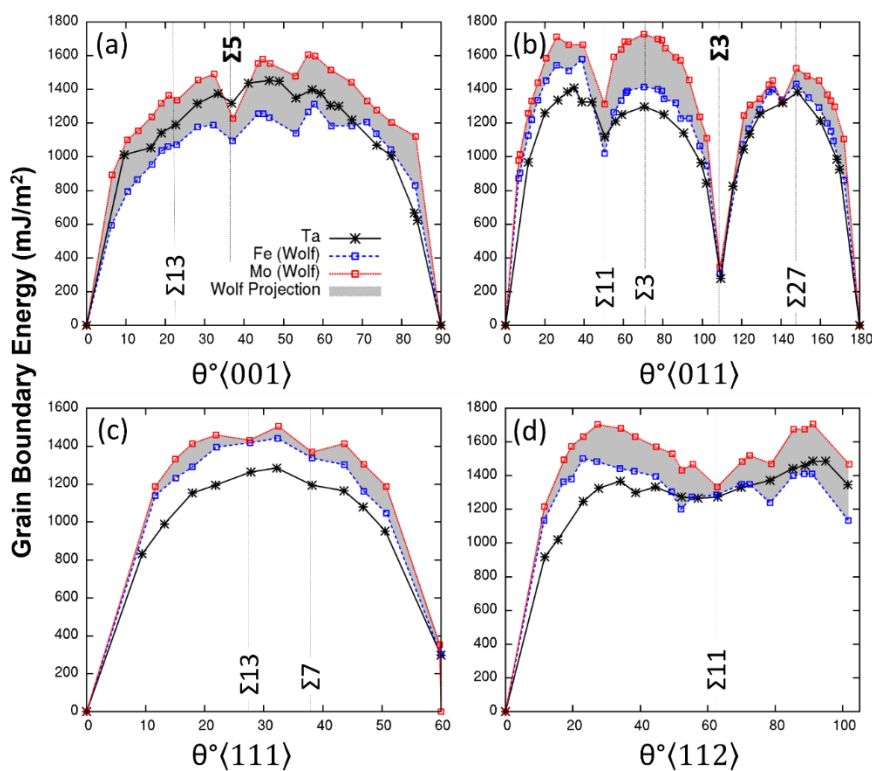


Figure 4-2. Grain boundary energy as a function of misorientation for four tilt axes. GBEs for Ta are shown as black asterisks. Also provided is predicted/extrapolated values from Wolf [126,283] using the energy values in Zhang et al. [287]. The gray region represents the predicted range of values for grain boundary energies for Tantalum.

Figure 4-2 also shows that the errors in extrapolated energy are commonly in the range of 15-20% and that the energy of the  $\Sigma 5$  boundary (the only grain boundary in Ta for which an energy value in literature exists) is a particularly poor benchmark due to the complexity and broken symmetry of this structure. This further emphasizes that the nature

of broken symmetry leads to structures with energies that simply cannot be determined from prior literature alone.

Table 4-1. Surface Energy ( $\text{mJ/m}^2$ ) for bcc Ta, Fe, and Mo. Data from Zhang et al. [287].

	$\gamma\text{-Ta}$	$\gamma\text{-Fe}$	$\gamma\text{-Ta}/\gamma\text{-Fe}$	$\gamma\text{-Mo}$	$\gamma\text{-Ta}/\gamma\text{-Mo}$
$\gamma_{100}$	3090.8	2565.1	1.2	3260.7	0.95
$\gamma_{110}$	2790.2	2369.6	1.18	2920	0.96
$\gamma_{111}$	3263.7	2684.9	1.22	3429.2	0.95
$\gamma_{112}$	3437	2582.7	1.33	3255.4	1.06

Two GB structures for the  $\Sigma 3$  twin boundary are obtained using EAM: a structure with a well-defined mirror plane ( $\Sigma 3$ , Figure 4-3a) and a structure with no mirror plane ( $\Sigma 3'$ , Figure 4-3b). The  $\Sigma 3'$  boundary is quasi-symmetric, i.e. grain normals are equal and opposite in sign, but crystallographic mirror symmetry across the GB plane is broken [290]. The  $\Sigma 3'$  structure can be obtained by shearing the coherent  $\Sigma 3$  boundary in the boundary plane. As a result, the boundary takes a zig-zag configuration (light blue atoms) which decreases its energy. In fact, the  $\Sigma 3'$  has the lowest observed energy of  $278 \text{ mJ/m}^2$  in comparison to  $293 \text{ mJ/m}^2$  for the  $\Sigma 3$  boundary. In order to verify the unique low energy structure of the  $\Sigma 3'$  we also used the SNAP potential. Figure 4-3c shows the SNAP predicted  $\Sigma 3'$  which also has a structure and energy similar to the one predicted by EAM, indicating that the  $\Sigma 3'$  structure is not a potential-dependent artificial GB structure. Simultaneously published, the structure was shown to be important to competing twinning mechanisms in bcc metals Shi and Singh [291].

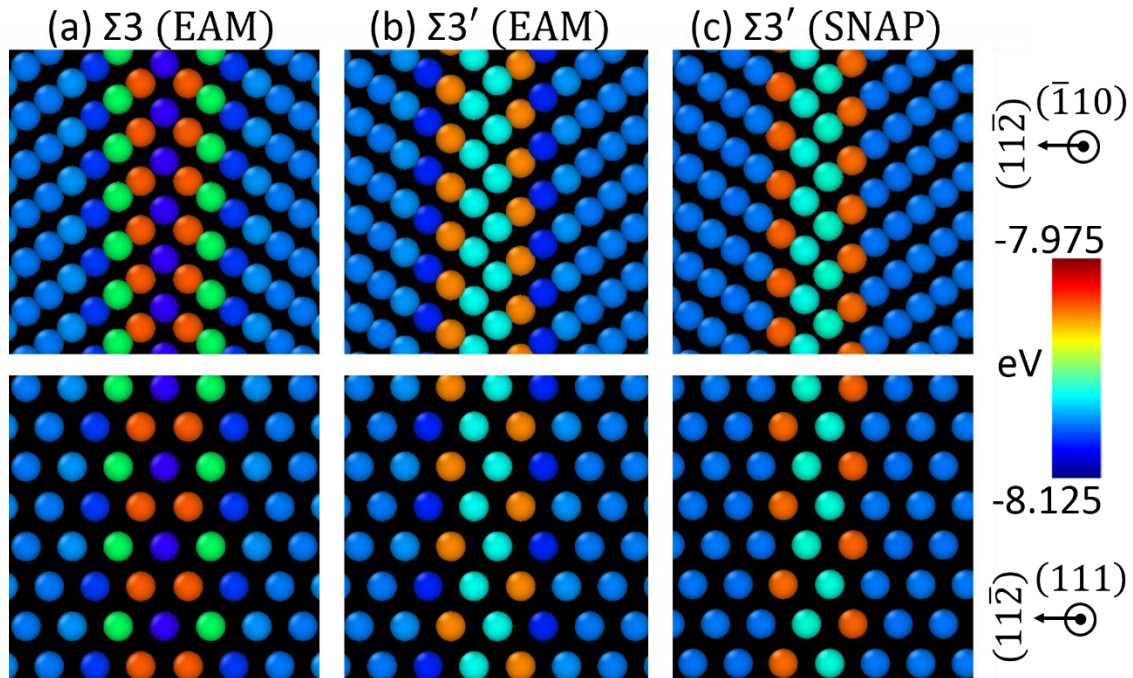


Figure 4-3. Configurations of  $\Sigma 3(011)$  boundary colored by eV/atom shown for two projections. In each projection the GB normal is horizontal. (Left) EAM symmetric twin boundary. (Middle) EAM quasi-symmetric boundary with broken mirror symmetry in both  $(110)$  and  $(111)$  projections. (Right) SNAP quasi-symmetric boundary.

Higher energy  $\Sigma 3$  boundaries ( $1027 \text{ mJ/m}^2$ ) are also identified when the GB plane is changed to  $(11\bar{1})$  from  $(11\bar{2})$  (tilt:  $\langle 011 \rangle$ ). *Ab-initio* calculations of the low energy  $\Sigma 3$  boundary in tungsten [292] and iron [101] only evidence fully symmetric structures, but such symmetry was reinforced by small system size in combination with *a priori* atom displacements and minimizations. Broken and/or conserved mirror symmetry ultimately serves as a primary indication of atomic accuracy in bcc transition metal potentials owing to the strong influence of non-spherically symmetric d-orbitals.

Similarly, the  $\Sigma 5$  boundary (Figure 4-4) structure breaks mirror symmetry; this contrasts early work of Ochs et al. [293], which shows, using simulations, that the Ta  $\Sigma 5$  GB has full mirror symmetry. However, the  $\Sigma 5$  is composed of “B” structural units

analogous to those identified in Fe [120]. The presently calculated GBE of  $1318 \text{ mJ/m}^2$  is markedly less than the previously predicted  $1544 \text{ mJ/m}^2$  [293]. More recent calculations using model generalized pseudopotential theory (MGPT) do predict a break in mirror symmetry for this boundary [285]. Ab-initio work by Ochs et al. [293] does, however, identify other bcc transition metal elements (Mo, W, and Nb) that break mirror symmetry. For Nb and Mo, there exist experimental high-resolution transmission electron microscopy (HRTEM) evidence for both structures with conserved and broken symmetry [278,294]. The relative shift across the boundary identified here for Ta is  $0.81 \text{ \AA}$  (as measured by the vertical displacement between opposing red atoms in Fig. 3b) as compared to  $\sim 0.78 \text{ \AA}$  for Mo.

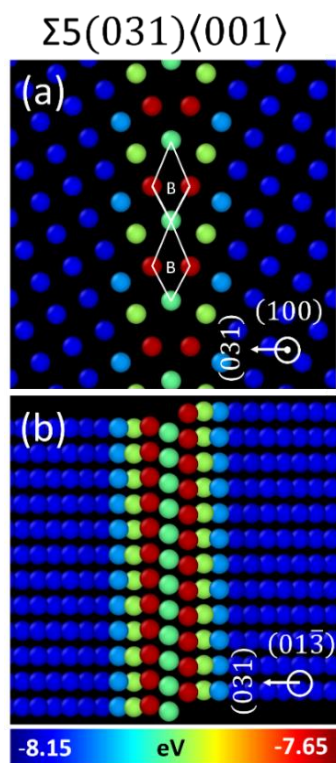


Figure 4-4.  $\Sigma 5$  boundary visualization with color according to atomic potential energy in eV/atom. (Top) Boundary structural unit  $B$  identified in the typical fashion [295]. (Bottom) Projection illustrating broken mirror symmetry shift.

Relative to the respective lattice parameter (3.304 Å for Ta and 3.147 Å for Mo) the displacements are within ~1% of one another. If instead the shift is measured as the distance between atomic planes projected across the boundary, the shift is 0.55 Å, showing superb agreement to the experimentally observed shift of ~0.55 Å in Ta [285] (the MGPT value is not explicitly stated [285]).

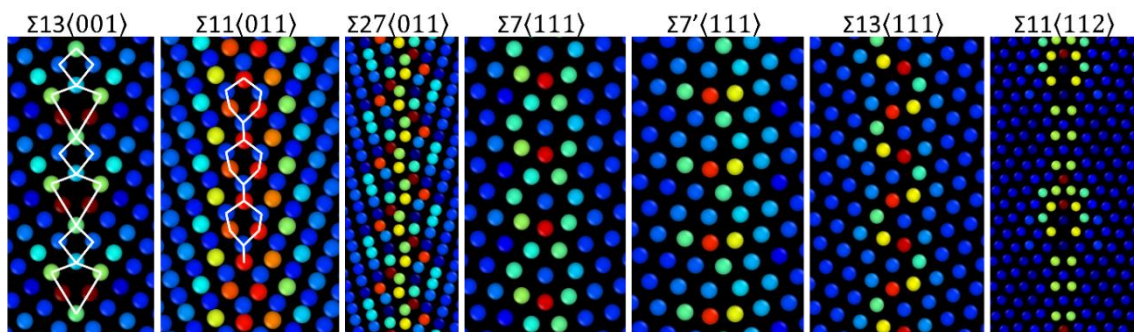


Figure 4-5. Assorted high coincident site density boundary structures for each of the four tilt axis with equivalent coloring scheme as Fig. 3. From left to right the boundaries are:  $\Sigma_{13}(051)\langle 001 \rangle$ ,  $\Sigma_{11}(332)\langle 011 \rangle$ ,  $\Sigma_{27}(552)\langle 011 \rangle$ ,  $\Sigma_7(231)\langle 111 \rangle$ ,  $\Sigma_{7'}(231)\langle 111 \rangle$ ,  $\Sigma_{13}(341)\langle 111 \rangle$ ,  $\Sigma_{11}(131)\langle 112 \rangle$ .

Other boundaries corresponding to various energy minima in Figure 4-1 were also explored. Figure 4-5 shows selected boundaries for each of the tilt axes. The structure of the  $\Sigma_{13}\langle 001 \rangle$  boundary is similar to the HRTEM observations of boundaries in Mo by Morita and Nakashima [289]. The  $\Sigma_{11}\langle 011 \rangle$  structure shown in Figure 4-5 also agrees well with the density functional theory (DFT) calculations of  $\Sigma_{11}$  boundary in iron [101]. A large majority of the  $\langle 112 \rangle$  tilt axis boundaries exhibit large (periodic) boundary unit cells such as that shown for the  $\Sigma_{11}\langle 112 \rangle$ . There exist multiple other predicted boundary structures that break mirror symmetry such as the  $\Sigma_{27}$ ,  $\Sigma_{7'}$  and  $\Sigma_{13}\langle 111 \rangle$ . The  $\Sigma_7$  boundary also exhibits both a symmetric and quasi-symmetric structure of nearly equivalent energies further suggesting that the phenomenon of symmetry breaking is prevalent for many boundaries in bcc transition metals.

#### 4.1.2. Tensile “Spall” Failure

At high strain rates, spallation or tensile damage caused by the nucleation, growth, and coalescence of voids is of critical interest due to the prevalence of spall damage in engineering applications. The difficulty in obtaining comprehensive material information during high-strain rate experimentation compounds the need for time-resolved data at the spall plane. There is a long history of shock-induced spallation spanning tensile strain rates from  $10^3$ - $10^8$   $s^{-1}$  using conventional explosive and gas-driven loading to the more modern laser-driven loading [23,32,35,205–210]. The majority of experimental approaches are limited to indirect methods of observation such as free surface velocimetry [211–213], postmortem metallographic analysis [50,300,301], or other imaging techniques [76]. Furthermore, for state-of-the-art laser-driven experiments the upper bound of repeatedly and reliably achievable strain rates is  $\sim 10^9$   $s^{-1}$  [54,302]. Nevertheless, current spall models strongly rely on empirical data or often semi-empirical continuum and multi-scale models of void nucleation and growth theories for which many parameters are critically under-informed.

The deformation of ductile metals relies on the materials' capacity to develop certain types of plasticity, such as the nucleation and motion of dislocations. For polycrystalline materials, grain boundaries often serve as heterogeneous nucleation sites and the structural deviations and frequency of boundaries plays a critical role in plasticity. Voids can nucleate at a lot of locations. We know grain boundaries are important and we need to quantify and explain why voids form at varying topological locations. During ductile tensile failure, the preferential sites for void nucleation, prior to their growth and coalescence, are thought to be related to the defective interface structure which may be



characterized by coincident site density, free volume, excess energy, boundary specific structural units, and misorientation, among other measures [59,104,108,109,111,174,175,303,304]. The propensity of the interface or defect structure to deform or contort by means other than cohesive failure is often associated with a greater spall strength - an important measure of material strength under tension.

To date, most molecular dynamics investigations of tensile failure in bcc polycrystalline tantalum have evidenced nucleation that is limited to grain boundary sites, simulations have also evidenced intergranular cracking [158,280,305,306]. Studies of polycrystals often neglect discussing why certain boundaries fail while others survive. Furthermore, results from previous literature may be strongly related to deficiencies stemming from the Voronoi polycrystal construction method producing non-equilibrium grains that persist through simple relaxation methods such as annealing. Relatedly, the typical small grain sizes or cross sections used in molecular dynamics simulations may present the following limitations: leave little intragranular room for the development of twin-twin intersections; may develop plasticity via grain boundary sliding or grain-grain coupled motion that limit the density of twins; provide mechanisms by which de-twinning occurs reducing twin density, may sample too few grains due to computational limitations; or may have a larger density of grain boundaries close to the spall plane available for nucleation.

MD simulations of spallation and void-related plasticity under non-shock conditions have primarily been focused on face-centered cubic metals [112,176,307–310], but, more recently, body-centered cubic metals have seen more study [158,196,310–313].

#### 4.1.2.1. Specific Spall Methods

Previous studies of tantalum were limited in cross sectional area [314] or of different focus and much space remains for directed MD simulations of shock-induced spall. In order to directly compare and contrast simulations with experiments it was necessary to devise a means to collect the free surface velocity. Figure 4-6 shows the result of a script written to track the rear surface position and then calculate a time derivative.

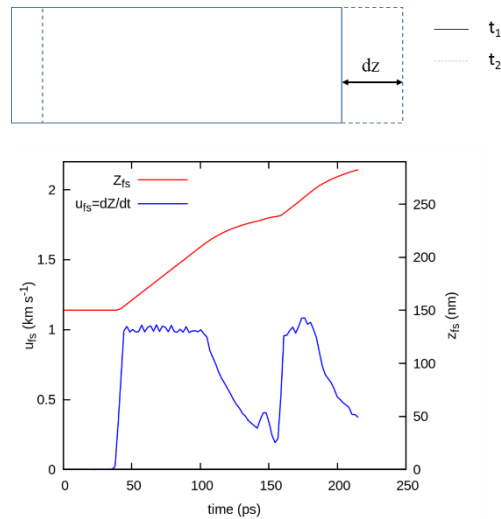


Figure 4-6. Illustration of free surface position and its temporal derivative to give free surface velocity.

The subsequent figures illustrate how sample dimensions were determined by taking into account computational costs, appropriate boundary conditions, and isolation of variables relating to the spall process. The length variation shown below in Figure 4-7 is used to determine the pressure decay as the shock pulse traverses a sample. In terms of free surface velocity this is determined to be:  $U_p = U_{p0} e^{-1.085 \cdot 10^2 Z}$ . Here  $z$  is the distance traveled by the wave in nanometers.

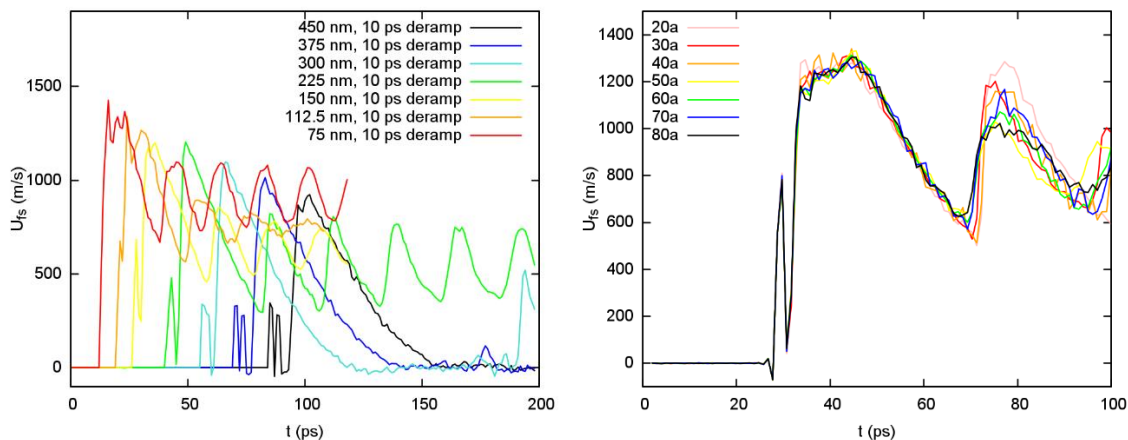


Figure 4-7. Simulated VISAR showing (a) shock pulse attenuation with increasing sample length and (b) effect of cross section on pullback signal.

Signals that do not display a pull-back signal represent samples that do not undergo spall.

The effect of cross section can be seen in Figure 4-7 and for dramatic effect the lowest and highest values are shown in Figure 4-8.

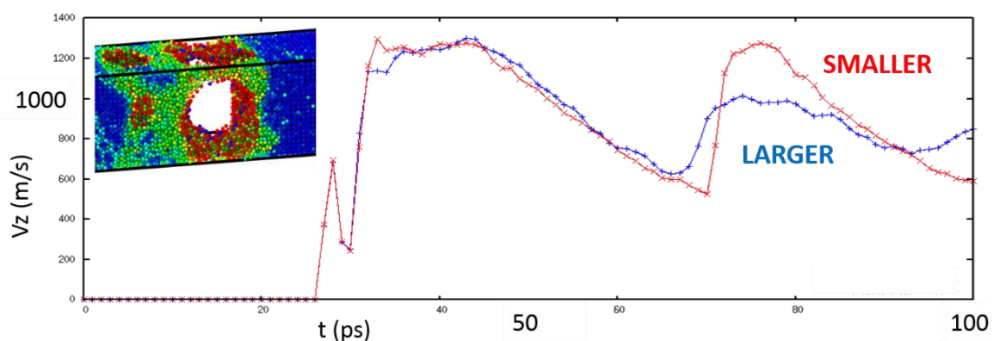


Figure 4-8. Cross section determined spall pullback response. The difference in signal is representative of defects and voids interacting with themselves across periodic boundaries. Inset corresponds to the small run where voids interact with themselves across periodic boundaries.

For subsequent runs the length was at least 150 nm ( $\sim 454$  lattice parameters) and cross sections of at least  $1000 \text{ nm}^2$  ( $100 \times 100$  lattice parameters). By controlling the piston with a specified function (Section 3.4.3) the simulated VISAR curve and the downslope indicative of tensile strain-rate slope was able to be controlled as shown in Figure 4-9.

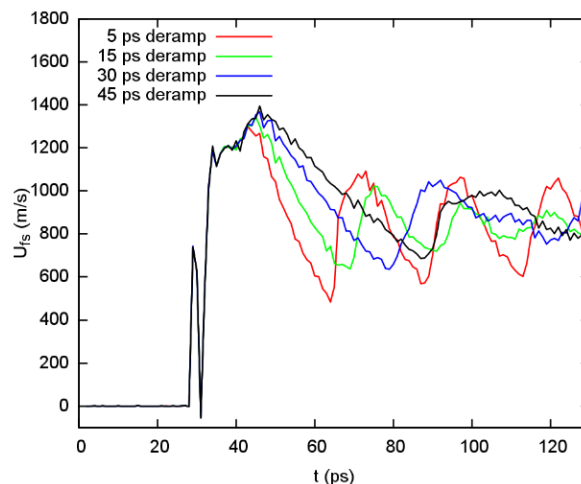


Figure 4-9. Controlled deramp/deceleration of piston velocity controls the release rate as measured by the free surface velocity as a function of time.

Figure 4-10 demonstrates that the limitation of this technique is computational time.

For longer decelerations, as required for lower strain-rates (approaching those of current experiments), the sample length must increase to allow for a majority of the wave form to be completed.

Up (km/s)	Deramp time	Strain-Rate (1/s)	Length
0.75	10 ps	1.10 E+10	34 nm
0.75	100 ps	1.10 E+09	340 nm
0.75	1 ns	1.10 E+08	3.4 $\mu\text{m}$
0.75	10 ns	1.10 E+07	34 $\mu\text{m}$
0.75	100 ns	1.10 E+06	340 $\mu\text{m}$
0.75	1 $\mu\text{s}$	1.10 E+05	3.4 mm

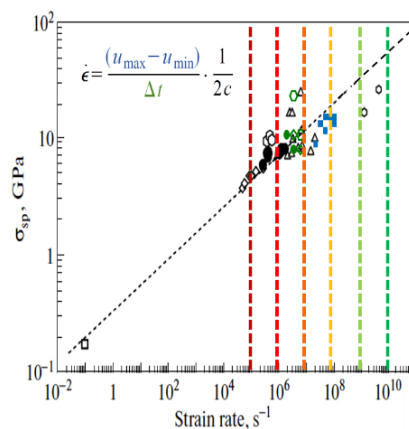


Figure 4-10. Strain rate as function of deceleration time and required sample length. Green indicates simulations that are easily achievable given current computational resources while red represents those that are currently impossible. The yellow and possibly orange lines may be achievable with dedicated allocations.

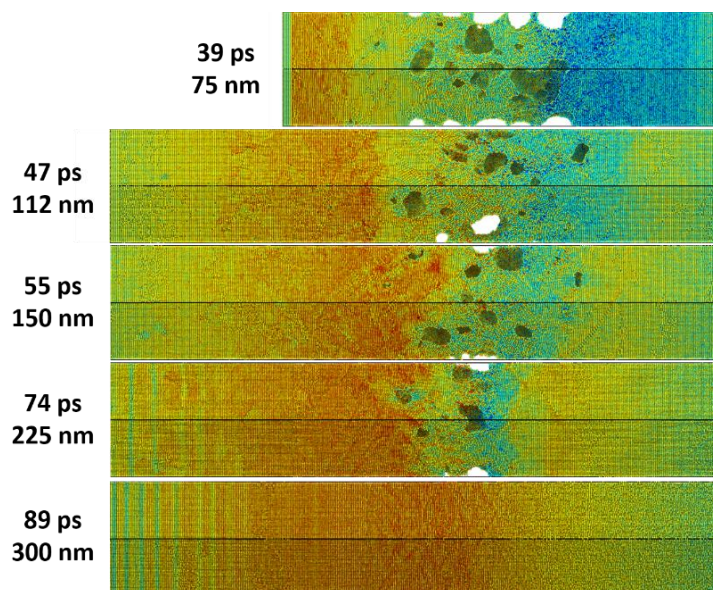


Figure 4-11. Spall damage as a function of sample length, each with an equivalent particle velocity drive.

Furthermore, a longer sample length also requires a longer simulation time to allow the wave to reach the rear surface and reflection into tension. Longer samples also introduce a need to account for the decay of the shock wave as it transverses the length of the sample as previously stated. For a particle velocity of 0.75 km/s, samples up to 225 nm in length show spall failure, but the decayed wave in a 300 nm sample is not sufficient to open a spall void as shown in Figure 4-11.

#### 4.1.2.2. Spall Strength as a Function of Strain Rate

Using the above mentioned techniques and the methods presented in Section 3.4.3, Figure 4-12 shows spall strength as a function of strain rate, including experimental and simulation results from literature. The plot confirms the pertinence of using molecular dynamics to explore the extreme strain-rate regime. Points are colored according to their grain size; black points represent [001] single crystals, blue/purple represent polycrystals, and red points represent nanocrystals.

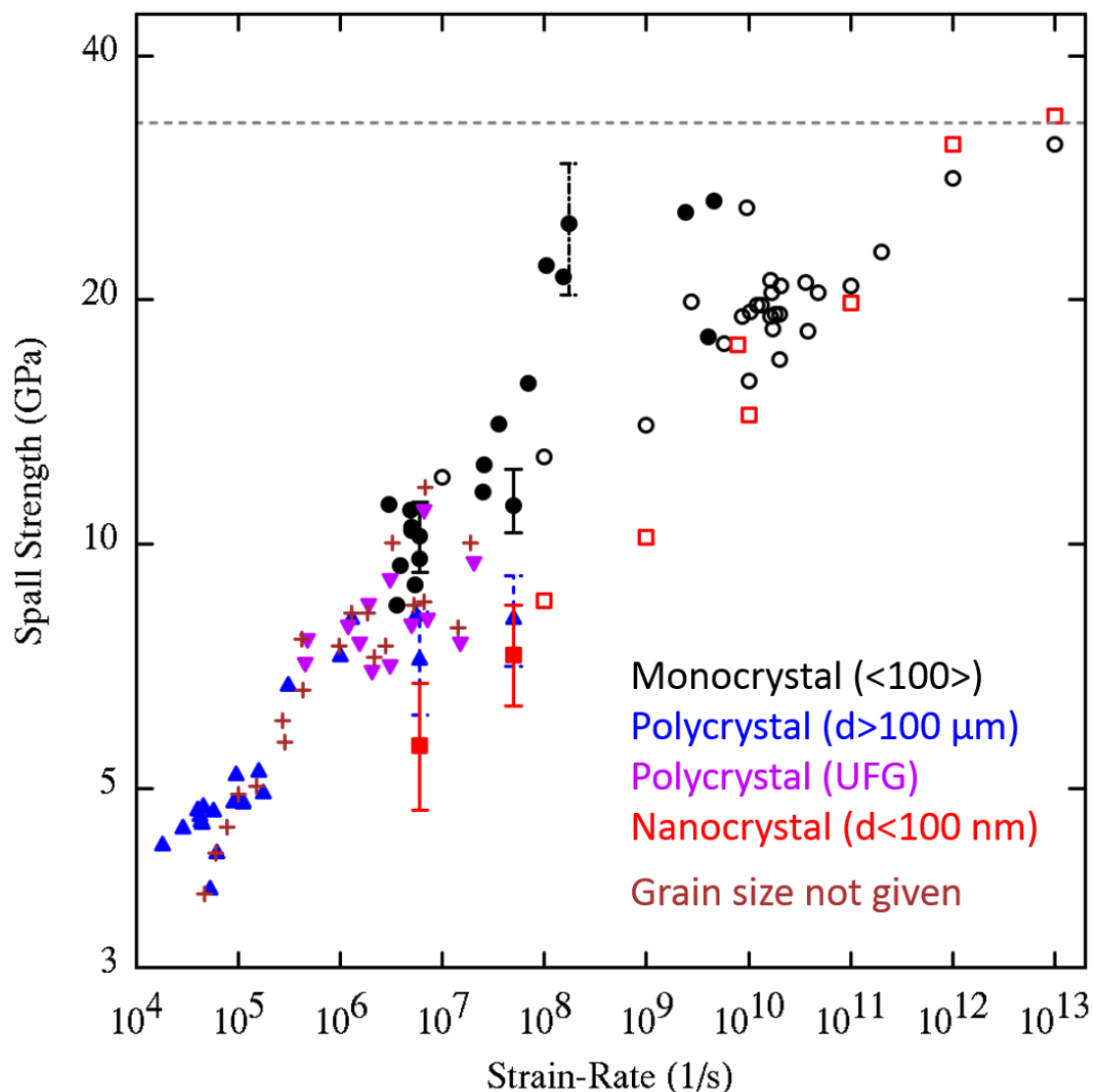


Figure 4-12. Compilation of reported spall strength as a function of strain rate. Different colors refer to different grain sizes: single crystal (black), polycrystal (blue), nanocrystal (red), ultra-fined grained (purple) and unknown (brown). Data are from multiple sources, including both experimental and simulation work [315,296,300,316,54,297,53,317–319,75,320,321,55,34]; experiments are closed symbols and simulations are portrayed as open symbols (with strain rates greater than the phonon frequency marked with crosses). A full set of references is provided in the supplemental material. The ultimate tensile strength is indicated by a horizontal dashed line at  $\sim 33$  GPa.

There is a clear difference in slope between the power law curves fit to mono, poly, and nanocrystalline data (Figure 4-13) and key aspects of failure within single crystalline and nanocrystalline samples are subsequently detailed. The behavior of materials under

extreme conditions is often modeled using hydrodynamic codes such as HYADES. A popular formulation of the spall strength as a function of strain rate is the strain-rate dependent Cochran-Banner [322] model. The parameters given by Steinberg [323] are:  $\sigma_0=4.4$  GPa and  $m=0.011$ .

Temperature plays an important role in the failure process and the effect is also described. The theoretical cohesive stress  $\sigma_{\max}$ , reached at strain rates exceeding the Debye frequency is similar for varying grain sizes, but does show a residual effect of the orientation/grain size.

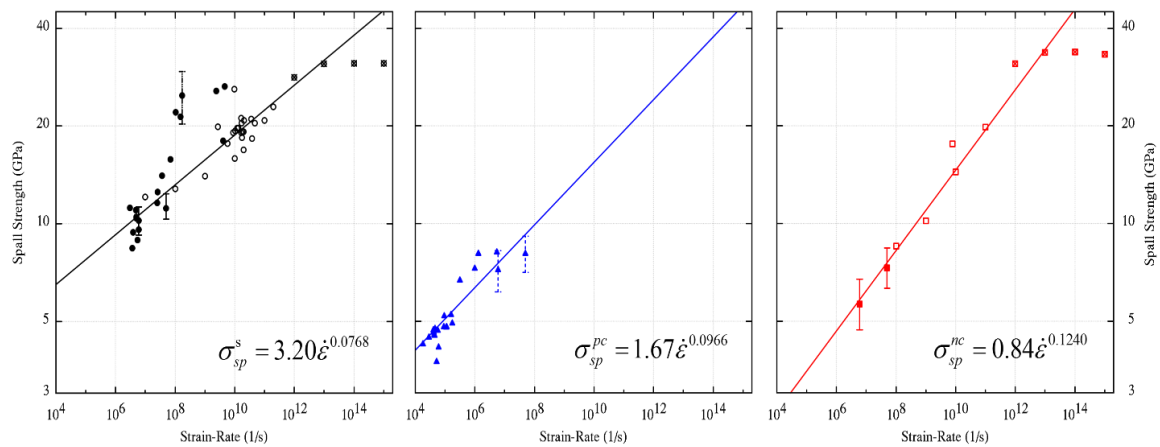


Figure 4-13. Power-law fits for single (black, left), polycrystal (blue, center), and nanocrystal (red, right) tantalum spall strength vs strain rate data. Solid data markers are experiments and open markers are simulations. Points with crosses through them were not included in fits. With increasing grain size the pre-factor increases and the exponent decreases.

Table 4-2. Simulations of single crystalline tantalum. Measurements at the peak tensile stress in the shock direction ( $\sigma_{zz}$ ) and the corresponding hydrostatic pressure (P), deviatoric shear stress( $\tau$ ), temperature (T), and strain ( $\epsilon$ ).

Method	$\dot{\epsilon}$ ( $s^{-1}$ )	$\sigma_{zz}$ (GPa)	P (GPa)	$\tau$ (GPa)	T (K)	$\epsilon$
QI	$10^7$	12.1	11.7	0.29	604	0.079
QI	$10^8$	12.8	12.2	0.51	647	0.087
QI	$10^9$	14.0	13.0	0.72	650	0.103
QI	$3 \times 10^9$	15.0	13.8	0.87	642	0.117
QI	$10^{10}$	15.9	14.8	0.84	644	0.139
Piston	$1.65 \times 10^{10}$	19.1	18.4	0.53	649	0.176
Flyer	$1.75 \times 10^{10}$	18.4	17.7	0.57	910	0.174
QI	$2 \times 10^{10}$	16.9	15.8	0.76	667	0.160
QI	$3 \times 10^{10}$	17.5	16.6	0.70	701	0.179
QI	$6 \times 10^{10}$	19.3	18.2	0.77	788	0.224
QI	$10^{11}$	20.8	19.5	1.03	898	0.270
QI	$2 \times 10^{11}$	22.9	20.7	1.67	1111	0.340
QI	$3 \times 10^{11}$	24.3	21.4	2.21	1174	0.380
QI	$10^{12}$	28.2	22.8	4.04	1307	0.485
QI	$10^{13}$	31.1	22.9	6.17	619	0.565

Table 4-3. Simulations of nanocrystalline tantalum,  $d = 21$  nm. Measurements at the peak tensile stress in the shock direction ( $\sigma_{zz}$ ) and the corresponding hydrostatic pressure (P), deviatoric shear stress( $\tau$ ), temperature (T), and strain ( $\epsilon$ ).

Method	$\dot{\epsilon}$ ( $s^{-1}$ )	$\sigma_{zz}$ (GPa)	P (GPa)	$\tau$ (GPa)	T (K)	$\epsilon$
QI	$10^8$	8.5	6.3	1.63	500	0.057
QI	$10^9$	10.2	7.8	1.80	523	0.070
Piston	$7.8 \times 10^9$	17.6	15.3	1.73	800	0.137
QI	$10^{10}$	14.4	12.0	1.81	620	0.123
QI	$10^{11}$	19.8	11.6	6.17	711	0.144
QI	$10^{12}$	31.1	16.6	10.92	484	0.224
QI	$10^{13}$	33.7	18.1	11.73	361	0.262



Key results at tensile strain rates spanning  $10^7$ - $10^{13}$   $s^{-1}$  are located in Table 4-2 and Table 4-3. In addition to the simulation method and tensile strain rate (which is directly imposed for QI, and indirectly for the flyer plate and piston methods), the peak tensile stress in the shock direction ( $\sigma_{zz}$ ) and the corresponding hydrostatic pressure (P), deviatoric shear stress( $\tau$ ), strain ( $\epsilon$ ), temperature (T) are given.

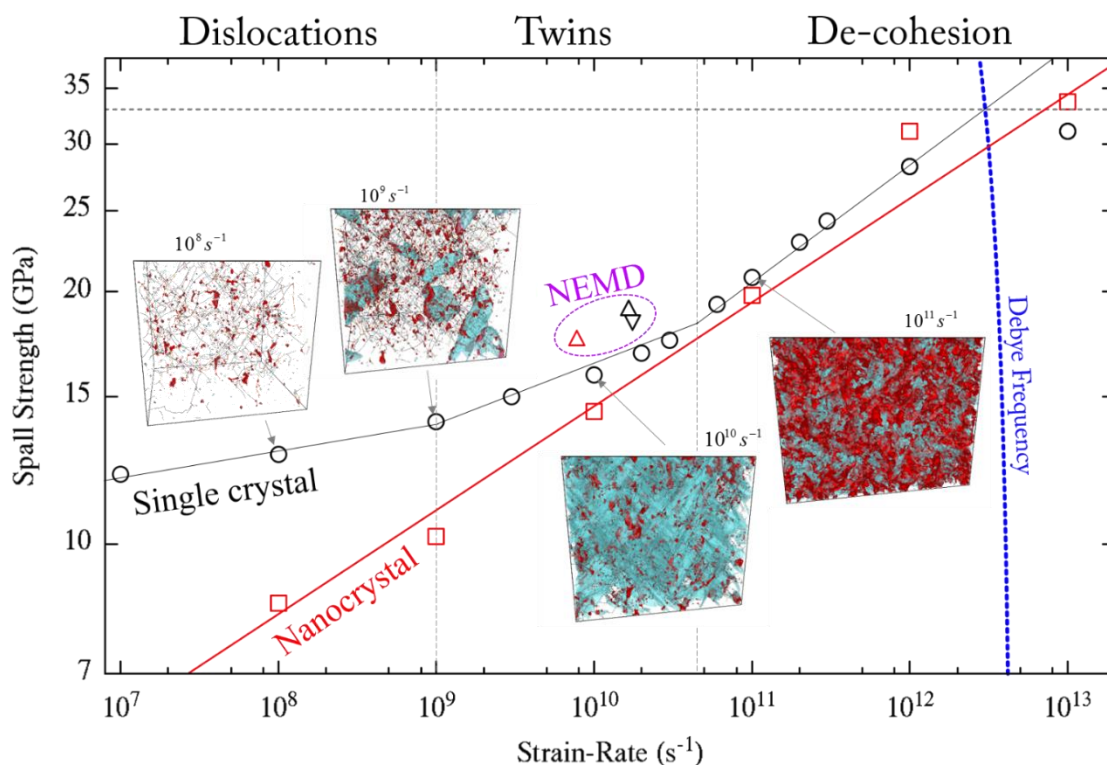


Figure 4-14. Measured spall strength vs strain rate (from Tables 4-2 and 4-3). Also plotted is the Debye/phonon frequency on the right hand side of the plot as a dashed blue line; it is expected that the frequency decreases with expansion just as it increases under compression. Phonon frequency as a function of negative pressure was extrapolated from Liu et al.[324]. Snapshots of quasi-isotropic simulations of [001] single crystals at different strain rates - shown at maximum tensile stress. Dislocations are shown as dark lines, twin boundaries as transparent turquoise surfaces, and voids as transparent red surfaces. Regions of dislocation, twin, and de-cohesion dominated spall processes are separated by vertical dashed lines. The strains at which each frame is displayed are provided in Table 4-2 and 4-3. NEMD simulations (Piston and Flyer-Target methods) lie off the main lines primarily due to differences in stress state, having lower contributions of shear stresses that aid in nucleating defects.

The peak tensile stress (i.e., the spall strength) as a function of strain rate is graphically shown in Figure 4-14 for single crystals. Insets within the figure demonstrate which deformation mechanism is dominant at a given strain rate. Power law trends depicted as linear fits in the log-log plot illustrate that the kinetics of spall is deformation mechanism dependent. At strain rates greater than  $5 \times 10^{10} \text{ s}^{-1}$  the mechanism governing tensile strength again changes.

At elevated strain rates the material has significantly less time to respond to the applied stress and failure occurs primarily by de-cohesion of atoms (Figure 4-14 inset). This primarily occurs in areas of reduced density, such as at twins that have excess volume (and energy) within the boundary layer [61]. A complete analysis of extreme strain rates is left for future study – the possibility of phase change at tensile strains in excess of 0.25 remains an open question [325] and exceeds the bounds the potential was fit to. The following tensile strain-rate regimes are delineated by their dominant deformation mechanism: dislocations,  $\dot{\epsilon} < 10^9 \text{ s}^{-1}$ ; twinning,  $10^9 \text{ s}^{-1} < \dot{\epsilon} < 5 \times 10^{10} \text{ s}^{-1}$ ; de-cohesion,  $\dot{\epsilon} > 5 \times 10^{10} \text{ s}^{-1}$ . The curved vertical line on the right hand side of the figure depicts the Debye frequency as a function of tension, which serves as a good estimate for where the material should exhibit its ultimate tensile strength [326]. The upper limit of tensile strength is indicated by a horizontal dashed line and a discussion of its value will follow at the end of this section.

#### **4.1.2.3. Spalling of Single Crystalline Tantalum**

Single crystal simulations show that dynamic spall proceeds via the nucleation of several distributed voids at defects that are generated during compression as well as in tension. A time series of the flyer-target and piston simulations are shown in Figure 4-15.

The snapshots correspond to the time of maximum tensile stress ( $t_{\max}$ ) and 6, 4, and 2 ps before  $t_{\max}$  as well as 2 and 4 ps afterwards. The local longitudinal stress state is represented by the atom's color, blue corresponding to compressive stress and orange to tensile stress. Defects are marked in dark green and void surfaces in dark red. For the flyer plate system,  $t_{\max} = 56$  ps, and for the piston-driven system,  $t_{\max} = 61$  ps.

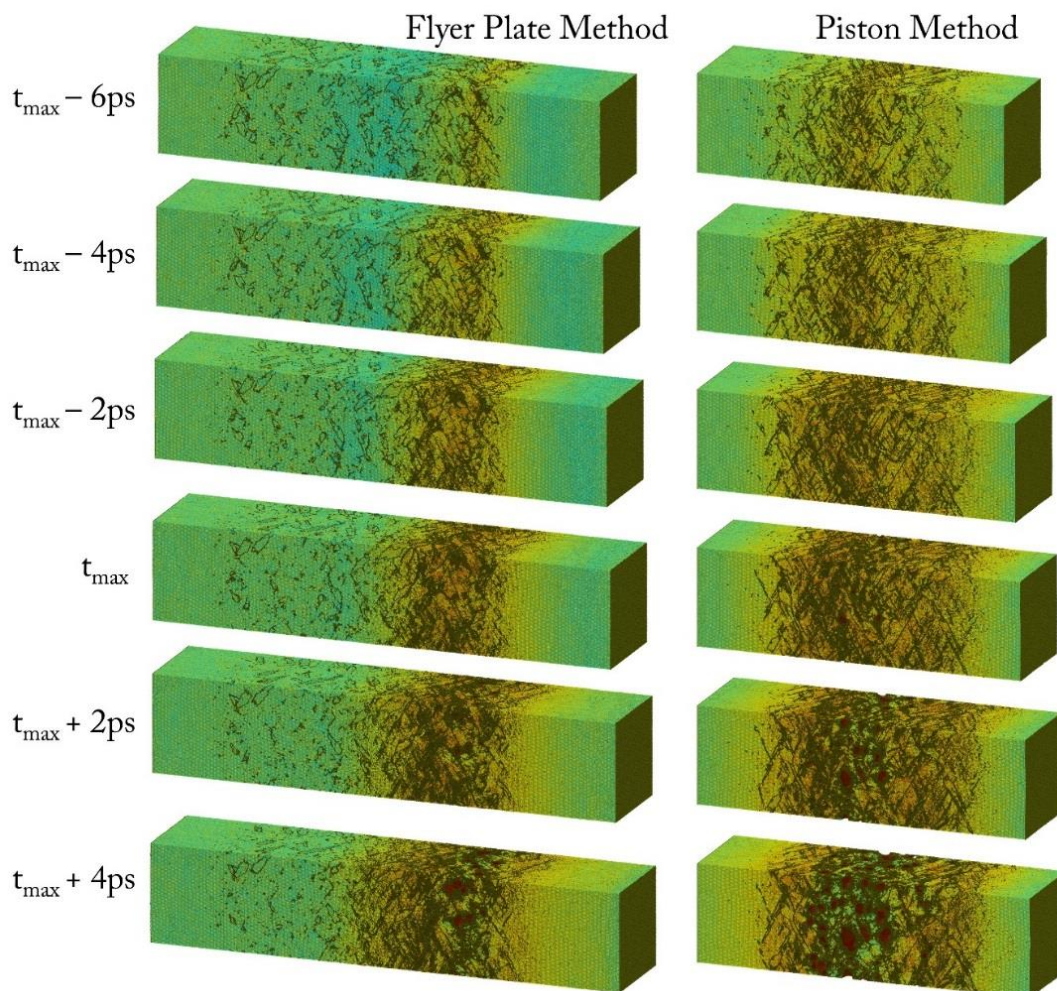


Figure 4-15. Snapshots of the spallation process for flyer plate and piston methods shocked along [001] single crystal Ta. Snapshots are given at the time of maximum tensile stress ( $t_{\max}$ ); and 2, 4, and 6 ps before and 2 and 4 ps after this time. For the flyer plate system  $t_{\max} = 56$  ps, and for the piston-driven system  $t_{\max} = 61$  ps. Stress, temperature, and volume profiles are provided in the supplemental material.

The difference in timing is in large part due to variances in pulse width/shape and the paths through which the waves travel. The spall plane for the flyer-driven system does not lie precisely at the geometrically prescribed location, but instead deviates proportionally to the change of the shock speed in the relative amounts of uncompressed, compressed, and expanded media the wave travels through, in addition to non-linear dispersion effects that cause the initial wave to broaden.

For both loading conditions, we observe that voids in single crystalline tantalum nucleate at twin-twin intersections. Cross-sections must be large enough to allow for sufficient twin-twin intersections to produce realistic spall damage (refer back to Figure 4-8).

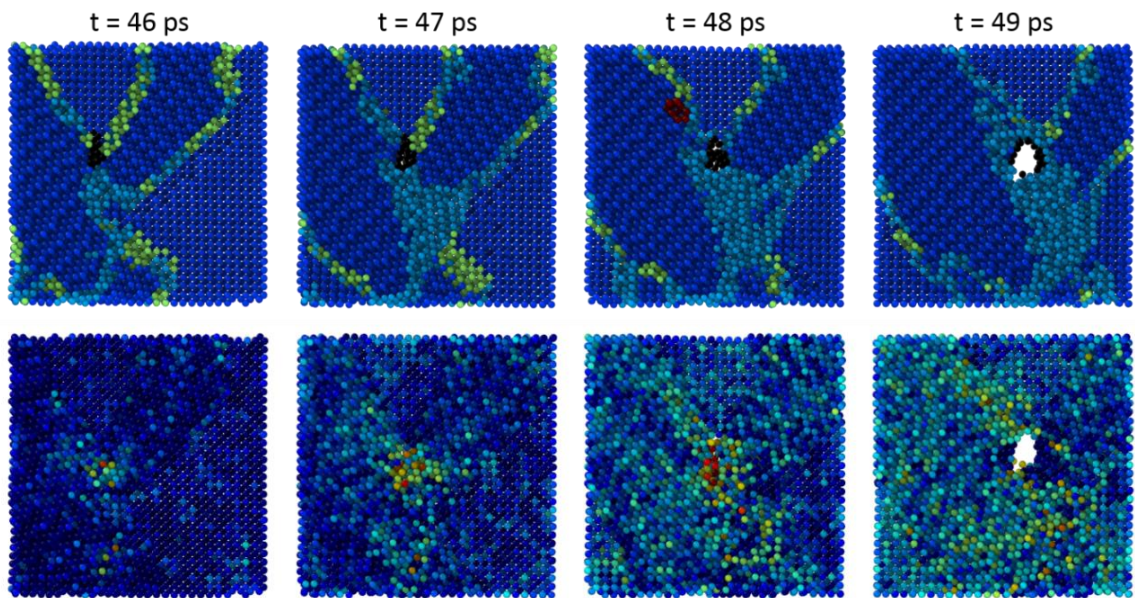


Figure 4-16. Site of first void nucleation during a  $U_p = 0.75$  km/s shock of 5-10-20 shock wave form (5 ps ramp, 10 ps hold, and 20 ps deramp). Twins are identified by green twin boundary atoms in the host 001 matrix.

Figure 4-16 shows the location of an initial void nucleating at a twin-twin intersection. Compatibility dictates that local stress concentrations build at such

intersections and deviation from the bulk stress state is indicated on a per atom basis in the bottom row of Figure 4-16. Black atoms are defined by the void surface at  $t=48$  ps and serve as tracker atoms in the 46, 47, and 49 ps timeframes.

Two three-dimensional views are given in Figure 4-17 where it is shown that voids nucleate specifically at special junctions of the twin-twin intersection. This implies that twin size/thickness will have a strong role in determining where voids nucleate in single crystals.

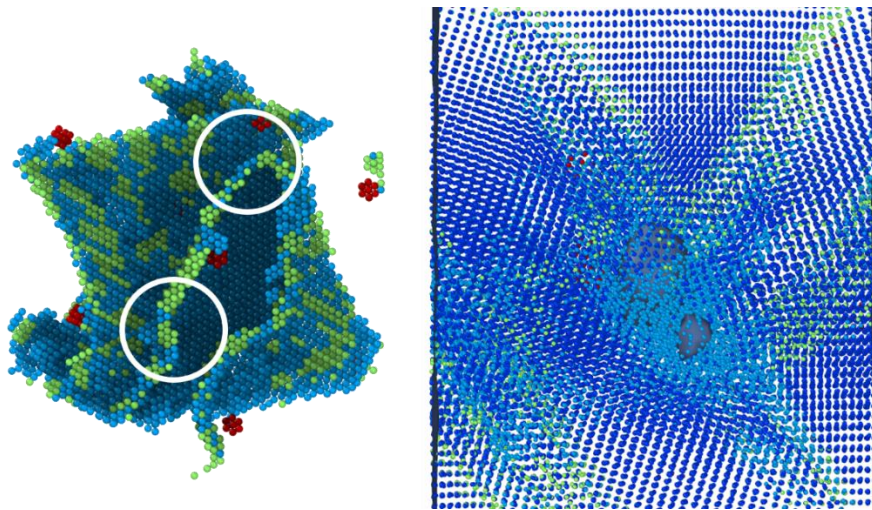


Figure 4-17. Three-dimensional views of void nucleation sites. Left, voids nucleate at the “tip” and “kinks” of twin-twin intersections. Void surfaces at  $t=48$  ps.

QI simulations at comparable strain rates show similar behavior with voids nucleating primarily at twin intersections where local stress concentrations arise (Figure 4-18). Additionally, we identify interconnected symmetric and sheared  $\Sigma 3$  twin boundaries [327] (inset in Fig. 6) which indicates that deformation twinning in tantalum favors dissociated  $1/12\langle 111 \rangle$  partials traveling along adjacent  $\{211\}$  planes as opposed to  $1/6\langle 111 \rangle$  dislocation glide [291]. The fact that all three simulation types (at comparable

strain rates) show similar defect and void mechanisms gives credence to comparisons between the methods.

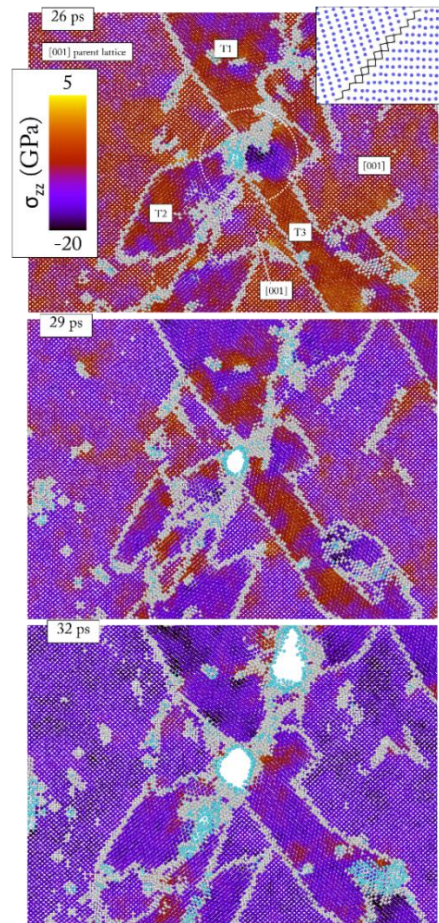


Figure 4-18. (a) Snapshot of twin structures at 26, 29, and 32 ps during QI expansion of a Ta [001] single crystal at a strain rate of  $1010 \text{ s}^{-1}$ . Defective atoms are colored off white and void surfaces are colored light blue. All other atoms are colored according to their local longitudinal stress. The inset in the 26 ps frame shows the atomic configuration of a selected tensile deformation twin with both a symmetric and non-symmetric  $\Sigma 3$  twin boundary, previously shown to be important in the twinning process of bcc metals [291,327]. The first figure also highlights the [001] parent lattice and the intersection of 3 twins which results in a local stress buildup due to compatibility between the twinned and parent orientations.

Figure 4-19 returns our focus to the piston NEMD simulation illustrating the evolution of twins and voids, as well as their relationship to the local longitudinal stress and temperature. Snapshots every 2 ps between 56 and 64 ps are shown highlighting the

early stages of void nucleation, growth, and rapid coalescence due to the proximity of the voids at high strain rates and high twin density. Three visualization schemes are shown.

The top row gives atoms identified by their potential energy, which serves to highlight twins and void surfaces. The middle row colors atoms according to the local stress in the shock direction. This allows for the identification of local stress concentrations due to compatibility requirements within the twinned microstructure and also shows the rapid release and relaxation of tensile stress during the growth of voids.

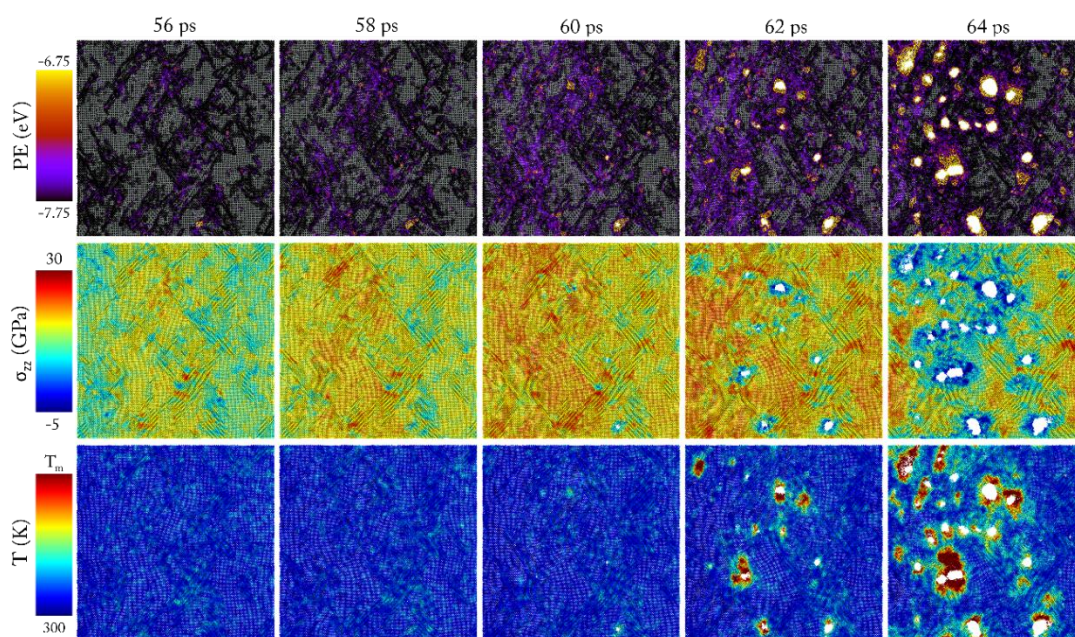


Figure 4-19. Evolution of voids from the early stages of nucleation, growth, and rapid coalescence. This piston-driven simulation contains a broad tensile pulse that passes through the system traveling to the left as the bulk motion continues to carry the system to the right. Shown in three different visualization schemes is a 50 nm x 50 nm transverse cross section 1.5 nm in thickness centered at 110 nm along the shock direction. The shock direction is left to right. The top row colors atoms by their local potential energy and allows for precise visualization of atoms belonging to void surfaces (yellow color). The early stages of the void can be seen in the 56 ps timeframe and a surface meshing algorithm [184] is able to detect a void volume at 58 ps using a 0.5 nm probe sphere radius. The middle row depicts atoms according to their local longitudinal stress value; tensile stress is represented by a positive value (red) and compressive stresses by negative values (blue). The stress value is the average value of the individual atom and neighboring atoms within a 0.66 nm radius, or a 1.2 nm<sup>3</sup> volume. The bottom row presents atoms according to a temperature evaluated for a local neighborhood, again evaluated spherically in a 1.2 nm<sup>3</sup> volume. The maximum stress occurs at 61 ps, 5 ps after the first void nucleated.

The maximum tensile stress of 19.1 GPa occurs at 61 ps, 5 ps after the first void nucleates at 15.9 GPa. A growing void's ability to relieve stress is proportional to its size.

This relationship is a ramification of the reduced stress required to nucleate dislocations for larger voids [310] in addition to the greater number of dislocation nucleation sites (which is proportional to the surface area of the void) and increased volume that nucleated dislocations can expand into [328]. It is not until sufficient void growth that the stress relaxation rate equals and surpasses the stress rate. Lower strain rates, and thus lower stress rates, require less cumulative damage to relax the structure. The bottom row presents the local temperature, which increases drastically during void growth due to the irreversible visco-plastic work. The effect of increased temperature will be discussed in greater detail later in the manuscript.

The propensity for deformation to occur via twinning or full dislocations depends on the strain rate (as well as grain size and orientation [95,313,329]). At lower strain rates, where dislocations are more favorable than twins, voids nucleate at individual dislocations or at nodes between them. This is visualized in Figure 4-20 for QI tension at a strain rate of  $10^7 \text{ s}^{-1}$ . The system was tracked for porosity and dislocation density during the principal void nucleation event and subsequent void growth. A series of snapshots in time are presented in Figure 4-20 alongside the evolution of void volume and dislocation density.

Our simulation corroborates the findings by Strachan et al. [314] that implicate a critical void volume prior to failure. In our simulation this occurs by the dynamic growth of a single critical void. Furthermore, previous calculations for void growth [310] are based upon dislocations "carrying away" volume from the growing void [64].



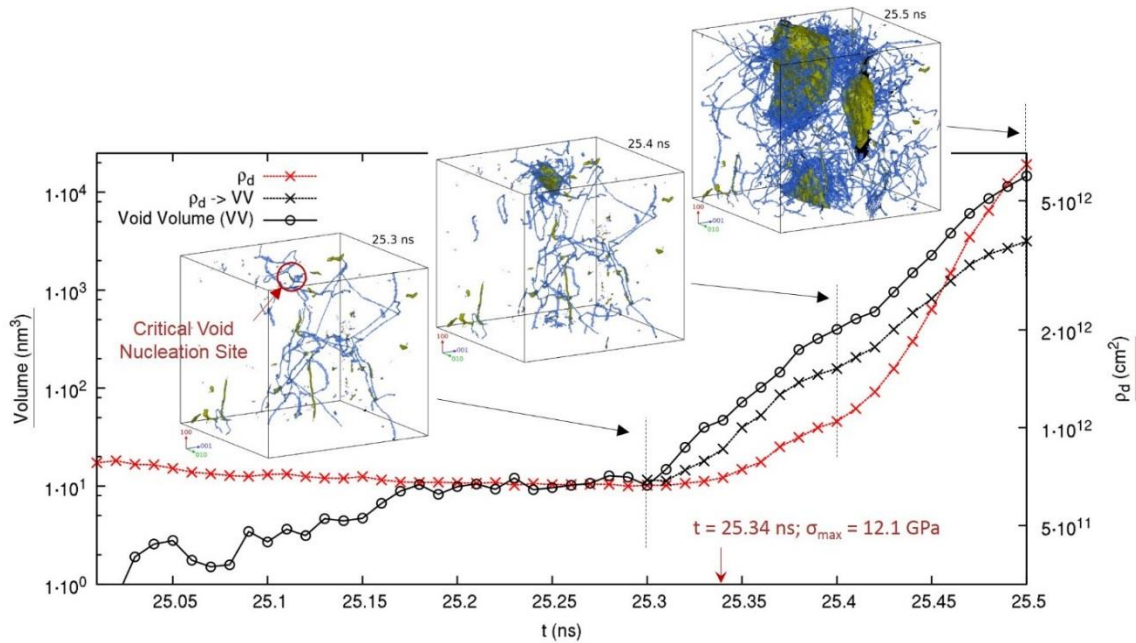


Figure 4-20. Evolution of porosity and dislocation density during the critical void nucleation and growth event for a strain rate of  $107 \text{ s}^{-1}$ . Insets show snapshots in time. The critical void nucleation site is along a dislocation running perpendicular to the loading direction. Analysis is halted at 25.5 ns due to significant interaction of the growing void field across periodic boundaries. Porosity and dislocation line lengths are evaluated using DXA.

The volume transported by a dislocation can be considered, as a first approximation, as the length of the dislocation times a core area. In tension, the dislocation core is larger than at equilibrium (which is approximately the square of the Burgers vector,  $b^2$ ), measuring  $10.7 \text{ \AA}^2$  at 25.3 ns (measured presently using a representative volume mesh [184] of defective atoms belonging to a dislocation core divided by the dislocation length). Figure 4-20 presents a calculation of dislocation density times the system volume (to give dislocation line length) multiplied by the average core area at each step. The analytical calculation begins at the critical void nucleation time, 25.3 ns. This time also corresponds to the minimum dislocation density as a consequence of dislocation annihilation in part due to the Bauschinger effect.

Figure 4-21 shows a magnified snapshot of the previous simulation at 24.5 ns; shear loops (attached to the void) and prismatic loops (detached) are identified. First, shear loops are emitted from the void surface. The edge component of the shear loops evolves, leaving behind the lateral sides, which have screw character. These can cross-slip into different  $\{110\}$  planes which intersect along the same  $[111]$ . Thus a “lasso-action” takes place, which creates, on closing itself, a prismatic loop. This “lasso” action mechanism was first observed in void growth in tantalum [310] and later confirmed in deformation under indentation at relatively high strain rates [270].

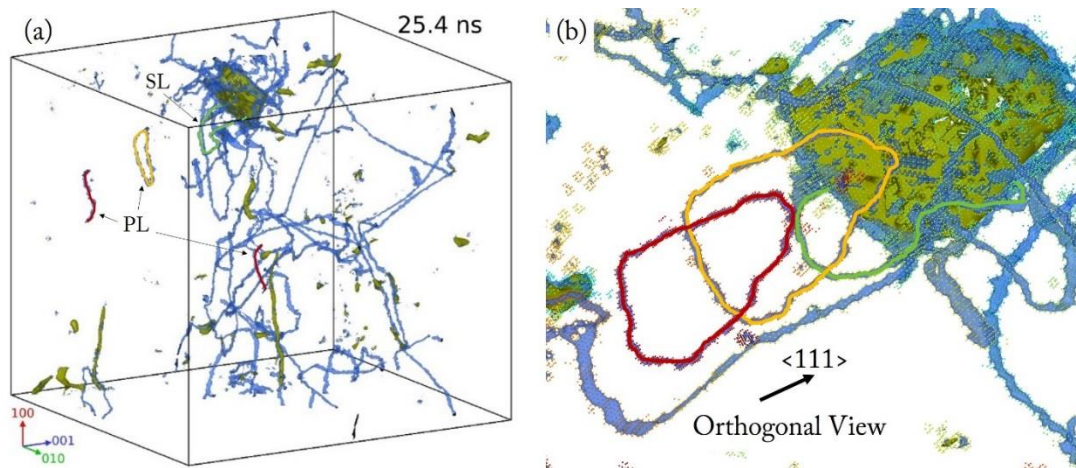


Figure 4-21. (a) Snapshot of dislocation structures at 25.4 ns during QI expansion at a strain rate of  $107 \text{ s}^{-1}$ ; larger version of inset within Fig. 8. (b) Orthogonal projection highlighting shear loops (SL) and prismatic loops (PL) and traveling along the  $\langle 111 \rangle$  direction. This nucleation event has been described previously by Remington et al. [270].

The quasi-isentropic simulations are set up such that the imposed uniaxial strain rate is constant. However, the resulting rates at which the stress components evolve are not constant. The rate of change of hydrostatic pressure with time can be estimated according to the pressure-volume. By taking the first derivative of the U-V curve we obtain a P-V relationship. Where the P-V curve is linear, the stress rate can be directly related to the strain rate, i.e., in the elastic regime. With increasing tensile strain, the rate at which

(negative) pressure increases per strain increment decreases – this is a ramification of the convexity. After void nucleation, the rate of pressure change will decrease due to stress relaxation of the growing voids, as well as the nucleation of additional voids. The size and number of voids will control the rate of plastic relaxation, which is tied to the dislocation density around the growing voids. The plastic relaxation rate will thus be a function of the dislocation generation and dislocation motion. After time, the relaxation rate and the rate of tensile loading will be equivalent; at this point the material has reached its maximum supported tensile stress, i.e., the spall strength. The material then returns to zero stress as voids continue to grow and coalesce. If the stress returns to zero before the coalescence of voids leads to a complete spall surface, the spall is incipient. This is especially the case for short pulse durations. Often the rate of pressure change goes to zero and reverses sign as the material around the voids is recompressed.

One difference between decaying and supported waves is worth further discussion here. For a supported wave the resulting voided volume must be larger to completely relax the stress of a larger volume of stressed material. This is simply because the tensile loading rate will be applied for a greater period of time - relaxation must also continue for a longer duration. A similar logic can be applied to higher strength shocks. Such shocks contain greater kinetic energy (and thus momentum) that must be accounted for. For events where the unloading rate is the same, but the shock strength is different, the material will continue undergoing a tensile driving force that is countered by the relaxation rate. The tensile pulse does not stop when the material begins to undergo spall; instead, a myriad of waves are emitted from growing void surfaces that counteract the loading pulse. The sum of these waves may negate the tension, but the tensile wave still "exists" even though it is masked

by the other waves. From this standpoint, a larger extent of damage can be expected for higher shock strengths or shocks of longer duration, but the spall strength of the material will be equivalent. This has been discussed previously in terms of square vs. triangular waves by Tonks et al. [330] and Koller et al.[331]. Square waves continue to provide a driving momentum to spall “scab”, or separated layer, for a greater duration than unsupported triangular waves. However, the temperature rise at the shock front (and the temperature increase due to visco-plastic deformation) has the ability to alter the spall strength as a result of thermal softening. It is to be expected that stronger shocks or longer shock pulses will cause a greater degree of plasticity and thus a larger decrease in spall strength if the compression wave is reflected and returns to the compressive defect field. One can imagine that for lower strain rates the plastic relaxation rate will be much larger than the respective tensile loading rate, and that the strain between nucleation and the maximum stress will be substantially reduced.

#### 4.1.2.4. Spall of Nano and Crystalline Tantalum

The spall strength of nanocrystalline tantalum ( $d = 21$  nm) as a function of strain rate is also given in Figure 4-14. Results for these simulations are provided in Table 4-3. Unlike single crystals, the nanocrystals demonstrate a single power law relationship over the strain rates of  $10^8$ - $10^{13}$   $s^{-1}$ , suggesting a single dominant mechanism.

Figure 4-22 shows snapshots of quasi-isentropic expansion at strain rates of  $10^8$  -  $10^{10}$   $s^{-1}$ . In contrast to simulations of tensile failure by Tang et al. [158] and Belak [180], and in agreement with Rudd [332], we observe that grain-boundary nucleation of voids occurs in concert with limited dislocation and twin nucleation.

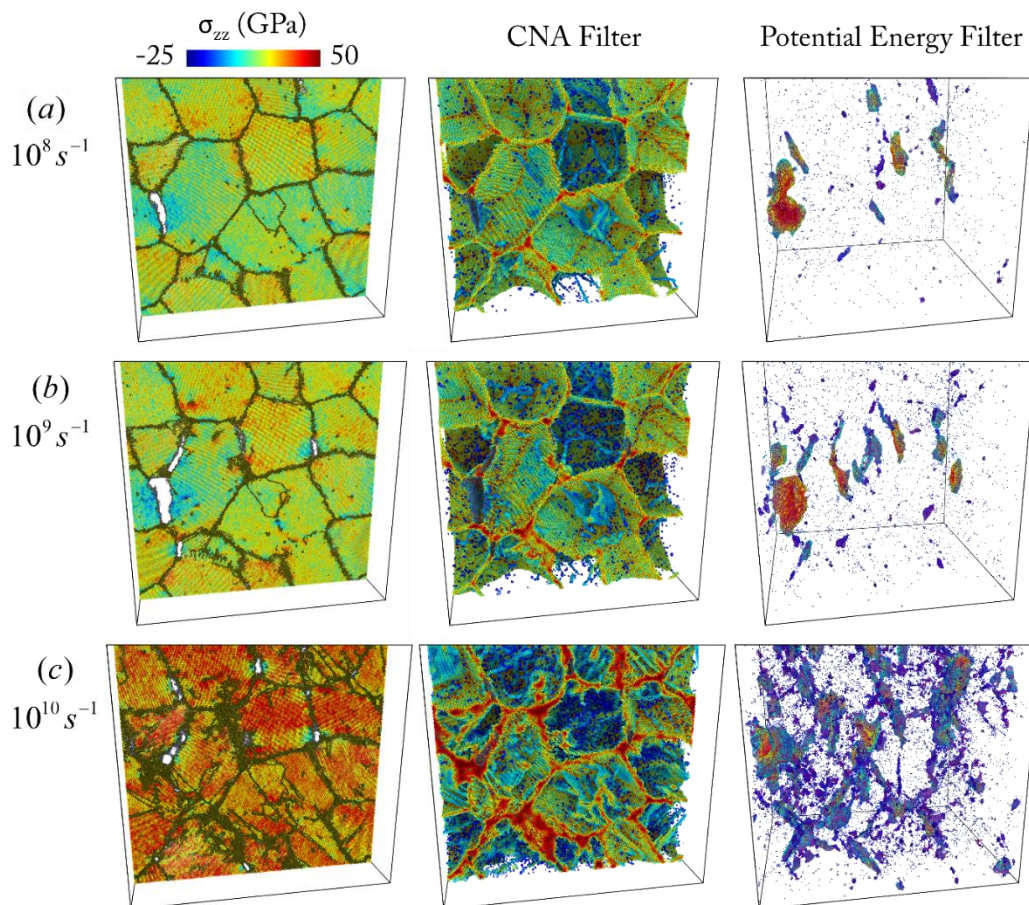


Figure 4-22. Snapshots of quasi-isentropic simulations of nanocrystalline tantalum ( $d=21$  nm) at different strain rates, each shown at the time of maximum tension. Strain rates are (a)  $10^8$  s $^{-1}$ , (b)  $10^9$  s $^{-1}$ , and (c)  $10^{10}$  s $^{-1}$ . The strains at which each frame is displayed are provided in Table 5. In the first column, atoms are colored according to the local longitudinal stress averaged over 500 Å volumes, positive stresses are tensile and negative stresses are compressive. The second column depicts atoms filtered by common neighbor analysis (CNA) using a 3.9 Å cutoff and colored by “defect coordination,” effectively allowing visualization of grain boundaries, dislocations, and twins. The third column shows atoms filtered by a potential energy cutoff of -7.2 eV which enables the visualization of void surfaces. The third column also utilizes a defect coordination coloring scheme where increasing void volume corresponds to blue, turquoise, yellow, orange and green. This method also allows a qualitative analysis of non-spherical voids; a completely spherical void would exhibit the same color along the entirety of its surface.

The first column of Figure 4-22 displays a sliced image that is colored according to longitudinal stresses averaged over  $0.5$  nm $^3$  spherical volumes. The second column depicts atoms filtered by adaptive common neighbor analysis [190] showing only defective atoms, this method determines an optimal cutoff radius automatically for each individual atom.

The atoms are colored by a “defect coordination” allowing for the visualization of grain boundaries, full dislocations, and twin surfaces. The third column uses a potential energy filter (with a cutoff of -7.2 eV) that only shows atoms on the surface of voids with higher average energy than the surrounding crystal, grain boundaries, or crystalline defects. A selective coordination coloring scheme is employed where increasing void volume corresponds to voids of blue, turquoise, yellow, orange and green coloring. Spherical voids would be constant in color; the degree of color change along the void surface is a qualitative measure of void eccentricity.

Figure 4-23 gives a side-by-side comparison between single and nanocrystalline samples, for piston loading to shock pressures of 56.5 GPa and 52 GPa in single crystal and nanocrystal respectively. The corresponding strain rate under release is  $1.65 \times 10^{10} \text{ s}^{-1}$  in the single crystal and  $7.8 \times 10^9 \text{ s}^{-1}$  in the nanocrystal. The top frames give the complete atomic pictures, while the bottom frames show surface meshes of the evolving voids. Within the single crystal, voids appear to nucleate randomly through the spall volume. In the nanocrystalline sample, voids nucleate along the grain boundaries. A qualitative analysis suggests that specific grain boundary misorientations do not play a large role, but that boundary orientation relative to the loading direction is important - boundaries that are perpendicular to the loading direction fail preferentially. A dedicated future study is needed to address the dependence of boundary structure on spall strength. As voids nucleate and grow along the grain boundaries the frequency of coalescence is increased due to their proximity to one another. At strain rates lower than  $10^{11} \text{ s}^{-1}$ , the spall strength of nanocrystalline Ta is below single crystalline Ta. This occurs in part due to the decreased flow stress of the grain boundaries; stress concentrations at grain boundaries that arise due

to compatibility; and the growing fraction of grain-boundary atoms as grain size is decreased into the nanocrystalline regime. At higher strain rates, the orientation of the crystal (or group of crystals in the case of a nanocrystal) will matter to a much greater extent as the orientation will significantly influence de-cohesion.

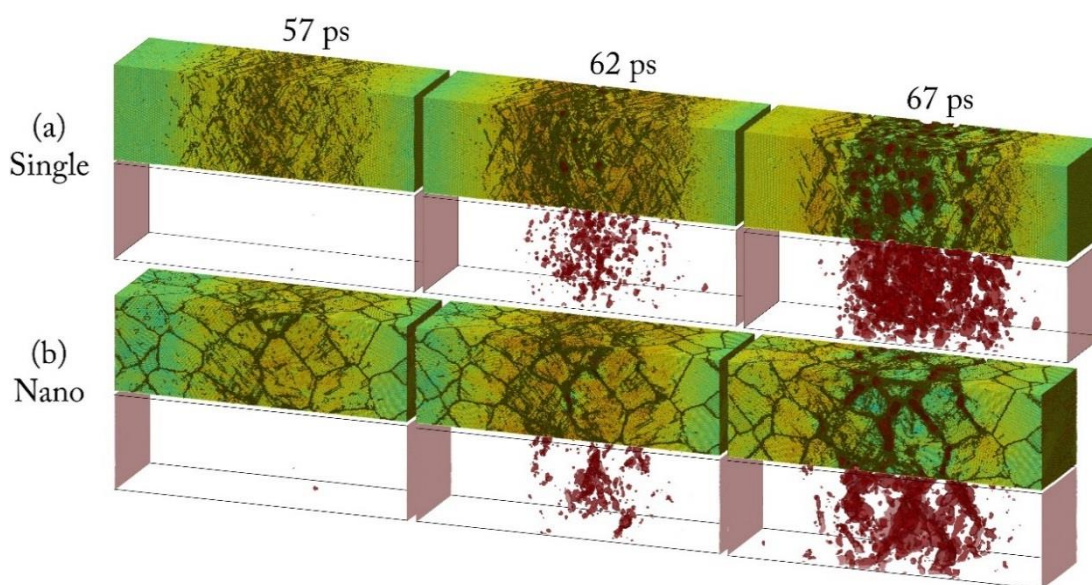


Figure 4-23. Comparison between single and nanocrystalline spall simulations using the piston methodology. Voids nucleate along the grain boundaries in the nanocrystal, typically at grain boundaries that are perpendicular to the loading direction. The particle velocity is 750 m/s corresponding to shock pressures of 56.5 GPa for the [001] shock and 52 GPa for the nanocrystalline shock. The release strain rate is  $1.65 \times 10^{10} \text{ s}^{-1}$  for the [001] shock and  $7.8 \times 10^9 \text{ s}^{-1}$  for the nanocrystalline shock. The lower strain rate is due to increased dispersion of the unsupported shock wave in the nanocrystalline sample.

#### Grain orientation

Taking a step back from the complex nature of nanocrystalline spall, bicrystals were simulated by flyer plate impact. Figure 4-25 shows x-t diagrams of a single crystal and bicrystal colored by number of atoms. Figure 4-26 shows the void structure for the simulation at 40 ps.

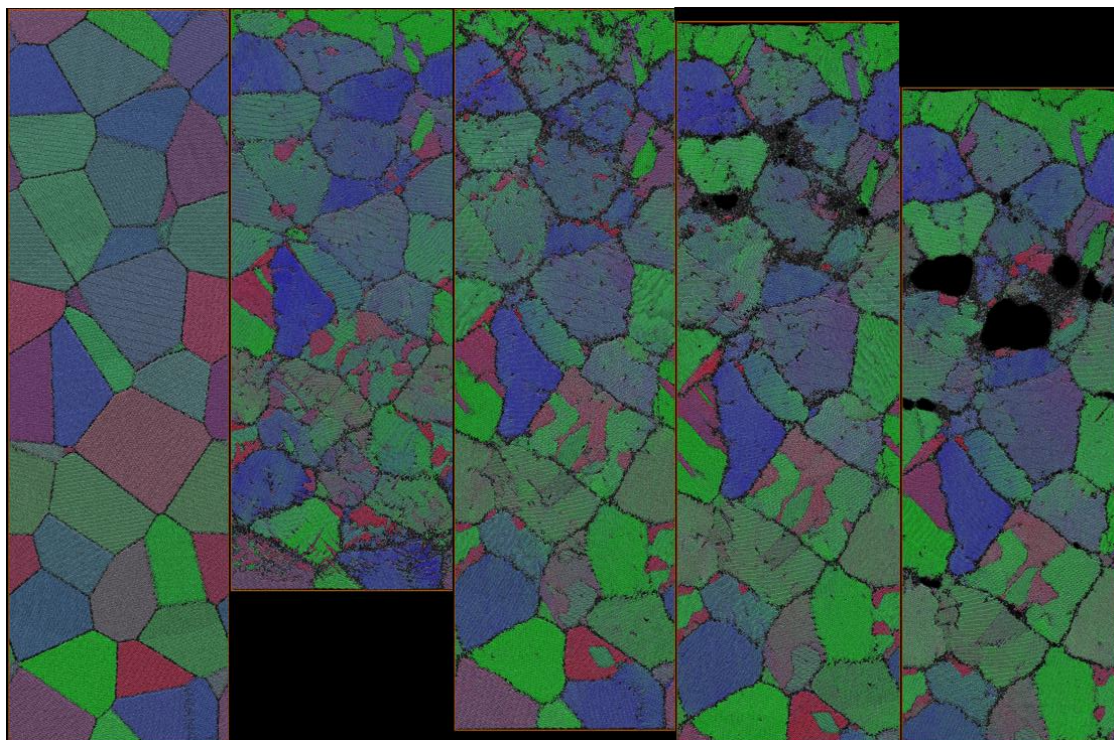


Figure 4-24. Spall process occurring in a 20 nm nanocrystal. Spall voids open at grain boundaries.

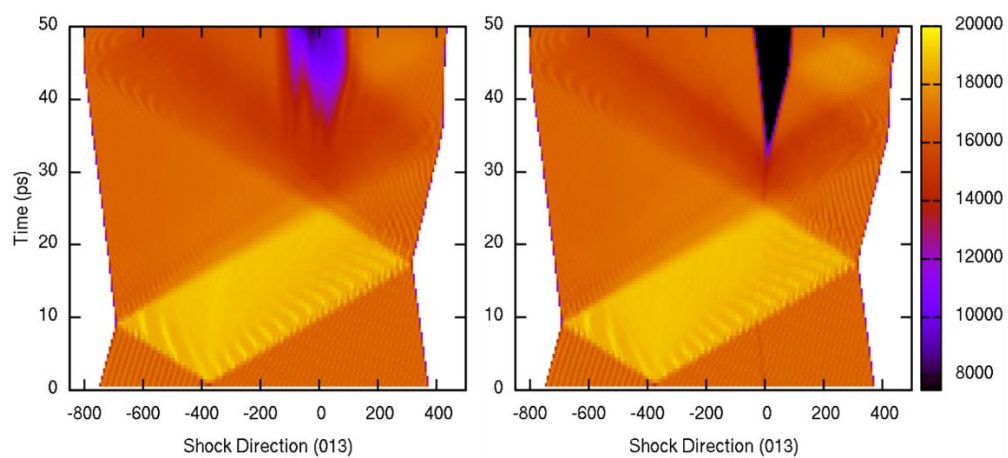


Figure 4-25. x-t diagram colored by atom count per voxel. Left, single crystal. Right,  $\Sigma 5$  bicrystal. Orange represents equilibrium, yellow compression, purple tension, and black complete spall.



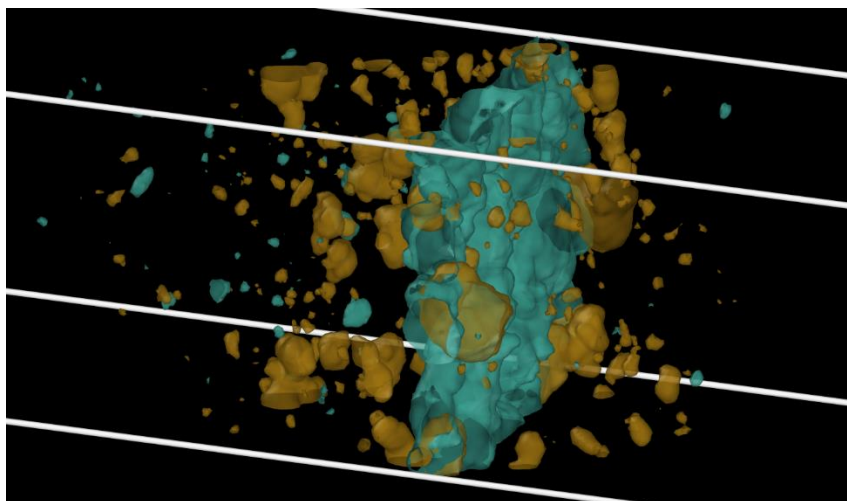


Figure 4-26 Overlay of void structure for single (teal) and  $\Sigma 5$  bicrystal (brown). Notice the extended spall volume for the single crystal.

The clear difference is the extended spall volume for the single crystal. Figure 4-27 show x-t diagrams of a single crystal and bicrystal colored by longitudinal stress. It is clear that the maximum tensile stress (black) does not correlate exactly with the void volume. This is indicative of the time-dependence of the spall and competition between relaxation and high tensile strain-rate.

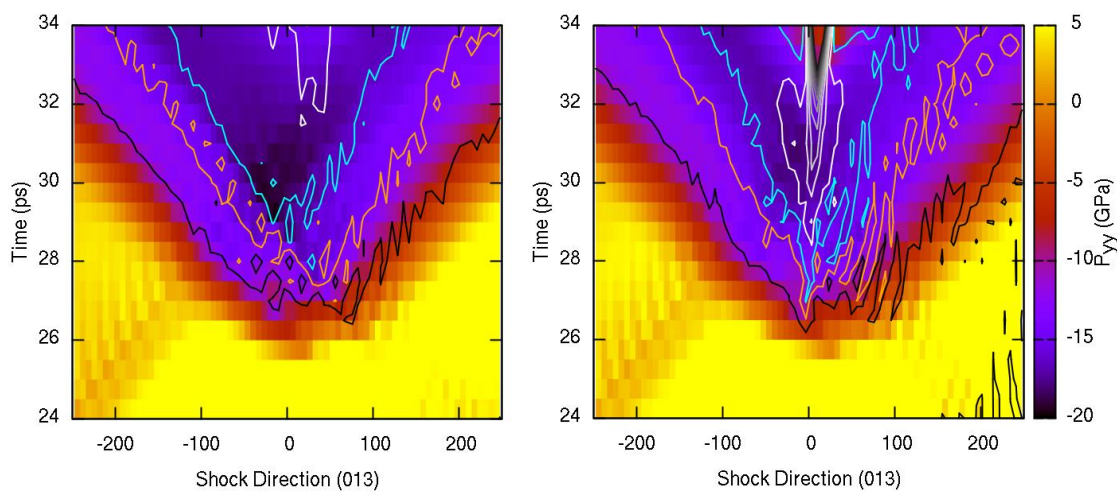


Figure 4-27 x-t diagram colored by longitudinal stress. Left, single crystal. Right,  $\Sigma 5$  bicrystal. Contours represent decreasing density as seen in the previous figure.

The single crystal has a strength of 21.25 GPa while the bicrystal has a strength of 19.5 GPa. It is also significant that a grain boundary is confined precisely to the spall plane and offers a large quantity of void nucleation sites, expediting relaxation by void nucleation, growth, coalescence and thus lowering the ultimate strength of the material.

#### **4.1.2.5. The Role of Temperature during and after Spall Failure**

Temperature plays an important role in the softening of tantalum prior to, and during spall. As mentioned in the Section 3.4.3 and by Ravelo et al. [179], QI simulations maintain constant temperature excluding the work and heat generated by plasticity. Thus, for a fixed strain rate, it is possible to vary the “initial” temperature and maintain a level of control over the eventual temperature at which spall occurs. For these select “temperature-varied” simulations, a procedure consistent with the QI simulations presented above is performed with one modification. We similarly begin QI compression at room temperature using a compressive strain rate of  $10^9 \text{ s}^{-1}$  until 0.17 compressive strain. At this point the temperature of the simulation is scaled to a target temperature and the system is equilibrated for 100 ps using a NPT ensemble (with the anisotropic pressure maintained at its final compressive state) – this differs from the previous simulations which use an NVE ensemble to allow for defect relaxation over 100 ps. Volume expansion and dislocation annealing is expected to occur during this period; the goal is to create specimens of roughly equivalent defect structures of varying temperature in order to isolate the effect of temperature on spall strength. If the simulation began at the specified temperature it would be expected that the resulting compressive state would differ. The method outlined above is designed to vary the temperature while maintaining roughly equivalent pre-compressed physical states.

We select a tensile strain rate of  $10^9 \text{ s}^{-1}$  to evaluate due to its correspondence to laser driven spall experiments [55]. Figure 4-28 presents the measured spall strength as a function of increasing temperature. The temperature is evaluated at the maximum spall strength and thus includes some of the heat generated through the visco-plastic work that is associated with the spall. Spall strength decreases with increasing temperature for both solid and liquid Ta.

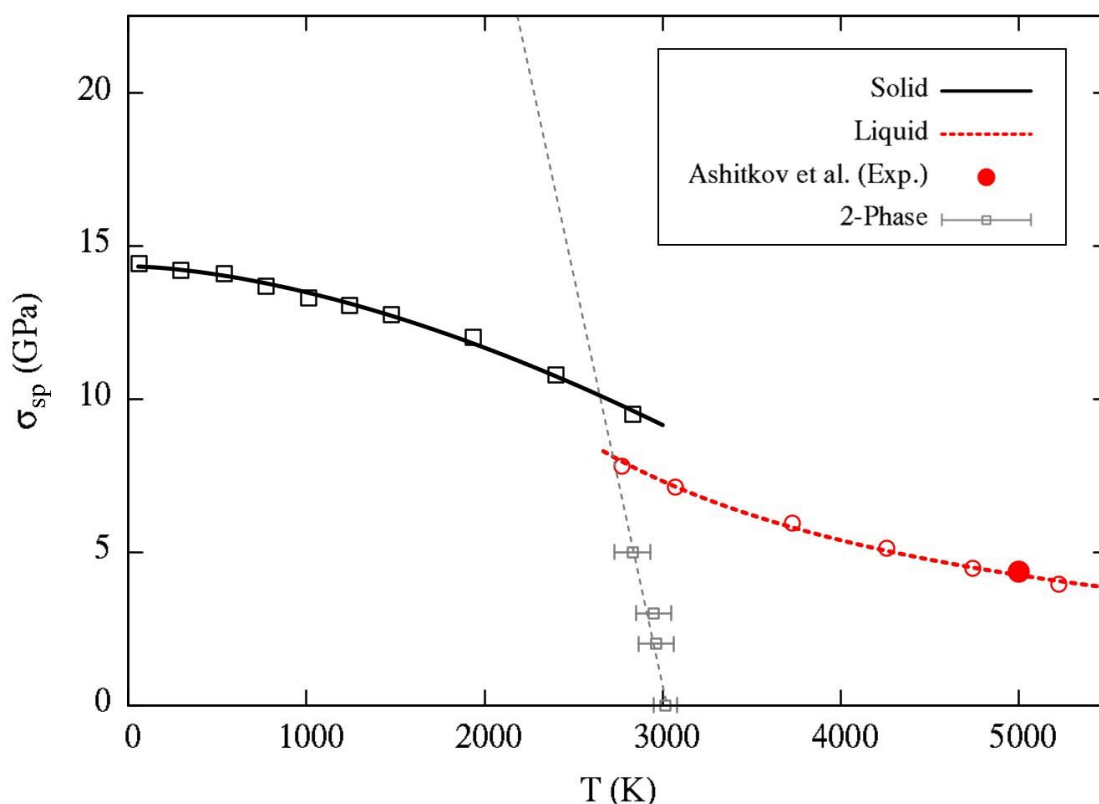


Figure 4-28. Spall strength as a function of temperature at a strain rate of  $10^9 \text{ s}^{-1}$ . The melting temperature as a function of pressure was determined from 2 phase simulations (full details can be found in the supplemental material). Ashitkov et al. [55] provides an experimental measurement (solid red circle) for the spall strength (cavitation strength) of liquid tantalum as melted under laser irradiation at an estimated strain rate of  $1.5 \times 10^9 \text{ s}^{-1}$  and a temperature of  $\sim 5000 \text{ K}$ .

We first focus on the spall strength of liquid Ta for simplicity. The cavitation strength of liquids has particular relevance to laser-driven systems where large

temperatures are generated through laser-matter interactions. They are also relevant to strong shock conditions where melting may occur under compression or during release. We identify a dependence of spall strength on  $\sim 1/T$ , agreeing with previous simulations of spall in liquid Cu [333] and other metals [334]. The exact relationship for cavitation strength identified is

$$\sigma_{cav}^{liq} \Big|_{10^9 \text{ s}^{-1}} = A_{liq} / T^{1.064} \quad (79)$$

where  $A_{liq}=36628 \text{ GPa}\cdot\text{K}$ . Ashitkov et al. [55] provide an experimental measurement of the spall strength (cavitation strength) of liquid tantalum as melted under laser irradiation, at an estimated strain rate of  $1.5 \times 10^9 \text{ s}^{-1}$  and a temperature of  $\sim 5000 \text{ K}$ . As seen in Figure 4-28 (solid red circle), this single data point for molten Ta agrees well with the present simulations.

There exists a discontinuous transition between the solid and liquid response; this indicates that plasticity continues to play an important role in failure up until the point of melting. In the solid regime, the decrease of the spall strength with temperature can be described with a power law relationship:

$$\sigma_{sp}^s \Big|_{10^9 \text{ s}^{-1}} = \sigma_0^s - A_s T^{1.646} \quad (80)$$

Here, the intrinsic spall strength,  $\sigma_0^s$ , at a reference strain rate of  $10^9 \text{ s}^{-1}$  and  $0 \text{ K}$  is equal to  $14.33 \text{ GPa}$ . The constant in front of the inverse temperature dependence,  $A_s = 9.8 \times 10^{-6} \text{ GPa/K}$ . A similar relationship form was observed for copper [333]. The origin of the equation is akin to the Simon equation which describes the temperature at which a material melts at a given pressure. In general it describes the softening of a material by a power law by making several thermodynamic assumptions [335]. Five ps after nucleation,

the local temperature around voids is significantly higher, indicative of a large degree of plastic work as shown in Figure 4-29.

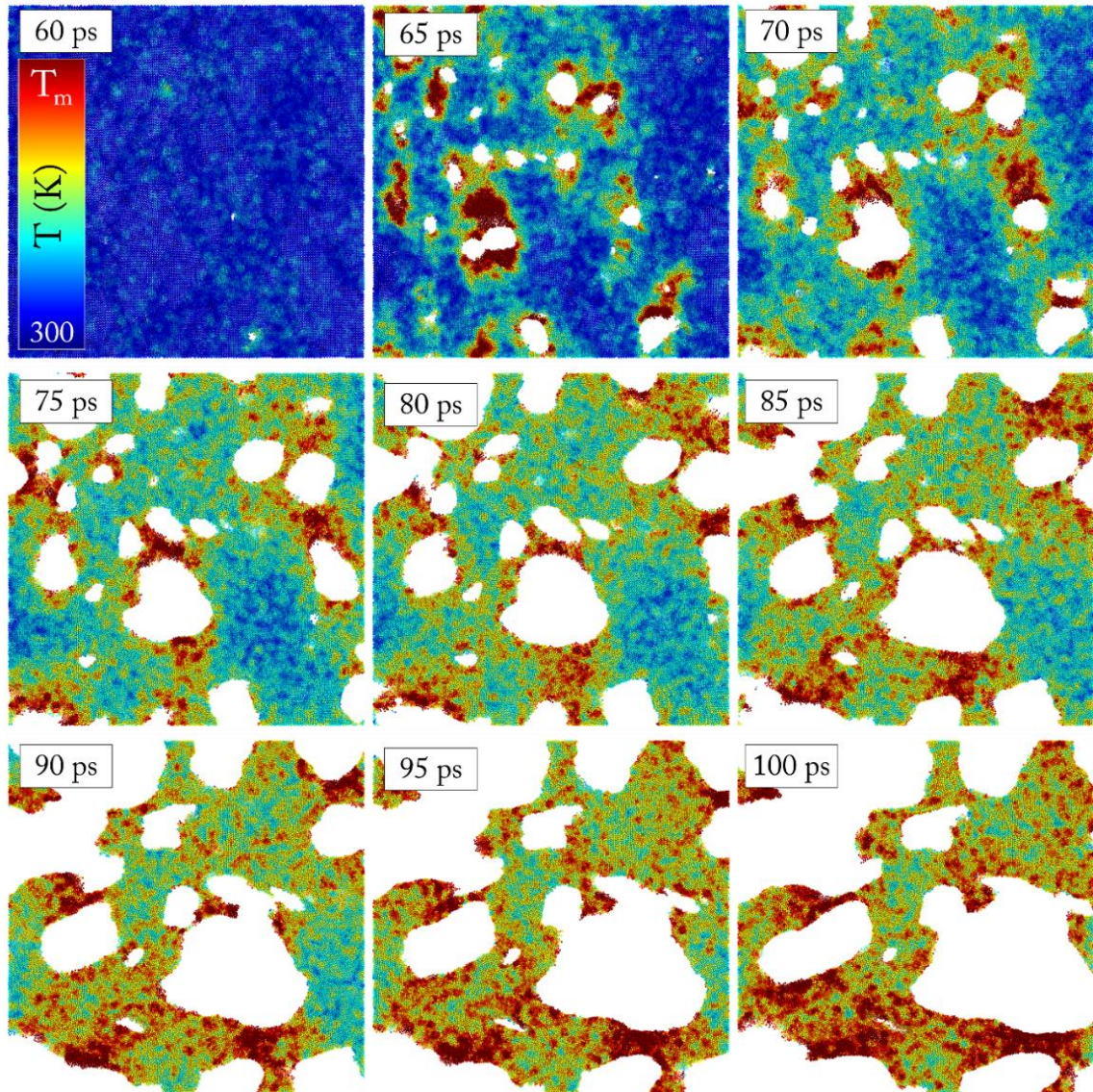


Figure 4-29. Spall temperature evolution of piston-driven simulation from 60 to 100 ps. After initial void nucleation and growth, coalescence is largely affected by regions of high temperature, some of which approach and exceed the melting temperature of tantalum.  $T_m$  is defined as the equilibrium melting temperature of 3033 K.

This is not unexpected as it has been shown previously that voids grow by dislocation emission and that the rate voids must grow at extreme strain rates will require

a large dislocation density [196,310,312] (also refer to Figure 4-20). In the spalled region the average temperature is often greater than 1500 K, or roughly half of the ambient melting temperature.

Figure 4-29 shows snapshots in time of a spalled system over a 40 ps timespan, demonstrating the localization and increase of temperature during void growth and the persistence of high temperature during coalescence and failure that results in long, ductile, and molten ligaments connecting the material together. Such ductile material linkages have been seen in other studies [336,337]. The high melting point of tantalum aids in its sustained ability to resist failure.

#### 4.1.2.6. Theoretical Predictions of Tensile Strength

The theoretical maximum cohesive stress can be investigated through an analysis of the material's equation of state [80], specifically the cold-pressure curve [46]. At their core, interatomic potentials provide the energy of an atom,  $U$ , with respect to its neighbors' positions,  $r_{ij}$ . The hydrostatic cold pressure is related to the volume an atom occupies,  $V_i$ , by  $P=dU/dV$ . A minimum value of pressure, corresponding to a maximum "negative" pressure, can be obtained by finding the critical zero value of the derivative of pressure with respect to volume:  $0=dP/dV$ . This process will yield a critical volume that can be input into the expression for pressure to yield a measure of the theoretical cohesive stress. Grady [46] used a simplified volumetric Morse potential in order to obtain an analytical solution:

$$P = \left( \frac{B_0 U_{coh}}{8v_0} \right)^{1/2}. \quad (81)$$

Using values from Rose et al. [80] ( $B_0=194.2$  GPa,  $U_{coh}=8.089$  eV, and  $v_0=0.202$  nm<sup>3</sup>), equation 81 predicts an ultimate tensile strength for tantalum of 39.4 GPa, The

procedure above can be completed for interatomic potentials (“molecular dynamics’ equations of state) and density functional theory calculations in order to provide more accurate predictions of the theoretical strength. This is shown in Figure 4-30, which compares the Ta1 EAM potential utilized here with the closely related Ta2 potential [95], an EOS derived by Rose et al. [80], a fit of a Morse potential in radial form ( $U = D_0[e^{-2\alpha(r-r_0)} - 2e^{-\alpha(r-r_0)}]$ ), and density functional theory (DFT) calculations by Ravelo et al. [95].

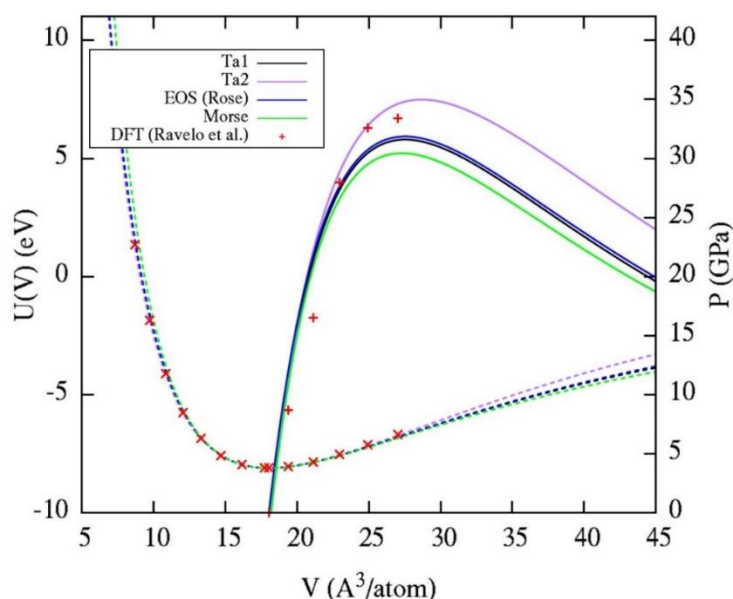


Figure 4-30. Simulated cold curves for tantalum. Two tantalum EAM potentials (Ta1 and Ta2 from Ravelo et al. [95]) are compared against an equation of state (EOS) from Rose et al.[80], a Morse potential, and density functional theory (DFT) calculations of Ravelo et al.[95]. Morse parameters [338,339] and parameters derived presently ( $D_0 = 0.76093$ ,  $\alpha=1.14113$ ,  $x_0=3.34342$  producing  $a_0=3.304$  Å,  $E_{\text{coh}}=8.1$  eV,  $B = 194.6$  GPa,  $C_{11}=209.9$  GPa,  $C_{12}= C_{44}=209.9$  GPa, and  $C_{11}/C_{12}=1.105$ ).

A comparison of other potentials is given in Figure 4-31. The prediction for the radial Morse potential is 30.5 GPa, Ta1 is 31.6 GPa and for DFT is 33.4 GPa, which compare remarkably well with 31-34 GPa strengths measured using NEMD simulations (Tables 4-2 and 4-3, Figure 4-12 and Figure 4-14). The fact that the radial Morse potential

has improved agreement as compared to the estimate stemming from the volumetric Morse form is due to differences in the coefficient “8”. Based on the present study, a coefficient of 13.4 inside the radical of Equation 81 provides a better estimate of the ultimate tensile strength of tantalum.

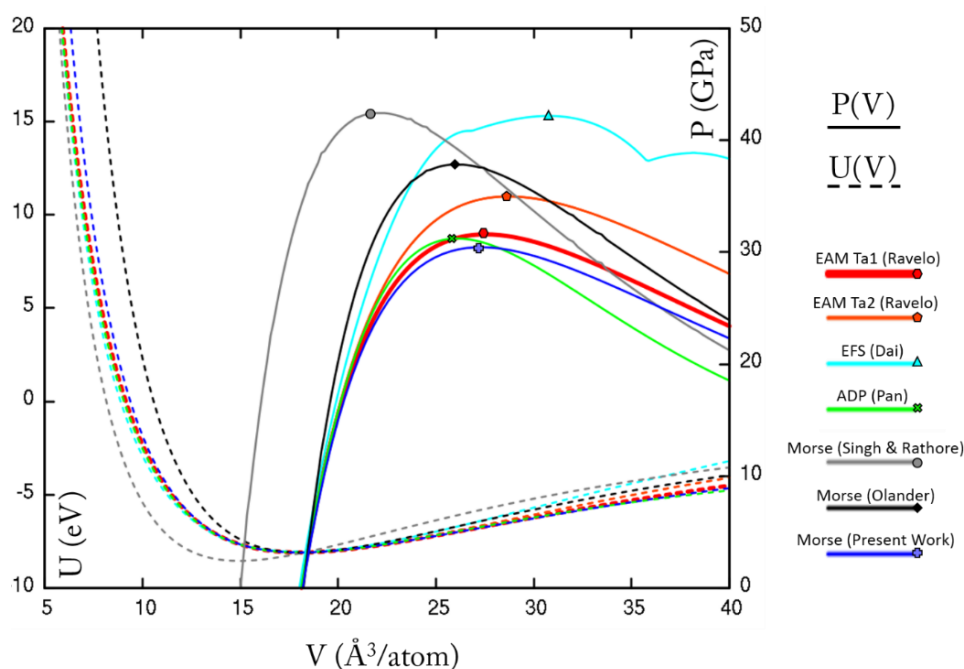


Figure 4-31. Simulated cold curves for varying tantalum potentials: EAM (Ta1 and Ta2), Ravelo et al. [340]; Extended Finnis-Sinclair (EFS), Dai et al.[341]; Angular-dependent interatomic potential (ADP), Pan et al.[342]; Morse parameters[338,339] and parameters derived presently ( $D_0 = 0.76093$ ,  $\alpha=1.14113$ ,  $x_0=3.34342$  producing  $a_0=3.304$  Å,  $E_{\text{coh}}=8.1$  eV,  $B = 194.6$  GPa,  $C_{11}=209.9$  GPa,  $C_{12}=C_{44}=209.9$  GPa, and  $C_{11}/C_{12}=1.105$ ).

### 4.1.3. Phase Transformation

Tantalum is normally studied due to the natural suppression of phase transformation. Its bcc phase is stable over a long range of pressures and temperatures. Yet phase stability is typically evaluated for purely hydrostatic environments and laser-shock conditions are characterized as uniaxial strain states containing large deviatoric



components. Some reports place a phase transition for polycrystals or alloys between 35 and 40 GPa [73,343]. Molecular dynamics simulations of shocked  $\langle 110 \rangle$  tantalum single crystals reveal a bcc-hexagonal phase transformation above a threshold pressure of 75 GPa and corresponding shear stress of 13 GPa. Simulations used a recently developed EAM potential for Ta [95]. Interestingly, the potential was developed to extend transferability to high pressure with no solid-solid phase transitions, explicitly showing that the bcc-hcp enthalpy barrier is negative up to 460 GPa [340] for an applied hydrostatic pressure. Other work using this potential has not revealed such a phase change even along preferential directions [196,313,344]. This is consistent with DFT simulations, which show no free-energy crossings as hydrostatic pressure is increased [345,346].

A significant volume fraction of hexagonal clusters immediately following the shock front can be seen in Figure 4-32. The clusters commonly nucleate near twin boundaries and appear to have high prevalence at twin-twin intersections. They vary in size from 10 atoms to 500 atoms, reaching a few nanometers in diameter. An example of a large cluster can be seen in Figure 4-32 showing approximate atomic radius packing and hexagonal bonding respectively. The identification of the hexagonal structure was enabled by adaptive common neighbor analysis [190], a methodology suited to distinguish components of multi-phase systems through an iteratively defined cutoff parameter. Figure 4-32 illustrates an orientation imaging map of the shock. The original crystal orientation,  $\langle 110 \rangle$ , is colored green and twins are colored red, near  $\langle 100 \rangle$  orientations. The shock front contains a higher number of twins and a greater volume of the hexagonal phase as compared to the material further behind the shock front. It can be speculated that

detwinning and shock induced dislocations might have a significant role in the stability and remaining volume fraction of the hexagonal phase.

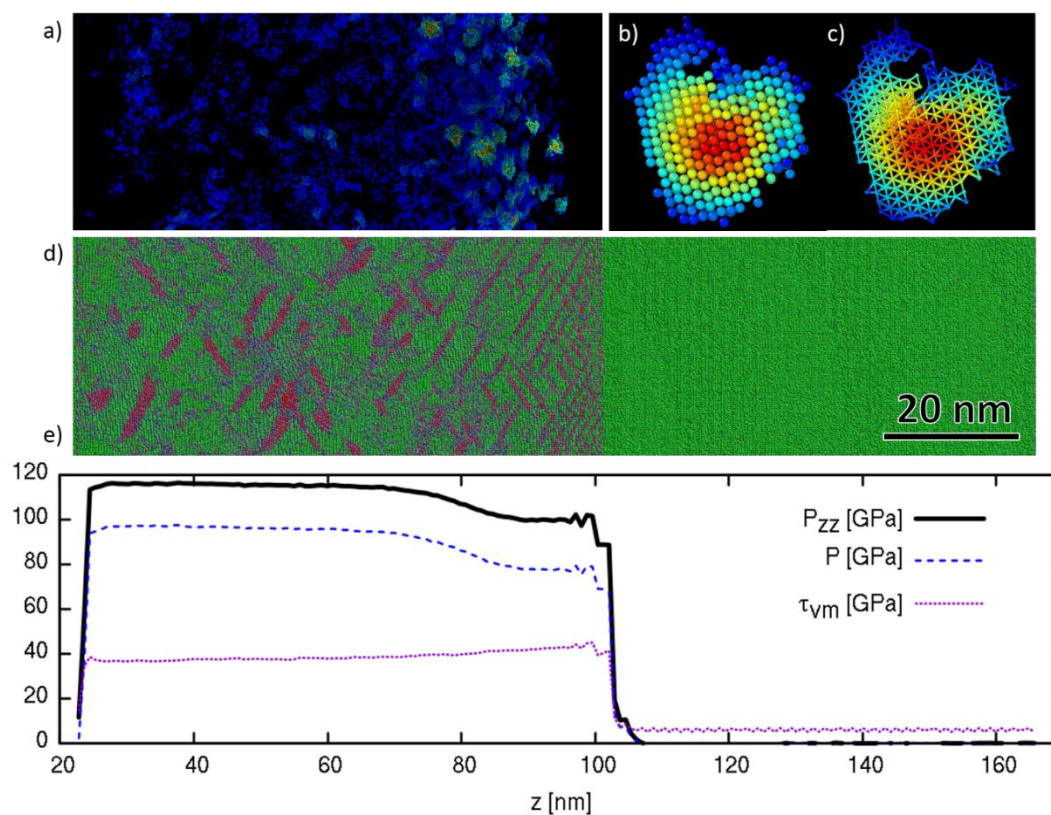


Figure 4-32. Molecular dynamics simulation of shocked  $\langle 110 \rangle$  tantalum crystal at a particle velocity of 1.1 km/s (shock pressure  $\sim 120$  GPa). (a) Hexagonal phase as filtered by adaptive common neighbor analysis [32] and colored by neighbor count. Close-up images of hexagonal clusters consisting of nearly 500 atoms showing (b) packing and (c) bonding (d) Orientation imaging map where green corresponds to  $\langle 110 \rangle$  direction and red to the  $\langle 100 \rangle$  direction. (e) Longitudinal, hydrostatic and von Mises stress profiles.

We also explore the possibility of phase transitions during tensile release. For Ta1, fcc and hcp become more stable under tensions above 21 GPa, 16% expansion. For Ta2, bcc becomes unstable under tension in favor of A15 structure for tensile pressures above 18 GPa corresponding to tensile strains (volumetric) of 12%.

The following tables show predicted phase changes under tension.

Table 4-4. Phase changes under tension for Ta1 potential.

Phase Change	Pressure	Strain
bcc -> A15	-25	0.22
bcc -> fcc	-21	0.16
bcc -> hcp	-21	0.16

Table 4-5. Phase changes under tension for Ta2 potential.

Phase Change	Pressure	Strain
bcc -> A15	-17.8	0.12
bcc -> fcc	-25	0.2
bcc -> hcp	-25	0.2

These values are taken by evaluating the relative enthalpies of each phase as compared to the bcc structure. The energy and enthalpy curves for Ta1 are shown below in Figure 4-33 and Figure 4-34.

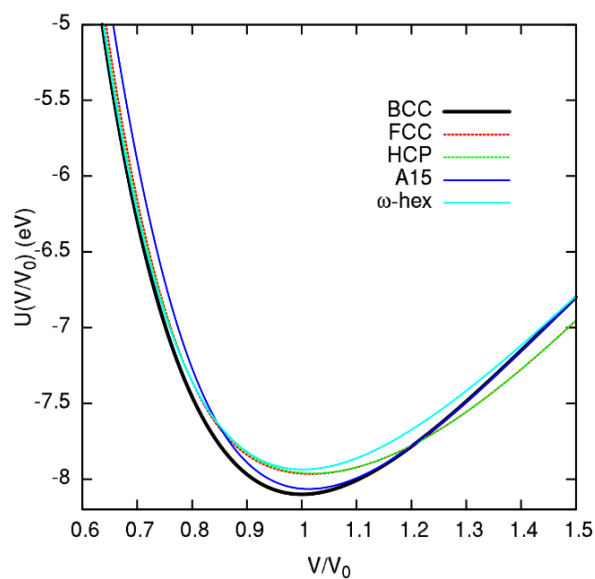


Figure 4-33. Internal energy (U) vs normalized volume curve for Ta1.

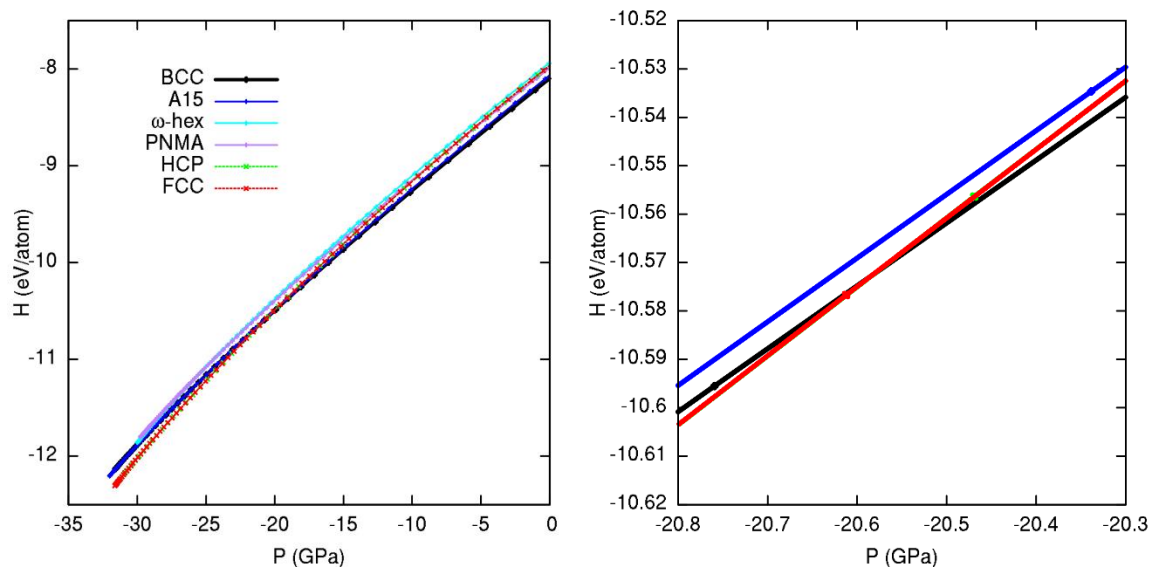


Figure 4-34. Enthalpy as a function of tensile pressure for Ta1.

During isentropic release of tantalum following shock compression, it is possible to observe quasi-stability of the fcc phase, which contains hcp stacking faults. Figure 4-35 gives a snapshot in time at 14.5% tensile strain. Voids are seen to form at twin boundaries, and may also form at fcc/twin and fcc/bcc interfaces. Upon relaxation of the stress by void growth, the fcc phase disappears. Limited experimental evidence exists for A15 and fcc tantalum phases, which were observed in thin films and large local strains generated by quasi-static tension [325].

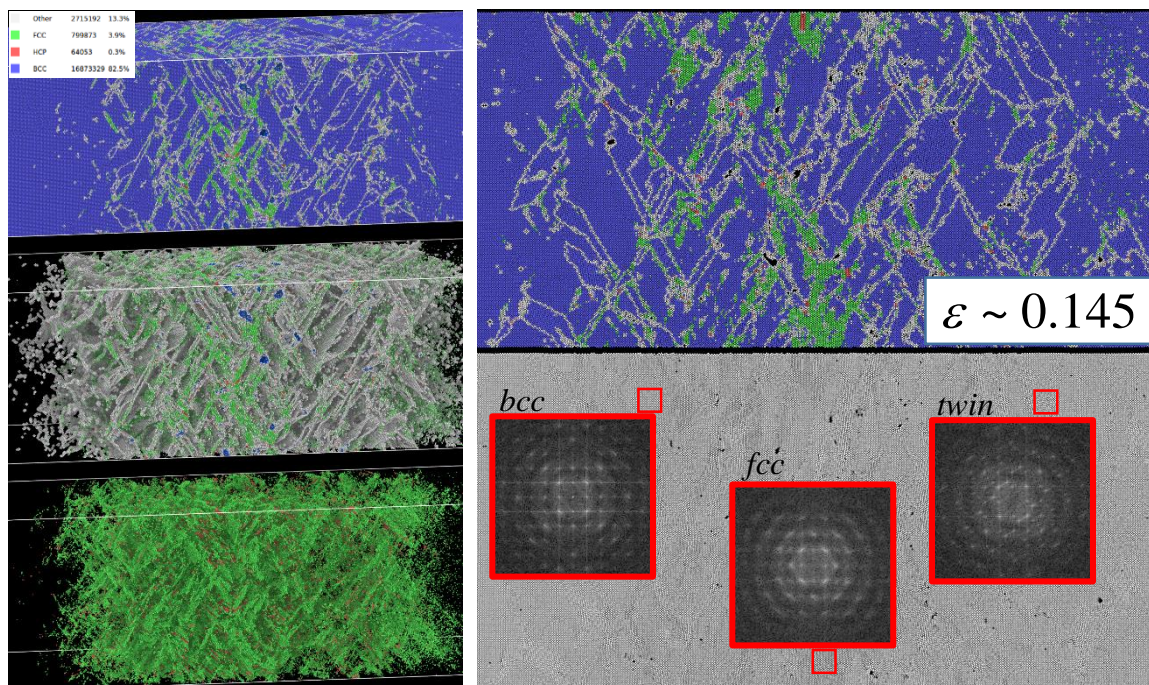


Figure 4-35. Limited stability of fcc phase during isentropic expansion following shock compression. Renders of the defective atoms (white) and fcc/hcp atoms (green/red) are shown compared to bcc atoms (blue). Selected diffraction patterns are generated along the [010] direction for the respective features.

## 4.2. Silicon

Silicon is one of the most studied elemental materials; there are a large variety of semi-empirical potentials and parameterizations fit for many different environments and desired properties. Supporting and/or contrasting simulations have fueled debate for shock responses ranging from phase changes, amorphization, twinning, and full dislocation activity [34,225,227,228,246,347–350]. However, none of the interatomic potentials developed and explored in the literature were fit with elevated pressure, nor substantial shear stresses, in mind. Individual atomic potentials succeed in reproducing thermal properties and melting temperatures [216,217,351], dislocation properties [218,219], phase transformations [220,249,250,352,353], defects and disordered phases [221–223], and brittle behavior [353–355], but no single potential currently has the capability or

transferability to reproduce all the properties of interest over a wide variety of environments - a challenge ubiquitous in computational materials science [356]. A comparison of a few potentials can be found in previous reports [216,224]. It must be emphasized that none of these potentials have been developed specifically for high stress conditions, and tremendous care must be taken to accurately simulate the uniaxial strain state achieved during shock loading of silicon.

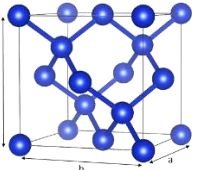
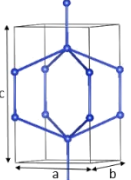
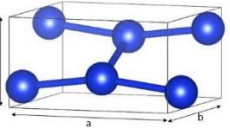
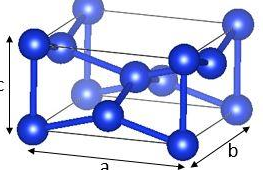
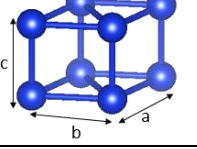
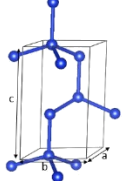
Plasticity and atomic structural transformations induced by high pressure shock compression in monocrystalline silicon has remained a prevalent research focus for a considerable period of time [34,252,256,257,357–364]. There are a number of shock experiments performed in silicon, including impact driven [257,362,365–367] and laser shock studies [252,357,359,360,363,368,369] as well as molecular dynamics shock simulations [225,227,228,347,348,370–372]. The quasi-brittle and quasi-ductile response of silicon under shock conditions continues to be especially challenging to model; capturing the brittle cracking that has been observed at the impact and rear surfaces [76,252,358] as well as the more ductile response of the confined material within remains an outstanding goal. Furthermore, as Smith et al. [252] discusses, with increased temperature or strain rate it is possible to form structures with different coordination systems, undergo amorphization or melting, as well as induce ductile dislocations.

Here we introduce several prominent molecular dynamics (MD) studies and their results. Oleynik et al. carried out large-scale shock simulations and showed that shocks could heal defects in bulk single crystal silicon [225]. In another study they showed that the Stillinger-Weber potential provided stress-strain curves for the diamond-cubic structure that compared well with ab-initio results when the strain is below 15-20%, translating to

shear stresses below 7.5 GPa [226] and a subsequent investigation reproduced two-wave shocks consisting of a plastic wave preceded by an elastic precursor when using an environmentally dependent interatomic potential [227]. Work by Mogni et al. [228] used a Tersoff-type potential (developed by Erhart and Albe [251]) compressed along the  $\langle 001 \rangle$  axis and identified an Imma phase transition, noting consistency with shear stress relief provided by direct shock-induced phase transition without intermediate plastic deformation. MOD, a more recent Tersoff-family bond order potential developed by Kumagai et al. [217], was developed to reproduce both elastic constants and melting point. The MOD potential has been shown to describe reasonably well crystalline as well as disordered phases such as liquid and solid amorphous structure, the kinetics of the crystalline to liquid transition [230], decrease of melting temperature with pressure between -1 and 3 GPa [231], and has been successfully applied to the shock regime to predict amorphization under shock compression [373].

Of foremost attention is the far from equilibrium phase space of silicon with respect to high pressures and temperatures as anticipated under shock compression. The need to characterize this space is emphasized by the variety of phase changes (Table 4-6) and variety of potentials (reference Supplemental Material) to draw from. The Stillinger-Weber potential was recently surveyed and the stability of a simple cubic allotrope, sc16, was shown to co-exist with the  $\beta$ -Sn structure between pressures of 9.54 and 13.67 GPa [232]. Si-III, or bc8, was shown to be energetically unfavorable compared to sc16 for all temperatures and pressures.

Table 4-6. Ambient and High Pressure ( $P < 25$  GPa) Polymorphs of Silicon. Data from multiple sources [239,369,374,375].

Author (Year)	Structure/Name	Space Group	Unit Cell
Tobbens et al. (2000)	Diamond cubic (dc) ( <i>Si-I</i> )	Fd-3m	$a=b=c=5.43053$ 
Boyer et al. (1991) Kaxiras et al. (1994) Kim et al. (2008) Gerbig et al. (2012) Zhang et al. (2016)	Body-centered tetragonal 5 (bct5)	I4/mmm	$a=6.686$ $b=6.686$ $c=11.264$ 
Mogni et al. (2014)	Imma	Imma	$a=4.373$ $b=4.502$ $c=2.550$ 
Smith et al. (2013) Cheng et al. (2001) Gaal-Nagy et al. (2006) Hennig et al. (2010) Durandurdu et al. (2010) Gerbig et al. (2012)	$\beta$ -Sn ( <i>Si-II</i> )	I41/amdS	$a=4.686$ $b=4.686$ $c=2.585$ 
Turneure et al. (2016)	Simple hexagonal (sh) ( <i>Si-IV</i> )	P6/mmm	$a=2.527$ $b=2.527$ $c=2.373$ 
Crain et al. (1994) Nemeth et al. (2014) Gogotsi et al. (2003)	Hexagonal diamond (hd)	P63mmc	$a=5.392$ $b=5.392$ $c=5.392$ 

The negative Clausius-Clapeyron melting temperature with increasing pressure is again demonstrated and a triple point (quadruple point including hexagonal diamond



structure of thermodynamically equivalence to dc) between dc, liquid, and sc16 at 1302 K and 7.28 GPa.

Three prominent experimental works identify additional phases. *In-situ* quasi-static investigations that indicate that amorphization results from an intermediate hexagonal diamond (hd) phase. State of the art experiments by Turneure et al. [363] completed at the Dynamic Compression Sector (located at the Advanced Photon Source) were able to identify a transition of dc silicon to a simple hexagonal (sh) structure at 19 GPa. Shock recovery efforts have identified bulk amorphization and directional amorphization in concert with dislocation activity, but no phase changes were reported in the recovered samples [34,357,358].

The plethora of available phase changes, deformation modes, and the interplay between one another strongly compels a comparative study of the predominant silicon potentials under shock conditions in order to evaluate our current capability to model silicon in extreme environments.

#### **4.2.1. Hugoniot Elastic-Plastic Limit**

Smith et al. [177] shocked silicon samples of different thicknesses in order to measure the elastic limit for silicon as a function of strain rate for strain rates reaching  $4 \cdot 10^8 \text{ s}^{-1}$ . For [001]-orientated single crystalline silicon about 1 micron in thickness, the Hugoniot Elastic Limit (HEL) was measured to be  $19 \pm 3 \text{ GPa}$  at  $10^8 \text{ s}^{-1}$ . The Gilman model including dislocation production was employed to explain the plastic relaxation rates and they fit their data using  $\text{HEL} = 0.32 \cdot \dot{\epsilon}^{0.21 \pm 0.02}$ . Thus, for  $\dot{\epsilon} = 5 \cdot 10^8 \text{ s}^{-1}$ , as achieved during typical atomistic shock simulations, the HEL is projected to lie between the wide range of 22.3 and 54 GPa. This may explain results by Kalantar and co-workers [22,360],

where no plastic relaxation was observed by dynamic diffraction taken of Si shocked to pressures somewhat lower than current estimates for the elastic limit.

The initiation of plasticity is due to emission of partial dislocations bounding stacking faults, on  $\{111\}$  and  $\{110\}$  planes (Figure 4-36).  $\{111\}$  defect geometry was believed to be observed in the (001) 2D VISAR of shock loaded Si by Smith et al.[252] as evidenced by 4-fold symmetry. This symmetry can also be observed in other  $\{001\}$  family planes and can be visualized as diamonds in the 4 ps snapshot of Figure 2. However, the  $\{110\}$  and  $\{111\}$  slip systems share a common  $[001]$  projection and cannot be distinguished based on 2D  $[001]$  projections alone. Partial dislocations of both slip systems can later react and lead to full dislocations.

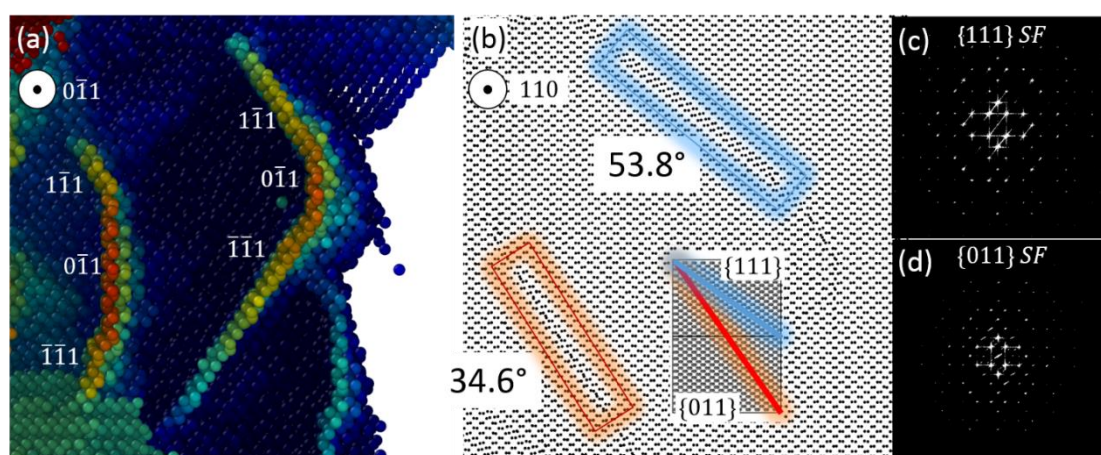


Figure 4-36. Snapshots from a shock simulation showing  $\{111\}$  and  $\{110\}$  stacking faults. (a) depth perspective showing interaction between the mutual stacking fault planes. (b) thin section illustrating the resultant angles of the  $\{111\}$  and  $\{110\}$  stacking fault planes with the  $\langle 110 \rangle$  direction. (c) simulated diffraction patterns of the faulted areas.

Something similar to this has been observed in the deformation of Si nanospheres compressed by a flat indenter, where partial dislocations were emitted from the curved surface of 10 nm and 5.16 nm radii spheres at normal stresses of 23.5 GPa and 21.3 GPa; further compression ultimately lead to the formation of a full dislocation [376]. We observe

that plasticity leads to relaxation perpendicular to the shock direction of the strain in  $\sim 10$  ps with longer simulations potentially leading to further relaxation. At large elastic strains we observe a preferential nucleation of  $\{110\}$  stacking faults opposed to  $\{111\}$  SFs. Subsequent SFs tend towards  $\{111\}$  slip as the strain relaxes. SFs were identified as intrinsic stacking faults consisting of a two atomic layers. The typical diamond stacking sequence is  $AA'BB'CC'$  where each letter denotes a set of positions on the  $\{111\}$  plane and prime indicates a plane separated by a covalent bond length in tetragonal arrangement. The diamond cubic structure is referred to in this form by two interpenetrated fcc unit cells with atoms at  $(0,0,0)$  and  $(\frac{a_0}{4}, \frac{a_0}{4}, \frac{a_0}{4})$ . The primary Burgers vector for silicon is  $b = \frac{a_0}{2} \langle 1,1,0 \rangle$  and during intermediate slip atoms on the untraditional  $\{110\}$  slip plane may move by  $\frac{b}{2} = \frac{a_0}{4} \langle 1,1,0 \rangle$  [229]. Recent simulations of plasticity in Si nanospheres employ the SW potential and show a  $\{110\}$  slip response in addition to the expected  $\{111\}$  shuffle/glide-set planes [229].

Density functional theory has been performed by others to evaluate the stacking fault energy and indicate a tendency to slip along  $\{110\}$  planes at uniaxial compressive strains between 0 and 20% strain [377] and a first order approximation places the transition around 12%. Achieving such elastic strains without prior nucleation of dislocations on  $\{111\}$  planes is possible in nanoscale structures lacking intrinsic dislocation structures and/or during shock loading conditions. A characteristic simulation of SW under shock at 2000 m/s exhibited 9.5% volumetric strain and 17% shear strain. Both Stillinger-Weber and MOD potentials have been shown to predict the quasi-stability of the  $\{110\}$  stacking faults under compression, but little experimental post shock evidence is expected to remain

due to some extent of unavoidable rarefaction wave [229]. Figure 4-37 shows the simultaneous activation of both slip systems during the shock loading of  $\langle 001 \rangle$  silicon at 12 GPa.

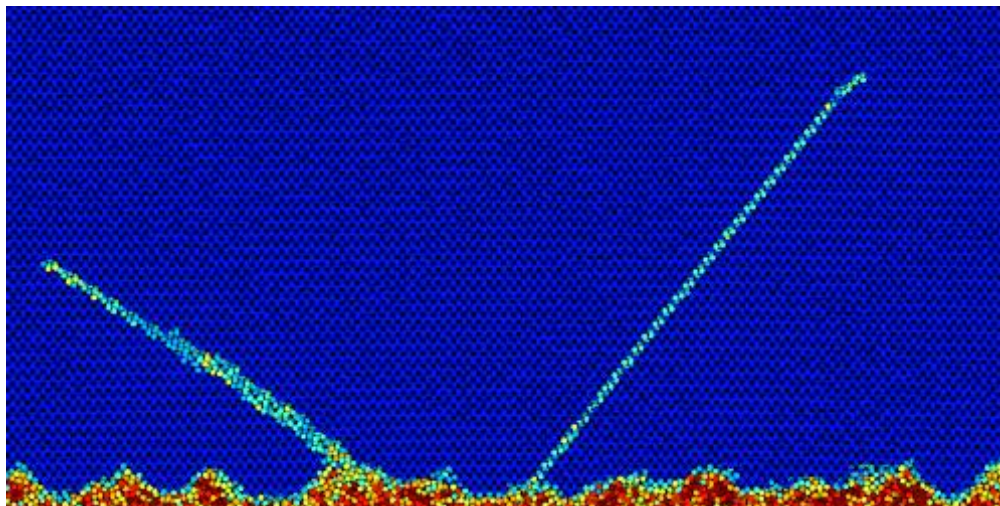


Figure 4-37 Observation of  $\{111\}$  and  $\{110\}$  stacking faults in Uniaxial impact loading of  $\langle 001 \rangle$  single crystalline silicon. Color indicated by coordination number. Snapshots taken at 0.85 km/s, 12 GPa.

Figure 4-38 shows the relationship between pressure and shear stress as they depend on particle velocity for a linearly ramped system.

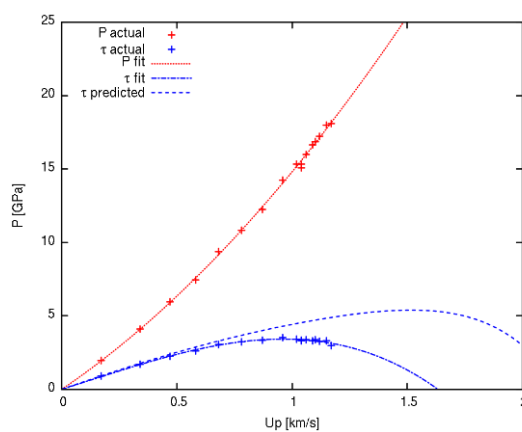


Figure 4-38. Shock pressure and resolved shear stress vs particle velocity. Crosses represent data points from a system undergoing shock compression. The dashed blue line is a curve fit to the

derived relationship between shear and pressure corresponding to the predicted shear stress based on the pressure.

Pressure is fit to the typical  $P = aU_p^2 + bU_p$  form where  $a = 4.2151 \text{ kg/km}^3$  and  $b = 10.595 \text{ kg/km}^2\text{s}$ , shown by a dotted red line in Figure 4-38. Shear is fit to:

$$\tau = 2.3622 U_p^3 + 0.8352 U_p^2 + 4.9351 U_p. \quad (82)$$

The relationship between shear and pressure ( $\tau/p$ ) is derived as follows for purely elastic deformation:

$$\sigma_{ij} = C_{ijkl}\varepsilon_{kl} = C_{ij33}\varepsilon_{33} \quad (83)$$

Here  $i,j = 1,2,3$  where 3 is taken as loading in the z direction. The hydrostatic pressure,  $P$ , can be obtained considering uniaxial strain  $\varepsilon_3$ , simplified from  $\varepsilon_{33}$ , and cubic symmetry accordingly:

$$P = \frac{1}{3} (\sigma_{11} + \sigma_{22} + \sigma_{33}) = \frac{(C_{11} + 2C_{12})}{3} \quad (84)$$

Along the same lines, the maximum shear,  $\tau_{max}$ , stress from the deviatoric components can be expressed as:

$$\tau_{max} = \frac{1}{2} (\sigma_{33} - \sigma_{11}) = \frac{(C_{11} - C_{12})}{2} \quad (85)$$

Therefore,  $\tau_{max}$  is related to  $P$  by,

$$\frac{\tau_{max}}{P} = \frac{3(C_{11} + 2C_{12})}{2(C_{11} - C_{12})} \quad (86)$$

The elastic constants for silicon at zero pressure are  $C_{11} = 165.7 \text{ GPa}$  and  $C_{12} = 63.9 \text{ GPa}$  [378] producing a ratio of shear to hydrostatic pressure of 0.52, but it is well known that these constants are pressure dependant and potential dependent as well. For MOD this ratio decreases with increasing pressure to a value of 0.26 at a pressure of 20 GPa. The

pressure dependence of  $C_{11}$ ,  $C_{12}$ , and  $C_{44}$  are shown in Figure 3-17 and Figure 3-19. From these relationships we define:

$$\frac{\tau_{max}}{P}(P) = -0.00000 P^3 + 0.0006 P^2 - 0.0211 P + 0.5085 \quad (87)$$

With this relationship and the Hugoniot relationship between particle velocity and pressure we can also produce a plot of predicted maximum shear stress which is shown as a blue dotted line in Figure 4-38. The actual shear stress is also shown in Figure 4-38. The difference between predicted and actual illustrate the elastic/plastic threshold where dislocations begin reducing the shear stress by plastic relaxation. By this logic, a deviation in expected shear stress can be thought of as relaxation and will serve as an indication plastic deformation. Taking a threshold of 5% deviation of shear stress as a first approximation of elastic/plastic transition, the transition pressure is  $7.5 \pm 1.5$  GPa and the shear stress is  $2.5 \pm 0.25$  GPa.

The discrepancy between yield strength shown here and shock simulations carried out by Mogni et al. [228] using the Erhart and Albe (EA) Tersoff parameterization [251] is rationalized via thermal activated dislocation nucleation relative to the melt temperature. The yield strength is generally a function of microstructure, strain-rate, and temperature. Holding microstructure and strain-rate constant, the role of temperature, especially in a material with a negative Clausius-Clapeyron slope, should not be ignored. From 0 K to  $T_m/3$ , thermally activated nucleation and motion plays a significant role in yield strength hardening. Above  $0.5T_m$  ( $\sim 800$  K [354,379]) the yield strength begins to drop quickly and, for silicon, the ductile to brittle transition is typically associated with this temperature as dislocation nucleation and motion is favored over brittle cleavage. The EA

parameterization for pure silicon, denoted EA2, exhibits  $T_m = 2150 \pm 25$  K (note that SW and MOD have  $T_m = 1688 \pm 26$  [380] and 1681 [217] respectively). This places the yield point between 700-1075 K for EA2 and 550-850 K for MOD at ambient pressure. During shock, pressure will have a dual effect on temperature through adiabatic heating at the shock front and suppression of the melting temperature due to the negative Clausius-Clapeyron dependence.

Coupled with a thermodynamic evaluation of melting temperature based on Deb et al. [261] and taking a first-order approximation of EA2 as  $T_m(P) = 1.28 \cdot T_{m0} + 0.72 dT/dP$  similar to an approximation of superheating effects [373] we can show the effect of temperature on yield stress through the ductile-to-brittle transition temperature taken as  $DBT(P) = 0.5 \cdot T_m(P)$ . The predicted DBT under shock loading for MOD and EA2 are  $\sim 10$  and  $\sim 14$  GPa respectively and give a good lower estimate of the elastic-plastic transition at high strain rates.

#### 4.2.2. Dislocation Density and Mobility

A snapshot of homogenous nucleation at the shock front can be seen in Figure 4-39, a close up near the shock front given in Figure 4-40. In order to identify partial dislocations in the system, the primary identification scheme utilized a coordination based evaluation. A potential energy criterion was also evaluated to confirm the identification of partials. There are a few challenges in applying a coordination based scheme and we will discuss them here. Foremost, the coordination is evaluated spherically and for uniaxial deformation this may give rise to spurious neighbors in the shock direction for a static coordination radius. Thus our selection of a cutoff radius is between 2.8 and 3.0 Å. Second, this value must be less than the expected neighbor distances in many polymorphs of silicon (3.2 Å)

as well as the equilibrium distance of the second neighbor shell ( $\sim 3.8 \text{ \AA}$ ), but notably corresponds closely to the distance formed by amorphous or bct5 structures ( $\sim 2.9 \text{ \AA}$ ) and relates roughly to the distance between “new neighbors” during a partial displacement shuffle.

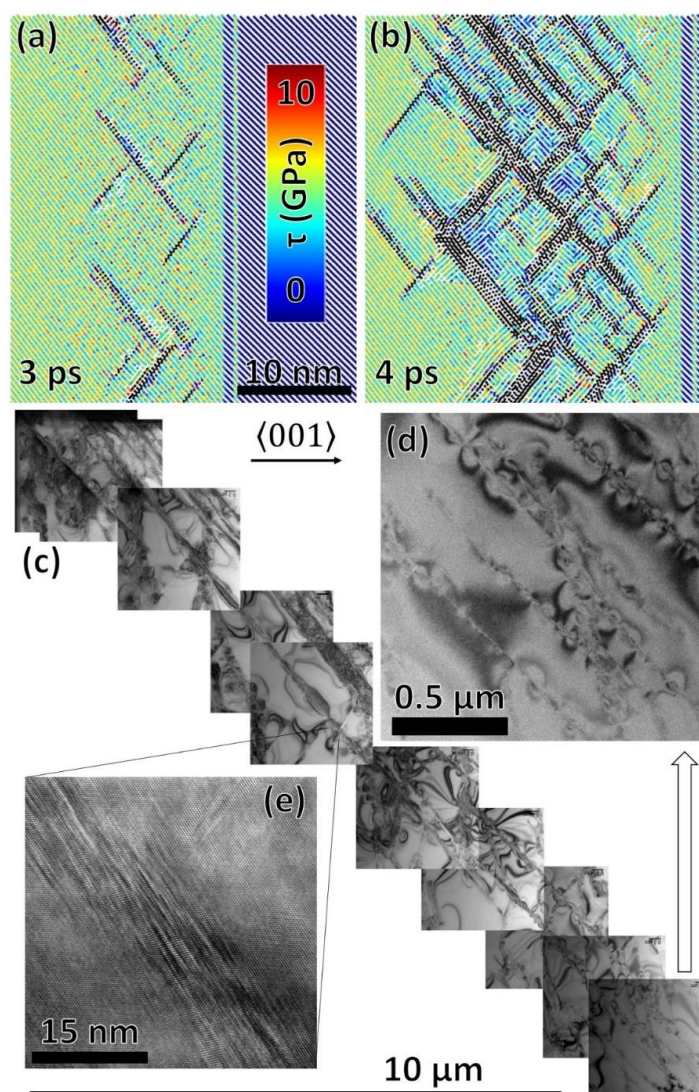


Figure 4-39 (a) Homogenous nucleation of stacking faults on  $\{111\}$  slip planes occurring at  $\sigma_z = 32.5 \text{ GPa}$  and  $\tau = 6.4 \text{ GPa}$  as a shock wave travels from left to right. Atomic color is indicative of the absolute value of the local shear stress. (b) Significant relaxation (blue color) is seen in the 4 ps time step. (c) Recovered microstructure from a 50 J laser-driven shock experiment:  $\sim 11 \text{ GPa}$  peak shock pressure[34,357]. (d,e) Magnifications showing the tip of the dislocation structure and large mass of stacking faults respectively. The growth of subsequent stacking fault layers can be seen in both molecular dynamics and laser experiments; this process occurs in order to expedite the relaxation of high shear stresses.



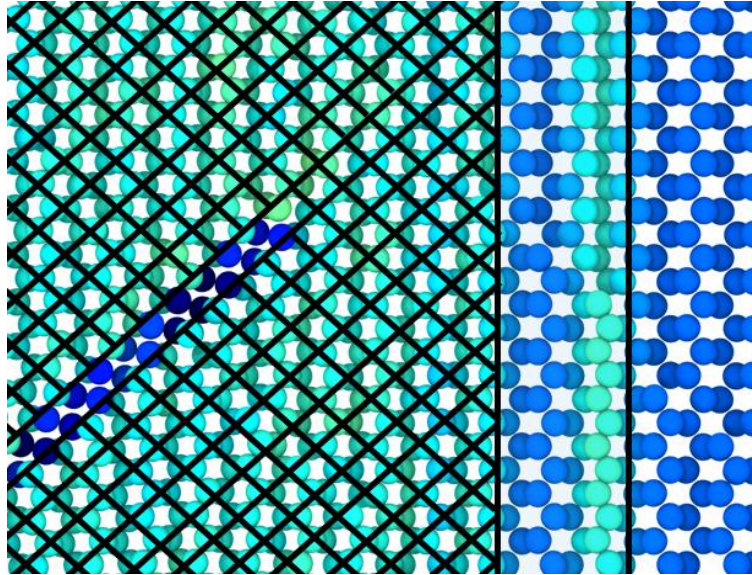


Figure 4-40. Identification of partial dislocation near shock front by potential energy criterion. The partial dislocation tip is identified by the furthest blue atom corresponding to a shift in the lattice across the stacking fault.

Homogenous thresholds for SW are consistent with experimental results and projected range detailed by Smith et al. [177]. Just as in Cu, systems of partial dislocations are nucleated in adjacent planes in order to more quickly relieve shear stress [381]. In 1958, Smith[382] proposed a shock front interface composed of supersonic dislocations. However, it did not predict a dislocation density increase due to shock which was resolved by sequential homogenous nucleation of dislocations at the shock front. This was calculated analytically by Meyers et al.[92,383,384] for Cu.

Here we adapt the analytical description developed by Meyers and leave in a strain-rate dependent HEL in addition to an increased separation of nucleation separation due to supersonic dislocation motion.

Dislocation density can be defined as the inverse separation of dislocations in two dimensions, lateral to the shock front,  $d$ , and aligned with the shock front,  $h_s$ . Accounting

for two dislocations per stacking fault, the following principal relationship for dislocation density can be written as:

$$\rho_d = \left( \frac{dh_s}{2} \right)^{-1}. \quad (88)$$

Taking a standard expression for lateral separation of dislocations ( $d$ ) in order to account for a given strain,  $\varepsilon$ , the following expressions can be written in terms of original and shocked lattice parameter ( $a_0$  and  $a_s$  respectively):

$$d = \frac{a_0}{\varepsilon}, \quad (89)$$

$$\varepsilon = \frac{a_0 - a_s}{a_0}. \quad (90)$$

The separation of dislocations can then be expressed in terms of lattice parameter,

$$d = \frac{a_0^2}{a_0 - a_s}. \quad (91)$$

The inverse of lateral separation can be manipulated into the following form:

$$d^{-1} = \frac{1}{a_0} - \frac{1}{a_0} \frac{a_s}{a_0}. \quad (92)$$

Taking a typical relationship between Burgers vector,  $b$ , and lattice parameter,

$$a_0 = b\sqrt{2}, \quad (93)$$

in addition to a relationship between instantaneous volume,  $V$ , and equilibrium volume,  $V_0$ , as related to the shock and equilibrium lattice parameter,

$$\left( \frac{a_s^3}{a_0^3} \right) = \frac{V}{V_0}. \quad (94)$$

We can now write an expression for  $d^{-1}$  in terms of only one variable,  $V$ :

$$d^{-1} = \frac{1}{b\sqrt{2}} \left( 1 - \left( \frac{V}{V_0} \right)^{1/3} \right), \quad (95)$$

Following formalism previously developed [92], the contribution of the stress field from each dislocation only produces stress in the  $\sigma_{12}$  component of the stress tensor. The sum of these contributions for a spacing of  $1/n^2$  dislocations extending infinitely along a planar shock front is equal to  $\pi^4/90$  and thus the expression for stress in terms of subsequent emission distances,  $h$ , can be written as:

$$\sigma_{12} = \frac{Gb}{2\pi(1-\nu)} \frac{2\sqrt{2}}{n^2 d^2} h = \frac{Gb\pi^3 h}{45\sqrt{2}(1-\nu)d^2}, \quad (96)$$

The critical shear stress,  $\sigma_{12}^c$ , required to nucleate a dislocation can be defined through the HEL:

$$\frac{\sigma_{12}^c}{\sigma_{HEL}} = \frac{(C_{11} - C_{12})}{2(C_{11})}, \quad (97)$$

$$\sigma_{12}^c = \frac{\sigma_{HEL}(C_{11} - C_{12})}{2(C_{11})}, \quad (98)$$

Setting  $\sigma_{12} = \sigma_{12}^c$ , the separation of subsequent partial dislocation nucleation sites is:

$$h = \frac{45(1-\nu)}{Gb\pi^3\sqrt{2}} \frac{(C_{11} - C_{12})}{2(C_{11})} \sigma_{HEL} d^2. \quad (99)$$

The effective separation,  $h_s$ , is then increased when accounting for mobile dislocations at the shock front which aid in relaxation:

$$h_s = h \left( 1 + \frac{kv_d}{U_s} \right). \quad (100)$$

Here,  $k$  is an orientation factor equal to 1 for  $\langle 001 \rangle$  shocks in fcc or diamond cubic materials. The shock speed,  $U_s$ , is well defined as:

$$U_s = \left( \frac{E_L}{\rho} \right)^{1/2}. \quad (101)$$

While the minimum supersonic dislocation velocity relative to the shock front,  $v_d$ , is defined as:

$$v_d = \sqrt{2} \frac{\sqrt{2}}{2} C_s = \left( \frac{E_T}{\rho} \right)^{1/2}. \quad (102)$$

The effective shock separation can now be written as:

$$h_s = h \left( 1 + k \left( \frac{\rho_0}{\rho} \right)^{1/2} \left( \frac{1-2\nu}{1-\nu} \right)^{1/2} \right) = h \left( 1 + k \left( \frac{V}{V_0} \right)^{1/2} \left( \frac{C_{44}}{C_{11}} \right)^{1/2} \right). \quad (103)$$

Substituting eq. (103) into eq. (88) gives:

$$\rho_d = \frac{2}{d^3} \frac{Gb\pi^3 \sqrt{2}}{45(1-\nu)} \frac{2(C_{11})}{(C_{11}-C_{12})} \frac{1}{\sigma_{HEL}} \left( 1 + k \left( \frac{V}{V_0} \right)^{1/2} \left( \frac{C_{44}}{C_{11}} \right)^{1/2} \right)^{-1}, \quad (104)$$

Substituting eq. (95) into eq. (104) now gives a final expression for dislocation density due to homogenous dislocation nucleation at the shock front:

$$\rho_d = \frac{2G\pi^3}{45b^2(1-\nu)\sigma_{HEL}} \frac{(C_{11})}{(C_{11}-C_{12})} \left( 1 + k \left( \frac{V}{V_0} \right)^{1/2} \left( \frac{C_{44}}{C_{11}} \right)^{1/2} \right)^{-1} \left( 1 - \left( \frac{V}{V_0} \right)^{1/3} \right)^3. \quad (105)$$

Between 2.2 and 3 ps, defects are only a single stacking fault thick and are circular to a first order approximation. OVITO's surface mesh modifier [184] was used to relate surface area and volume of defective atoms to an average partial separation of 14.6 Å at 3 ps and separation reaches a steady state at 31.2 Å due to interaction with neighboring dislocations.

Taking the dislocation line length as  $\pi l_d$  for  $n$  total stacking faults over the shocked volume we obtain an estimate of dislocation density plotted against the prediction in Figure 4-41. At nucleation the dislocation density is  $4.4 \times 10^{11} \text{ cm}^{-2}$  and reaches a steady value of  $1.5 \times 10^{12} \text{ cm}^{-2}$  at 3.8 ps.

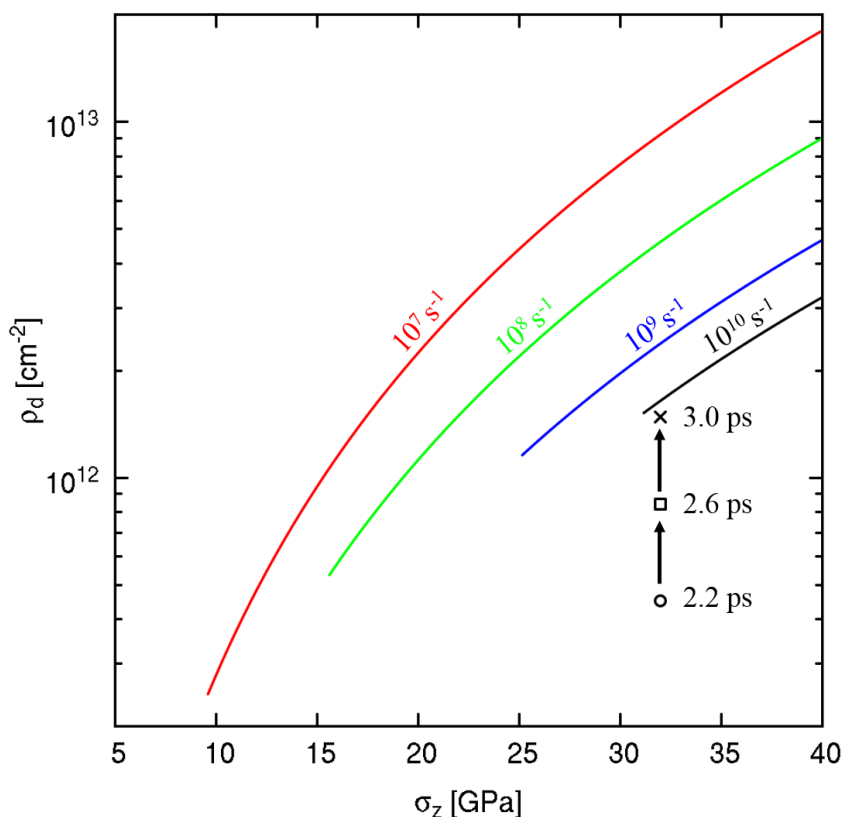


Figure 4-41. Analytical dislocation density prediction where each curve represents a unique strain rate. The dislocation density is highly dependent on the HEL and curves are truncated below this limit corresponding to an elastic response; the material would have a dislocation density unchanged from its intrinsic value. The symbols track the dislocation density evolution observed during the simulation. At 3.0 ps, the MD dislocation density approaches the one analytically predicted for  $10^{10} \text{ s}^{-1}$ , demonstrating the agreement between the two approaches (analytical and MD).

At the high strain-rate elastic-plastic limit for silicon the shear stress is  $\sim 6 \text{ GPa}$  and is near or greater than the theoretical measure of shear strength,  $G/10$ . The motion of dislocations in this regime is thus likely to be transitory in nature as shear stress waxes and wanes with plastic relaxation at the shock front. Consequently, evaluating dislocation

motion under shock conditions adds a degree of realism beyond measuring dislocation velocities under simple shear as has been documented previously in simulations [385–387]. Regardless of observation in simulated conditions, supersonic dislocations have yet to be directly observed in three-dimensional material experiments.

Figure 4-42 exemplifies that we are not merely looking at a pair of equal and opposite partial dislocation dipoles, but a defect with correlated motion in multiple directions relative to the shock direction. Red dotted arrows are drawn in the direction of maximum dislocation velocity and correspond to the following measurements of dislocation motion.

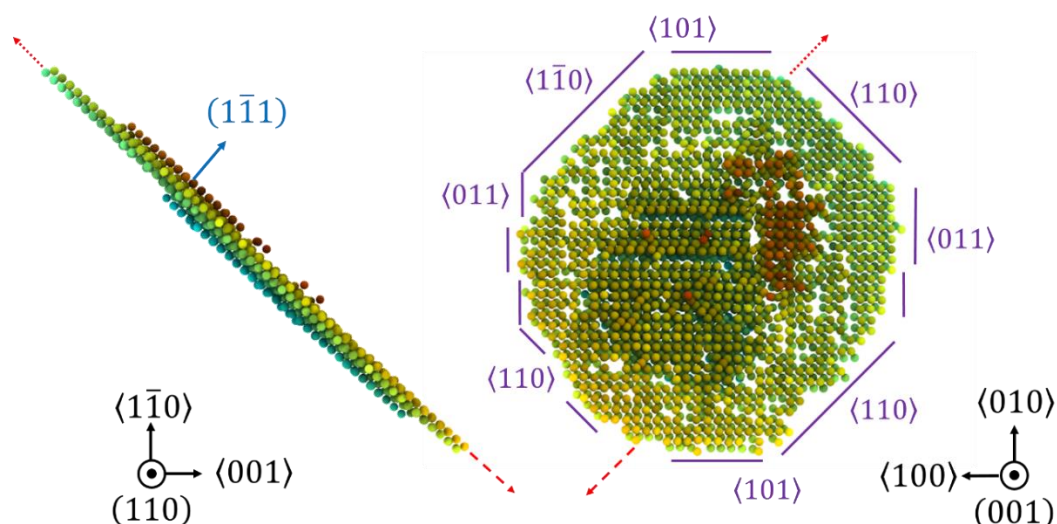


Figure 4-42. Dual projection view showing  $\{111\}$  slip plane several activated burgers slip directions giving rise to a stacking fault of representative shape. Arrows indicate the fastest moving partials, the distance between which the length and corresponding velocity are measured for.

Figure 4-43 shows a time sequence from 2.2 to 2.9 ps where the stacking fault is shown to grow both towards (right) and away from (left) the shock front. The particle velocity dictates a moving center of mass by  $U_p \Delta t$  that serves as the reference point for each half of the stacking fault. The forward partial dislocation's velocity bursts upon nucleation at 2.2 ps for  $\sim 0.1$  ps at 12000 m/s and subsequently slows down to 8200 m/s,

matching the rear moving partial dislocation velocity. For comparison, the leading elastic soliton travels at 8800 m/s before the shock reaches steady state and the elastic-plastic wave travels at 8650 m/s.

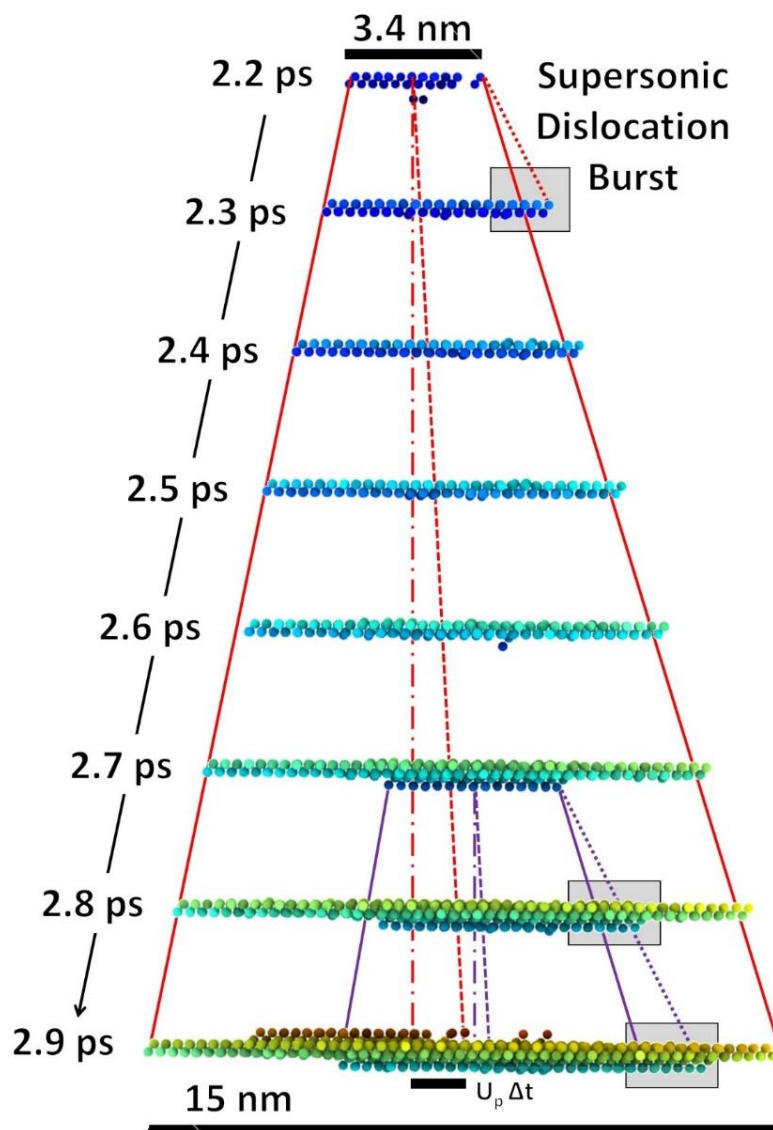


Figure 4-43. Time sequence from 2.2 to 2.9 ps showing partial dislocation velocity burst at 2.2 ps and velocity burst of secondary partial between 2.7 and 2.9 ps. Solid lines indicate motion at  $\sqrt{2}C_t$ , dashed lines represent motion attributed for non-zero center of mass velocity and thus a non-stationary reference point, and dotted lines represent supersonic velocity bursts.

Figure 4-43 corresponds to a shock pressure of 32 GPa, hydrostatic pressure of 23.5 GPa, and shear stress of 6 GPa. Transverse and longitudinal wave speeds depend on pressure dependent stiffness [388] and were used to determine  $C_t = \sqrt{(C_{11}-C_{12} + C_{14})/3\rho}$  and  $C_l = \sqrt{(C_{11}+2C_{12} + 2C_{14})/3\rho}$ . For  $P = 23.5$  GPa,  $C_l = 11800$  m/s,  $\sqrt{2}C_t = 7600$  m/s, and  $C_t = 5400$  m/s; these values indicate that, for a brief period of time, a partial dislocation was able to travel at or above the supersonic threshold in an attempt to catch up the shock front and relieve shear stress. A secondary set of partial dislocations is nucleated underneath the first stacking fault at 2.7 ps in order to further relieve stress and quickly accelerates to reach an astonishing transient velocity of 15000 m/s for at least 0.2 ps before interaction with surrounding partial dislocations interferes. While convenient to observe homogenous nucleation within the silicon sample during simulation it is considered unlikely during an experiment unless surface effects leading to heterogeneous nucleation can be eliminated.

#### 4.2.3. Shear Induced Amorphization/Melting

The interaction of the mutually perpetuating slip systems leads to unique intersections that manifest as nanotwinning and phase transitions preceding directional amorphization. Another method to evaluate the energetic driving force for amorphization of silicon is through the elastic strain energy provided by a field of dislocations.

Taking the line energy of an edge dislocation as,

$$E = \frac{\mu b^2}{4\pi(1-\nu)} \ln\left(\frac{R}{R_c}\right) + E_c. \quad (106)$$

We arrive at the relationship,

$$E = 3.84 \cdot \rho_d \cdot 10^{-13} \text{ (kJ/mol)}. \quad (107)$$



This precise formulation was previously worked out by Huang et al. [389] for an energetic/deformation induced driving force for partial amorphization of ball-milled silicon. It was pointed out that, for ball milled silicon, the resultant dislocation density was low, on the order of  $10^{11} \text{ cm}^{-2}$ , but localized such that 2.5% amorphous phase by volume was produced. Silicon is typically available as well oriented, low impurity, and low intrinsic dislocation density as low as  $10^5 \text{ cm}^{-2}$ . The strain energy introduced by a field of dislocations needs to be equivalent to  $11.9 \text{ kJ mol}^{-1}$ , the crystallization energy of fully amorphous silicon by ion implantation [390,391], in order to produce amorphization from plastic energy. Defects such as stacking faults, twins, and surface tension must also contribute to the elevation of energy within a silicon crystal.

The evolution of defects in time and their role in amorphization was informed by molecular dynamics simulations. Figure 4-44 exemplifies three modes of amorphization: bulk surface amorphization, amorphization along bands of stacking faults, and amorphization at stacking fault intersections. At  $t = 8 \text{ ps}$  we see the formation of a disordered band within the stacking fault band at the bottom of the frame. At  $t = 10 \text{ ps}$  the first intersection of stacking faults takes place and at  $t = 13 \text{ ps}$  an amorphous nucleus is formed at this intersection while others intersect with a greater number of stacking faults.

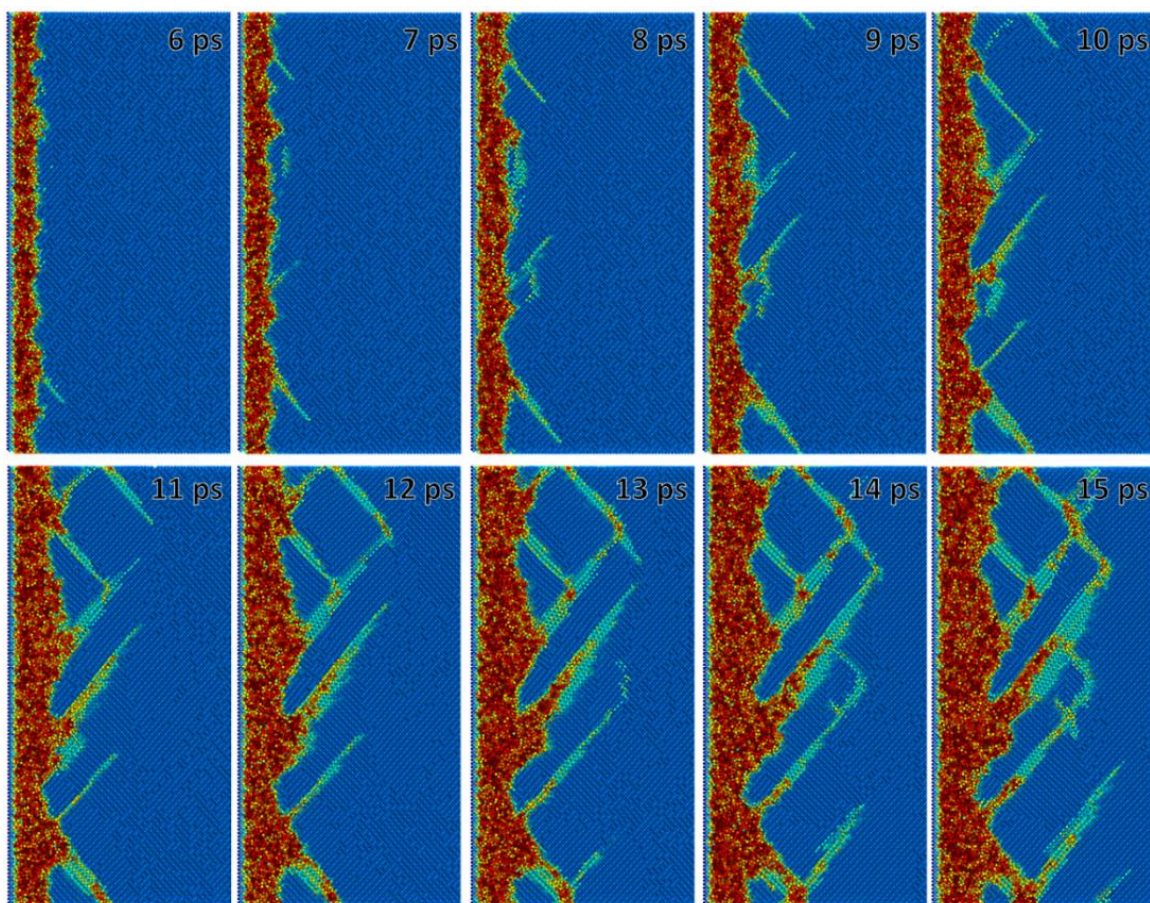


Figure 4-44. Molecular dynamics time evolution showing formation of amorphous nucleus following inter snapshot at 15 ps of a [001] silicon crystal shocked to 14.5 GPa

A tridimensional view of the MD simulated microstructure of shocked silicon is presented in Figure 4-45 with marks indicating multiple stacking-fault variants. Such interaction of these stacking faults is expected to occur under experimental laser shock compression, leading to large defect densities and defect localization effects such as loss of atomic order and plastic heating.

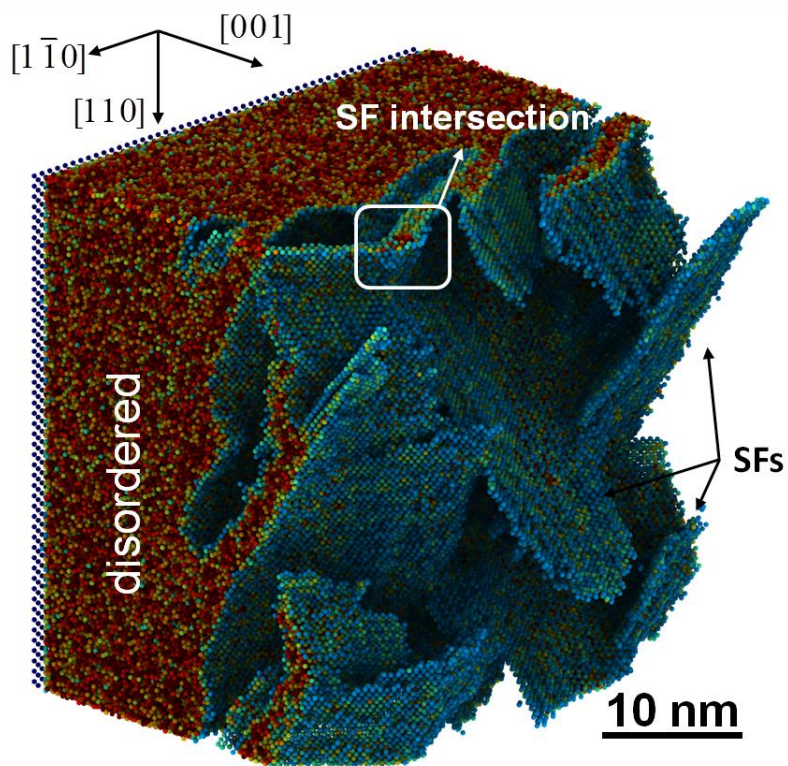


Figure 4-45. Tridimensional view of the stacking faults (SF) as the precursors of the amorphization: multiple stacking faults and their intersections can be observed ahead of the disordered region. A disordered region was left behind.

The plastic front consisting of partial dislocation loops traveling along  $\{111\}$  and  $\{110\}$  planes leads to a relaxation of shear stresses and plastic heat manifested by a temperature rise. After defect nucleation, the shear stress begins to relax and then drops to zero within the amorphous region. Full relaxation of shear stress does not confirm or deny this as a solid state process. A melt would be unable to sustain shear stress, but full 3D relaxation during amorphization is just as plausible. Silicon is known to have at least two amorphous phases, one high density and one low density, in addition to the disordered liquid phase.

Figure 4-46 shows an orthogonal (near  $\{110\}$ ) view of a stacking fault and its transition into an amorphous band colored by two different schemes.

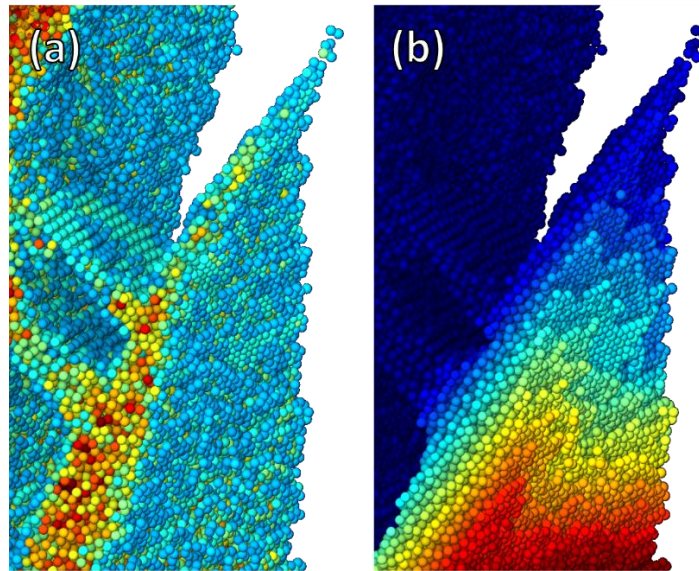


Figure 4-46. Piston/particle velocity of 1.5 km/s. Near-[110] projection view. (a) Coordination indicating the relatively higher average coordination  $\sim 5$  (light blue) of the stacking fault layer and the even higher average coordination of the molten layer  $\sim 4$  to 10 (green-yellow to dark red). (b) Depth perpendicular to primary slip direction, a uniaxially compressed  $\{111\}$  plane, showing sequential stacking fault steps that bound the amorphous layer may be similar to those for twin propagation.

Both images show only “defective” atoms filtered by coordination number not equal to four. It should be noted that this will also remove 4 coordinated atoms in the amorphous and liquid phases as well as 4-coordinated defects, such as reconstructed dislocation cores, but to date this is the best available method for evaluating complex structures in diamond cubic silicon. Figure 4-47 compares the simulation to experimental results.

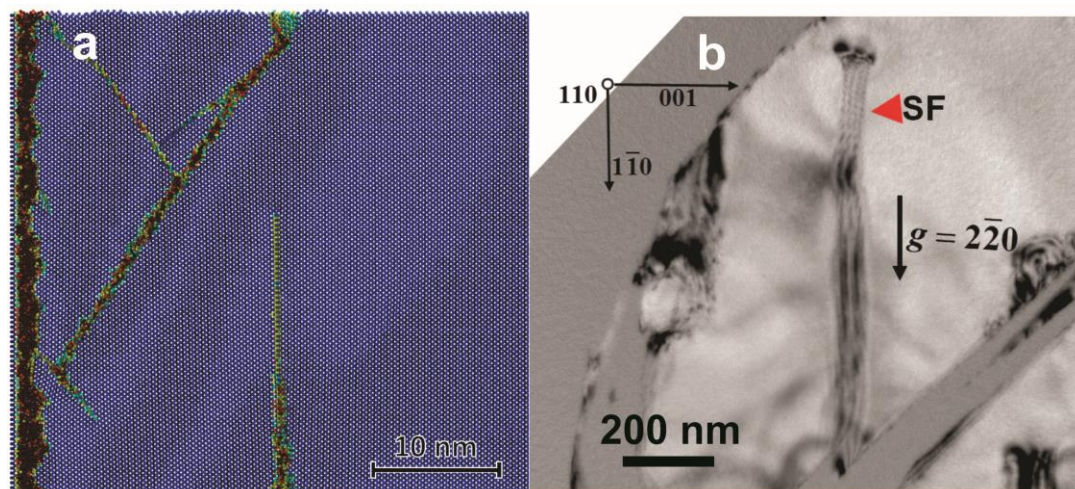


Figure 4-47. MD simulation (a) shows several  $\{111\}$  stacking fault as the precursor of the amorphization; and TEM observation (b) also shows stacking faults bounding the amorphous materials.

Notably, experimental images are of shock recovered silicon. Thus far, only the state of the sample during loading (on the ps scale) has been shown, and further loading and/or unloading might modify the microstructure. A simulated recovery experiment was carried out with the following simulation components: a deceleration of the piston to  $V_z = 0$  during 5 ps following 15 ps of compression. Within the NVE microcanonical ensemble, the run was continued with a stationary piston for 20 ps and contained a viscous damp at the rear surface of the sample to minimize reflections. Subsequently, a Langevin thermostat at 300 K was applied to the entire sample for 20 ps while maintaining “shrink-wrap” boundary conditions in the shock direction allowing for the relaxation of  $P_{zz}$  to near 0 GPa.

Figure 4-48 shows that the most noticeable microstructural difference after simulated recovery is the retraction of stacking faults not immediately bounding amorphous bands. The molecular dynamics simulation does not contain any intrinsic defects - such as dislocations, impurities, or vacancies - that would increase the stability of such stacking faults by pinning.

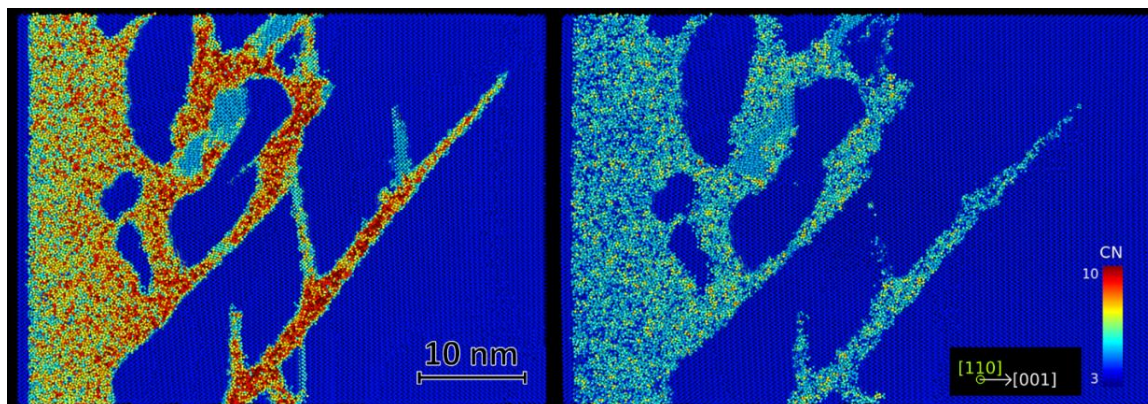


Figure 4-48. Simulated recovery of shock loaded Si at 1.1 km/s. Left, during compressive loading. Right, after recovery as detailed above. Color according to local coordination. Unloading reduces unstable stacking faults and decreases the average coordination from 6.7 to 5.1 within the amorphous region.

During loading, coordination in the hot amorphous region has an average value of 6.7, which compares extremely well with the nominal 6.4 coordination of a liquid [250]. The recovered sample has cold amorphous regions with a coordination of 5.1, which compares favorably to the nominal 4-coordination of amorphous silicon [250], given that our simulated recovery spans a relatively short time scale and thus a high quenching rate.

Furthermore, the long time scale of the experiment might lead to structural changes which are thermally activated and which cannot be sampled by our MD simulations. However, given the tremendous agreement in spatial scales where amorphous bands are only about 5 nm thick, with stacking faults which are only 1 nm thick - and patterns between MD and the experiments, it seems possible that the structural crystal to amorphous transition occurs within the same time frame observed in the simulations, and the material is “locked” there, despite the possible occurrence of late thermally-activated events.

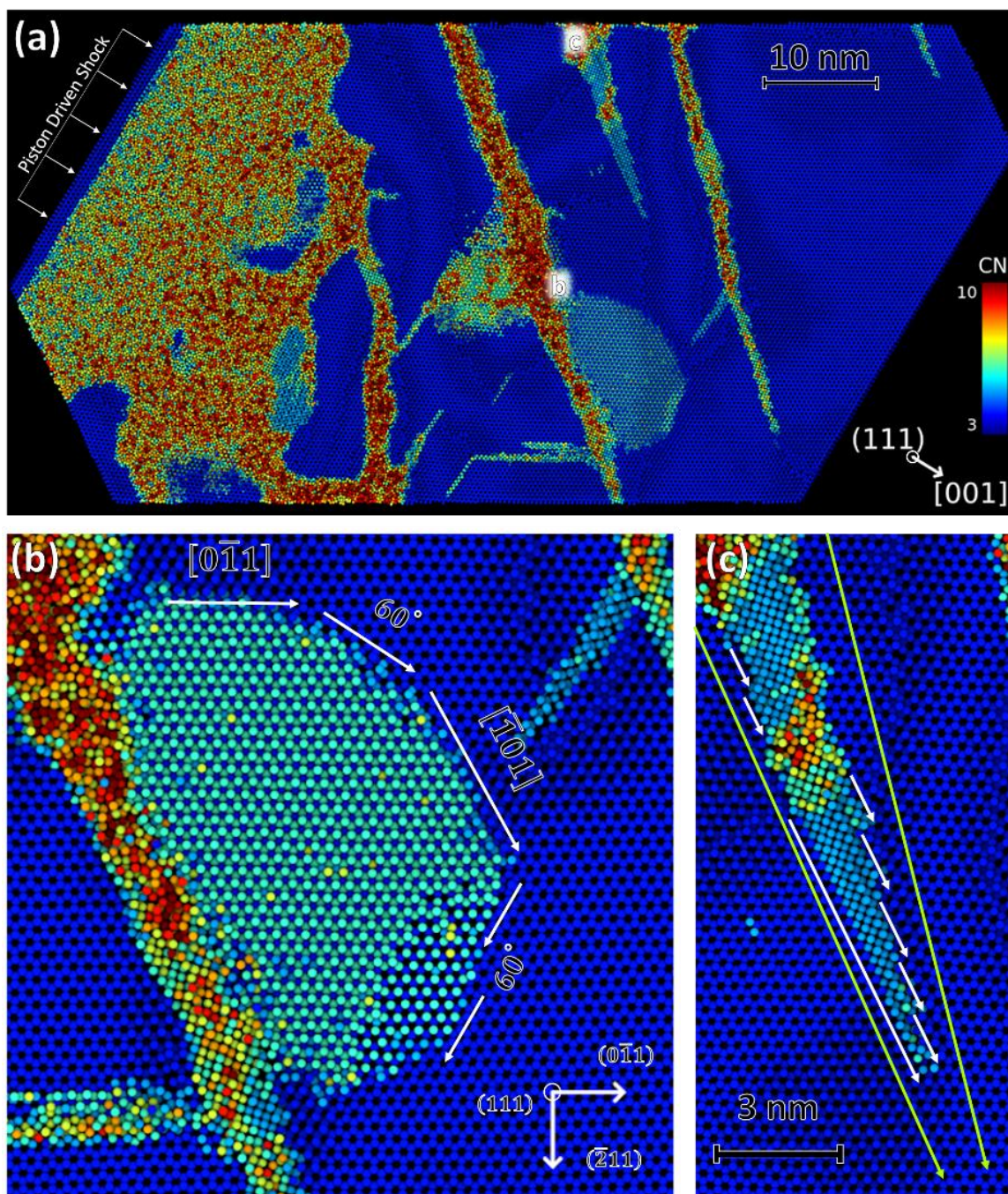


Figure 4-49. Slice along the  $[111]$  direction of a MD simulation of  $[100]$  shocked silicon using the MOD potential. Bulk amorphization/melting near the shocked surface, directional amorphization/melting, partial dislocation activity, and formation of bct5 bands can be identified. Atoms are colored according to local coordination evaluated with a cutoff of 0.3 nm.

Chapter 4, in part, has been accepted for publication of the material as it may appear in: E.N. Hahn, T.C. Germann, R.J. Ravelo, J.E. Hammerberg, M.A. Meyers, Non-Equilibrium Molecular Dynamics Simulations of Spall in Single Crystal Tantalum, AIP Conference Proceedings. In press (2016). The thesis author was the first and corresponding author of this article.

Chapter 4, in part, has been submitted for publication of the material as it may appear in: E.N. Hahn, T.C. Germann, R.J. Ravelo, J. Hammerberg, M.A. Meyers, On the Ultimate Tensile Strength of Tantalum, Acta Materialia. (2016). The thesis author was the first and corresponding author of this article.

Chapter 4, in part, is currently being prepared for submission for publication: E.N. Hahn, M.A. Meyers, Laser-Driven Shocks and Dynamic Failure. The thesis author was the first author of this article.

Chapter 4, in part, is currently being prepared for submission for publication: T.P. Remington, J.C.E. Mertens, E.N. Hahn, S. Sabbaghianrad, T.G. Langdon, C.E. Wehrenberg, B.R. Maddox, D.C. Swift, B.A. Remington, N. Chawla, M.A. Meyers, Spall Strength Dependence on Strain Rate and Grain Size in Tantalum. The thesis author was the third author of this article.

Chapter 4, in part, is a reprint of material that has been published: C.-H. Lu, E.N. Hahn, B.A. Remington, B.R. Maddox, E.M. Bringa, M.A. Meyers, Phase Transformation in Tantalum under Extreme Laser Deformation, Scientific Reports. 5 (2015) 15064. doi:10.1038/srep15064. The thesis author was the second author of this article.

Chapter 4, in part, is a reprint of material that has been published: E.N. Hahn, S. Zhao, E.M. Bringa, M.A. Meyers, Supersonic Dislocation Bursts in Silicon, Scientific



Reports. 6 (2016) 26977. doi:10.1038/srep26977. The thesis author was the first author of this article.

Chapter 4, in part, is a reprint of material that has been published: S. Zhao, B. Kad, E.N. Hahn, B.A. Remington, C.E. Wehrenberg, C.M. Huntington, H.-S. Park, E.M. Bringa, K.L. More, M.A. Meyers, Pressure and shear-induced amorphization of silicon, *Extreme Mechanics Letters*. 5 (2015) 74–80. doi:10.1016/j.eml.2015.10.001. The thesis author was the third author of this article.

Chapter 4, in part, is a reprint of material that has been published: S. Zhao, E.N. Hahn, B. Kad, B.A. Remington, E.M. Bringa, M.A. Meyers, Shock compression of [001] single crystal silicon, *Eur. Phys. J. Spec. Top.* (2016) 1–7. doi:10.1140/epjst/e2016-02634-7. The thesis author was the second author of this article.

Chapter 4, in part, is a reprint of material that has been published: S. Zhao, E.N. Hahn, B. Kad, B.A. Remington, C.E. Wehrenberg, E.M. Bringa, M.A. Meyers, Amorphization and nanocrystallization of silicon under shock compression, *Acta Materialia*. 103 (2016) 519–533. doi:10.1016/j.actamat.2015.09.022. The thesis author was the second author of this article.

Chapter 4, in part, is currently being prepared for submission for publication: E.N. Hahn N., Y. Wang, R. Flanagan, S. Zhao, M.A. Meyers, Computational Evaluation of Silicon under Shock Compression, (2016). The thesis author was the first and corresponding author of this article.

## 5. Conclusions

Connecting back to the questions that drove the present research, several key advances have been made.

- *What role does shear instability and phase change play in silicon?*

The modified Tersoff potential (Figure 4-49) has been shown to apply particularly well to shocked silicon including the following results and their experimental counterparts:

- ✓ Heterogeneous nucleation of dislocations at 10 GPa for  $U_p=0.82$  km/s; Gust and Royce [257].
- ✓ Mutual slip along  $\{110\}$  and  $\{111\}$  planes in agreement with nanostructures under high compressive strain; Chrobak et al. [376].
- ✓ Defect mediated metastable phase transitions from dc to bct5 related to those observed under nanoloading; Gerbig et al. [243,244].
- ✓ Impact melting akin to nanodroplet shock; Gamero et al.[367,392].
- ✓ Shear and defect driven directional amorphization; Zhao et al.[373], He et al. [393].

This set of simulations emphasize the need for new experiments at ultra-high strain rates in order to explore the lattice response at the sub-ns time scale. Particularly important is our ability to examine plastic deformation as it occurs with sub-picosecond and atomic resolution in order to observe the intricacies of defect formation and motion. Experiments that are able to pre-heat the target should be able to nucleate dislocations at lower shock pressures by reducing the amount of adiabatic heating required to overcome thermally activated nucleation barriers associated with the ductile-brittle transition. This will also aid

in successful recovery of normally brittle silicon samples. Picosecond lasers may operate for just long enough to nucleate dislocations and observe their subsequent velocity bursts through back calculation of dislocation penetration via pre- and post-mortem characterization.

- *What role, if any, do defects and grain boundaries play in spall failure process when the sample goes into dynamic tension?*
  - *What do grain boundary structures in bcc tantalum look like?*

We determine a large number of grain boundary energies for tantalum, as a function of misorientation for rotation around  $\langle 100 \rangle$ ,  $\langle 110 \rangle$ ,  $\langle 111 \rangle$ , and  $\langle 112 \rangle$  axes, in order to inform future studies such as those investigating abnormal grain growth [124], heterogeneous deformation of poly and nanocrystals [123,268], and deformation twinning [125]. Specifically, deformation twinning involves the nucleation of  $\Sigma 3$  coherent twin boundaries through the movement of twinning dislocations. It is shown here that there is a decrease in energy associated with the formation of quasi-symmetric boundaries. In many cases, twin boundaries are not fully coherent and are likely combinations of symmetric, asymmetric, and quasi-symmetric components. This metastability of quasi-symmetric  $\Sigma 3'$  boundaries in bcc tantalum, identified using both EAM and SNAP interatomic potentials, may play a governing role in determining the mechanism for plastic deformation via the twinning vs. slip transition. Experimental evidence has shown quasi-symmetric boundaries in Nb, Mo, and Ta  $\Sigma 5$  GBs and here we show symmetry breaking  $\Sigma 3$ ,  $\Sigma 5$ , and  $\Sigma 7$  GBs (among others) in Ta. These quasi-symmetric structures appear to be unique to bcc transition metals and are not explicitly reported for fcc GB structures.

- *How are dynamic experimental results correlated to local phenomena and measures obtained through molecular dynamics?*
  - *What is the relationship between spall strength and strain rate?*

The ultimate strength of materials is an important property and represents the stress at which the interatomic forces can no longer sustain the cohesion of the structure. In quasi-static tension the value is never reached or even approached as a variety of mechanisms conspire to lower the maximum sustained tensile stress. However, as the strain rate is increased, this value rises and in the shock wave regime the stress state (uniaxial strain) and the kinetics of void/crack nucleation, growth, and coalescence are such that the ultimate stress is reached. The roles of temperature, microstructure, and strain rate were evaluated for tensile failure bcc tantalum.

The sustained stress at failure is dependent upon the kinetics of the dominant defect mechanism. We identify a transition between dislocation and twin dominated spall of [001] single crystals at  $10^9 \text{ s}^{-1}$  and show that small nanocrystals ( $d=21 \text{ nm}$ ) do not exhibit a change in mechanism for strain rates greater than  $10^8 \text{ s}^{-1}$ . Above the threshold for decohesion,  $\sim 5 \times 10^{10} \text{ s}^{-1}$ , strength again follows a power law dependence up until the vibrational frequency, after which the stress saturates at an ultimate value. In each spall process, the temperature induced via plasticity (and the shock Hugoniot for NEMD simulations) decreases the resulting spall strength. Artificial adjustment of the temperature prior to spall shows that softening persists up until melting where the spall strength of liquid decreases further in proportion to  $\sim 1/T$ .

The classically-accepted cleavage strength of tantalum is 39.4 GPa based upon a cohesive energy criterion [36,394]. Several potential forms were assessed in order to more accurately estimate the tensile strength. The maximum predicted strength of the Ravelo et al. [95] potential utilized here (Ta1) is 31.6 GPa (Ta2 predicts a theoretical strength of 35 GPa). These both show good agreement with DFT and general EOS forms, and with the

measured ultimate tensile strengths in the current MD simulations of single and nanocrystalline tantalum, ~31 and ~34 GPa, respectively.

➤ *What are the mechanisms of void initiation and growth?*

Calculations reveal that voids form at regions where defects are generated on shock compression. These are twin-twin intersections in monocrystals; additionally, grain boundary-defects are regions of initiation in nanocrystals. The growth of voids takes place by the emission of shear loops from the voids. These subsequently transition to prismatic loops by the cross-slip of the screw components of dislocations.

Chapter 5, in part, is currently being prepared for submission for publication: E.N. Hahn N., Y. Wang, R. Flanagan, S. Zhao, M.A. Meyers, Computational Evaluation of Silicon under Shock Compression, (2016). The thesis author was the first and corresponding author of this article.

Chapter 5, in part, is a reprint of material that has been published: E.N. Hahn, S.J. Fensin, T.C. Germann, M.A. Meyers, Symmetric tilt boundaries in body-centered cubic tantalum, Scripta Materialia. 116 (2016) 108–111. doi:10.1016/j.scriptamat.2016.01.038. The thesis author was the first and corresponding author of this article.

Chapter 5, in part, has been submitted for publication of the material as it may appear in: E.N. Hahn, T.C. Germann, R.J. Ravelo, J. Hammerberg, M.A. Meyers, On the Ultimate Tensile Strength of Tantalum, Acta Materialia. (2016). The thesis author was the first and corresponding author of this article.

## References

- [1] R.E. Rudd, T.C. Germann, B.A. Remington, J.S. Wark, Metal deformation and phase transitions at extremely high strain rates, *MRS Bull.* 35 (2010) 999–1006. doi:10.1557/mrs2010.705.
- [2] C.W. Barnes, D.J. Funk, M.P. Hockaday, J.L. Sarrao, M.F. Stevens, The science of dynamic compression at the mesoscale and the Matter-Radiation Interactions in Extremes (MaRIE) project, *J. Phys. Conf. Ser.* 500 (2014) 92001. doi:10.1088/1742-6596/500/9/092001.
- [3] D. Funk, G.T. Gray III, T.C. Germann, R. Martineau, A Summary Report on the 21st Century Needs and Challenges of Compression Science Workshop, Santa Fe, NM, 2009.
- [4] B.A. Remington, G. Bazan, J. Belak, E. Bringa, J.D. Colvin, M.J. Edwards, S.G. Glendinning, D.H. Kalantar, M. Kumar, B.F. Lasinski, K.T. Lorenz, J.M. McNaney, S.M. Pollaine, D. Rowley, J.S. Stölken, S.V. Weber, W.G. Wolfer, M. Caturla, D.S. Ivanov, L.V. Zhigilei, B. Kad, M.A. Meyers, M. Schneider, D.D. Meyerhofer, B. Yaakobi, J.S. Wark, Materials science under extreme conditions of pressure and strain rate, *Metall. Mater. Trans. A.* 35 (2004) 2587–2607. doi:10.1007/s11661-004-0205-6.
- [5] B.A. Remington, R.E. Rudd, J.S. Wark, From microjoules to megajoules and kilobars to gigabars: Probing matter at extreme states of deformation, *Phys. Plasmas* 1994-Present. 22 (2015) 90501. doi:10.1063/1.4930134.
- [6] C. Anders, E.M. Bringa, G. Ziegenhain, G.A. Graham, J.F. Hansen, N. Park, N.E. Teslich, H.M. Urbassek, Why Nanoprojectiles Work Differently than Macroimpactors: The Role of Plastic Flow, *Phys. Rev. Lett.* 108 (2012) 27601. doi:10.1103/PhysRevLett.108.027601.
- [7] R.M. Canup, Accretion of the Earth, *Philos. Trans. R. Soc. Lond. Math. Phys. Eng. Sci.* 366 (2008) 4061–4075. doi:10.1098/rsta.2008.0101.
- [8] H. Sakagami, K. Nishihara, Rayleigh–Taylor instability on the pusher–fuel contact surface of stagnating targets, *Phys. Fluids B Plasma Phys.* 1989-1993. 2 (1990) 2715–2730. doi:10.1063/1.859395.
- [9] I. Hachisu, T. Matsuda, K. 'ichi Nomoto, T. Shigeyama, Rayleigh-Taylor instabilities and mixing in the helium star models for Type Ib/Ic supernovae, *Astrophys. J.* 368 (1991) L27–L30.

- [10] E.M. Bringa, A. Caro, Y. Wang, M. Victoria, J.M. McNaney, B.A. Remington, R.F. Smith, B.R. Torralva, H.V. Swygenhoven, Ultrahigh Strength in Nanocrystalline Materials Under Shock Loading, *Science*. 309 (2005) 1838–1841. doi:10.1126/science.1116723.
- [11] J.R. Asay, The use of shock-structure methods for evaluating high-pressure material properties, *Int. J. Impact Eng.* 20 (1997) 27–61. doi:10.1016/S0734-743X(97)87478-7.
- [12] A. Stukowski, Visualization and Analysis Strategies for Atomistic Simulations, in: C.R. Weinberger, G.J. Tucker (Eds.), *Multiscale Mater. Model. Nanomechanics*, Springer International Publishing, 2016: pp. 317–336. [http://link.springer.com/chapter/10.1007/978-3-319-33480-6\\_10](http://link.springer.com/chapter/10.1007/978-3-319-33480-6_10) (accessed October 10, 2016).
- [13] M.A. Meyers, *Dynamic Behavior of Materials*, John Wiley & Sons, 1994.
- [14] E. Teller, On the Speed of Reactions at High Pressures, *J. Chem. Phys.* 36 (1962) 901–903. doi:10.1063/1.1732687.
- [15] P.W. Bridgman, Effects of High Shearing Stress Combined with High Hydrostatic Pressure, *Phys. Rev.* 48 (1935) 825–847. doi:10.1103/PhysRev.48.825.
- [16] H.C. Chen, J.C. LaSalvia, V.F. Nesterenko, M.A. Meyers, Shear localization and chemical reaction in high-strain, high-strain-rate deformation of Ti–Si powder mixtures, *Acta Mater.* 46 (1998) 3033–3046. doi:10.1016/S1359-6454(98)00016-0.
- [17] W.J.M. Rankine, On the Thermodynamic Theory of Waves of Finite Longitudinal Disturbance, *Philos. Trans. R. Soc. Lond.* 160 (1870) 277–288. doi:10.1098/rstl.1870.0015.
- [18] H. Hugoniot, Sur un théorème général relatif à la propagation du mouvement dans les corps, *CR Acad Sci Paris*. 102 (1886) 858–860.
- [19] M.D. Salas, The curious events leading to the theory of Shock Waves, (2007). <http://link.springer.com/article/10.1007/s00193-007-0084-z> (accessed July 10, 2015).
- [20] E.N. Hahn, T.C. Germann, R.J. Ravelo, J.E. Hammerberg, M.A. Meyers, Non-Equilibrium Molecular Dynamics Simulations of Spall in Single Crystal Tantalum, *AIP Conf. Proc.* In press (2016).
- [21] B.A. Remington, P. Allen, E.M. Bringa, J. Hawreliak, D. Ho, K.T. Lorenz, H. Lorenzana, J.M. McNaney, M.A. Meyers, S.W. Pollaine, K. Rosolankova, B. Sadik, M.S. Schneider, D. Swift, J. Wark, B. Yaakobi, Material dynamics under extreme conditions of pressure and strain rate, *Mater. Sci. Technol.* 22 (2006) 474–488. doi:10.1179/174328406X91069.

- [22] D.H. Kalantar, B.A. Remington, J.D. Colvin, K.O. Mikaelian, S.V. Weber, L.G. Wiley, J.S. Wark, A. Loveridge, A.M. Allen, A.A. Hauer, M.A. Meyers, Solid-state experiments at high pressure and strain rate, *Phys. Plasmas* 1994-Present. 7 (2000) 1999–2006. doi:10.1063/1.874021.
- [23] G. Askaryon, E. Morez, Use of Laser Generated Shocks to Improve Metals & Alloys, *JETP LETT.* 16 (1963) 1638.
- [24] R.M. White, Generation of elastic waves by transient surface heating, *J. Appl. Phys.* 34 (1963) 3559–3567.
- [25] N. Anderholm, Laser-generated stress waves, *Appl. Phys. Lett.* 16 (1970) 113–115.
- [26] O. Inal, L. Murr, Laser-shock-induced microstructural changes and a comparison with explosive-shock-induced phenomena in metals: Field-ion and electron microscopic studies, *J. Appl. Phys.* 49 (1978) 2427–2434.
- [27] B. Rethfeld, K. Sokolowski-Tinten, D. von der Linde, S.I. Anisimov, Timescales in the response of materials to femtosecond laser excitation, *Appl. Phys. A.* 79 (2004) 767–769. doi:10.1007/s00339-004-2805-9.
- [28] L.V. Zhigilei, Z. Lin, D.S. Ivanov, Atomistic Modeling of Short Pulse Laser Ablation of Metals: Connections between Melting, Spallation, and Phase Explosion†, *J. Phys. Chem. C.* 113 (2009) 11892–11906. doi:10.1021/jp902294m.
- [29] J.D. Lindl, P. Amendt, R.L. Berger, S.G. Glendinning, S.H. Glenzer, S.W. Haan, R.L. Kauffman, O.L. Landen, L.J. Suter, The physics basis for ignition using indirect-drive targets on the National Ignition Facility, *Phys. Plasmas* 1994-Present. 11 (2004) 339–491. doi:10.1063/1.1578638.
- [30] C.R. Phipps, L. Zhigilei, P. Polynkin, T. Baumert, T. Sarnet, N. Bulgakova, W. Bohn, J. Reif, Laser interaction with materials: introduction, *Appl. Opt.* 53 (2014) LIM1. doi:10.1364/AO.53.00LIM1.
- [31] M.A. Meyers, B.A. Remington, B. Maddox, E.M. Bringa, Laser shocking of materials: Toward the national ignition facility, *JOM.* 62 (2010) 24–30. doi:10.1007/s11837-010-0006-x.
- [32] S. Luo, D. Swift, T. Tierney IV, D. Paisley, G. Kyrala, R. Johnson, A. Hauer, O. Tschauner, P.D. Asimow, Laser-induced shock waves in condensed matter: some techniques and applications, *High Press. Res.* 24 (2004) 409–422.
- [33] D.C. Swift, J.G. Niemczura, D.L. Paisley, R.P. Johnson, S.-N. Luo, T.E.T. Iv, Laser-launched flyer plates for shock physics experiments, *Rev. Sci. Instrum.* 76 (2005) 93907. doi:10.1063/1.2052593.



- [34] S. Zhao, B. Kad, E.N. Hahn, B.A. Remington, C.E. Wehrenberg, C.M. Huntington, H.-S. Park, E.M. Bringa, K.L. More, M.A. Meyers, Pressure and shear-induced amorphization of silicon, *Extreme Mech. Lett.* 5 (2015) 74–80. doi:10.1016/j.eml.2015.10.001.
- [35] L. Tollier, R. Fabbro, E. Bartnicki, Study of the laser-driven spallation process by the velocity interferometer system for any reflector interferometry technique. I. Laser-shock characterization, *J. Appl. Phys.* 83 (1998) 1224–1230. doi:10.1063/1.366819.
- [36] H. Jarmakani, B. Maddox, C.T. Wei, D. Kalantar, M.A. Meyers, Laser shock-induced spalling and fragmentation in vanadium, *Acta Mater.* 58 (2010) 4604–4628. doi:10.1016/j.actamat.2010.04.027.
- [37] B. Hopkinson, A Method of Measuring the Pressure Produced in the Detonation of High Explosives or by the Impact of Bullets, *Philos. Trans. R. Soc. Lond. Ser. Contain. Pap. Math. Phys. Character.* 213 (1914) 437–456.
- [38] H. Kolsky, *Stress Waves in Solids*, Courier Dover Publications, 1963.
- [39] Smith, *Symposium on Dynamic Behavior of Material*, ASTM International, 1963.
- [40] J.S. Rinehart, J. Pearson, *Behavior of metals under impulsive loads*, Dover Publications, 1965.
- [41] B.R. Breed, C.L. Mader, D. Venable, Technique for the Determination of Dynamic-Tensile-Strength Characteristics, *J. Appl. Phys.* 38 (1967) 3271–3275. doi:10.1063/1.1710098.
- [42] F.R. Tuler, B.M. Butcher, A criterion for the time dependence of dynamic fracture, *Int. J. Fract. Mech.* 4 (1968) 431–437. doi:10.1007/BF00186808.
- [43] A. Tobolsky, H. Eyring, Mechanical Properties of Polymeric Materials, *J. Chem. Phys.* 11 (1943) 125–134. doi:10.1063/1.1723812.
- [44] S.N. Zhurkov, Kinetic Concept of the Strength of Solids, in: *ICF1 Jpn. 1965*, 2012. <http://www.gruppofrattura.it/ocs/index.php/ICF/ICF1/paper/view/1534> (accessed July 27, 2014).
- [45] S. Arrhenius, On the reaction rate of the inversion of non-refined sugar upon souring, *Z Phys Chem.* 4 (1889) 226–248.
- [46] D.E. Grady, The spall strength of condensed matter, *J. Mech. Phys. Solids.* 36 (1988) 353–384. doi:10.1016/0022-5096(88)90015-4.
- [47] D.E. Grady, M.E. Kipp, Fragmentation properties of metals, *Int. J. Impact Eng.* 20 (1997) 293–308. doi:10.1016/S0734-743X(97)87502-1.

- [48] M.E. Kipp, D.E. Grady, Experimental and Numerical Studies of High-Velocity Impact Fragmentation, in: L. Davison, D.E. Grady, M. Shahinpoor (Eds.), High-Press. Shock Compression Solids II, Springer New York, 1996: pp. 282–339. [http://link.springer.com/chapter/10.1007/978-1-4612-2320-7\\_12](http://link.springer.com/chapter/10.1007/978-1-4612-2320-7_12) (accessed July 27, 2014).
- [49] L. Davison, A.L. Stevens, M.E. Kipp, Theory of spall damage accumulation in ductile metals, *J. Mech. Phys. Solids*. 25 (1977) 11–28. doi:10.1016/0022-5096(77)90017-5.
- [50] M.A. Meyers, C.T. Aimone, Dynamic fracture (spalling) of metals, *Prog. Mater. Sci.* 28 (1983) 1–96. doi:10.1016/0079-6425(83)90003-8.
- [51] V.E. Fortov, V.V. Kostin, S. Eliezer, Spallation of metals under laser irradiation, *J. Appl. Phys.* 70 (1991) 4524–4531. doi:10.1063/1.349087.
- [52] T. Antoun, *Spall Fracture*, Springer New York, 2003.
- [53] S.V. Razorenov, G.I. Kanel, G.V. Garkushin, O.N. Ignatova, Resistance to dynamic deformation and fracture of tantalum with different grain and defect structures, *Phys. Solid State*. 54 (2012) 790–797. doi:10.1134/S1063783412040233.
- [54] J.P. Cuq-Lelandais, M. Boustie, L. Berthe, T. de Rességuier, P. Combis, J.P. Colombier, M. Nivard, A. Claverie, Spallation generated by femtosecond laser driven shocks in thin metallic targets, *J. Phys. Appl. Phys.* 42 (2009) 65402. doi:10.1088/0022-3727/42/6/065402.
- [55] S.I. Ashitkov, P.S. Komarov, E.V. Struleva, M.B. Agranat, G.I. Kanel, K.V. Khishchenko, The behavior of tantalum under ultrashort loads induced by femtosecond laser, *J. Phys. Conf. Ser.* 653 (2015) 12001. doi:10.1088/1742-6596/653/1/012001.
- [56] E. Moshe, S. Eliezer, E. Dekel, A. Ludmirsky, Z. Henis, M. Werdiger, I.B. Goldberg, N. Eliaz, D. Eliezer, An increase of the spall strength in aluminum, copper, and Metglas at strain rates larger than  $10^7$  s<sup>-1</sup>, *J. Appl. Phys.* 83 (1998) 4004–4011. doi:10.1063/1.367222.
- [57] G.I. Kanel, Unusual behaviour of usual materials in shock waves, *J. Phys. Conf. Ser.* 500 (2014) 12001. doi:10.1088/1742-6596/500/1/012001.
- [58] E. Dekel, S. Eliezer, Z. Henis, E. Moshe, A. Ludmirsky, I.B. Goldberg, Spallation model for the high strain rates range, *J. Appl. Phys.* 84 (1998) 4851–4858. doi:10.1063/1.368727.
- [59] S.J. Fensin, E.K. Cerreta, G.T. Gray III, S.M. Valone, Why are some Interfaces in Materials Stronger than others?, *Sci. Rep.* 4 (2014) 5461. doi:10.1038/srep05461.

- [60] K. Mackenchery, R.R. Valisetty, R.R. Namburu, A. Stukowski, A.M. Rajendran, A.M. Dongare, Dislocation evolution and peak spall strengths in single crystal and nanocrystalline Cu, *J. Appl. Phys.* 119 (2016) 44301. doi:10.1063/1.4939867.
- [61] S. Christy, H. Pak, M. Meyers, *Metallurgical applications of shock wave and high-strain-rate phenomena*, N. Y. Basel. (1986).
- [62] M.A. Meyers, R.W. Armstrong, H.O. Kirchner, *Mechanics and materials: fundamentals and linkages*, Wiley-VCH, 1999.
- [63] A.K. Zurek, M.A. Meyers, Microstructural aspects of dynamic failure, in: *High-Press. Shock Compression Solids II*, Springer, 1996: pp. 25–70.
- [64] V.A. Lubarda, M.S. Schneider, D.H. Kalantar, B.A. Remington, M.A. Meyers, Void growth by dislocation emission, *Acta Mater.* 52 (2004) 1397–1408. doi:10.1016/j.actamat.2003.11.022.
- [65] G.I. Kanel, S.V. Razorenov, A. Bogatch, A.V. Utkin, V.E. Fortov, D.E. Grady, Spall fracture properties of aluminum and magnesium at high temperatures, *J. Appl. Phys.* 79 (1996) 8310–8317.
- [66] G.I. Kanel, S.V. Razorenov, A.V. Utkin, V.E. Fortov, K. Baumung, H.U. Karow, D. Rusch, V. Licht, Spall strength of molybdenum single crystals, *J. Appl. Phys.* 74 (1993) 7162–7165. doi:10.1063/1.355032.
- [67] G. Kanel, V. Fortov, Mechanical properties of condensed media under high-intensity impact loading, *Uspekhi Mekhaniki-Adv. Mech.* 10 (1987) 3–82.
- [68] Y.B. Zel'dovich, Y.P. Raizer, *Physics of Shock Waves and High-Temperature Hydrodynamic Phenomena*, Vol. I (1966) and Vol. II (1967), Academic Press, New York. Reprinted in a single volume by Dover Publications, Mineola, New York, 2002.
- [69] A. Bushman, *Intense dynamic loading of condensed matter* Taylor & Francis, London, 1993.
- [70] L. Toller, R. Fabbro, Study of the laser-driven spallation process by the VISAR interferometry technique. II. Experiment and simulation of the spallation process, *J. Appl. Phys.* 83 (1998) 1231–1237. doi:10.1063/1.366820.
- [71] D. Milathianaki, S. Boutet, G.J. Williams, A. Higginbotham, D. Ratner, A.E. Gleason, M. Messerschmidt, M.M. Seibert, D.C. Swift, P. Hering, J. Robinson, W.E. White, J.S. Wark, Femtosecond Visualization of Lattice Dynamics in Shock-Compressed Matter, *Science*. 342 (2013) 220–223. doi:10.1126/science.1239566.
- [72] C.E. Wehrenberg, A.J. Comley, N.R. Barton, F. Coppari, D. Fratanduono, C.M. Huntington, B.R. Maddox, H.-S. Park, C. Plechaty, S.T. Prsbrey, B.A. Remington,

- R.E. Rudd, Lattice-level observation of the elastic-to-plastic relaxation process with subnanosecond resolution in shock-compressed Ta using time-resolved *in situ* Laue diffraction, *Phys. Rev. B.* 92 (2015) 104305. doi:10.1103/PhysRevB.92.104305.
- [73] P.A. Rigg, R.J. Scharff, R.S. Hixson, Sound speed measurements in tantalum using the front surface impact technique, *J. Phys. Conf. Ser.* 500 (2014) 32018. doi:10.1088/1742-6596/500/3/032018.
- [74] D. Chen, Y. Yu, Z. Yin, H. Wang, G. Liu, On the validity of the traditional measurement of spall strength, *Int. J. Impact Eng.* 31 (2005) 811–824. doi:10.1016/j.ijimpeng.2004.04.006.
- [75] G.T. Gray III, N.K. Bourne, V. Livescu, C.P. Trujillo, S. MacDonald, P. Withers, The influence of shock-loading path on the spallation response of Ta, *J. Phys. Conf. Ser.* 500 (2014) 112031. doi:10.1088/1742-6596/500/11/112031.
- [76] O.T. Kingstedt, J. Lambros, Ultra-high Speed Imaging of Laser-Induced Spallation, *Exp. Mech.* 55 (2015) 587–598. doi:10.1007/s11340-014-9973-0.
- [77] C. Czarnota, S. Mercier, A. Molinari, Modelling of nucleation and void growth in dynamic pressure loading, application to spall test on tantalum, *Int. J. Fract.* 141 (2006) 177–194. doi:10.1007/s10704-006-0070-y.
- [78] C. Bronkhorst, G. Gray III, F. Addessio, V. Livescu, N. Bourne, S. MacDonald, P. Withers, Response and representation of ductile damage under varying shock loading conditions in tantalum, *J. Appl. Phys.* 119 (2016) 85103.
- [79] L.A. Girifalco, V.G. Weizer, Application of the Morse Potential Function to Cubic Metals, *Phys. Rev.* 114 (1959) 687–690. doi:10.1103/PhysRev.114.687.
- [80] J.H. Rose, J.R. Smith, F. Guinea, J. Ferrante, Universal features of the equation of state of metals, *Phys. Rev. B.* 29 (1984) 2963–2969. doi:10.1103/PhysRevB.29.2963.
- [81] P. Vinet, J.H. Rose, J. Ferrante, J.R. Smith, Universal features of the equation of state of solids, *J. Phys. Condens. Matter.* 1 (1989) 1941. doi:10.1088/0953-8984/1/11/002.
- [82] T.P. Remington, Private Communication, (2015). Private Communication.
- [83] E. Orowan, The crystal plasticity. III: about the mechanism of the sliding, *Phys.* 1934.
- [84] G. Taylor, The formation of emulsions in definable fields of flow, *Proc. R. Soc. Lond. Ser. Contain. Pap. Math. Phys. Character.* (1934) 501–523.

- [85] I. Horiuti, M. Polanyi, Exchange reactions of hydrogen on metallic catalysts, *Trans. Faraday Soc.* 30 (1934) 1164–1172.
- [86] V. Volterra, Sur l'équilibre des corps élastiques multiplément connexes, in: *Ann. Sci. Ecole Norm. Supérieure, Société mathématique de France*, 1907: pp. 401–517.
- [87] J.M. Burgers, Some considerations on the fields of stress connected with dislocations in a regular crystal lattice. I, *Koninklijke Nederlandse Akademie van Wetenschappen*, 1939.
- [88] J.M. Burgers, Geometrical considerations concerning the structural irregularities to be assumed in a crystal, *Proc. Phys. Soc.* 52 (1940) 23. doi:10.1088/0959-5309/52/1/304.
- [89] A.H. Cottrell, LXXXVI. A note on the Portevin-Le Chatelier effect, *Lond. Edinb. Dublin Philos. Mag. J. Sci.* 44 (1953) 829–832. doi:10.1080/14786440808520347.
- [90] F.R.N. Nabarro, Z.S. Basinski, D. Holt, The plasticity of pure single crystals, *Adv. Phys.* 13 (1964) 193–323.
- [91] J.D. Eshelby, F.C. Frank, F.R.N. Nabarro, XLI. The equilibrium of linear arrays of dislocations., *Lond. Edinb. Dublin Philos. Mag. J. Sci.* 42 (1951) 351–364. doi:10.1080/14786445108561060.
- [92] M.A. Meyers, H. Jarmakani, E.M. Bringa, B.A. Remington, Chapter 89 Dislocations in Shock Compression and Release, in: L. Kubin, J.P. Hirth (Eds.), *Dislocations Solids*, Elsevier, 2009: pp. 91–197. <http://www.sciencedirect.com/science/article/pii/S1572485909015022> (accessed April 10, 2015).
- [93] D. Hull, D.J. Bacon, *Introduction to Dislocations*, Elsevier, 2011.
- [94] V. Bulatov, W. Cai, *Computer Simulations of Dislocations*, Oxford University Press, 2006.
- [95] R. Ravelo, T.C. Germann, O. Guerrero, Q. An, B.L. Holian, Shock-induced plasticity in tantalum single crystals: Interatomic potentials and large-scale molecular-dynamics simulations, *Phys. Rev. B.* 88 (2013) 134101. doi:10.1103/PhysRevB.88.134101.
- [96] M.A. Tschopp, H.A. Murdoch, L.J. Kecskes, K.A. Darling, “Bulk” Nanocrystalline Metals: Review of the Current State of the Art and Future Opportunities for Copper and Copper Alloys, *JOM.* 66 (2014) 1000–1019. doi:10.1007/s11837-014-0978-z.
- [97] M.A. Meyers, A. Mishra, D.J. Benson, Mechanical properties of nanocrystalline materials, *Prog. Mater. Sci.* 51 (2006) 427–556. doi:10.1016/j.pmatsci.2005.08.003.

- [98] H. Conrad, J. Narayan, On the grain size softening in nanocrystalline materials, *Scr. Mater.* 42 (2000) 1025–1030. doi:10.1016/S1359-6462(00)00320-1.
- [99] J.C.M. Li, *Mechanical Properties of Nanocrystalline Materials*, CRC Press, 2011.
- [100] M.F. Ashby, The deformation of plastically non-homogeneous materials, *Philos. Mag.* 21 (1970) 399–424. doi:10.1080/14786437008238426.
- [101] S.K. Bhattacharya, S. Tanaka, Y. Shiihara, M. Kohyama, Ab initio study of symmetrical tilt grain boundaries in bcc Fe: structural units, magnetic moments, interfacial bonding, local energy and local stress, *J. Phys. Condens. Matter.* 25 (2013) 135004. doi:10.1088/0953-8984/25/13/135004.
- [102] D. Terentyev, X. He, A. Serra, J. Kuriplach, Structure and strength of  $\langle 110 \rangle$  tilt grain boundaries in bcc Fe: An atomistic study, *Comput. Mater. Sci.* 49 (2010) 419–429. doi:10.1016/j.commatsci.2010.05.033.
- [103] G. Gottstein, L.S. Shvindlerman, *Grain Boundary Migration in Metals: Thermodynamics, Kinetics, Applications*, CRC Press, 1999.
- [104] D.E. Spearot, M.A. Tschopp, K.I. Jacob, D.L. McDowell, Tensile strength of  $\langle 100 \rangle$  and  $\langle 110 \rangle$  tilt bicrystal copper interfaces, *Acta Mater.* 55 (2007) 705–714. doi:10.1016/j.actamat.2006.08.060.
- [105] M. Koiwa, H. Seyazaki, T. Ogura, A systematic study of symmetric tilt-boundaries in hard-sphere f.c.c. crystals, *Acta Metall.* 32 (1984) 171–182. doi:10.1016/0001-6160(84)90214-1.
- [106] A.P. Sutton, V. Vitek, On the Structure of Tilt Grain Boundaries in Cubic Metals I. Symmetrical Tilt Boundaries, *Philos. Trans. R. Soc. Lond. Ser. Math. Phys. Sci.* 309 (1983) 1–36. doi:10.1098/rsta.1983.0020.
- [107] A.P. Sutton, R.W. Ballufi, Rules for combining structural units of grain boundaries, *Philos. Mag. Lett.* 61 (1990) 91–94. doi:10.1080/09500839008206485.
- [108] S.J. Fensin, S.M. Valone, E.K. Cerreta, J.P. Escobedo-Diaz, G.T. Gray III, K. Kang, J. Wang, Effect of grain boundary structure on plastic deformation during shock compression using molecular dynamics, *Model. Simul. Mater. Sci. Eng.* 21 (2013) 15011. doi:10.1088/0965-0393/21/1/015011.
- [109] S.J. Fensin, C. Brandl, E.K. Cerreta, G.T. Gray III, T.C. Germann, S.M. Valone, Nanoscale Plasticity at Grain Boundaries in Face-centered Cubic Copper Under Shock Loading, *JOM.* 65 (2013) 410–418. doi:10.1007/s11837-012-0546-3.

- [110] J. Bian, X. Niu, H. Zhang, G. Wang, Atomistic deformation mechanisms in twinned copper nanospheres, *Nanoscale Res. Lett.* 9 (2014) 1–7. doi:10.1186/1556-276X-9-335.
- [111] S.J. Fensin, S.M. Valone, E.K. Cerreta, G.T. Gray III, Influence of grain boundary properties on spall strength: Grain boundary energy and excess volume, *J. Appl. Phys.* 112 (2012) 83529. doi:10.1063/1.4761816.
- [112] S.-N. Luo, T.C. Germann, D.L. Tonks, Q. An, Shock wave loading and spallation of copper bicrystals with asymmetric  $\Sigma 3\langle 110 \rangle$  tilt grain boundaries, *J. Appl. Phys.* 108 (2010) 93526. doi:10.1063/1.3506707.
- [113] D.E. Spearot, K.I. Jacob, D.L. McDowell, Nucleation of dislocations from [0 0 1] bicrystal interfaces in aluminum, *Acta Mater.* 53 (2005) 3579–3589. doi:10.1016/j.actamat.2005.04.012.
- [114] D.E. Spearot, D.L. McDowell, Atomistic Modeling of Grain Boundaries and Dislocation Processes in Metallic Polycrystalline Materials, *J. Eng. Mater. Technol.* 131 (2009) 041204–041204. doi:10.1115/1.3183776.
- [115] D.L. Zheng, S.D. Chen, A.K. Soh, Y. Ma, Molecular dynamics simulations of glide dislocations induced by misfit dislocations at the Ni/Al interface, *Comput. Mater. Sci.* 48 (2010) 551–555. doi:10.1016/j.commatsci.2010.02.022.
- [116] A. Hasnaoui, P.M. Derlet, H. Van Swygenhoven, Interaction between dislocations and grain boundaries under an indenter – a molecular dynamics simulation, *Acta Mater.* 52 (2004) 2251–2258. doi:10.1016/j.actamat.2004.01.018.
- [117] T. Frolov, D.L. Olmsted, M. Asta, Y. Mishin, Structural phase transformations in metallic grain boundaries, *Nat. Commun.* 4 (2013) 1899. doi:10.1038/ncomms2919.
- [118] Y. Mishin, M. Asta, J. Li, Atomistic modeling of interfaces and their impact on microstructure and properties, *Acta Mater.* 58 (2010) 1117–1151. doi:10.1016/j.actamat.2009.10.049.
- [119] G.S. Rohrer, Grain boundary energy anisotropy: a review, *J. Mater. Sci.* 46 (2011) 5881–5895.
- [120] M.A. Tschopp, K.N. Solanki, F. Gao, X. Sun, M.A. Khaleel, M.F. Horstemeyer, Probing grain boundary sink strength at the nanoscale: Energetics and length scales of vacancy and interstitial absorption by grain boundaries in  $\alpha$ -Fe, *Phys. Rev. B.* 85 (2012) 64108. doi:10.1103/PhysRevB.85.064108.
- [121] G.J. Tucker, M.A. Tschopp, D.L. McDowell, Evolution of structure and free volume in symmetric tilt grain boundaries during dislocation nucleation, *Acta Mater.* 58 (2010) 6464–6473. doi:10.1016/j.actamat.2010.08.008.

- [122] E.N. Hahn, M.A. Meyers, Grain-size dependent mechanical behavior of nanocrystalline metals, *Mater. Sci. Eng. A.* 646 (2015) 101–134. doi:10.1016/j.msea.2015.07.075.
- [123] T.R. Bieler, S.C. Sutton, B.E. Dunlap, Z.A. Keith, P. Eisenlohr, M.A. Crimp, B.L. Boyce, Grain Boundary Responses to Heterogeneous Deformation in Tantalum Polycrystals, *JOM.* 66 (2013) 121–128. doi:10.1007/s11837-013-0821-y.
- [124] N.A. Pedrazas, T.E. Buchheit, E.A. Holm, E.M. Taleff, Dynamic abnormal grain growth in tantalum, *Mater. Sci. Eng. A.* 610 (2014) 76–84. doi:10.1016/j.msea.2014.05.031.
- [125] V. Livescu, J.F. Bingert, T.A. Mason, Deformation twinning in explosively-driven tantalum, *Mater. Sci. Eng. A.* 556 (2012) 155–163. doi:10.1016/j.msea.2012.06.071.
- [126] D. Wolf, Correlation between the energy and structure of grain boundaries in b.c.c. metals. II. Symmetrical tilt boundaries, *Philos. Mag. A.* 62 (1990) 447–464. doi:10.1080/01418619008244790.
- [127] D.L. Olmsted, E.A. Holm, S.M. Foiles, Survey of computed grain boundary properties in face-centered cubic metals—II: Grain boundary mobility, *Acta Mater.* 57 (2009) 3704–3713. doi:10.1016/j.actamat.2009.04.015.
- [128] S. Ratanaphan, D.L. Olmsted, V.V. Bulatov, E.A. Holm, A.D. Rollett, G.S. Rohrer, Grain boundary energies in body-centered cubic metals, *Acta Mater.* 88 (2015) 346–354. doi:10.1016/j.actamat.2015.01.069.
- [129] E.O. Hall, The Deformation and Ageing of Mild Steel: III Discussion of Results, *Proc. Phys. Soc. Sect. B.* 64 (1951) 747. doi:10.1088/0370-1301/64/9/303.
- [130] N.J. Petch, The Cleavage Strength of Polycrystals, *J Iron Steel Inst.* 174 (1953) 25–28.
- [131] R.W. Armstrong, 60 Years of Hall-Petch: Past to Present Nano-Scale Connections, *Mater. Trans.* 55 (2014) 2–12. doi:10.2320/matertrans.MA201302.
- [132] J.D. Embury, R.M. Fisher, The structure and properties of drawn pearlite, *Acta Metall.* 14 (1966) 147–159. doi:10.1016/0001-6160(66)90296-3.
- [133] J.S.C. Jang, C.C. Koch, The hall-petch relationship in nanocrystalline iron produced by ball milling, *Scr. Metall. Mater.* 24 (1990) 1599–1604. doi:10.1016/0956-716X(90)90439-N.
- [134] M.A. Meyers, E. Ashworth, A model for the effect of grain size on the yield stress of metals, *Philos. Mag. A.* 46 (1982) 737–759. doi:10.1080/01418618208236928.



- [135] H. Gleiter, Nanocrystalline materials, *Prog. Mater. Sci.* 33 (1989) 223–315. doi:10.1016/0079-6425(89)90001-7.
- [136] H. Gleiter, Materials with ultra-fine grain sizes, in: *Deform. Polycrystals Mech. Microstruct.*, 1981, 1981.
- [137] A.H. Chokshi, A. Rosen, J. Karch, H. Gleiter, On the validity of the hall-petch relationship in nanocrystalline materials, *Scr. Metall.* 23 (1989) 1679–1683. doi:10.1016/0036-9748(89)90342-6.
- [138] C.C. Koch, J. Narayan, The Inverse Hall-Petch Effect—Fact or Artifact?, in: *Symp. B – Struct. Mech. Prop. Nanophase Mater.-Theory Comput. Simul. Vs Exp.*, 2000. doi:10.1557/PROC-634-B5.1.1.
- [139] T.G. Nieh, J. Wadsworth, Hall-petch relation in nanocrystalline solids, *Scr. Metall. Mater.* 25 (1991) 955–958. doi:10.1016/0956-716X(91)90256-Z.
- [140] D. Wolf, V. Yamakov, S.R. Phillpot, A. Mukherjee, H. Gleiter, Deformation of nanocrystalline materials by molecular-dynamics simulation: relationship to experiments?, *Acta Mater.* 53 (2005) 1–40. doi:10.1016/j.actamat.2004.08.045.
- [141] N.R. Barton, J.V. Bernier, R. Becker, A. Arsenlis, R. Cavallo, J. Marian, M. Rhee, H.-S. Park, B.A. Remington, R.T. Olson, A multiscale strength model for extreme loading conditions, *J. Appl. Phys.* 109 (2011) 73501. doi:10.1063/1.3553718.
- [142] S. Benkassam, L. Capolungo, M. Cherkaoui, Mechanical properties and multi-scale modeling of nanocrystalline materials, *Acta Mater.* 55 (2007) 3563–3572. doi:10.1016/j.actamat.2007.02.010.
- [143] L. Capolungo, D.E. Spearot, M. Cherkaoui, D.L. McDowell, J. Qu, K.I. Jacob, Dislocation nucleation from bicrystal interfaces and grain boundary ledges: Relationship to nanocrystalline deformation, *J. Mech. Phys. Solids.* 55 (2007) 2300–2327. doi:10.1016/j.jmps.2007.04.001.
- [144] J. Hafner, Atomic-scale computational materials science, *Acta Mater.* 48 (2000) 71–92. doi:10.1016/S1359-6454(99)00288-8.
- [145] T.E. Karakasidis, C.A. Charitidis, Multiscale modeling in nanomaterials science, *Mater. Sci. Eng. C.* 27 (2007) 1082–1089. doi:10.1016/j.msec.2006.06.029.
- [146] V. Péron-Lühns, A. Jérusalem, F. Sansoz, L. Stainier, L. Noels, A two-scale model predicting the mechanical behavior of nanocrystalline solids, *J. Mech. Phys. Solids.* 61 (2013) 1895–1914. doi:10.1016/j.jmps.2013.04.009.
- [147] S. Yip, ed., *Handbook of Materials Modeling*, Springer Netherlands, Dordrecht, 2005. <http://www.springer.com/us/book/9781402032875> (accessed February 10, 2015).

- [148] T.M. Pollock, R. LeSar, The feedback loop between theory, simulation and experiment for plasticity and property modeling, *Curr. Opin. Solid State Mater. Sci.* 17 (2013) 10–18. doi:10.1016/j.cossms.2013.03.003.
- [149] H. Van Swygenhoven, P.M. Derlet, Grain-boundary sliding in nanocrystalline fcc metals, *Phys. Rev. B.* 64 (2001) 224105. doi:10.1103/PhysRevB.64.224105.
- [150] D. Farkas, Atomistic simulations of metallic microstructures, *Curr. Opin. Solid State Mater. Sci.* 17 (2013) 284–297. doi:10.1016/j.cossms.2013.11.002.
- [151] K. Kadau, T.C. Germann, P.S. Lomdahl, B.L. Holian, Atomistic simulations of shock-induced transformations and their orientation dependence in bcc Fe single crystals, *Phys. Rev. B.* 72 (2005) 64120. doi:10.1103/PhysRevB.72.064120.
- [152] C. Wu, E.T. Karim, A.N. Volkov, L.V. Zhigilei, Atomic Movies of Laser-Induced Structural and Phase Transformations from Molecular Dynamics Simulations, in: M. Castillejo, P.M. Ossi, L. Zhigilei (Eds.), *Lasers Mater. Sci.*, Springer International Publishing, 2014: pp. 67–100. [http://link.springer.com/chapter/10.1007/978-3-319-02898-9\\_4](http://link.springer.com/chapter/10.1007/978-3-319-02898-9_4) (accessed January 9, 2015).
- [153] T.C. Germann, K. Kadau, Trillion-Atom Molecular Dynamics Becomes a Reality, *Int. J. Mod. Phys. C.* 19 (2008) 1315–1319. doi:10.1142/S0129183108012911.
- [154] J. Milhans, J.E. Hammerberg, R. Ravelo, T.C. Germann, B.L. Holian, Large scale NEMD simulations of polycrystalline Al sliding interfaces, in: *APS Meet. Abstr.*, 2012: p. 26006. <http://adsabs.harvard.edu/abs/2012APS..MARL26006M> (accessed June 17, 2014).
- [155] T.C. Germann, Exascale Co-design for Modeling Materials in Extreme Environments, (2014). <http://www.osti.gov/scitech/biblio/1136467>.
- [156] J.E. Hammerberg, Sequoia Computation, (2015).
- [157] J. Schiøtz, K.W. Jacobsen, A Maximum in the Strength of Nanocrystalline Copper, *Science.* 301 (2003) 1357–1359. doi:10.1126/science.1086636.
- [158] Y. Tang, E.M. Bringa, M.A. Meyers, Inverse Hall–Petch relationship in nanocrystalline tantalum, *Mater. Sci. Eng. A.* 580 (2013) 414–426. doi:10.1016/j.msea.2013.05.024.
- [159] L. Verlet, Computer “Experiments” on Classical Fluids. I. Thermodynamical Properties of Lennard-Jones Molecules, *Phys. Rev.* 159 (1967) 98–103. doi:10.1103/PhysRev.159.98.
- [160] D. Levesque, L. Verlet, Molecular dynamics and time reversibility, *J. Stat. Phys.* 72 (n.d.) 519–537. doi:10.1007/BF01048022.

- [161] S.J. Plimpton, J.D. Gale, Developing community codes for materials modeling, *Curr. Opin. Solid State Mater. Sci.* 17 (2013) 271–276. doi:10.1016/j.cossms.2013.09.005.
- [162] S. Plimpton, Fast Parallel Algorithms for Short-Range Molecular Dynamics, *J. Comput. Phys.* 117 (1995) 1–19. doi:10.1006/jcph.1995.1039.
- [163] D.M. Beazley, P.S. Lomdahl, Message-Passing Multi-Cell Molecular Dynamics on the Connection Machine 5, *ArXivcomp-Gas9303002*. (1993). <http://arxiv.org/abs/comp-gas/9303002> (accessed August 3, 2014).
- [164] D.M. Beazley, P.S. Lomdahl, Message-passing multi-cell molecular dynamics on the connection machine 5, *Parallel Comput.* 20 (1994) 173–195. doi:10.1016/0167-8191(94)90080-9.
- [165] D.M. Beazley, P.S. Lomdahl, Lightweight Computational Steering of Very Large Scale Molecular Dynamics Simulations, in: *Proc. 1996 ACMIEEE Conf. Supercomput. 1996*, 1996: pp. 50–50. doi:10.1109/SUPERC.1996.183551.
- [166] P.S. Lomdahl, P. Tamayo, N. Gronbech-Jensen, D.M. Beazley, 50 GFlops molecular dynamics on the Connection Machine-5, in: *Supercomput. 93 Proc.*, 1993: pp. 520–527. doi:10.1109/SUPERC.1993.1263501.
- [167] P.S. Lomdahl, D.M. Beazley, P. Tamayo, N. Gronbech-Jensen, Multi-Million Particle Molecular Dynamics on The CM-5, *Int. J. Mod. Phys. C.* 4 (1993) 1075–1084. doi:10.1142/S0129183193000835.
- [168] M.S. Warren, T.C. Germann, P.S. Lomdahl, D.M. Beazley, J.K. Salmon, Avalon: An Alpha/Linux Cluster Achieves 10 Gflops for \$15K, in: *Proc. 1998 ACMIEEE Conf. Supercomput., IEEE Computer Society, Washington, DC, USA, 1998*: pp. 1–11. <http://dl.acm.org/citation.cfm?id=509058.509130> (accessed August 3, 2014).
- [169] A.G. Frøseth, H. Van Swygenhoven, P.M. Derlet, Developing realistic grain boundary networks for use in molecular dynamics simulations, *Acta Mater.* 53 (2005) 4847–4856. doi:10.1016/j.actamat.2005.06.032.
- [170] T. Xu, M. Li, Geometric methods for microstructure rendition and atomic characterization of poly- and nano-crystalline materials, *Philos. Mag.* 90 (2010) 2191–2222. doi:10.1080/14786431003630843.
- [171] M. Li, T. Xu, Topological and atomic scale characterization of grain boundary networks in polycrystalline and nanocrystalline materials, *Prog. Mater. Sci.* 56 (2011) 864–899. doi:10.1016/j.pmatsci.2011.01.011.
- [172] S. Jolles, Primäre und sekundäre polare Räume einer linearen Strahlenkongruenz., *J. Für Reine Angew. Math.* 134 (1908) 1–14.

- [173] M.I. Mendelson, Average Grain Size in Polycrystalline Ceramics, *J. Am. Ceram. Soc.* 52 (1969) 443–446. doi:10.1111/j.1151-2916.1969.tb11975.x.
- [174] M.A. Tschopp, D.L. McDowell, Asymmetric tilt grain boundary structure and energy in copper and aluminium, *Philos. Mag.* 87 (2007) 3871–3892. doi:10.1080/14786430701455321.
- [175] M.A. Tschopp, G.J. Tucker, D.L. McDowell, Atomistic simulations of tension–compression asymmetry in dislocation nucleation for copper grain boundaries, *Comput. Mater. Sci.* 44 (2008) 351–362. doi:10.1016/j.commatsci.2008.03.041.
- [176] S.-N. Luo, T.C. Germann, D.L. Tonks, Spall damage of copper under supported and decaying shock loading, *J. Appl. Phys.* 106 (2009) 123518. doi:10.1063/1.3271414.
- [177] R.F. Smith, R.W. Minich, R.E. Rudd, J.H. Eggert, C.A. Bolme, S.L. Brygoo, A.M. Jones, G.W. Collins, Orientation and rate dependence in high strain-rate compression of single-crystal silicon, *Phys. Rev. B.* 86 (2012) 245204. doi:10.1103/PhysRevB.86.245204.
- [178] C.-H. Lu, E.N. Hahn, B.A. Remington, B.R. Maddox, E.M. Bringa, M.A. Meyers, Phase Transformation in Tantalum under Extreme Laser Deformation, *Sci. Rep.* 5 (2015) 15064. doi:10.1038/srep15064.
- [179] R. Ravelo, B.L. Holian, T.C. Germann, High Strain Rates Effects in Quasi-Isentropic Compression of Solids, *AIP Conf. Proc.* 1195 (2009) 825–828.
- [180] J. Belak, On the nucleation and growth of voids at high strain-rates, *J. Comput.-Aided Mater. Des.* 5 (1998) 193–206. doi:10.1023/A:1008685029849.
- [181] J.W. Swegle, D.E. Grady, Shock viscosity and the prediction of shock wave rise times, *J. Appl. Phys.* 58 (1985) 692–701. doi:10.1063/1.336184.
- [182] L.E. Murr, M.A. Meyers, C.-S. Niou, Y.J. Chen, S. Pappu, C. Kennedy, Shock-induced deformation twinning in tantalum, *Acta Mater.* 45 (1997) 157–175. doi:10.1016/S1359-6454(96)00145-0.
- [183] Hirth, Swygenhoven, *Dislocations in Solids: A Tribute to F.R.N. Nabarro*, Elsevier, 2011.
- [184] A. Stukowski, Computational Analysis Methods in Atomistic Modeling of Crystals, *JOM.* 66 (2013) 399–407. doi:10.1007/s11837-013-0827-5.
- [185] A. Stukowski, Visualization and analysis of atomistic simulation data with OVITO—the Open Visualization Tool, *Model. Simul. Mater. Sci. Eng.* 18 (2010) 15012. doi:10.1088/0965-0393/18/1/015012.

- [186] A.P. Thompson, S.J. Plimpton, W. Mattson, General formulation of pressure and stress tensor for arbitrary many-body interaction potentials under periodic boundary conditions, *J. Chem. Phys.* 131 (2009) 154107. doi:10.1063/1.3245303.
- [187] B.L. Holian, P.S. Lomdahl, Plasticity Induced by Shock Waves in Nonequilibrium Molecular-Dynamics Simulations, *Science*. 280 (1998) 2085–2088. doi:10.1126/science.280.5372.2085.
- [188] S. Plimpton, A.P. Thompson, P. Crozier, A. Kohlmeyer, LAMMPS Molecular Dynamics Simulator, n.d.
- [189] H. Tsuzuki, P.S. Branicio, J.P. Rino, Structural characterization of deformed crystals by analysis of common atomic neighborhood, *Comput. Phys. Commun.* 177 (2007) 518–523. doi:10.1016/j.cpc.2007.05.018.
- [190] A. Stukowski, Structure identification methods for atomistic simulations of crystalline materials, *Model. Simul. Mater. Sci. Eng.* 20 (2012) 45021. doi:10.1088/0965-0393/20/4/045021.
- [191] J.D. Honeycutt, H.C. Andersen, Molecular dynamics study of melting and freezing of small Lennard-Jones clusters, *J. Phys. Chem.* 91 (1987) 4950–4963. doi:10.1021/j100303a014.
- [192] D. Faken, H. Jónsson, Systematic analysis of local atomic structure combined with 3D computer graphics, *Comput. Mater. Sci.* 2 (1994) 279–286. doi:10.1016/0927-0256(94)90109-0.
- [193] K.S. Vahvaselk?, J.M. Mangs, X-ray diffraction study of liquid sulfur, *Phys. Scr.* 38 (1988) 737. doi:10.1088/0031-8949/38/5/017.
- [194] Y. Waseda, *The structure of non-crystalline materials: liquids and amorphous solids*, McGraw-Hill International Book Co., 1980.
- [195] Alexander, K. Albe, Dislocation detection algorithm for atomistic simulations, *Model. Simul. Mater. Sci. Eng.* 18 (2010) 25016. doi:10.1088/0965-0393/18/2/025016.
- [196] C.J. Ruestes, E.M. Bringa, A. Stukowski, J.F. Rodríguez Nieva, Y. Tang, M.A. Meyers, Plastic deformation of a porous bcc metal containing nanometer sized voids, *Comput. Mater. Sci.* 88 (2014) 92–102. doi:10.1016/j.commatsci.2014.02.047.
- [197] R.E. Rudd, High-Rate Plastic Deformation of Nanocrystalline Tantalum to Large Strains: Molecular Dynamics Simulation, *Mater. Sci. Forum.* 633–634 (2009) 3–19. doi:10.4028/www.scientific.net/MSF.633-634.3.
- [198] R.E. Rudd, Plasticity and Failure in Nanocrystalline BCC Metals via Molecular Dynamics Simulation, Lawrence Livermore National Lab., Livermore, CA (United

- States). Funding organisation: US Department of Energy (United States), 2010. [http://inis.iaea.org/Search/search.aspx?orig\\_q=RN:41134004](http://inis.iaea.org/Search/search.aspx?orig_q=RN:41134004) (accessed January 9, 2015).
- [199] L. Wang, J.C. E, Y. Cai, F. Zhao, D. Fan, S.N. Luo, Shock-induced deformation of nanocrystalline Al: Characterization with orientation mapping and selected area electron diffraction, *J. Appl. Phys.* 117 (2015) 84301. doi:10.1063/1.4907672.
- [200] M.S. Daw, M.I. Baskes, Embedded-atom method: Derivation and application to impurities, surfaces, and other defects in metals, *Phys. Rev. B.* 29 (1984) 6443–6453. doi:10.1103/PhysRevB.29.6443.
- [201] S.M. Foiles, M.I. Baskes, Contributions of the embedded-atom method to materials science and engineering, *MRS Bull.* 37 (2012) 485–491. doi:10.1557/mrs.2012.93.
- [202] S.M. Foiles, Embedded-Atom and Related Methods for Modeling Metallic Systems., *MRS Bull.* 21 (1996) 24–28. doi:10.1557/S0883769400046261.
- [203] M. w. Finnis, Concepts for simulating and understanding materials at the atomic scale, *MRS Bull.* 37 (2012) 477–484. doi:10.1557/mrs.2012.92.
- [204] S.J. Plimpton, A.P. Thompson, Computational aspects of many-body potentials, *MRS Bull.* 37 (2012) 513–521. doi:10.1557/mrs.2012.96.
- [205] N. US Department of Commerce, Interatomic Potentials Repository Project, (n.d.). <http://www.ctcms.nist.gov/potentials/> (accessed May 29, 2015).
- [206] H.W. Sheng, M.J. Kramer, A. Cadien, T. Fujita, M.W. Chen, Highly optimized embedded-atom-method potentials for fourteen fcc metals, *Phys. Rev. B.* 83 (2011) 134118. doi:10.1103/PhysRevB.83.134118.
- [207] Z.-L. Liu, L.-C. Cai, X.-R. Chen, F.-Q. Jing, Molecular dynamics simulations of the melting curve of tantalum under pressure, *Phys. Rev. B.* 77 (2008) 24103. doi:10.1103/PhysRevB.77.024103.
- [208] J.A. Moriarty, Density-functional formulation of the generalized pseudopotential theory, *Phys. Rev. B.* 16 (1977) 2537–2555. doi:10.1103/PhysRevB.16.2537.
- [209] J.A. Moriarty, Density-functional formulation of the generalized pseudopotential theory. II, *Phys. Rev. B.* 26 (1982) 1754–1780. doi:10.1103/PhysRevB.26.1754.
- [210] J.A. Moriarty, Density-functional formulation of the generalized pseudopotential theory. III. Transition-metal interatomic potentials, *Phys. Rev. B.* 38 (1988) 3199–3231. doi:10.1103/PhysRevB.38.3199.
- [211] J.A. Moriarty, L.X. Benedict, J.N. Glosli, R.Q. Hood, D.A. Orlikowski, M.V. Patel, P. Söderlind, F.H. Streitz, M. Tang, L.H. Yang, Robust quantum-based interatomic

- potentials for multiscale modeling in transition metals, *J. Mater. Res.* 21 (2006) 563–573. doi:10.1557/jmr.2006.0070.
- [212] F.H. Streitz, J.N. Glosli, M.V. Patel, B. Chan, R.K. Yates, B.R. de Supinski, J. Sexton, J.A. Gunnels, Simulating solidification in metals at high pressure: The drive to petascale computing, *J. Phys. Conf. Ser.* 46 (2006) 254. doi:10.1088/1742-6596/46/1/037.
- [213] T. Opperstrup, A. Stukowski, J. Marian, A Highly Efficient MGPT Implementation for LAMMPS; with Strong Scaling, (2011). <http://www.osti.gov/scitech/biblio/1034136>.
- [214] A.P. Bartók, R. Kondor, G. Csányi, On representing chemical environments, *Phys. Rev. B.* 87 (2013) 184115. doi:10.1103/PhysRevB.87.184115.
- [215] A.P. Bartók, M.C. Payne, R. Kondor, G. Csányi, Gaussian Approximation Potentials: The Accuracy of Quantum Mechanics, without the Electrons, *Phys. Rev. Lett.* 104 (2010) 136403. doi:10.1103/PhysRevLett.104.136403.
- [216] W. Cai, V.V. Bulatov, J.F. Justo, A.S. Argon, S. Yip, Intrinsic Mobility of a Dissociated Dislocation in Silicon, *Phys. Rev. Lett.* 84 (2000) 3346–3349. doi:10.1103/PhysRevLett.84.3346.
- [217] T. Kumagai, S. Izumi, S. Hara, S. Sakai, Development of bond-order potentials that can reproduce the elastic constants and melting point of silicon for classical molecular dynamics simulation, *Comput. Mater. Sci.* 39 (2007) 457–464. doi:10.1016/j.commatsci.2006.07.013.
- [218] F.H. Stillinger, T.A. Weber, Computer simulation of local order in condensed phases of silicon, *Phys. Rev. B.* 31 (1985) 5262–5271. doi:10.1103/PhysRevB.31.5262.
- [219] K. Nordlund, M. Ghaly, R.S. Averback, M. Caturla, T. Diaz de la Rubia, J. Tarus, Defect production in collision cascades in elemental semiconductors and fcc metals, *Phys. Rev. B.* 57 (1998) 7556–7570. doi:10.1103/PhysRevB.57.7556.
- [220] J. Tersoff, Modeling solid-state chemistry: Interatomic potentials for multicomponent systems, *Phys. Rev. B.* 39 (1989) 5566–5568. doi:10.1103/PhysRevB.39.5566.
- [221] M.Z. Bazant, E. Kaxiras, J.F. Justo, Environment Dependent Interatomic Potential for Bulk Silicon, *Phys. Rev. B.* 56 (1997) 8542–8552. doi:10.1103/PhysRevB.56.8542.
- [222] J.F. Justo, M.Z. Bazant, E. Kaxiras, V.V. Bulatov, S. Yip, Interatomic Potential for Silicon Defects and Disordered Phases, *Phys. Rev. B.* 58 (1998) 2539–2550. doi:10.1103/PhysRevB.58.2539.

- [223] M.Z. Bazant, E. Kaxiras, Modeling of Covalent Bonding in Solids by Inversion of Cohesive Energy Curves, *Phys. Rev. Lett.* 77 (1996) 4370–4373. doi:10.1103/PhysRevLett.77.4370.
- [224] J. Godet, L. Pizzagalli, S. Brochard, P. Beauchamp, Comparison between classical potentials and ab initio methods for silicon under large shear, *J. Phys. Condens. Matter.* 15 (2003) 6943. doi:10.1088/0953-8984/15/41/004.
- [225] X. Gu, Y. Lin, I.I. Oleynik, C.T. White, Molecular Dynamics Simulations of Shock-Induced Defect Healing in Silicon, *AIP Conf. Proc.* 1195 (2009) 793–796. doi:10.1063/1.3295260.
- [226] I.I. Oleynik, S.V. Zybin, M.L. Elert, C.T. White, Shear Stresses in Shock-Compressed Covalent Solids, 845 (2006) 417–420. doi:10.1063/1.2263350.
- [227] I.I. Oleynik, S.V. Zybin, M.L. Elert, C.T. White, Nanoscale Molecular Dynamics Simulation of Shock Compression of Silicon, *AIP Conf. Proc.* 845 (2006) 413–416. doi:10.1063/1.2263349.
- [228] G. Mogni, A. Higginbotham, K. Gaál-Nagy, N. Park, J.S. Wark, Molecular dynamics simulations of shock-compressed single-crystal silicon, *Phys. Rev. B.* 89 (2014) 64104. doi:10.1103/PhysRevB.89.064104.
- [229] L.M. Hale, D.-B. Zhang, X. Zhou, J.A. Zimmerman, N.R. Moody, T. Dumitrica, R. Ballarini, W.W. Gerberich, Dislocation morphology and nucleation within compressed Si nanospheres: A molecular dynamics study, *Comput. Mater. Sci.* 54 (2012) 280–286. doi:10.1016/j.commatsci.2011.11.004.
- [230] P.K. Schelling, Phase behavior and kinetics of a new bond-order potential for silicon, *Comput. Mater. Sci.* 44 (2008) 274–279. doi:10.1016/j.commatsci.2008.03.023.
- [231] V.S. Dozhikov, A.Y. Basharin, P.R. Levashov, Two-phase simulation of the crystalline silicon melting line at pressures from –1 to 3 GPa, *J. Chem. Phys.* 137 (2012) 54502. doi:10.1063/1.4739085.
- [232] F. Romano, J. Russo, H. Tanaka, Novel stable crystalline phase for the Stillinger-Weber potential, *Phys. Rev. B.* 90 (2014) 14204. doi:10.1103/PhysRevB.90.014204.
- [233] J. Crain, R.O. Piltz, G.J. Ackland, S.J. Clark, M.C. Payne, V. Milman, J.S. Lin, P.D. Hatton, Y.H. Nam, Tetrahedral structures and phase transitions in III-V semiconductors, *Phys. Rev. B.* 50 (1994) 8389–8401. doi:10.1103/PhysRevB.50.8389.
- [234] P. Németh, L.A.J. Garvie, T. Aoki, N. Dubrovinskaia, L. Dubrovinsky, P.R. Buseck, Lonsdaleite is faulted and twinned cubic diamond and does not exist as a discrete material, *Nat. Commun.* 5 (2014). doi:10.1038/ncomms6447.



- [235] Y. Gogotsi, V. Domnich, High Pressure Surface Science and Engineering, CRC Press, 2003.
- [236] A. Fissel, C. Wang, E. Bugiel, H.J. Osten, Epitaxial growth of non-cubic silicon, *Microelectron. J.* 36 (2005) 506–509. doi:10.1016/j.mejo.2005.02.064.
- [237] V. Domnich, Y. Gogotsi, Y. Aratyn, W.M. Kriven, Temperature dependence of silicon hardness: Experimental evidence of phase transformations, *Rev. Adv. Mater. Sci.* (17) 2008.
- [238] S. Goel, X. Luo, A. Agrawal, R.L. Reuben, Diamond machining of silicon: A review of advances in molecular dynamics simulation, *Int. J. Mach. Tools Manuf.* 88 (2015) 131–164. doi:10.1016/j.ijmachtools.2014.09.013.
- [239] L.L. Boyer, E. Kaxiras, J.L. Feldman, J.Q. Broughton, M.J. Mehl, New low-energy crystal structure for silicon, *Phys. Rev. Lett.* 67 (1991) 715–718. doi:10.1103/PhysRevLett.67.715.
- [240] C. Cheng, W.H. Huang, H.J. Li, Thermodynamics of uniaxial phase transition: *Ab initio* study of the diamond-to- $\beta$ -tin transition in Si and Ge, *Phys. Rev. B.* 63 (2001) 153202. doi:10.1103/PhysRevB.63.153202.
- [241] K. Gaál-Nagy, D. Strauch, Transition pressures and enthalpy barriers for the cubic diamond  $\rightarrow \beta$ -tin transition in Si and Ge under nonhydrostatic conditions, *Phys. Rev. B.* 73 (2006) 134101. doi:10.1103/PhysRevB.73.134101.
- [242] R.G. Hennig, A. Wadehra, K.P. Driver, W.D. Parker, C.J. Umrigar, J.W. Wilkins, Phase transformation in Si from semiconducting diamond to metallic  $\beta$ -Sn phase in QMC and DFT under hydrostatic and anisotropic stress, *Phys. Rev. B.* 82 (2010) 14101. doi:10.1103/PhysRevB.82.014101.
- [243] Y.B. Gerbig, C.A. Michaels, A.M. Forster, R.F. Cook, *In situ* observation of the indentation-induced phase transformation of silicon thin films, *Phys. Rev. B.* 85 (2012) 104102. doi:10.1103/PhysRevB.85.104102.
- [244] Y.B. Gerbig, C.A. Michaels, R.F. Cook, In situ observation of the spatial distribution of crystalline phases during pressure-induced transformations of indented silicon thin films, *J. Mater. Res.* 30 (2015) 390–406. doi:10.1557/jmr.2014.316.
- [245] C.F. Sanz-Navarro, S.D. Kenny, R. Smith, Atomistic simulations of structural transformations of silicon surfaces under nanoindentation, *Nanotechnology.* 15 (2004) 692. doi:10.1088/0957-4484/15/5/049.
- [246] D.E. Kim, S.I. Oh, Atomistic simulation of structural phase transformations in monocrystalline silicon induced by nanoindentation, *Nanotechnology.* 17 (2006) 2259. doi:10.1088/0957-4484/17/9/031.

- [247] D.E. Kim, S.I. Oh, Deformation pathway to high-pressure phases of silicon during nanoindentation, *J. Appl. Phys.* 104 (2008) 13502. doi:10.1063/1.2949404.
- [248] Y.-H. Lin, S.-R. Jian, Y.-S. Lai, P.-F. Yang, Molecular Dynamics Simulation of Nanoindentation-induced Mechanical Deformation and Phase Transformation in Monocrystalline Silicon, *Nanoscale Res. Lett.* 3 (2008) 71. doi:10.1007/s11671-008-9119-3.
- [249] J. Tersoff, New empirical model for the structural properties of silicon, *Phys. Rev. Lett.* 56 (1986) 632–635. doi:10.1103/PhysRevLett.56.632.
- [250] J. Tersoff, Empirical interatomic potential for silicon with improved elastic properties, *Phys. Rev. B.* 38 (1988) 9902–9905. doi:10.1103/PhysRevB.38.9902.
- [251] P. Erhart, K. Albe, Analytical potential for atomistic simulations of silicon, carbon, and silicon carbide, *Phys. Rev. B.* 71 (2005) 35211. doi:10.1103/PhysRevB.71.035211.
- [252] R.F. Smith, C.A. Bolme, D.J. Erskine, P.M. Celliers, S. Ali, J.H. Eggert, S.L. Brygoo, B.D. Hammel, J. Wang, G.W. Collins, Heterogeneous flow and brittle failure in shock-compressed silicon, *J. Appl. Phys.* 114 (2013) 133504. doi:10.1063/1.4820927.
- [253] H. Kishimura, H. Matsumoto, Effect of phase transition in shock-recovered silicon, *J. Appl. Phys.* 103 (2008) 23505. doi:10.1063/1.2830805.
- [254] H. Kishimura, H. Matsumoto, N.N. Thadhani, Effect of shock compression on single crystalline silicon, *J. Phys. Conf. Ser.* 215 (2010) 12145. doi:10.1088/1742-6596/215/1/012145.
- [255] M.C. Gupta, A.L. Ruoff, Static compression of silicon in the [100] and in the [111] directions, *J. Appl. Phys.* 51 (1980) 1072–1075. doi:10.1063/1.327714.
- [256] S.J. Turneaure, Y.M. Gupta, Inelastic deformation and phase transformation of shock compressed silicon single crystals, *Appl. Phys. Lett.* 91 (2007) 201913. doi:10.1063/1.2814067.
- [257] W.H. Gust, E.B. Royce, Axial Yield Strengths and Two Successive Phase Transition Stresses for Crystalline Silicon, *J. Appl. Phys.* 42 (1971) 1897–1905. doi:10.1063/1.1660465.
- [258] B.B. Karki, G.J. Ackland, J. Crain, Elastic instabilities in crystals from ab initio stress - strain relations, *J. Phys. Condens. Matter.* 9 (1997) 8579. doi:10.1088/0953-8984/9/41/005.

- [259] A.C.T. van Duin, A. Strachan, S. Stewman, Q. Zhang, X. Xu, W.A. Goddard, ReaxFFSiO Reactive Force Field for Silicon and Silicon Oxide Systems, *J. Phys. Chem. A*. 107 (2003) 3803–3811. doi:10.1021/jp0276303.
- [260] V. Mazhukin, A. Shapranov, O. Koroleva, A. Rudenko, Molecular dynamics simulation of critical point parameters for silicon, *Math. Montisnigri*. 31 (2014) 64–77.
- [261] S.K. Deb, M. Wilding, M. Somayazulu, P.F. McMillan, Pressure-induced amorphization and an amorphous–amorphous transition in densified porous silicon, *Nature*. 414 (2001) 528–530. doi:10.1038/35107036.
- [262] V. Mazhukin, A. Shapranov, O. Koroleva, A. Rudenko, Molecular dynamics simulation of critical point parameters for silicon, *Math. Montisnigri*. 31 (2014) 64–77.
- [263] E.J. Reed, L.E. Fried, J.D. Joannopoulos, A Method for Tractable Dynamical Studies of Single and Double Shock Compression, *Phys. Rev. Lett.* 90 (2003) 235503. doi:10.1103/PhysRevLett.90.235503.
- [264] T. Goto, T. Sato, Y. Syono, Reduction of Shear Strength and Phase-Transition in Shock-Loaded Silicon, *Jpn. J. Appl. Phys.* 21 (1982) L369. doi:10.1143/JJAP.21.L369.
- [265] W.R. Grigsby, Experimental studies of high energy density silicon using ultra-fast lasers, Thesis, 2007. <https://repositories.lib.utexas.edu/handle/2152/3222> (accessed August 1, 2016).
- [266] M. Pavlovskii, Formation of metallic modifications of germanium and silicon under shock loading, *Sov. Phys.-Solid State*. 9 (1968) 2514–2518.
- [267] O. Strickson, E. Artacho,  $\mathit{Ab}$   $\mathit{initio}$  calculation of the shock Hugoniot of bulk silicon, *Phys. Rev. B*. 93 (2016) 94107. doi:10.1103/PhysRevB.93.094107.
- [268] C.H. Lu, B.A. Remington, B.R. Maddox, B. Kad, H.S. Park, M. Kawasaki, T.G. Langdon, M.A. Meyers, Laser compression of nanocrystalline tantalum, *Acta Mater.* 61 (2013) 7767–7780. doi:10.1016/j.actamat.2013.09.016.
- [269] C.H. Lu, B.A. Remington, B.R. Maddox, B. Kad, H.S. Park, S.T. Prisbrey, M.A. Meyers, Laser compression of monocrystalline tantalum, *Acta Mater.* 60 (2012) 6601–6620. doi:10.1016/j.actamat.2012.08.026.
- [270] T.P. Remington, C.J. Ruestes, E.M. Bringa, B.A. Remington, C.H. Lu, B. Kad, M.A. Meyers, Plastic deformation in nanoindentation of tantalum: A new mechanism for prismatic loop formation, *Acta Mater.* 78 (2014) 378–393. doi:10.1016/j.actamat.2014.06.058.

- [271] J. Monk, B. Hyde, D. Farkas, The role of partial grain boundary dislocations in grain boundary sliding and coupled grain boundary motion, *J. Mater. Sci.* 41 (2006) 7741–7746. doi:10.1007/s10853-006-0552-3.
- [272] H.-B. Zhou, Y.-L. Liu, C. Duan, S. Jin, Y. Zhang, F. Gao, X. Shu, G.-H. Lu, Effect of vacancy on the sliding of an iron grain boundary, *J. Appl. Phys.* 109 (2011) 113512. doi:10.1063/1.3593182.
- [273] N. Gao, C.-C. Fu, M. Samaras, R. Schäublin, M. Victoria, W. Hoffelner, Multiscale modelling of bi-crystal grain boundaries in bcc iron, *J. Nucl. Mater.* 385 (2009) 262–267. doi:10.1016/j.jnucmat.2008.12.016.
- [274] B. Hyde, D. Farkas, M.J. Caturla, Atomistic sliding mechanisms of the  $\Sigma=5$  symmetric tilt grain boundary in bcc iron, *Philos. Mag.* 85 (2005) 3795–3807. doi:10.1080/14786430500256342.
- [275] Y. Shibuta, S. Takamoto, T. Suzuki, A Molecular Dynamics Study of the Energy and Structure of the Symmetric Tilt Boundary of Iron, *ISIJ Int.* 48 (2008) 1582–1591. doi:10.2355/isijinternational.48.1582.
- [276] D. Saraev, S. Schmauder, Atomic-scale simulations of the interaction between dislocations and tilt grain boundaries in  $\alpha$ -iron, *Phys. Status Solidi B.* 240 (2003) 81–90. doi:10.1002/pssb.200301883.
- [277] A. Latapie, D. Farkas, Molecular dynamics investigation of the fracture behavior of nanocrystalline  $\alpha$ -Fe, *Phys. Rev. B.* 69 (2004) 134110. doi:10.1103/PhysRevB.69.134110.
- [278] G.H. Campbell, J. Belak, J.A. Moriarty, Atomic structure of the  $\Sigma 5$  (310)/[001] symmetric tilt grain boundary in molybdenum, *Acta Mater.* 47 (1999) 3977–3985. doi:10.1016/S1359-6454(99)00258-X.
- [279] J.M. Pénisson, M. Bacia, M. Biscondi, New carbides observed by high-resolution electron microscopy in a molybdenum bicrystal containing a  $\sigma=5$  symmetrical boundary, *Philos. Mag. A.* 73 (1996) 859–869. doi:10.1080/01418619608243692.
- [280] L. Wang, F. Zhao, F.P. Zhao, Y. Cai, Q. An, S.N. Luo, Grain boundary orientation effects on deformation of Ta bicrystal nanopillars under high strain-rate compression, *J. Appl. Phys.* 115 (2014) 53528. doi:10.1063/1.4864427.
- [281] M.J. Mills, M.S. Daw, G.J. Thomas, F. Cosandey, High-resolution transmission electron microscopy of grain boundaries in aluminum and correlation with atomistic calculations, *Ultramicroscopy.* 40 (1992) 247–257. doi:10.1016/0304-3991(92)90121-Y.

- [282] A.F. Wright, S.R. Atlas, Density-functional calculations for grain boundaries in aluminum, *Phys. Rev. B.* 50 (1994) 15248–15260. doi:10.1103/PhysRevB.50.15248.
- [283] D. Wolf, Correlation between the energy and structure of grain boundaries in b.c.c. metals I. Symmetrical boundaries on the (110) and (100) planes, *Philos. Mag. Part B.* 59 (1989) 667–680. doi:10.1080/13642818908211183.
- [284] D. Yeşiltepe, T.A. Arias, Atomic-level physics of grain boundaries in bcc molybdenum, *Phys. Rev. B.* 64 (2001) 174101. doi:10.1103/PhysRevB.64.174101.
- [285] G.H. Campbell, J. Belak, J.A. Moriarty, Atomic structure of the  $\sigma_5$  (310)/[001] symmetric tilt grain boundary in tantalum, *Scr. Mater.* 43 (2000) 659–664. doi:10.1016/S1359-6462(00)00475-9.
- [286] G.H. Campbell, W.E. King, J. Belak, J.A. Moriarty, S.M. Foiles, Electronic Effects on Grain Boundary Structure in Bcc Metals, in: *Symp. Q – Adv. Mater. Probl. Solving Electron Microsc.*, 1999. doi:10.1557/PROC-589-347.
- [287] J.-M. Zhang, D.-D. Wang, K.-W. Xu, Calculation of the surface energy of bcc transition metals by using the second nearest-neighbor modified embedded atom method, *Appl. Surf. Sci.* 252 (2006) 8217–8222. doi:10.1016/j.apsusc.2005.10.043.
- [288] T. Ochs, C. Elsässer, M. Mrovec, V. Vitek, J. Belak, J.A. Moriarty, Symmetrical tilt grain boundaries in bcc transition metals: Comparison of semiempirical with ab-initio total-energy calculations, *Philos. Mag. A.* 80 (2000) 2405–2423. doi:10.1080/01418610008216481.
- [289] K. Morita, H. Nakashima, Atomic periodicity of  $\langle 001 \rangle$  symmetric tilt boundary in molybdenum, *Mater. Sci. Eng. A.* 234–236 (1997) 1053–1056. doi:10.1016/S0921-5093(97)00306-7.
- [290] A. Morawiec, On “interface-plane scheme” and symmetric grain boundaries, *Z. Für Krist. Cryst. Mater.* 227 (2012) 199–206.
- [291] Z. Shi, C.V. Singh, Competing twinning mechanisms in body-centered cubic metallic nanowires, *Scr. Mater.* 113 (2016) 214–217. doi:10.1016/j.scriptamat.2015.11.006.
- [292] L. Zhi-Wu, K. Xiang-Shan, Liu-Wei, L. Chang-Song, F. Qian-Feng, Segregation of alloying atoms at a tilt symmetric grain boundary in tungsten and their strengthening and embrittling effects, *Chin. Phys. B.* 23 (2014) 106107. doi:10.1088/1674-1056/23/10/106107.

- [293] T. Ochs, O. Beck, C. Elsässer, B. Meyer, Symmetrical tilt grain boundaries in body-centred cubic transition metals: An ab initio local-density-functional study, *Philos. Mag. A.* 80 (2000) 351–372. doi:10.1080/01418610008212057.
- [294] G.H. Campbell, S.M. Foiles, P. Gumbsch, M. Rühle, W.E. King, Atomic structure of the (310) twin in niobium: Experimental determination and comparison with theoretical predictions, *Phys. Rev. Lett.* 70 (1993) 449–452. doi:10.1103/PhysRevLett.70.449.
- [295] A.P. Sutton, V. Vitek, On the Structure of Tilt Grain Boundaries in Cubic Metals. III. Generalizations of the Structural Study and Implications for the Properties of Grain Boundaries, *Philos. Trans. R. Soc. Lond. Math. Phys. Eng. Sci.* 309 (1983) 55–68. doi:10.1098/rsta.1983.0022.
- [296] A.K. Zurek, W.R. Thissell, J.N. Johnson, D.L. Tonks, R. Hixson, Micromechanics of spall and damage in tantalum, *J. Mater. Process. Technol.* 60 (1996) 261–267. doi:10.1016/0924-0136(96)02340-0.
- [297] L. Soulard, J. Bontaz-Carion, J.P. Cuq-Lelandais, Experimental and numerical study of the tantalum single crystal spallation, *Eur. Phys. J. B.* 85 (2012) 1–15. doi:10.1140/epjb/e2012-30269-9.
- [298] L.M. Barker, R.E. Hollenbach, Laser interferometer for measuring high velocities of any reflecting surface, *J. Appl. Phys.* 43 (1972) 4669–4675. doi:10.1063/1.1660986.
- [299] L. Tollier, R. Fabbro, Study of the laser-driven spallation process by the VISAR interferometry technique. II. Experiment and simulation of the spallation process, *J. Appl. Phys.* 83 (1998) 1231–1237. doi:10.1063/1.366820.
- [300] J.M. Rivas, A.K. Zurek, W.R. Thissell, D.L. Tonks, R.S. Hixson, Quantitative description of damage evolution in ductile fracture of tantalum, *Metall. Mater. Trans. A.* 31 (2000) 845–851. doi:10.1007/s11661-000-1004-3.
- [301] J.-P. Cuq-Lelandais, M. Boustie, L. Soulard, L. Berthe, J. Bontaz-Carion, T. de Resseguier, Investigation of laser shock induced ductile damage at ultra-high strain rate by using large scale MD simulations, *AIP Conf. Proc.* 1426 (2012) 1167–1170. doi:10.1063/1.3686487.
- [302] S.I. Ashitkov, M.B. Agranat, G.I. Kanel', P.S. Komarov, V.E. Fortov, Behavior of aluminum near an ultimate theoretical strength in experiments with femtosecond laser pulses, *JETP Lett.* 92 (2010) 516–520. doi:10.1134/S0021364010200051.
- [303] S.J. Fensin, J.P. Escobedo-Diaz, C. Brandl, E.K. Cerreta, G.T. Gray III, T.C. Germann, S.M. Valone, Effect of loading direction on grain boundary failure under shock loading, *Acta Mater.* 64 (2014) 113–122. doi:10.1016/j.actamat.2013.11.026.

- [304] D.E. Spearot, K.I. Jacob, D.L. McDowell, Dislocation nucleation from bicrystal interfaces with dissociated structure, *Int. J. Plast.* 23 (2007) 143–160. doi:10.1016/j.ijplas.2006.03.008.
- [305] L. Smith, J.A. Zimmerman, L.M. Hale, D. Farkas, Molecular dynamics study of deformation and fracture in a tantalum nano-crystalline thin film, *Model. Simul. Mater. Sci. Eng.* 22 (2014) 45010. doi:10.1088/0965-0393/22/4/045010.
- [306] Z. Pan, Y. Li, Q. Wei, Tensile properties of nanocrystalline tantalum from molecular dynamics simulations, *Acta Mater.* 56 (2008) 3470–3480. doi:10.1016/j.actamat.2008.03.025.
- [307] Q. An, W.Z. Han, S.N. Luo, T.C. Germann, D.L. Tonks, W.A.G. Iii, Left-right loading dependence of shock response of (111)/(112) Cu bicrystals: Deformation and spallation, *J. Appl. Phys.* 111 (2012) 53525. doi:10.1063/1.3692079.
- [308] S.-N. Luo, T.C. Germann, Q. An, L.-B. Han, Shock-Induced Spall in Copper: The Effects of Anisotropy, Temperature, Defects and Loading Pulse, *AIP Conf. Proc.* 1195 (2009) 1015–1018. doi:10.1063/1.3294971.
- [309] E.M. Bringa, S. Traiviratana, M.A. Meyers, Void initiation in fcc metals: Effect of loading orientation and nanocrystalline effects, *Acta Mater.* 58 (2010) 4458–4477. doi:10.1016/j.actamat.2010.04.043.
- [310] Y. Tang, E.M. Bringa, M.A. Meyers, Ductile tensile failure in metals through initiation and growth of nanosized voids, *Acta Mater.* 60 (2012) 4856–4865. doi:10.1016/j.actamat.2012.05.030.
- [311] S.-N. Luo, Shock compression and spallation of single crystal tantalum, in: 2012: pp. 1259–1262. doi:10.1063/1.3686509.
- [312] Y. Tang, E.M. Bringa, B.A. Remington, M.A. Meyers, Growth and collapse of nanovoids in tantalum monocrystals, *Acta Mater.* 59 (2011) 1354–1372. doi:10.1016/j.actamat.2010.11.001.
- [313] D. Tramontina, P. Erhart, T. Germann, J. Hawreliak, A. Higginbotham, N. Park, R. Ravelo, A. Stukowski, M. Suggit, Y. Tang, J. Wark, E. Bringa, Molecular dynamics simulations of shock-induced plasticity in tantalum, *High Energy Density Phys.* 10 (2014) 9–15. doi:10.1016/j.hedp.2013.10.007.
- [314] A. Strachan, T. Çağın, W. Goddard, Critical behavior in spallation failure of metals, *Phys. Rev. B.* 63 (2001). doi:10.1103/PhysRevB.63.060103.
- [315] J.N. Johnson, R.S. Hixson, D.L. Tonks, A.K. Zurek, Rate-dependent spallation properties of tantalum, *AIP Conf. Proc.* 370 (1996) 523–526. doi:10.1063/1.50651.

- [316] G. Roy, Vers une modélisation approfondie de l'endommagement ductile dynamique: investigation expérimentale d'une nuance de tantale et développements théoriques, Ph.D. Thesis, Poitiers, 2003.
- [317] Q. An, R. Ravelo, T.C. Germann, W.Z. Han, S.-N.N. Luo, D.L. Tonks, I.I.I. W. A. Goddard, Shock compression and spallation of single crystal tantalum, *AIP Conf. Proc.* 1426 (2012) 1259–1262. doi:10.1063/1.3686509.
- [318] J.C.F. Millett, G. Whiteman, N.T. Park, S. Case, N.K. Bourne, The role of cold work on the shock response of tantalum, *J. Appl. Phys.* 113 (2013) 233502. doi:10.1063/1.4810896.
- [319] S.A. Abrosimov, A.P. Bazhulin, V.V. Voronov, A.A. Geras'kin, I.K. Krasnyuk, P.P. Pashinin, A.Y. Semenov, I.A. Stuchebryukhov, K.V. Khishchenko, V.E. Fortov, Specific features of the behaviour of targets under negative pressures created by a picosecond laser pulse, *Quantum Electron.* 43 (2013) 246–251. doi:10.1070/QE2013v043n03ABEH015106.
- [320] B. Glam, M. Werdiger, Y. Horovitz, E. Moshe, S.L. Pistinner, Dynamic strength of tantalum under impact, *J. Phys. Conf. Ser.* 500 (2014) 112029. doi:10.1088/1742-6596/500/11/112029.
- [321] T.P. Remington, Extreme Response in Tension and Compression of Tantalum, Ph.D. Thesis, University of California San Diego, 2015. <http://www.escholarship.org/uc/item/42d8330s>.
- [322] S. Cochran, D. Banner, Spall studies in uranium, *J. Appl. Phys.* 48 (1977) 2729–2737. doi:10.1063/1.324125.
- [323] D. Steinberg, Equation of state and strength properties of selected materials, Lawrence Livermore National Laboratory Livermore, CA, 1996.
- [324] Z.-L. Liu, L.-C. Cai, X.-R. Chen, Q. Wu, F.-Q. Jing, Ab initio refinement of the thermal equation of state for bcc tantalum: the effect of bonding on anharmonicity, *J. Phys. Condens. Matter.* 21 (2009) 95408. doi:10.1088/0953-8984/21/9/095408.
- [325] B.L. Boyce, B.G. Clark, P. Lu, J.D. Carroll, C.R. Weinberger, The Morphology of Tensile Failure in Tantalum, *Metall. Mater. Trans. A.* 44 (2013) 4567–4580. doi:10.1007/s11661-013-1814-8.
- [326] N.J. Wagner, B.L. Holian, A.F. Voter, Molecular-dynamics simulations of two-dimensional materials at high strain rates, *Phys. Rev. A.* 45 (1992) 8457–8470. doi:10.1103/PhysRevA.45.8457.
- [327] E.N. Hahn, S.J. Fensin, T.C. Germann, M.A. Meyers, Symmetric tilt boundaries in body-centered cubic tantalum, *Scr. Mater.* 116 (2016) 108–111. doi:10.1016/j.scriptamat.2016.01.038.



- [328] H.-J. Chang, J. Segurado, O.R. de la Fuente, B.M. Pabón, J. LLorca, Molecular dynamics modeling and simulation of void growth in two dimensions, *Model. Simul. Mater. Sci. Eng.* 21 (2013) 75010. doi:10.1088/0965-0393/21/7/075010.
- [329] D.R. Tramontina, E.N. Hahn, M.A. Meyers, E.M. Bringa, Simulation of Tantalum Nanocrystals Under Shock Wave Loading: Dislocations and Twinning, *AIP Conf. Proc.* In press (2016).
- [330] D. Tonks, C.A. Bronkhorst, J. Bingert, M.L. Elert, W.T. Buttler, J.P. Borg, J.L. Jordan, T.J. Vogler, A comparison of calculated damage from square waves and triangular waves, *AIP Conf. Proc.* 1426 (2012) 1045.
- [331] D. Koller, R. Hixson, G. Gray III, P. Rigg, L. Addessio, E. Cerreta, J. Maestas, C. Yablinsky, Influence of shock-wave profile shape on dynamically induced damage in high-purity copper, *J. Appl. Phys.* 98 (2005) 103518.
- [332] R.E. Rudd, Void growth in bcc metals simulated with molecular dynamics using the Finnis–Sinclair potential, *Philos. Mag.* 89 (2009) 3133–3161.
- [333] S.-N. Luo, Q. An, T.C. Germann, L.-B. Han, Shock-induced spall in solid and liquid Cu at extreme strain rates, *J. Appl. Phys.* 106 (2009) 13502. doi:10.1063/1.3158062.
- [334] A.E. Mayer, P.N. Mayer, Continuum model of tensile fracture of metal melts and its application to a problem of high-current electron irradiation of metals, *J. Appl. Phys.* 118 (2015) 35903. doi:10.1063/1.4926861.
- [335] Y.Y. Boguslavskii, Equation for the Melting Curve of Solids under High Pressure, *Phys. Status Solidi B.* 109 (1982) 145–151. doi:10.1002/pssb.2221090115.
- [336] D.B. Holtkamp, D.A. Clark, E.N. Ferm, R.A. Gallegos, D. Hammon, W.F. Hemsing, G.E. Hogan, V.H. Holmes, N.S.P. King, R. Liljestrang, R.P. Lopez, F.E. Merrill, C.L. Morris, K.B. Morley, M.M. Murray, P.D. Pazuchanics, K.P. Prestridge, J.P. Quintana, A. Saunders, T. Schafer, M.A. Shinas, H.L. Stacy, A Survey of High Explosive-Induced Damage and Spall in Selected Metals Using Proton Radiography, in: *AIP Conf. Proc.*, AIP Publishing, 2004: pp. 477–482. doi:10.1063/1.1780281.
- [337] C. Wu, L.V. Zhigilei, Microscopic mechanisms of laser spallation and ablation of metal targets from large-scale molecular dynamics simulations, *Appl. Phys. A.* 114 (2013) 11–32. doi:10.1007/s00339-013-8086-4.
- [338] G. Singh, R.P.S. Rathore, Generalised morse potential for B.C.C. complex metals, *Phys. Status Solidi B.* 135 (1986) 513–518. doi:10.1002/pssb.2221350208.
- [339] D.R. Olander, Description of the hydrogen-metal interaction by a morse potential function, *J. Phys. Chem. Solids.* 32 (1971) 2499–2516. doi:10.1016/S0022-3697(71)80097-5.

- [340] R. Ravelo, Q. An, T.C. Germann, B.L. Holian, Large-scale molecular dynamics simulations of shock induced plasticity in tantalum single crystals, *AIP Conf. Proc.* 1426 (2012) 1263–1266. doi:10.1063/1.3686510.
- [341] X.D. Dai, Y. Kong, J.H. Li, B.X. Liu, Extended Finnis–Sinclair potential for bcc and fcc metals and alloys, *J. Phys. Condens. Matter.* 18 (2006) 4527. doi:10.1088/0953-8984/18/19/008.
- [342] G.P. Purja Pun, K.A. Darling, L.J. Kecskes, Y. Mishin, Angular-dependent interatomic potential for the Cu–Ta system and its application to structural stability of nano-crystalline alloys, *Acta Mater.* 100 (2015) 377–391. doi:10.1016/j.actamat.2015.08.052.
- [343] L.M. Hsiung, D.H. Lassila, Shock-induced deformation twinning and omega transformation in tantalum and tantalum–tungsten alloys, *Acta Mater.* 48 (2000) 4851–4865. doi:10.1016/S1359-6454(00)00287-1.
- [344] C.J. Ruestes, E.M. Bringa, A. Stukowski, J.F. Rodríguez Nieva, G. Bertolino, Y. Tang, M.A. Meyers, Atomistic simulation of the mechanical response of a nanoporous body-centered cubic metal, *Scr. Mater.* 68 (2013) 817–820. doi:10.1016/j.scriptamat.2013.01.035.
- [345] L. Burakovsky, S.P. Chen, D.L. Preston, A.B. Belonoshko, A. Rosengren, A.S. Mikhaylushkin, S.I. Simak, J.A. Moriarty, High-Pressure-High-Temperature Polymorphism in Ta: Resolving an Ongoing Experimental Controversy, *Phys. Rev. Lett.* 104 (2010). doi:10.1103/PhysRevLett.104.255702.
- [346] D. Mukherjee, K.D. Joshi, S.C. Gupta, On high pressure  $\beta \rightarrow \omega$  phase transition in Ta and Zr-Nb, *J. Phys. Conf. Ser.* 377 (2012) 12072. doi:10.1088/1742-6596/377/1/012072.
- [347] E.N. Hahn, S. Zhao, E.M. Bringa, M.A. Meyers, Supersonic Dislocation Bursts in Silicon, *Sci. Rep.* 6 (2016) 26977. doi:10.1038/srep26977.
- [348] J.M.D. Lane, A.P. Thompson, T.J. Vogler, Enhanced densification under shock compression in porous silicon, *Phys. Rev. B.* 90 (2014) 134311. doi:10.1103/PhysRevB.90.134311.
- [349] K. Mylvaganam, L.C. Zhang, Nanotwinning in monocrystalline silicon upon nanoscratching, *Scr. Mater.* 65 (2011) 214–216. doi:10.1016/j.scriptamat.2011.04.012.
- [350] L.M. Hale, X. Zhou, J.A. Zimmerman, N.R. Moody, R. Ballarini, W.W. Gerberich, Phase transformations, dislocations and hardening behavior in uniaxially compressed silicon nanospheres, *Comput. Mater. Sci.* 50 (2011) 1651–1660. doi:10.1016/j.commatsci.2010.12.023.

- [351] P.M. Agrawal, L.M. Raff, R. Komanduri, Monte Carlo simulations of void-nucleated melting of silicon via modification in the Tersoff potential parameters, *Phys. Rev. B.* 72 (2005) 125206. doi:10.1103/PhysRevB.72.125206.
- [352] M. Timonova, B.J. Thijsse, Thermodynamic properties and phase transitions of silicon using a new MEAM potential, *Comput. Mater. Sci.* 48 (2010) 609–620. doi:10.1016/j.commatsci.2010.02.029.
- [353] S. Ryu, C.R. Weinberger, M.I. Baskes, W. Cai, Improved modified embedded-atom method potentials for gold and silicon, *Model. Simul. Mater. Sci. Eng.* 17 (2009) 75008. doi:10.1088/0965-0393/17/7/075008.
- [354] D. Sen, A. Cohen, A.P. Thompson, A. Van Duin, W.A. Goddard III, M.J. Buehler, Direct atomistic simulation of brittle-to-ductile transition in silicon single crystals, in: *Symp. KKLLNNOOPP – Integr. Miniaturized Mater.- Self-Assem. Device Integr.*, 2010. doi:10.1557/PROC-1272-PP04-13.
- [355] L. Pastewka, A. Klemenz, P. Gumbsch, M. Moseler, Screened empirical bond-order potentials for Si-C, *Phys. Rev. B.* 87 (2013) 205410. doi:10.1103/PhysRevB.87.205410.
- [356] C.A. Becker, F. Tavazza, Z.T. Trautt, R.A. Buarque de Macedo, Considerations for choosing and using force fields and interatomic potentials in materials science and engineering, *Curr. Opin. Solid State Mater. Sci.* 17 (2013) 277–283. doi:10.1016/j.cossms.2013.10.001.
- [357] S. Zhao, E.N. Hahn, B. Kad, B.A. Remington, C.E. Wehrenberg, E.M. Bringa, M.A. Meyers, Amorphization and nanocrystallization of silicon under shock compression, *Acta Mater.* 103 (2016) 519–533. doi:10.1016/j.actamat.2015.09.022.
- [358] S. Zhao, E.N. Hahn, B. Kad, B.A. Remington, E.M. Bringa, M.A. Meyers, Shock compression of [001] single crystal silicon, *Eur. Phys. J. Spec. Top.* 225 (2016) 335–341. doi:10.1140/epjst/e2016-02634-7.
- [359] A. Higginbotham, P.G. Stubbley, A.J. Comley, J.H. Eggert, J.M. Foster, D.H. Kalantar, D. McGonegle, S. Patel, L.J. Peacock, S.D. Rothman, R.F. Smith, M.J. Suggit, J.S. Wark, Inelastic response of silicon to shock compression, *Sci. Rep.* 6 (2016) 24211. doi:10.1038/srep24211.
- [360] A. Loveridge-Smith, A. Allen, J. Belak, T. Boehly, A. Hauer, B. Holian, D. Kalantar, G. Kyrala, R.W. Lee, P. Lomdahl, M.A. Meyers, D. Paisley, S. Pollaine, B. Remington, D.C. Swift, S. Weber, J.S. Wark, Anomalous Elastic Response of Silicon to Uniaxial Shock Compression on Nanosecond Time Scales, *Phys. Rev. Lett.* 86 (2001) 2349–2352. doi:10.1103/PhysRevLett.86.2349.

- [361] G.J. Cheng, M.A. Shehadeh, Dislocation behavior in silicon crystal induced by laser shock peening: A multiscale simulation approach, *Scr. Mater.* 53 (2005) 1013–1018. doi:10.1016/j.scriptamat.2005.07.014.
- [362] N.L. Coleburn, J.W. Forbes, H.D. Jones, Electrical measurements in silicon under shock-wave compression, *J. Appl. Phys.* 43 (1972) 5007–5012. doi:10.1063/1.1661061.
- [363] S.J. Turneaure, N. Sinclair, Y.M. Gupta, Real-Time Examination of Atomistic Mechanisms during Shock-Induced Structural Transformation in Silicon, *Phys. Rev. Lett.* 117 (2016) 45502. doi:10.1103/PhysRevLett.117.045502.
- [364] D.C. Swift, G.J. Ackland, A. Hauer, G.A. Kyrala, First-principles equations of state for simulations of shock waves in silicon, *Phys. Rev. B.* 64 (2001) 214107. doi:10.1103/PhysRevB.64.214107.
- [365] S.J. Turneaure, Y.M. Gupta, Real-time x-ray diffraction at the impact surface of shocked crystals, *J. Appl. Phys.* 111 (2012) 26101. doi:10.1063/1.3674276.
- [366] S.J. Turneaure, Y.M. Gupta, X-ray diffraction and continuum measurements in silicon crystals shocked below the elastic limit, *Appl. Phys. Lett.* 90 (2007) 51905. doi:10.1063/1.2436638.
- [367] M. Gamero-Castaño, A. Torrents, L. Valdevit, J.-G. Zheng, Pressure-Induced Amorphization in Silicon Caused by the Impact of Electrosprayed Nanodroplets, *Phys. Rev. Lett.* 105 (2010) 145701. doi:10.1103/PhysRevLett.105.145701.
- [368] J.S. Wark, R.R. Whitlock, A. Hauer, J.E. Swain, P.J. Solone, Shock launching in silicon studied with use of pulsed x-ray diffraction, *Phys. Rev. B.* 35 (1987) 9391–9394. doi:10.1103/PhysRevB.35.9391.
- [369] L. Rapp, B. Haberl, C.J. Pickard, J.E. Bradby, E.G. Gamaly, J.S. Williams, A.V. Rode, Experimental evidence of new tetragonal polymorphs of silicon formed through ultrafast laser-induced confined microexplosion, *Nat. Commun.* 6 (2015). doi:10.1038/ncomms8555.
- [370] R. Chen, J. Luo, D. Guo, H. Lei, Dynamic phase transformation of crystalline silicon under the dry and wet impact studied by molecular dynamics simulation, *J. Appl. Phys.* 108 (2010) 73521. doi:10.1063/1.3490757.
- [371] F. Saiz, M. Gamero-Castaño, Amorphization of silicon induced by nanodroplet impact: A molecular dynamics study, *J. Appl. Phys.* 112 (2012) 54302. doi:10.1063/1.4748177.
- [372] F. Saiz, M. Gamero-Castaño, Atomistic modeling of the sputtering of silicon by electrosprayed nanodroplets, *J. Appl. Phys.* 116 (2014) 54303. doi:10.1063/1.4892442.

- [373] S. Zhao, E.N. Hahn, Pressure and Shear Induced Amorphization of Silicon, (n.d.).
- [374] D. Többsen, N. Stübner, K. Knorr, H. Mayer, G. Lampert, E9: The new high-resolution neutron powder diffractometer at the Berlin neutron scattering center, in: *Mater. Sci. Forum, Trans Tech Publ*, 2001: pp. 288–293.
- [375] S. Wippermann, Y. He, M. Vörös, G. Galli, Novel silicon phases and nanostructures for solar energy conversion, *Appl. Phys. Rev.* 3 (2016) 40807. doi:10.1063/1.4961724.
- [376] D. Chrobak, N. Tymiak, A. Beaber, O. Ugurlu, W.W. Gerberich, R. Nowak, Deconfinement leads to changes in the nanoscale plasticity of silicon, *Nat. Nanotechnol.* 6 (2011) 480–484. doi:10.1038/nnano.2011.118.
- [377] J. Guérolé, S. Brochard, J. Godet, Unexpected slip mechanism induced by the reduced dimensions in silicon nanostructures: Atomistic study, *Acta Mater.* 59 (2011) 7464–7472. doi:10.1016/j.actamat.2011.08.039.
- [378] M.A. Hopcroft, W.D. Nix, T.W. Kenny, What is the Young's Modulus of Silicon?, *J. Microelectromechanical Syst.* 19 (2010) 229–238. doi:10.1109/JMEMS.2009.2039697.
- [379] C.S. John, The brittle-to-ductile transition in pre-cleaved silicon single crystals, *Philos. Mag.* 32 (1975) 1193–1212. doi:10.1080/14786437508228099.
- [380] S.J. Cook, P. Clancy, Comparison of semi-empirical potential functions for silicon and germanium, *Phys. Rev. B.* 47 (1993) 7686–7699. doi:10.1103/PhysRevB.47.7686.
- [381] H. Tsuzuki, P.S. Branicio, J.P. Rino, Molecular dynamics simulation of fast dislocations in copper, *Acta Mater.* 57 (2009) 1843–1855. doi:10.1016/j.actamat.2008.12.025.
- [382] C.S. Smith, *Metallographic Studies of Metals After Explosive Shock*, *Trans Met Soc AIME*. Vol: 212 (1958) 574–589.
- [383] M.A. Meyers, F. Gregori, B.K. Kad, M.S. Schneider, D.H. Kalantar, B.A. Remington, G. Ravichandran, T. Boehly, J.S. Wark, Laser-induced shock compression of monocrystalline copper: characterization and analysis, *Acta Mater.* 51 (2003) 1211–1228. doi:10.1016/S1359-6454(02)00420-2.
- [384] M.A. Meyers, A mechanism for dislocation generation in shock-wave deformation, *Scr. Metall.* 12 (1978) 21–26. doi:10.1016/0036-9748(78)90219-3.
- [385] P. Gumbsch, H. Gao, Dislocations Faster than the Speed of Sound, *Science*. 283 (1999) 965–968. doi:10.1126/science.283.5404.965.

- [386] Z. Jin, H. Gao, P. Gumbsch, Energy radiation and limiting speeds of fast moving edge dislocations in tungsten, *Phys. Rev. B.* 77 (2008) 94303. doi:10.1103/PhysRevB.77.094303.
- [387] Q. Li, S.-Q. Shi, Dislocation jumping over the sound barrier in tungsten, *Appl. Phys. Lett.* 80 (2002) 3069–3071. doi:10.1063/1.1473865.
- [388] A.K. Ghatak, L.S. Kothari, *An introduction to lattice dynamics*, Addison-Wesley London, 1972.
- [389] J.Y. Huang, H. Yasuda, H. Mori, Deformation-induced amorphization in ball-milled silicon, *Philos. Mag. Lett.* 79 (1999) 305–314. doi:10.1080/095008399177147.
- [390] E.P. Donovan, F. Spaepen, D. Turnbull, J.M. Poate, D.C. Jacobson, Calorimetric studies of crystallization and relaxation of amorphous Si and Ge prepared by ion implantation, *J. Appl. Phys.* 57 (1985) 1795–1804. doi:10.1063/1.334406.
- [391] E.P. Donovan, F. Spaepen, D. Turnbull, J.M. Poate, D.C. Jacobson, Heat of crystallization and melting point of amorphous silicon, *Appl. Phys. Lett.* 42 (1983) 698–700. doi:10.1063/1.94077.
- [392] M. Gamero-Castaño, A. Torrents, R. Borrajo-Pelaez, J.-G. Zheng, Amorphization of hard crystalline materials by electrosprayed nanodroplet impact, *J. Appl. Phys.* 116 (2014) 174309. doi:10.1063/1.4901287.
- [393] Y. He, L. Zhong, F. Fan, C. Wang, T. Zhu, S.X. Mao, In situ observation of shear-driven amorphization in silicon crystals, *Nat. Nanotechnol.* advance online publication (2016). doi:10.1038/nnano.2016.166.
- [394] D.E. Grady, The spall strength of condensed matter, *J. Mech. Phys. Solids.* 36 (1988) 353–384. doi:10.1016/0022-5096(88)90015-4.
- [395] M.A. Tschopp, G.J. Tucker, D.L. McDowell, Structure and free volume of  $\langle 110 \rangle$  symmetric tilt grain boundaries with the E structural unit, *Acta Mater.* 55 (2007) 3959–3969. doi:10.1016/j.actamat.2007.03.012.
- [396] A.P. Thompson, L.P. Swiler, C.R. Trott, S.M. Foiles, G.J. Tucker, Spectral neighbor analysis method for automated generation of quantum-accurate interatomic potentials, *J. Comput. Phys.* 285 (2015) 316–330. doi:10.1016/j.jcp.2014.12.018.

## Appendix A – LAMMPS Input Files

In the present work we have simulated the energy of 79 grain boundaries in bcc tantalum, as described by the coincident site lattice (CSL) model, and examined grain boundary structures to facilitate discussion and comparison. The supplemental material details complete tilt axis  $\langle abc \rangle$ , grain boundary normal  $(hkl)$ ,  $\Sigma$  index, misorientation, and conversion of these values into appropriate simulation basis for four tilt axes:  $\langle 001 \rangle$ ,  $\langle 011 \rangle$ ,  $\langle 111 \rangle$ , and  $\langle 112 \rangle$ . We use the MD code LAMMPS [162] to generate and relax the various bicrystal structures based on the scheme of Tschopp et al. [174,175,395]. Briefly, one crystal is sequentially shifted with respect to another along its  $\gamma$ -surface, atoms that exceed an overlap criteria are selectively removed, and the boundary is relaxed in the GB normal direction. The grain boundary energy (GBE) is calculated by evaluating the excess energy of the system per grain boundary unit area, taking into account that each simulation contains two parallel grain boundaries. The embedded atom model (EAM) potential developed by Ravelo et al. [95] is principally employed, but the importance of the  $\Sigma 3$  coherent twin boundary to deformation behavior warranted a “quantum accurate” investigation using a spectral neighbor analysis potential (SNAP) developed by Thompson et al. [396]. Depending on the boundary orientations, between hundreds and thousands of possible atomic structures containing up to fifty thousand atoms were sampled to produce each minimum energy configuration, thus neither density functional theory (DFT) nor extended use of SNAP is practical for the present study.

**A-1, Bicrystal Grain Boundaries**

```

# Filename: in.GB_Ta_STGB
# LAMMPS Input File for Bicrystal Grain Boundaries

# ----- Setup Variables -----
variable etol equal 1.0e-25
variable ftol equal 1.0e-25
variable maxiter equal 5000
variable maxeval equal 10000
variable latparam equal 3.304
variable minimumenergy equal -8.100
variable overlapboth equal 1
variable gbnam index Ta_Sigma5
variable counter equal 0
variable inc equal "v_latparam / 12"

# ----- How Big -----
# -- measured in unit cells -----
variable xuh equal 4
variable yuh equal 4
variable zuh equal 4

variable xul equal -4
variable yul equal -4
variable zul equal -4

# ----- Grain1 -----

# These variable can be hardwired as written or read into lammmps via the command line
# at run time
variable 1x1 equal 0
variable 1x2 equal 1
variable 1x3 equal -3

variable 1y1 equal 0
variable 1y2 equal 3
variable 1y3 equal 1

variable 1z1 equal 1
variable 1z2 equal 0
variable 1z3 equal 0

# ----- Grain2 -----

```



```

variable 2x1 equal ${1x1}
variable 2x2 equal -1*${1x2}
variable 2x3 equal ${1x3}

variable 2y1 equal -1*${1y1}
variable 2y2 equal ${1y2}
variable 2y3 equal -1*${1y3}

variable 2z1 equal ${1z1}
variable 2z2 equal -${1z2}
variable 2z3 equal ${1z3}

# Insert x,y,z sizes in LU and calculate in Angstroms
variable xsize1 equal "sqrt(v_1x1^2 + v_1x2^2 + v_1x3^2)"
variable ysize1 equal "sqrt(v_1y1^2 + v_1y2^2 + v_1y3^2)"
variable zsize1 equal "sqrt(v_1z1^2 + v_1z2^2 + v_1z3^2)"
variable xsize2 equal "sqrt(v_2x1^2 + v_2x2^2 + v_2x3^2)"
variable ysize2 equal "sqrt(v_2y1^2 + v_2y2^2 + v_2y3^2)"
variable zsize2 equal "sqrt(v_2z1^2 + v_2z2^2 + v_2z3^2)"
if "${xsize1} <= ${xsize2}" then "variable xsize equal ${xsize1}" else "variable xsize
equal ${xsize2}"
if "${zsize1} <= ${zsize2}" then "variable zsize equal ${zsize1}" else "variable zsize equal
${zsize2}"
variable xlen equal "v_xsize * v_latparam"
variable zlen equal "v_zsize * v_latparam"

# Determine number of increments for displacement grid in the in-plane GB directions
variable xinc equal "floor(v_xlen / v_inc)"
variable zinc equal "floor(v_zlen / v_inc)"

# Implement overlap criterion
variable overlapinc equal 86

# ----- Define loops for simulation -----
label loopa
variable a loop ${xinc}
variable tx equal "(v_a-1) / v_xinc * v_xsize"
label loopb
variable b loop ${zinc}
variable tz equal "(v_b-1) / v_zinc * v_zsize"
label loopd
variable d loop ${overlapboth}
label loopc
variable c loop ${overlapinc}
variable overlapdist equal "(0.275 + 0.005 * (v_c-1))*v_latparam"

```

```

# ----- Calculate counter and create data directory -----
variable ctemp equal ${counter}+1
variable counter equal ${ctemp}
variable ctemp delete
print "Counter: ${counter}"
shell mkdir ${gbname}

# ----- Initialize Simulation -----
clear
units metal
dimension 3
boundary p p p
atom_style atomic

# ----- Create Atomistic Structure -----
#lattice bcc ${latparam} spacing ${xsize1} ${ysize1} ${zsize1}
lattice bcc ${latparam} orient x ${1x1} ${1x2} ${1x3} orient y ${1y1} ${1y2} ${1y3}
orient z ${1z1} ${1z2} ${1z3} spacing ${xsize1} ${ysize1} ${zsize1}
region whole block ${xul} ${xuh} ${yul} ${yuh} ${zul} ${zuh} units lattice
create_box 2 whole
region upper block INF INF 0.0 ${yuh} INF INF units lattice
create_atoms 1 region upper
lattice bcc ${latparam} orient x ${2x1} ${2x2} ${2x3} orient y ${2y1} ${2y2} ${2y3}
orient z ${2z1} ${2z2} ${2z3} spacing ${xsize2} ${ysize2} ${zsize2}
region lower block INF INF ${yul} 0.0 INF INF units lattice
create_atoms 2 region lower
group upper type 1
group lower type 2

# ----- Define Interatomic Potential -----
pair_style eam/alloy
pair_coeff * * Ta-v13.setfl Ta Ta
neighbor 2.0 bin
neigh_modify delay 10 check yes

# ----- Displace atoms and delete overlapping atoms -----
displace_atoms upper move ${tx} 0 ${tz} units lattice
if "$d == 1" then "delete_atoms overlap ${overlapdist} lower upper"
if "$d == 2" then "delete_atoms overlap ${overlapdist} upper lower"
if "$c == 1" then "variable atmprev equal 1"
variable natoms equal "count(all)"
print "Previous: ${atmprev}, Present: ${natoms}"
if "${atmprev} == ${natoms}" then "jump in.GB_Ta_STGB loopend"

```

```

# ----- Define Settings -----
compute csym all centro/atom bcc
compute eng all pe/atom
compute eatoms all reduce sum c_eng
# compute 4 all stress/atom pair

# ----- Run Minimization -----
reset_timestep 0
thermo 10
thermo_style custom step pe lx ly lz press pxx pyy pzz c_eatoms
min_style cg
minimize ${etol} ${ftol} ${maxiter} ${maxeval}

# ----- Run Minimization 2-----
# Now allow the box to expand/contract perpendicular to the grain boundary
reset_timestep 0
thermo 10
thermo_style custom step pe lx ly lz press pxx pyy pzz c_eatoms
fix 1 all box/relax y 0.0 vmax 0.001
min_style cg
minimize ${etol} ${ftol} ${maxiter} ${maxeval}

# ----- Calculate GB Energy -----
variable esum equal "v_minimumenergy * count(all)"
variable xseng equal "c_eatoms - (v_minimumenergy * count(all))"
variable gbarea equal "lx * lz * 2"
variable gbe equal "(c_eatoms - (v_minimumenergy * count(all)))/v_gbarea"
variable gbemJm2 equal ${gbe}*16021.7733
variable gbernd equal round(${gbemJm2})
print "After third minimization:"
print "GB energy is ${gbemJm2} mJ/m^2"

# Store number of atoms for overlap criterion, i.e., do not rerun equivalent configurations
variable atompPrev equal "v_natoms"

#predump
if "${counter} < 2" then "dump 1 all custom 1000 dump.${gbname}.pre id type x y z
c_csym c_eng"

# ----- Dump data into Data file -----
reset_timestep 0
timestep 0.001
velocity all create 10 95812384
fix 2 all nvt temp 5 5 100
#fix 2 all npt temp 5 5 100 iso 0 0 100 drag 0.2

```

```
dump 2 all custom 1000 dump.${gbyname}_${gbernd} id type x y z c_csym c_eng  
run 0  
#shell cd ..
```

```
# ----- End of loop structure -----  
label loopend  
next c  
jump in.GB_Ta_STGB loopc  
variable c delete  
next d  
jump in.GB_Ta_STGB loopd  
variable d delete  
next b  
jump in.GB_Ta_STGB loopb  
variable b delete  
next a  
jump in.GB_Ta_STGB loopa  
print "All done"
```

**A-2, Piston-Driven Shock**

```

# A few variables to make the piston velocity loop hardwired...
# The length (in timesteps) of the ramp
Variable      ramp_timeup  equal 5000 #
variable      ramp_timedown equal 50000 #
# The no. of steps in the ramp (more steps=closer to linear ramp)
variable      ramp_steps  equal 1000
# This is the final shock strength in A per ps
variable      shock equal 7.5
variable      oblq equal 0.0
variable      ratio equal ${oblq}/${shock}

#Initialization

units        metal
boundary     p p s
atom_style   atomic
neighbor     1.0 bin
neigh_modify every 1 delay 2 check yes

#100 Lattice
lattice      bcc 3.304 orient x 1 0 0 orient y 0 1 0 orient z 0 0 1

region       box block -50 50 -50 50 0 1515 units lattice
create_box   1 box
create_atoms 1 box

pair_style    eam/alloy
pair_coeff    * * ./Ta1-Ravelo.setfl Ta

minimize 1.0e-4 1.0e-6 100 1000
velocity     all create 600.0 482748 dist gaussian
fix init all temp/rescale 1 300 300 1 1
fix          1 all nve
run 10000
reset_timestep 0

compute 1 all ke/atom
compute 2 all centro/atom 14
compute 3 all pe/atom
compute 4 all stress/atom pair
compute 5 all cna/atom 3.9

```

```
thermo_style custom step temp ke pe etotal press pxx pyy pzz pxy pxz pyz ly lx lz vol zhi
thermo_modify      lost warn norm yes
thermo             100
```

```
reset_timestep 0
```

```
# Apply shock fixes
region piston block INF INF INF INF 0 2 units lattice
group piston region piston
fix      2 piston setforce 0.0 0.0 0.0
```

```
#Set thermo and dump for run
```

```
thermo             100
```

```
dump OUT1 all custom 1000 dump.Ta_piston_all.* id x y z vx vy vz c_1 c_2 c_3 c_5
c_4[1] c_4[2] c_4[3] c_4[4] c_4[5] c_4[6]
```

```
dump OUT2 all custom 10000 dump.Ta_piston_defects.* id x y z vx vy vz c_5 c_4[3]
## modify to get only non-bcc atoms (cna!=3)
dump_modify OUT2 thresh c_5 != 3
```

```
# THIS LOOP DOES THE RAMP UP
```

```
variable i loop ${ramp_steps}
label loop
variable piston_vel equal ${shock}/${ramp_steps}/${i}
print      "Vel=${piston_vel}"
variable Up equal ${piston_vel}
variable Vp equal ${piston_vel}*${ratio}
velocity piston set 0.0 ${Vp} ${Up} sum no units box
variable runfor equal ($ramp_timeup)/${ramp_steps}
print      "DIAG2 - Piston velocity is ${Up}:${Vp}, run for ${runfor}"
run        ${runfor}
next i
```

```
# THIS LINE MUST CHANGE IF YOU CHANGE THE FILENAME.....
```

```
jump in.spall-sc100_UpVp loop
```

```
run 50000
```

```
# THIS LOOP DOES THE RAMP DOWN
```

```
variable j loop ${ramp_steps}
label loop2
variable piston_vel equal ${shock}-${shock}/${ramp_steps}/${j}
print      "Vel=${piston_vel}"
```

```
variable    Up equal ${piston_vel}
variable    Vp equal ${piston_vel}*${ratio}
velocity    piston set 0.0 ${Vp} ${Up} sum no units box
variable    runfor equal (${ramp_timedown}/${ramp_steps})
print       "DIAG2 - Piston velocity is ${piston_vel}, run for ${runfor}"
run         ${runfor}
next j

# THIS LINE MUST CHANGE IF YOU CHANGE THE FILENAME.....
jump in.spall-sc100_UpVp loop2

undump OUT1
dump OUT3 all custom 500 dump.Ta_piston.* id x y z vx vy vz c_1 c_2 c_3 c_5 c_4[1]
c_4[2] c_4[3] c_4[4] c_4[5] c_4[6]

run 100000
```

**A-3, Flyer-Target Shock**

```

units          metal
boundary       p p s
atom_style     atomic
neighbor       1.0 bin
neigh_modify   every 1 delay 2 check yes

#VARIABLES
#Target and projectile size, etc,
variable       T equal 454.0
variable       CS equal 75.0
variable       F equal "v_T*0.5"
variable       Up equal 7.5
variable       Tu equal "v_Up*-2/3"
variable       Fu equal "v_Up*4/3"
variable       LO equal 4/3
variable       RO equal 2/3
variable       Tbox equal "v_T+v_RO"
variable       Fbox equal "v_F+v_LO"

# The Flyer plate and target are assigned initial velocities of 4/3 Up and -2/3 Up

# CREATE GEOMETRY
lattice        bcc 3.304 orient x 1 0 0 orient y 0 1 0 orient z 0 0 1
region         box block -${CS} ${CS} -${CS} ${CS} -${Fbox} ${Tbox} units lattice
create_box     1 box

region         flyer block -${CS} ${CS} -${CS} ${CS} -${Fbox} -${LO}
create_atoms   1 region flyer
group flyer region flyer

region         target block -${CS} ${CS} -${CS} ${CS} ${RO} ${Tbox}
create_atoms   1 region target
group target region target

pair_style     eam/alloy
pair_coeff     * * ./Ta1-Ravelo.setfl Ta

velocity       all create 300.0 482748 dist gaussian
minimize       1.0e-4 1.0e-6 100 1000

thermo_style   custom step temp ke pe etotal press pxx pyy pzz pxy pxz pyz ly lx lz vol
thermo_modify  lost warn norm yes
thermo        5

```



```
fix e all nvt temp 300.0 300.0 1.0
fix t all temp/rescale 1 300.0 300.0 1.0 1.0
# equilibration for 2000 steps
run 2000
unfix e
unfix t
reset_timestep 0

compute 1 all ke/atom
compute 2 all centro/atom 14
compute 3 all pe/atom
compute 4 all stress/atom pair
compute 5 all cna/atom 3.9

thermo 100
fix          1 all nve
velocity flyer set NULL NULL ${Fu} sum yes units box
velocity target set NULL NULL ${Tu} sum yes units box

dump OUT1 all custom 1000 dump.flyer.spall.all100_454a_150a_300K_U750.* id x y z
vx vy vz c_1 c_2 c_3 c_5 c_4[1] c_4[2] c_4[3] c_4[4] c_4[5] c_4[6]
dump OUT2 all custom 1000 dump.flyer.spall.notBCC_454a_150a_300K_U750.* id x y
z vx vy vz c_3 c_4[1] c_4[2] c_4[3]
## modify to get only non-bcc atoms (cna!=3)
dump_modify OUT2 thresh c_5 != 3

run 100000
```

**A-4, Quasi Isentropic Loading**

```

# ----- INITIALIZATION -----
units          metal
dimension      3
boundary       p      p      p
atom_style     atomic
variable latparam equal 3.304

# ----- ATOM DEFINITION -----

#lattice      bcc 3.304 orient x 1 0 0 orient y 0 1 0 orient z 0 0 1
#region       box block -150 150 -150 150 -150 150 units lattice
#create_box   1 box

read_data data.example

pair_style     eam/alloy
pair_coeff     * * ./Ta1-Ravelo.setfl Ta

# ----- SETTINGS -----
compute 1 all ke/atom
compute 3 all pe/atom
compute 4 all stress/atom
compute 5 all cna/atom 3.9

#####
thermo_style  custom step temp ke pe etotal press pxx pyy pzz pxy pxz pyz ly lx lz vol
thermo_modify  lost warn norm yes
thermo         100

reset_timestep 0

# Store final cell length for strain calculations
variable tmp equal "lz"
variable L0 equal ${tmp}
print "Initial Length, L0: ${L0}"

#####
# DEFORMATION
fix           1 all nve

# Output strain and stress info to file

```

```

# for units metal, pressure is in [bars] = 100 [kPa] = 1/10000 [GPa]
# p2, p3, p4 are in GPa
variable strain equal "(lz - v_L0)/v_L0"
variable p1 equal "v_strain"
variable p2 equal "-pxx/10000"
variable p3 equal "-pyy/10000"
variable p4 equal "-pzz/10000"
variable p5 equal "temp"
variable p6 equal "step"
variable p7 equal "lz"

fix def1 all print 100 "${p1} ${p2} ${p3} ${p4} ${p5} ${p6} ${p7}" file Ta_QI.def.txt
screen no

# Dump for Ovito post processing

dump OUT1 all custom 1000 dump.QI.* id x y z vx vy vz c_1 c_3 c_5 c_4[1] c_4[2]
c_4[3] c_4[4] c_4[5] c_4[6]

dump OUT2 all custom 500 dump.QI_defects.* id x y z vx vy vz c_3 c_5 c_4[3]
## modify to get only non-bcc atoms (cna!=3)
dump_modify OUT2 thresh c_5 != 3

variable sratet equal 1.0e9
variable sratet1 equal "v_sratet / 1.0e12"

fix      2 all deform 1 z erate ${sratet1} units box remap x
run 500000

#####
# SIMULATION DONE
print "All done!"

```

## Appendix B – Orientation Algorithm

- A. Find nearest 8 neighbors for each bcc atom.
- B. Create 8 pairs of atoms to create the  $\langle 111 \rangle$  family of directions.
- C. Assign  $\hat{n}_{111}$  such that  $\hat{n}_{ix} + \hat{n}_{iy} + \hat{n}_{iz}$  is maximized
- D. Take  $\hat{e}_{111} = \hat{n}_{111}/|\hat{n}_{111}|$
- E. Assign  $\hat{n}_{\bar{1}11}$  such that  $-\hat{n}_{ix} + \hat{n}_{iy} + \hat{n}_{iz}$  is maximized
- F. Take  $\hat{e}_{\bar{1}11} = \hat{n}_{\bar{1}11}/|\hat{n}_{\bar{1}11}|$
- G. Take  $\hat{e}_{0\bar{2}2} = \hat{e}_{111} \times \hat{e}_{\bar{1}11}/|\hat{e}_{111} \times \hat{e}_{\bar{1}11}|$
- H. Take  $\hat{e}_{\bar{4}22} = \hat{e}_{0\bar{2}2} \times \hat{e}_{111}/|\hat{e}_{0\bar{2}2} \times \hat{e}_{111}|$
- I. Take  $\hat{e}_{100} = \frac{1}{\sqrt{3}}\hat{e}_{111} - \frac{2}{\sqrt{6}}\hat{e}_{\bar{4}22}$
- J. Take  $\hat{e}_{010} = \frac{1}{\sqrt{3}}\hat{e}_{111} - \frac{1}{\sqrt{2}}\hat{e}_{0\bar{2}2} + \frac{1}{\sqrt{6}}\hat{e}_{\bar{4}22}$
- K. Take  $\hat{e}_{001} = \frac{1}{\sqrt{3}}\hat{e}_{111} + \frac{1}{\sqrt{2}}\hat{e}_{0\bar{2}2} + \frac{1}{\sqrt{6}}\hat{e}_{\bar{4}22}$
- L. Providing we use a right handed notation and pre-multiply a rotation matrix to transform a reference identity matrix " $\bar{I}$ " to our determined orientation  $\bar{O}$  the resulting rotation matrix  $\bar{R}$  will be equivalent to  $\bar{O}$ .
- M. Taking the orientation to be a function of Euler angles consisting of:  $z(\varphi), y(\theta), z(\psi)$
- N. Take  $\theta = \cos^{-1}(R_{33})$
- O. If  $\theta = 0$ , the solution is not unique as the function represents two undistinguishable rotations about the z axis.
  - a. Take  $\varphi = \cos^{-1}(R_{11})$
  - b. Take  $\psi = 0$
- P. If  $\theta \neq 0$ ,
  - a. Take  $\varphi = \sin^{-1}(R_{31}/\sin\theta)$
  - b. Take  $\psi = \sin^{-1}(R_{13}/\sin\theta)$
- Q. Quaternions can be determined as follows:
  - a.  $q_0 = \cos\left(\frac{\theta}{2}\right)\cos\left(\frac{\varphi+\psi}{2}\right)$
  - b.  $q_1 = \sin\left(\frac{\theta}{2}\right)\cos\left(\frac{\varphi-\psi}{2}\right)$
  - c.  $q_2 = \sin\left(\frac{\theta}{2}\right)\sin\left(\frac{\varphi-\psi}{2}\right)$
  - d.  $q_3 = \cos\left(\frac{\theta}{2}\right)\sin\left(\frac{\varphi+\psi}{2}\right)$
- R. The spatial components of the quaternion vector  $(q_1, q_2, q_3)$  can be intensity mapped to RGB color values in the normal way.
- S. Rudd offers an alternate color mapping function of the form:  $\left[\left(\frac{1}{\sqrt{3}}\right)\sin\psi + \frac{1}{2}\right]\hat{n}_{111}$ .

## Appendix C – Bicrystal Data

(hkl)[y]	Tilt[z]	Ortho.[x]	$\Sigma$	$\theta(^{\circ})$	GBE(mJ/m <sup>2</sup> )
0 1 0	1 0 0	0 0 -1	1	0	0
0 1 2 1	1 0 0	0 1 -1 2	145	9.53	1012
0 7 1	1 0 0	0 1 -7	25	16.26	1053
0 6 1	1 0 0	0 1 -6	37	18.92	1142
0 5 1	1 0 0	0 1 -5	13	22.62	1191
0 4 1	1 0 0	0 1 -4	17	28.07	1314
0 1 0 3	1 0 0	0 3 -1 0	109	33.4	1376
0 3 1	1 0 0	0 1 -3	5	36.87	1318
0 8 3	1 0 0	0 3 -8	73	41.11	1438
0 7 3	1 0 0	0 3 -7	29	46.4	1452
0 1 1 5	1 0 0	0 5 -1 1	73	48.89	1448
0 2 1	1 0 0	0 1 -2	5	53.13	1348
0 1 1 6	1 0 0	0 6 -1 1	157	57.22	1399
0 7 4	1 0 0	0 4 -7	65	59.49	1376
0 5 3	1 0 0	0 3 -5	17	61.93	1306
0 8 5	1 0 0	0 5 -8	89	64.01	1299
0 3 2	1 0 0	0 2 -3	13	67.38	1220
0 4 3	1 0 0	0 3 -4	25	73.74	1068
0 5 4	1 0 0	0 4 -5	41	77.32	1006
0 9 8	1 0 0	0 8 -9	145	83.27	666
0 1 0 9	1 0 0	0 9 -1 0	181	83.97	624
0 1 1	1 0 0	0 1 -1	1	90	0

(hkl)[y]	Tilt[z]	Ortho.[x]	$\Sigma$	$\theta(^{\circ})$	GBE(mJ/m <sup>2</sup> )
1 1 0	-1 1 0	0 0 2	1	0	0
7 7 1	-1 1 0	-1 -1 1 4	99	11.54	968
4 4 1	-1 1 0	-1 -1 8	33	20.05	1262
3 3 1	-1 1 0	-1 -1 6	19	26.53	1335
5 5 2	-1 1 0	-2 -2 1 0	27	31.59	1384
9 9 4	-1 1 0	-4 -4 1 8	89	34.89	1408
2 2 1	-1 1 0	-1 -1 4	9	38.94	1326
7 7 4	-1 1 0	-4 -4 1 4	57	44	1326
3 3 2	-1 1 0	-2 -2 6	11	50.48	1118
4 4 3	-1 1 0	-3 -3 8	41	55.88	1211
5 5 4	-1 1 0	-4 -4 1 0	33	58.99	1250
1 1 -1	-1 1 0	1 1 2	3	70.53	1298

5 5 6	-1 1 0	-6 -6 10	43	80.63	1250
7 7 10	-1 1 0	-10 -10 14	99	90.58	1141
3 3 5	-1 1 0	-5 -5 6	43	99.37	964
4 4 7	-1 1 0	-7 -7 8	81	102.12	844
1 1 -2	-1 1 0	2 2 2	3	109.47	278
4 4 9	-1 1 0	-9 -9 8	113	115.7	825
2 2 5	-1 1 0	-5 -5 4	22	121.01	1045
3 3 8	-1 1 0	-8 -8 6	41	124.12	1136
1 1 3	-1 1 0	-3 -3 2	11	129.52	1255
1 1 4	-1 1 0	-4 -4 2	9	141.06	1320
1 1 5	-1 1 0	-5 -5 2	27	148.41	1385
1 1 8	-1 1 0	-8 -8 2	33	159.95	1215
1 1 14	-1 1 0	-14 -14 2	99	168.46	987
1 1 16	-1 1 0	-16 -16 2	129	169.9	926
0 0 1	-1 1 0	-1 -1 0	1	180	0

(hkl)[y]	Tilt[z]	Ortho.[x]	$\Sigma$	$\theta(^{\circ})$	GBE(mJ/m <sup>2</sup> )
1 1 0	-1 1 -1	-1 1 2	1	0	0
10 11 1	-1 1 -1	-12 9 21	37	9.43	832
7 8 1	-1 1 -1	-9 6 15	19	13.17	990
5 6 1	-1 1 -1	-7 4 11	31	17.9	1153
4 5 1	-1 1 -1	-6 3 9	7	21.79	1194
3 4 1	-1 1 -1	-5 2 7	13	27.8	1264
5 7 2	-1 1 -1	-9 3 12	13	32.2	1285
2 3 1	-1 1 -1	-4 1 5	7	38.21	1194
5 8 3	-1 1 -1	-11 2 13	49	43.57	1165
3 5 2	-1 1 -1	-7 1 8	19	46.83	1078
4 7 3	-1 1 -1	-10 1 11	37	50.57	953
1 2 1	-1 1 -1	-3 0 3	3	60	298

(hkl)[y]	Tilt[z]	Ortho.[x]	$\Sigma$	$\theta(^{\circ})$	GBE(mJ/m <sup>2</sup> )
1 1 0	1 -1 2	2 -2 -2	1	0	0
11 13 1	1 -1 2	27 -21 -24	97	11.66	919
8 10 1	1 -1 2	21 -15 -18	55	15.5	1020
5 7 1	1 -1 2	15 -9 -12	25	23.07	1247
4 6 1	1 -1 2	13 -7 -10	53	27.53	1325
3 5 1	1 -1 2	11 -5 -8	35	34.05	1368
5 9 2	1 -1 2	20 -8 -14	55	38.57	1299
2 4 1	1 -1 2	9 -3 -6	7	44.42	1332
3 7 2	1 -1 2	16 -4 -10	31	52.2	1273

5 13 4	1 -1 2	30 -6 -18	35	57.12	1266
1 3 1	1 -1 2	7 -1 -4	11	62.96	1274
3 11 4	1 -1 2	26 -2 -14	73	69.97	1330
1 5 2	1 -1 2	12 0 -6	15	78.46	1372
1 7 3	1 -1 2	17 1 -8	59	85.14	1443
1 9 4	1 -1 2	22 2 -10	49	88.83	1461
1 11 5	1 -1 2	27 3 -12	49	91.17	1486
1 17 8	1 -1 2	42 6 -18	59	94.86	1486
0 2 1	1 -1 2	5 1 -2	5	101.54	1346

## Appendix D – HYADES

HYADES is a radiation hydrodynamics code for laser-plasma and hot dense matter studies developed by J.T. Larsen [211,212].

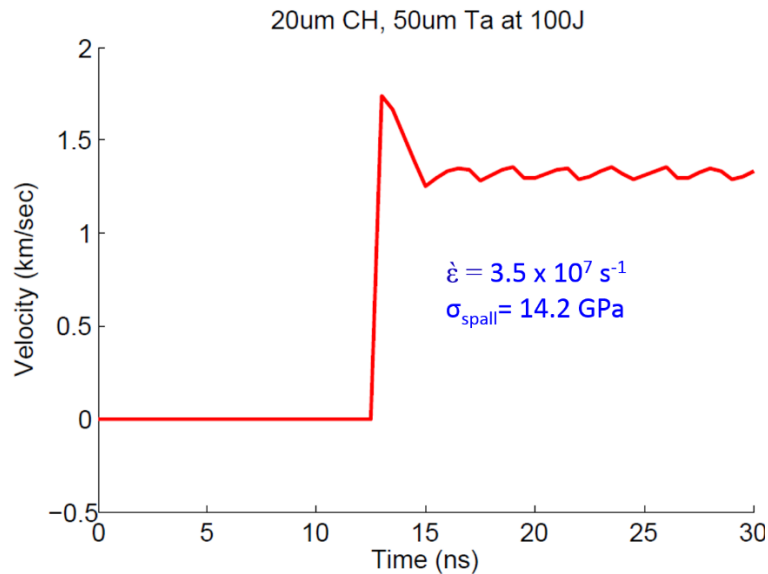


Figure A-1. Hyades simulation 100J pulse with 3 mm spot size interacting with 20  $\mu\text{m}$  CH and 50  $\mu\text{m}$  Ta.

HYADES incorporates laser-matter interaction and determines the physical response through an input EOS table and strength/melt models. The simulations run for tantalum use the following models and parameters:

- Shear: Steinberg [6.9e+11,1.45e-12,1.3e+3]
- Yield: Steinberg-Guinan [7.7e+9,22,0,0.283,1.1e+10]
- Spall: Cochran-Banner [4.4e9\*10,0.011]
- Melt: Lindemann [3.74e-4,1.3,1.67]

A sweep of experimental parameters and specimen dimensions was completed in order to select combinations that produced the largest strain-rates.



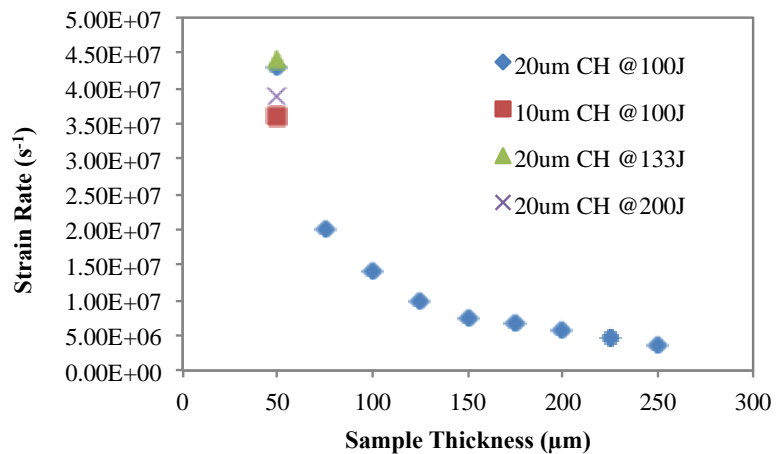


Figure A-2. Figure showing relationship between sample thickness and strain rate. For the smallest sample a scan of CH thickness and laser energy was also explored.

## Appendix E – Two Phase Method

The two phase method was implemented in LAMMPS [162]. We follow the general methodology used by Dozhdikov et al. [231]. The initial bcc crystalline Ta sample is  $75a_0$  long and  $10a_0$  in each of the lateral directions; all boundaries are periodic in nature and the computational cell contains 30000 atoms. The center two thirds are defined to remain solid and the outer third is marked to become liquid. The subsequent steps are followed.

1. For a chosen (P,T) point to evaluate, the system is seeded with a random velocity equivalent to half of T.
2. A Nose-Hoover thermostat-barostat (NPT) is applied, taking the system from (0,0.5T) to (P,0.75T) over  $6 \times 10^4$  femtosecond (fs) using 1 fs timesteps.
3. NPT is applied, maintaining the pressure at P and taking the temperature from 0.75 T to T over  $6 \times 10^4$  fs.
4. NPT is applied, maintaining the pressure at P and T for  $6 \times 10^4$  fs.
5. An anisotropic Nose-Hoover thermostat-barostat ( $NP_{xx}T$ ) is applied to the liquid region allowing for constant y/z cell dimensions while a micro-canonical ensemble (NVE) is applied to the solid region. The  $NP_{xx}T$  takes the material from T to 1.5T over  $6 \times 10^4$  fs.
6. NVE is applied to the solid regime while the liquid undergoes a  $NP_{xx}T$  returning the system from 1.5T to T over  $6 \times 10^4$  fs.
7. The entire system is allowed to evolve under NVE conditions for between  $2 \times 10^5$  and  $10^7$  fs depending on the level of accuracy needed. The time step is often increased at this stage to decrease the computational costs, but always allows for at least 10 steps per vibrational frequency, which is both pressure and temperature dependent.

In order to identify structural differences between solid and melted regions, Voronoi analysis was carried out using Ovito (<http://ovito.org>) [185]. Using Schlaefli notation, we tracked,  $n$ , the number of faces with 6 edges, which corresponds to the sixth index. Taking 150 bins along the long axis, the mean  $n$  was calculated for each bin and the first (spatial) derivative was taken. For systems in equilibrium, there will be a large spike in the derivative at the initial position of the solid-liquid interface. For systems below the melting temperature, the derivative peak will move into the initial liquid regime as the material solidifies – for systems above the melting temperature, the material will melt at the front and the solid will be consumed moving the derivative inwards. It is critical that enough simulation time be applied to observe the motion of the interface. Reduced error bars require much larger simulation times to observe measurable changes in the amounts of solid and liquid material near the melting point. The accuracy bars in the main text

correspond to simulations where the material is entirely solid or entirely liquid after a sufficiently long time has elapsed. The melting temperature at a given pressure is determined to be the simulation for which the interface showed the smallest (or no measureable) motion. Figure 5 shows two snapshots for a system evolving under a NVE ensemble at 2900 K at negative 2 GPa (2 GPa in tension). Growth of the solid phase represents that the selected P,T conditions lie within the solid (bcc) portion of the phase diagram.

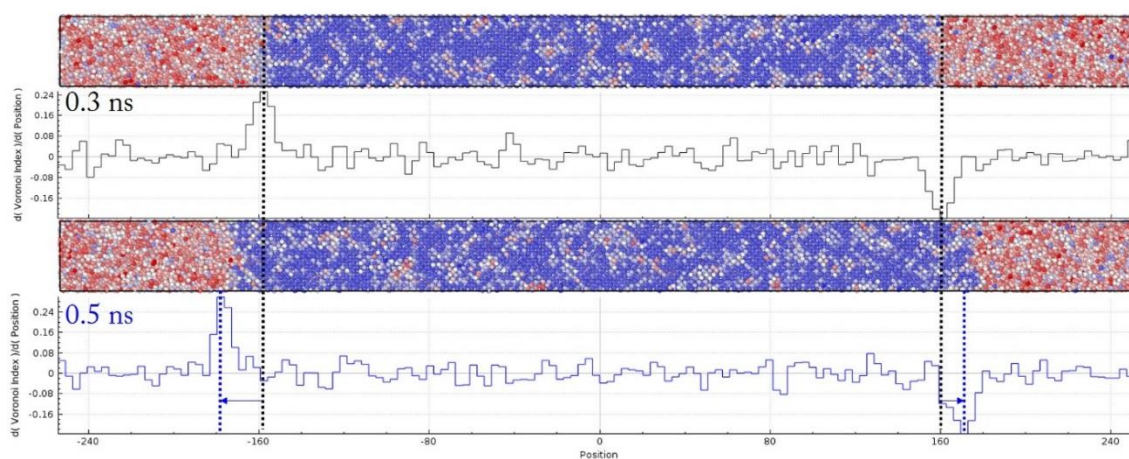


Figure A-3. Two phase simulation evaluated at 2900 K at -2 GPa showing solidification over 0.2 ns during NVE integration. The two phase system is colored by the 6th Voronoi index where blue atoms have 10 faces with 6 edges, red atoms have 0 faces with 6 edges, and white atoms have an intermediate 5 faces with 6 edges.

## Appendix F – Quasi-Isentropic Loading

An isentropic process is a thermodynamic process where there is no transfer of heat or matter. Additionally the process is fully reversible. The simulations here utilize a microcanonical (NVE) ensemble integrated using a velocity-Verlet algorithm as implemented in LAMMPS [162].

The analytical Verlet algorithm is inherently time reversible; by changing the arrow of time a system of atoms will retrace their forward trajectories [160]. In application of this algorithm, the positions and forces are taken as floating point numbers which inherently incorporates rounding procedures, the practical result is a very small random noise that deteriorates the symmetry of the algorithm.

The NVE ensemble maintains the system in isolation from the environment such that the total energy (E) and mass (here N for atoms) remains exactly known as the time goes on. If there is no other driver of the system, the volume (V) also remains exactly known. We introduce an external strain rate to the system by homogenously scaling the system points by a specified strain rate. The resulting molecular dynamics (MD) equations of motions (beginning with the momentum) can be written as follows:

$$\dot{r}_{i,n} = \frac{p_{i,n}}{m_n} + \dot{\epsilon}_i r_{i,n}, \quad (1)$$

where  $i=x,y,z$ ; and  $n$  is the particle number for the position  $r$ , momentum  $p$ , mass  $m$ , and strain-rate,  $d\epsilon/dt$ . Subsequently the time derivative of momentum can be defined by the force  $F$  and the system length  $L$  by the strain rate.

$$\dot{p}_{i,n} = F_{i,n} - \dot{\epsilon}_i p_{i,n}, \quad (2)$$

$$\dot{L}_i = \dot{\epsilon}_i L_i, \quad (3)$$

The resulting work done can be described as:

$$\dot{E} = \dot{Q} - \dot{W} = -P\dot{V} = \dot{W} \rightarrow \dot{Q} = 0, \quad (6)$$

Thus, it can be seen that the method implemented method introduces no external heat nor mass and that the evolution of the system can be time reversible. It is important to note that we use the term quasi-isentropic for two reasons. First, the method of integration introduces small variations by using efficient numerical integration methods that subtly remove the time reversibility by introducing small rounding errors. Secondly, the system will undergo plastic deformation which introduces visco-plastic work. The system's temperature will evolve in proportion to the amount of plasticity that takes place.